

Appendix B

RL 1150 m Subsidence Assessment Report (BECK Engineering 2023b)



ABN: 19 113 083 060




SUITE 223
813 PACIFIC HIGHWAY
CHATSWOOD
NSW 2067
AUSTRALIA

Telephone: +61 2 6421 1082
Mobile: +61 400 482 184
cdrover@beck.engineering
www.beck.engineering

ERNEST HENRY SLC TO 1150 mRL CAVE PROPAGATION & SUBSIDENCE ASSESSMENT

PREPARED FOR EVOLUTION MINING

DOCUMENT CONTROL

Date	Version	Comments	Signed
2023JAN13	DRAFT01	Initial draft for client review & comments.	
2023FEB09	DRAFT02	Re-submitted with changes following client feedback.	
2023APR22	FINAL	Re-submitted following additional client feedback.	
COPYRIGHT NOTICE Copyright of this document is retained by Beck Engineering Pty Ltd. Copyright is enforced to protect client interests.			

EXECUTIVE SUMMARY

Beck Engineering (BE) has conducted a cave propagation and surface subsidence assessment for Evolution Mining's Ernest Henry operations, located near Cloncurry in Queensland, Australia. This project aims were to:

1. Perform 3D non-linear modelling of the proposed Sublevel Caving (SLC) mining operations to the 1150 mRL, including forecasts of:
 - a. cave propagation
 - b. surface subsidence impact (i.e. displacements, strains, angular distortions and cave zone extent).
2. Use a hydro-mechanically coupled model to assess the groundwater effect on rock mass damage, subsidence and cave propagation, including long-term surface subsidence forecasts extending +100 years after the cessation of mining, including the effects of re-flooding of the mine back to a stable long-term groundwater table.
3. Forecast the subsidence impact to the southern waste dump, including estimates of the volume of waste material mobilised into the subsidence crater above the cave.

Our assessment is based on numerical modelling using finite element (FE) methods. An overview of the assessment, including the main findings, risks and recommendations is summarised below. More extensive details are provided in Section 3 of this report.

Main findings

1. This project updates the cave shape and surface subsidence forecasts for the Ernest Henry mine, which were previously made by Board, et al. (2009), as a part of the feasibility assessment for underground mining. BE's numerical simulation implements a mechanical-flow-hydro coupled simulation framework, in the Abaqus Explicit finite element and FS4 flow codes, in order to realistically simulate the complex physics of the underground sublevel caving mining process, as well as the inter-dependencies between mining and the local hydrogeology. This modelling approach has been used at Ernest Henry for several years and the forecasts of cave performance and subsidence have been robustly calibrated to numerous real observations during that time.
2. Close calibration between several iterations of BEs model forecasts and real observations at the mine have been achieved over several years utilising a combination of seismic data, surveys of the actual cave muckpile profile, aerial photography as well as GPS and INSAR displacement readings at the surface. Further information on those calibrations is available to review in prior reports by Beck (2021) and Campbell (2022). The model calibration was updated for this 2023 phase of surface subsidence modelling and assessment.
3. Historic sublevel caving operations at the Ernest Henry mine have resulted in a progressive collapse and unravelling of the southern wall of the original open pit mine. This process of caving is forecast to continue as the SLC operations advance to the 1150 mRL. This is a necessary part of the cave mining process in order to prevent the formation of an airgap. A zone of rock mass damage envelops the cave zone, as does a zone of rock mass movement, with the magnitude of the displacements being highest around the immediate cave zone boundary and decreasing with distance away from the cave.
4. Beyond the immediate limits of the cave zone and subsidence crater that the cave creates on the surface, the east, west and north original walls of the open pit are forecast to remain stable as the underground mining of the SLC operations advances as deep as the 1150 Level.
5. When SLC operations are completed on the 1150 Level, the cave zone will extend from the 1150 mRL to the 2156 mRL in the south of the mining zone. At that time, the cave is forecast to have propagated southwards as far as the 37840 mN position (mine grid), which is approximately 370 m to the south of the southern-most point of the original crest of the open pit mine.
6. The cave zone is forecast to propagate into the southern waste dump (volume ~ 112,000,000 m³) during 2024. Given the forecast final extents of the cave zone on surface, a total of 7,019,705 m³ or 6.3 % of the southern waste dump material is expected to become progressively undercut by the cave over time and enter the subsidence crater (i.e. flow zone). Some of the waste dump material could be expected to rill into the original open pit. All caved waste dump material would be contained within the final subsidence crater.

7. Approximately 31,576,916 m³ of caved rock is forecast to fill the lower benches of the open pit at the end of the 1150 SLC mining. This material would be primarily composed of broken rock which has caved from around the orebody, as well as some waste dump material that has rilled into the cave from above.
8. The top of the cave muckpile would have a variable shape after mining, with some basin sections and also steeper slopes being created due to the subsidence and rilling effects of the broken material during the caving process. The depth of the surface subsidence crater will vary, but our forecasts indicate a maximum depth in the order of 360 m below the natural ground level, once the SLC is completed to the 1150 mRL.
9. Decommissioning of the mine dewatering and bore field pumps after mining the SLC to the 1150 mRL would result in a gradual flooding of the underground and open pit mine. Our hydro-mechanically coupled simulation of the post-mining period of flooding indicates that the groundwater table would re-charge up to the 2100 mRL¹, which is approximately 56 m below the natural ground surface elevation. All excavations of the underground and open pit mine would be flooded below this elevation.
10. The effect of re-flooding the rock mass and mine voids is an uplift effect to the rock mass in the order of 100 mm or less, with the larger uplift effect occurring closer to the mine voids and mainly in the south (hangingwall) of the orebody. This occurs due to a poro-elastic rebound effect. The drawdown of the groundwater table creates a minor and temporary subsidence effect as an elastic displacement response of the rock mass. This process is reversed as the groundwater recharges after mining is completed and dewatering activities are ended. The 100 mm uplift occurs very gradually as the phreatic surface recovers, likely taking several decades.
11. As the groundwater table rises, there is a minor increase in rock mass damage in the open pit slopes due to pore water pressure increase. This damage transitions from a *Negligible* severity prior to groundwater recharge to a *Minor* severity in most areas. The damage effect is superficial in nature and typically extends ~ 10 m into the pit slope. As a result, minor batter scale instabilities of the pit slope could be expected to occur during flooding, such as loosening and sloughing of small rock blocks off the submerged parts of the pit slope. However, no major slope instability is indicated by the damage severity forecasts.
12. The AM fault in the deep footwall of the underground mine also experiences a modest damage increase during flooding but this is a managed risk with *Negligible* forecast impact, as this fault does not intersect the pit slopes and no adverse impact would be apparent at the surface. Affected underground excavations would be flooded, contained and completely inaccessible at the time.
13. The flow simulations do not indicate that any significant airgaps remain in the cave zone after mining. Furthermore, at this time there are no voids such as large open stopes existing or planned to be excavated close to surface which have the potential to experience a “chimneying” style of instability and collapse over time. As a result, there is a *Negligible* risk of further significant subsidence events occurring after mining is completed.
14. Beyond the *Negligible* subsidence impact contour, the southern waste rock dump is not forecast to experience any adverse subsidence-related impact.

In summary, our main findings and conclusions from the model forecasts are:

1. The planned underground mining of the SLC to 1150 mRL results in progressive caving of the orebody and the surface expression of the cave zone continues to propagate and expand, primarily towards the south, southeast and southwest. Relatively large steps in cave growth occur during 2024 and 2026.
2. The cave zone eventually consumes in excess of 7 million cubic metres of the southern waste dump. For context, this represents 6.3 % of the 112 million cubic metres of the dump that exists at present. The waste dump material would rill into the subsidence crater and open pit. The Clay Pit Access haul road and nearby laydown yard are also consumed by the cave over time.

¹ This elevation of the final post-mining phreatic surface is simulated in the Abaqus numerical model for excavation stability assessment purposes. It represents the long-term far-field mean phreatic surface elevation and does not account for the detailed surface catchment features and mine closure planning.

3. There are no significant air gaps forecast to remain within the cave zone at the conclusion of the underground mine plan and no further growth of the cave is forecast as a result of groundwater recharge and mine flooding.
4. After decommissioning the mine dewatering infrastructure and bore field, the groundwater recharge is forecast to gradually return to a long-term phreatic surface at the 2100 mRL, which is approximately 56 m below the natural ground surface elevation.
5. Re-flooding of the rock mass in the mining precinct has a minor uplift displacement effect on the rock mass. It also causes a modest but superficial increase in rock mass damage to the open pit walls. Minor batter-scale instabilities of the pit walls could occur during the re-flooding process due to local pore water pressure increase at the batter face, but no large scale pit slope instability is forecast at any time.

Recommendations

Given the findings of this assessment, BE recommend:

1. The closure plan for the mine should include the subsidence zone and areas of related geotechnical impacts. Permanent exclusion barriers, such as solid rock bunds, should be established around the subsidence zone to barricade and prevent vehicle, animal and foot access to the subsidence-affected region. The position of the barriers should be based on measured subsidence and a risk assessment after completion of all mining, however the subsidence extents are forecast. Permanent earth bunds to restrict access to the subsidence zone are recommended to be placed outside the *Negligible* subsidence impact contour (see Figure 3-48 & Figure 3-49) and around the waste dumps and open pit, plus a further stand-off of 30 m, or to legislated requirements.
2. Ongoing monitoring of cave propagation, groundwater conditions and subsidence effects using a range of geotechnical instrumentation. The mine already has a comprehensive monitoring programme underway. This should be continued and new instruments installed, as necessary, to monitor the evolution of conditions as the cave increases in size and replace any monitoring ability which may be lost over time, where safely accessible.
3. Ongoing subsidence model calibration and validation of forecasts or updates, as required from time to time.
4. Ongoing groundwater monitoring and regular verification of groundwater modelling through comparison to water balance and water system responses.

Limitations

In addition to the normal resolution limits associated with the current finite element model, the main limitations of this project are:

- A 3D groundwater model and current groundwater surface were not provided as part of this project. The groundwater in the model was simulated using the pre-mining groundwater level and hydraulic conductivities provided. The phreatic surface forecast do not account for the detailed surface catchment features and closure planning at the mine and are made for excavation stability assessment purposes only.
- The current understanding of rockmass strength properties and in-situ stress, particularly at depth and/or in future mining areas where measurements are limited.
- Resolution of the structural model, especially close to surface where small and intermediate scale-structures can play a significant role in the evolution of the instability around the edges of the cave zone, but also in other areas, such as the cave abutments at depth.

Enquiries

Please direct further enquiries to the undersigned.



Christopher Drover

PhD MEngSc BE (Hons) BSc

Principal Engineer, Mining & Rock Mechanics

TABLE OF CONTENTS

1	INTRODUCTION	10
2	PROJECT WORKFLOW, BACKGROUND DATA & MODEL COMPOSITION	12
2.1	Project workflow & simulation framework.....	12
2.2	Caving criterion & cave properties.....	13
2.3	FS4 model parameters, constants & assumptions.....	13
2.4	Topography.....	14
2.5	Stress Field.....	14
2.6	Geotechnical domain assignment.....	15
2.6.1	Estimated material properties for modelling.....	15
2.7	Structural model resolution.....	20
2.8	Hydrogeological Conditions	25
2.9	Mining methods, geometry & sequence	28
2.10	Draw schedule.....	32
2.11	Calibration	33
3	FORECASTS, INTERPRETATION & DISCUSSION	41
3.1	Rockmass damage scale	41
3.2	Forecasts – SLC to 1150 mRL	43
3.3	Other mechanisms of post closure movement.....	99
4	CONCLUSIONS, RECOMMENDATIONS & LIMITATIONS.....	102
	REFERENCES.....	105
	APPENDIX A - LRX CONSTITUTIVE FRAMEWORK.....	106
	Constitutive model and physical composition.....	106
	The LR2 constitutive framework.....	106
	Constitutive model for the continuum parts	106
	Representation of explicit structure.....	110
	Extension for the case of transversal isotropy	110
	Model parameter to determine rock strength.....	112
	Modelling softening behaviour	113
	The common damage scale	114
	Assessing seismic potential with RER.....	114
	Mechanical response in the presence of pore-water pressure	115
	Additional References.....	115
	APPENDIX – MATERIAL STRENGTH ENVELOPE CHARTS.....	117

LIST OF FIGURES

Figure 1-1 Mine excavation geometry, model and mine design basic specifications..... 11

Figure 2-1 Overview of the FE-FS4 cave coupling simulation methodology..... 13

Figure 2-2 Principal stress orientations for the Ernest Henry mine model..... 15

Figure 2-3 Simulated pre-mining stress state along a vertical sample path for three locations in the model space.16

Figure 2-4: Perspective view showing the main rockmass domains in the model 17

Figure 2-5: Indicative rockmass softening curve demonstrating the plastic strain transition points ϵ_1 and ϵ_2 20

Figure 2-6 Structural model of the Ernest Henry mine..... 22

Figure 2-7 Structural model of the Ernest Henry mine (Top view, clipped at 1200 mRL)..... 23

Figure 2-8 DFN groups of explicitly modelled intermediate and small-scale structures..... 24

Figure 2-9 Variation of hydraulic conductivity as a function of rockmass damage 27

Figure 2-10 Example of variation of hydraulic conductivity (Y-axis) with LogP (X-axis) in the hydro-coupled model. 27

Figure 2-11 Evolution of the phreatic surface recovery to near pre-mining levels following mine closure and re-flooding. 28

Figure 2-12 Global geometry of the finite-element simulation domain for the Ernest Henry models..... 29

Figure 2-13 Geometric detail of the finite element representation of underground mining excavations of the future SLC. 30

Figure 2-14 Simulated extraction sequence for the open pit and underground mining. 31

Figure 2-15 Planned production draw tonnes input to the FS4 flow simulation..... 32

Figure 2-16 Example of simulated production draw for one sublevel of the SLC (top view, 1200 Level)..... 32

Figure 2-17 Mine-scale view of the calibrated model forecast for cave propagation as at 2022 Q4..... 34

Figure 2-18 Latest aerial photograph showing the southern limits of the surface subsidence crater..... 35

Figure 2-19 Match between modelled and observed spatial extent of the surface subsidence crater in 2022..... 36

Figure 2-20 Modelled versus measured displacement match in the X (east) direction in (2019 Q4 to 2022 Q4)..... 37

Figure 2-21 Modelled versus measured displacement match in the Y (north) direction (2019 Q4 to 2022 Q4)..... 38

Figure 2-22 Modelled versus measured displacement match in the Z (vertical) direction (2019 Q4 to 2022 Q4)..... 39

Figure 2-23 Comparison of modelled and measured (via INSAR) surface displacement during 2022..... 40

Figure 3-1: Rockmass damage scale 41

Figure 3-2 Stress vs. Strain chart showing corresponding rockmass damage levels..... 42

Figure 3-3 South wall of the Ernest Henry open pit and cave zone (photo taken January 2023). 48

Figure 3-4 Current mining geometry (solid) and future mining to 1150 mRL (wireframe), view north. 49

Figure 3-5 3D view of the phreatic surface evolution at stages of re-flooding from the end of mining to 100 years after mine closure, view northwest 50

Figure 3-6 Cave and damage zone forecast for mining to 2022 Q4 (F091), view west. 51

Figure 3-7 Cave and damage zone forecast for mining to 2024 Q4 (F099), view west. 52

Figure 3-8 Cave and damage zone forecast for mining to 2026 Q4 (F107), view west. 53

Figure 3-9 Cave and damage zone forecast at the conclusion of underground mining to 1150 mRL (F115), view west. 54

Figure 3-10 Cave and damage zone forecast 100 years after completion of mining with water @ 2100 mRL, view west. 55

EVOLUTION MINING: ERNEST HENRY SLC TO 1150 mRL CAVE PROPAGATION & SUBSIDENCE ASSESSMENT

Figure 3-11	Cave and damage zone forecast at the conclusion of underground mining (i.e. SLC to 1150 mRL), view north.	56
Figure 3-12	Cave and damage zone forecast 100 years after completion of mining with water @ 2100 mRL, view north.	57
Figure 3-13	Cut away section showing the phreatic surface evolution during groundwater recharge and cave/pit flooding (inclined slice along SLC hangingwall), view north.....	58
Figure 3-14	Cut away section showing the phreatic surface evolution during groundwater recharge and cave/pit flooding (sliced at easting central to SLC), view west.....	59
Figure 3-15	Cutaway section showing phreatic surface evolution during groundwater recharge and cave/pit flooding (sliced at main hoist shaft northing), view northwest.....	60
Figure 3-16	Plan view showing forecast rockmass damage and cave outline (2022 Q4).	61
Figure 3-17	Plan view showing forecast rockmass damage and cave outline (2024 Q4).	62
Figure 3-18	Plan view showing forecast rockmass damage and the cave outline (2026 Q4).....	63
Figure 3-19	Plan view showing forecast rockmass damage and the cave outline at the end of mining and before pit flooding.	64
Figure 3-20	Plan view showing rockmass damage and the cave outline after 100 years of groundwater recharge post-mining.	65
Figure 3-21	Long section of forecast rockmass damage and the cave zone at the end of mining to 1150 mRL (view east).	66
Figure 3-22	Long section of forecast rockmass damage and the cave zone after 100 years of groundwater recharge post-mining (view east).	67
Figure 3-23	Long section of total displacement (post open pit mining) at the end of mining to 1150 mRL (view east).	68
Figure 3-24	Long section of total displacement (post open pit mining) after 100 years of groundwater recharge (view east).	69
Figure 3-25	Long section showing displacement magnitude and direction induced by groundwater recharge to the long-term equilibrium (view east).....	70
Figure 3-26	Forecast surface movement due to underground mining the SLC to 1150 mRL, before groundwater recharge.	71
Figure 3-27	Forecast surface movement due to underground mining the SLC to 1150 mRL and after 100 years of groundwater recharge	72
Figure 3-28	Spatial extent of the surface subsidence crater (cave zone) at the present time (2022 Q4).....	73
Figure 3-29	Forecast spatial extents of the subsidence crater (2023 Q4).....	74
Figure 3-30	Forecast spatial extents of the subsidence crater (2024 Q4).....	75
Figure 3-31	Forecast spatial extents of the subsidence crater (2025 Q4).....	76
Figure 3-32	Forecast spatial extents of the subsidence crater (2026 Q4).....	77
Figure 3-33	Forecast spatial extents of the subsidence crater (2027 Q4).....	78
Figure 3-34	Forecast spatial extents of the subsidence crater (end of mining to 1150 mRL).	79
Figure 3-35	Forecast spatial extents of the subsidence crater (end of mining +100 years).....	80
Figure 3-36	The final geometry of the excavated mine voids, including the open pit and underground mine, at the end of mining (view east, cave not shown).....	81
Figure 3-37	Final shape of the excavated mine voids and cave zone, showing the final surface profile of the rilling muckpile inside the subsidence crater (view east).....	82
Figure 3-38	Final shape of the excavated mine voids and cave zone showing the major dimensions (view east).....	83

Figure 3-39	Final geometry of the original open pit and cave zone expression at the surface and the major dimensions (top view).....	84
Figure 3-40	Isosurfaces of underground mining-induced displacement after 100 years of groundwater recharge (view east). 85	
Figure 3-41	Isosurfaces of underground mining-induced displacement after 100 years of groundwater recharge (perspective view).	86
Figure 3-42	Isosurfaces of underground mining-induced displacement after 100 years of groundwater recharge (view north). 87	
Figure 3-43	Isosurface of the caving-induced fracture zone (plastic strain of 0.2 %) relative to the cave boundary at the end of mining + 100 years flooding (view east)	88
Figure 3-44	Isosurface of the caving-induced fracture zone (plastic strain of 0.2 %) relative to the cave boundary at the end of mining + 100 years flooding (view north).....	89
Figure 3-45	Surface infrastructure subsidence impact severity assessment scheme based on Boscardin & Cording (1989). 90	
Figure 3-46	Surface subsidence impact severity forecast at the end of mining.	91
Figure 3-47	Surface subsidence impact severity forecast after 100 years of groundwater recharge post-mining.....	92
Figure 3-48	Contours of surface subsidence impact severity at the 2156 mRL at the end of mining and proposed long-term exclusion zone boundary	93
Figure 3-49	Contours of surface subsidence impact severity at the 2156 mRL after 100 years of groundwater recharge post-mining and proposed long-term exclusion zone boundary.	94
Figure 3-50	Mining-related voids and the cave zone and their respective volumes (2022 Q4).....	95
Figure 3-51	Mining-related voids and the cave zone and their respective volumes (2024 Q4).....	96
Figure 3-52	Mining-related voids and the cave zone and their respective volumes (2026 Q4).....	97
Figure 3-53	Mining-related voids and the cave zone and their respective volumes at the end of mining to 1150 mRL. 98	
Figure 3-54	Assumed settlement curves for the cave muckpile.....	100

LIST OF TABLES

Table 2-1	Summary of FS4 parameters.	13
Table 2-2	In-situ stress field input for the Ernest Henry mine model.	14
Table 2-3:	Material properties for the Ernest Henry numerical simulations.	18
Table 2-4	List of all fault structures included in the Ernest Henry model.....	21
Table 2-5	Water inflow and hydraulic conductivity for EHM.....	26
Table 2-6	Hydraulic conductivity values applied to the major geological domains in the model.	26
Table 2-7	Summary of model sequences with corresponding calendar dates and milestones.....	28
Table 3-1	Surface subsidence impact classification criteria	42
Table 3-2	Forecast annual rate of cave growth towards the south direction at the surface.....	45
Table 3-3	Summary of mining-related voids relative volumes at selected times.....	46

1 INTRODUCTION

Beck Engineering (BE) has conducted a series of numerical simulations of the Ernest Henry mine, located near Cloncurry in Queensland, Australia.

The aim of this project was to:

1. Build and implement a 3D, non-linear, finite-element numerical simulation of the SLC to 1150 mRL case at Ernest Henry, including both the historical excavations and those proposed for the future.
2. Provide forecasts of cave propagation and underground mining-induced surface subsidence (i.e. displacement, strain, angular distortion/tilt) for the surface precinct at specific intervals throughout the future mine plan, including 2024/2026/2028/+100 years post-mining.
3. Conduct hydro-mechanical coupled modelling to assess the groundwater effect on rockmass damage, subsidence and cave propagation, including long-term surface subsidence forecasts extending 100 years after the cessation of mining, considering the flooding of the mine back to a groundwater elevation similar to the pre-mining phreatic surface.
4. Forecast the cave muckpile volume at regular intervals and also the volume of the southern waste dump material that is likely to be mobilised into the subsidence crater.

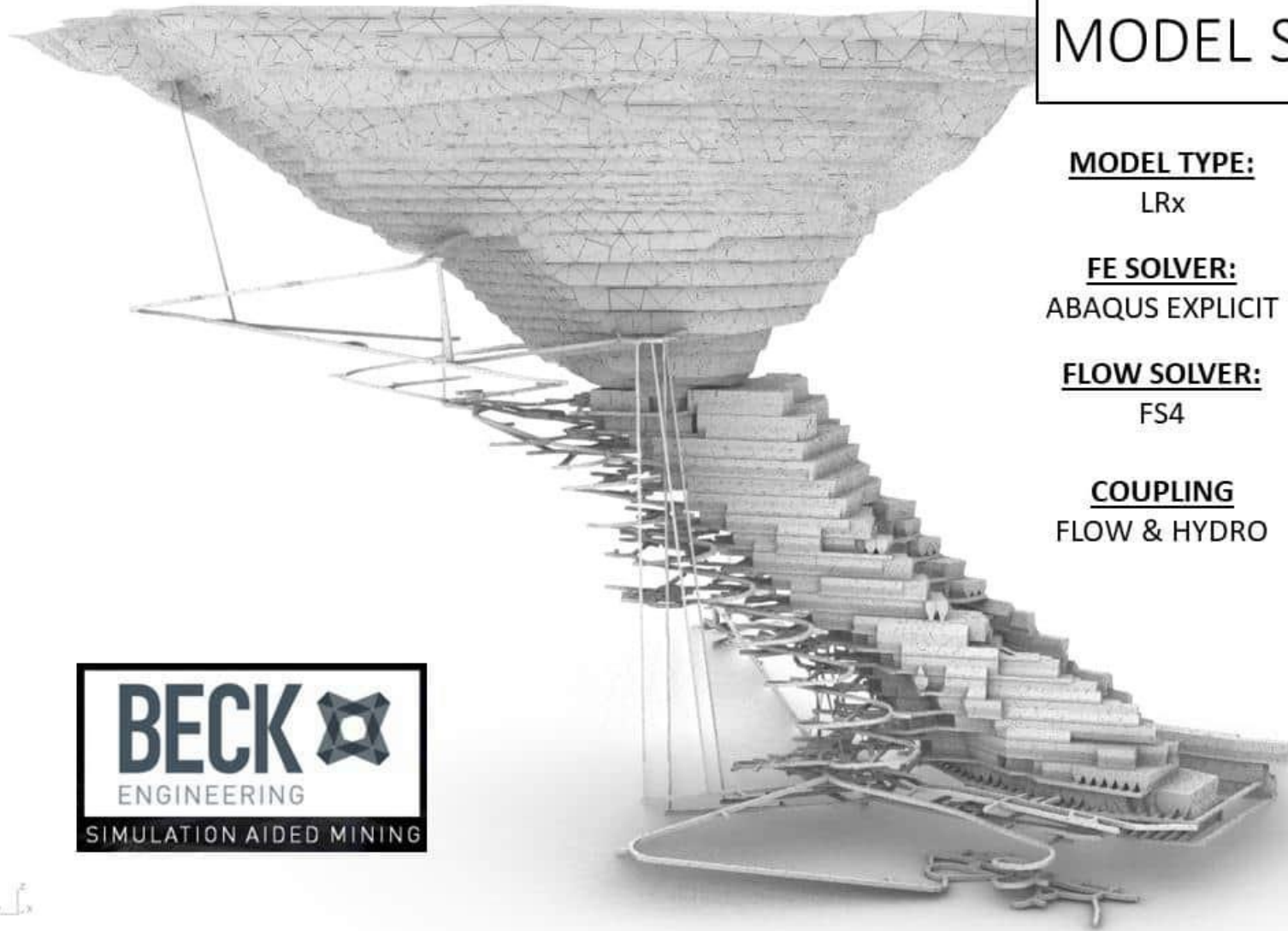
Figure 1-1 illustrates the mine excavation geometry and basic specifications of the model and mine design.

This assessment did not include:

- Sub-modelling of any part of the mine,
- Modelling of ground support,
- Seismic hazard forecasting,
- Detailed stability forecasts for all individual SLC levels,
- A site visit.

This report documents our analysis method, results, associated interpretation, conclusions and our recommendations for Evolution Mining's consideration.

MODEL SPECIFICATION



MODEL TYPE:
LRx

FE SOLVER:
ABAQUS EXPLICIT

FLOW SOLVER:
FS4

COUPLING
FLOW & HYDRO

MINING METHOD:
SUBLEVEL CAVING

SUBLEVEL INTERVAL:
25.0 m

XC SPACING:
15.0 m

XC PROFILE:
4.8 mH x 6.0 mW

MINE DESIGN:
CAVE ROTATION AT 1200 L
SLC TO 1150 L

SLC DRAW:
73,421,118 tonnes

Figure 1-1 Mine excavation geometry, model and mine design basic specifications.

2 PROJECT WORKFLOW, BACKGROUND DATA & MODEL COMPOSITION

This section summarises the project workflow, the available background data and assumptions relevant to the project and describes how these data and assumptions have been incorporated into the workflow.

2.1 Project workflow & simulation framework

The Abaqus Explicit finite element (FE) solver was used to simulate rockmass deformation and cave growth. Abaqus Explicit is a commercial, general purpose, 3D, non-linear, continuum or discontinuum FE analysis package designed specifically for analysing problems with significant plasticity, large strain gradients, high deformation levels and large numbers of material domains.

Cave flow simulation uses the FS4 flow solver developed by BE. FS4 is a physics based particle to particle simulation that has replaced the previous stochastic LGCA flow simulation technique used by BE in the past. The coupling technique between the Abaqus FE model and the FS4 flow model remains largely unchanged from the previous workflow. FS4 permits evolution of more realistic cave phenomena at higher resolution and differentiation between courses of action that could not be differentiated by stochastic flow codes. FS4 includes particle to particle kinematics and dynamics and enables higher resolution of granular flow and cave maturation which can more realistically replicate complex cave behaviour compared to previous FE-CA coupled simulations. PBD-FE simulation of flow is not a stochastic method (where cell scale interaction and material transfer are fixed by the user). Instead, the nature of flow and the resulting muckpile inside the cave evolves from the constitutive properties of individual particles. This lets the models better differentiate adverse from favourable flow conditions, which improves the resolution and reliability of the coupled discontinuum large strain forecasts of subsidence, instability and energy release.

The Levkovitch-Reusch (LRx) discontinuum constitutive framework was applied in Abaqus to describe the mechanical behaviour of the rockmass and structures. The LRx framework includes:

1. Three-dimensional (3D) geometry, with the mine excavations sequenced in a sufficient number of separate excavation steps (called frames) to capture the necessary temporal resolution for the project scope.
2. Strain-softening dilatant constitutive model for the rockmass and structures with a generalised Hoek-Brown yield criterion. Different material properties are assigned to each geotechnical domain.
3. Discontinuum formulation using cohesive finite elements to model discrete structures. Cohesive elements are free to dislocate, dilate and degrade and can realistically capture the behaviour of thin structures which tetrahedral finite elements cannot achieve as effectively. The complete interpreted structural model at the required resolution can be included, and where appropriate, can be supplemented with a discrete fracture network (DFN) to improve the structural resolution.
4. Structures less persistent than those modelled explicitly can be represented by "smearing" the effects of structures within the continuum regions of the modelled rockmass.
5. Hydromechanical coupling to capture the effects of pore water pressure on the rockmass yield surface, or to estimate water flow rates.

The LRx modelling framework aims for physical similitude, by making the fewest possible assumptions about the governing physics of the entire mine system within a single physics-based numerical model, at the required scale of the analysis. This results in a realistic but complex model, since complexity is the reality of all mines. Building a realistic mine model by including the governing physics means that realistic rockmass behaviour evolves naturally in the model and is therefore essential for developing a detailed understanding of the likely rockmass response to mining.

The modelling workflow for this project was:

1. An initial mining engineering and rock mechanics appreciation of the project and then updating of all relevant mine design and geological geometric data into a 3D CAD database using commercial software,
2. Discontinuum finite element (FE) mesh construction using commercial software and in-house scripting tools. Higher-order finite elements were used for all volume elements,
3. Assignment of the geotechnical domains, material properties, initial conditions, boundary conditions and excavation construction sequence to the FE mesh,

4. Assignment of caving parameters and draw schedule to the FS4 flow solver,
5. Solution of the stress, strain and displacement fields and released energy for each step in the modelled mining sequence using the Abaqus Explicit FE solver with a large strain formulation, coupled with FS4 for simulating the flow of fragmented material within the cave, air gap formation and cave stiffness. Commercial software and in-house post-processing scripts are used to process the Abaqus and FS4 outputs and visualise the results,
6. Forecasting of future behaviour for the current mine plan. Section 3 documents the model results, our interpretation of the results and associated discussion.

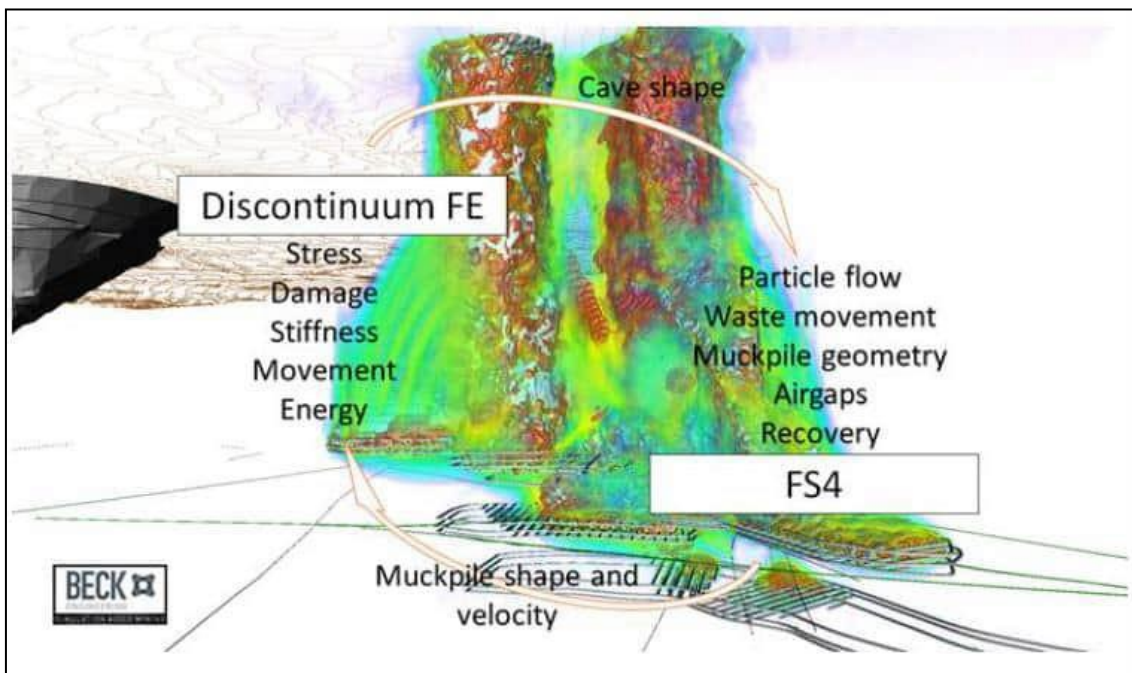


Figure 2-1 Overview of the FE-FS4 cave coupling simulation methodology.

2.2 Caving criterion & cave properties

A two-step caving criterion was applied in the FE simulation to determine the finite elements to switch to cave at each frame of the modelled mining sequence. This criterion was based on the incremental vertical displacement of each element during each frame (i.e. incremental displacement, not total displacement), denoted ΔU_z . The criterion was:

$\Delta U_z = -750\text{mm}$ for elastic rockmass.

$\Delta U_z = -315\text{mm}$ for rockmass with plastic strain of $\epsilon_p < 3\%$

$\Delta U_z = -270\text{mm}$ for rockmass with plastic strain of $\epsilon_0 > 3\%$

The caving criterion values were calibrated for this project and achieved a close match to measured cave extents. The cave was modelled elastically with the Young’s modulus E calculated according to the FS4 cave flow velocity estimate. The static cave stiffness was set at 10% of the source rock stiffness. The Poisson’s ratio for caved material was unchanged.

2.3 FS4 model parameters, constants & assumptions

The simulation included coupling handshakes between the Abaqus FE solver and FS4. These handshakes span the entire cave draw schedule. This frequency of data exchange is sufficient for mine-scale coupled simulations. The FS4 parameters are summarised in **Table 2-1**. The swell factor of 20% is a typical mean value for caves in a strong rockmass.

Table 2-1 Summary of FS4 parameters.

Swell factor s	$s = 120\%$
Angle of repose for caved rock	Confined - Static: 38° Unconfined - Static: 38° Dynamic: 38°
Drawpoint shut-off rule	Tonnes (not grade)

2.4 Topography

The natural ground surface at Ernest Henry is predominantly flat. The supplied topographic data of the deposit were used to build the surface profile, with extensions out to the model boundaries. Surface topographical features of note are man-made, such as the open pit and waste dumps.

2.5 Stress Field

The stress field input that has been applied for the Ernest Henry numerical model has been derived as the Euclidean mean stress of the historical stress measurements that have been conducted at the mine. Ten stress measurements have been used to derive the principal stresses for the model inputs, including five WASM AE, one ANZI, three CSIRO HI Cell and one DRA. The orientation and magnitude of the principal stress inputs are defined in **Table 2-2** and **Figure 2-2**. These inputs are unchanged from the cave rotation project conducted by BE in early 2022. The measured and model input stress fields are a close match to the regional stress field in the North Queensland (Mt Isa) region, as described by Lee et al. (2010).

Table 2-2 In-situ stress field input for the Ernest Henry mine model.

Principal stress component	Magnitude gradient (MPa/km)	Dip (degrees)	Dip azimuth (degrees)	σ_i/σ_{zz}
σ_1	51.4	05°	227°	1.94
σ_2	35.1	11°	318°	1.32
σ_3	26.0	78°	112°	0.98
Stress gradients applied from reference $z = 2,135$ mRL.				
Cartesian stress tensor at 1,000m:				
$\begin{matrix} \sigma_{xx} & \sigma_{xy} & \sigma_{zx} & \sigma_{EE} & \sigma_{EN} & \sigma_{UE} & 42.5 & 8.2 & 2.75 \\ [\sigma_{xy} & \sigma_{yy} & \sigma_{yz}] = [\sigma_{EN} & \sigma_{NN} & \sigma_{NU}] = [& 8.2 & 43.5 & 0.3] \text{ MPa} \\ \sigma_{zx} & \sigma_{yz} & \sigma_{zz} & \sigma_{UE} & \sigma_{NU} & \sigma_{UU} & 2.75 & 0.3 & 26.5 \end{matrix}$				
Note: x is east on the local mine grid, y is north and z is up.				
Ratio of average horizontal stress to vertical stress: (Brady & Brown 2006:159)				
$k = \frac{k_x + k_y}{2} = \frac{\sigma_{xx} + \sigma_{yy}}{2\sigma_{zz}} = 1.62$				

The pre-mining stress field for each of the simulations were generated in the FE model by ramping the stresses in each element from an initial zero stress state to the target initial stress gradients over an appropriate number of computational steps. This part of the simulation procedure is called the equilibrium step and aims to evolve an initial stress field in the mine precinct that is mechanically compatible with the modelled structures, geotechnical domains, material properties and topography. This procedure generates a variable in situ stress field in the mine precinct which is characteristic of the variability typically measured in mines. This normal variability in the principal stress orientation and magnitude with depth is illustrated in **Figure 2-3**, which shows the modelled principal stresses sampled along a vertical path at three locations in the model space at the completion of the equilibrium step.

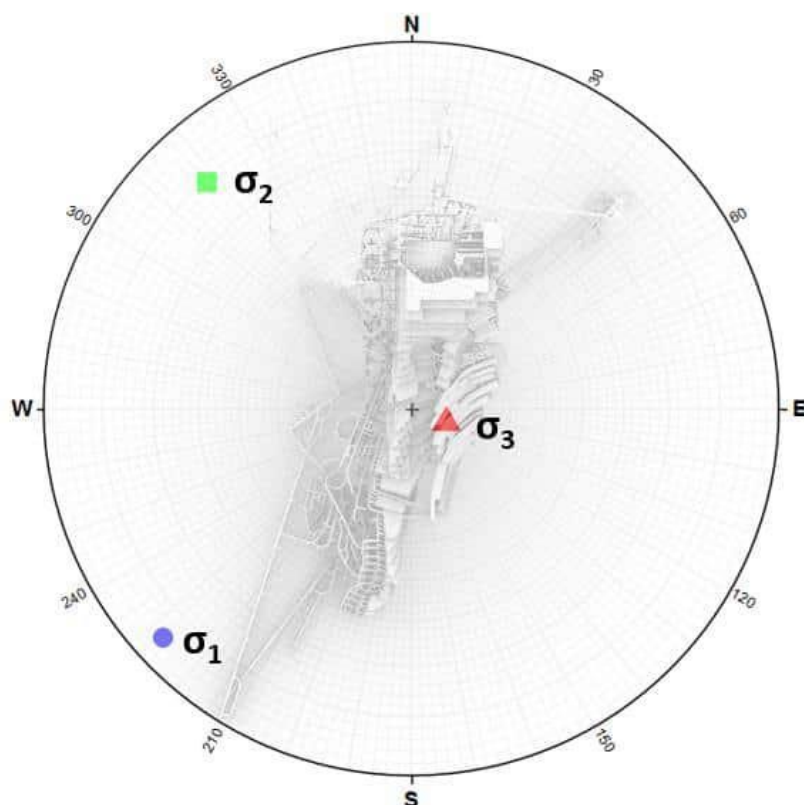


Figure 2-2 Principal stress orientations for the Ernest Henry mine model.

2.6 Geotechnical domain assignment

The material properties have been applied according to the lithology. This domaining approach is a necessary assumption in the absence of a separate detailed geotechnical domain model, but from our general understanding of rockmass conditions at Ernest Henry, this assumption is appropriate. **Figure 2-4** shows the complexity of the lithology domains which were applied in the model, as well as a complete list of all 3D wireframes that were utilised to define those domains. We note that the current lithology model reflects a major update and improvement in terms of resolution and detail, compared to the geological model that was used for prior subsidence assessments, such as the 2021 project (see Beck, 2021).

2.6.1 Estimated material properties for modelling

The material strength properties assigned to the lithology domains of the model were carried over from the Cave Rotation project that BE conducted in early 2022 (Campbell, 2022). The values used for the model inputs are given in **Table 2-3**. Strength envelop definitions are provided in Appendix A. Faults (excluding volume faults/shears) were modelled using zero-volume cohesive elements with an assigned LRx constitutive thickness of ~ 1 metre, rather than with Mohr-Coulomb properties. This approach allowed the FE-mesh of the fault geometry to be simplified to a surface while also allowing the faults to respond to 3D strain change as if they had real thickness.

The following nomenclature is used in Table 2-3:

UCS = uniaxial compressive strength.

GSI = geological strength index.

ϵ_0 = 0 = plastic strain at start of peak strength stage (see Figure 2-5).

ϵ_1 = plastic strain at start of transitional strength stage (see Figure 2-5).

ϵ_2 = plastic strain at start of residual strength stage (see Figure 2-5).

E = Young's modulus for the rockmass.

ν = Poisson's ratio for the rockmass.

s, m, a = generalised HB yield parameters for the rockmass.

d = rockmass dilation parameter.

e = deviatoric eccentricity constant.

κ = $s\sigma_c^{1/a}$ = Generalised HB cohesion parameter for the rockmass. Units are $\text{MPa}^{1/a}$.

Φ = $m\sigma_c^{1/a-1}$ = Generalised HB friction parameter for the rockmass. Units are $\text{MPa}^{1/a-1}$.

Project	EHM2022OCT
Angles	bearing + plunge

Model	EHM2022OCT_R01_RST01_G01_Q01_M01
Offset coordinates	x=0m; y=0m; z=0m

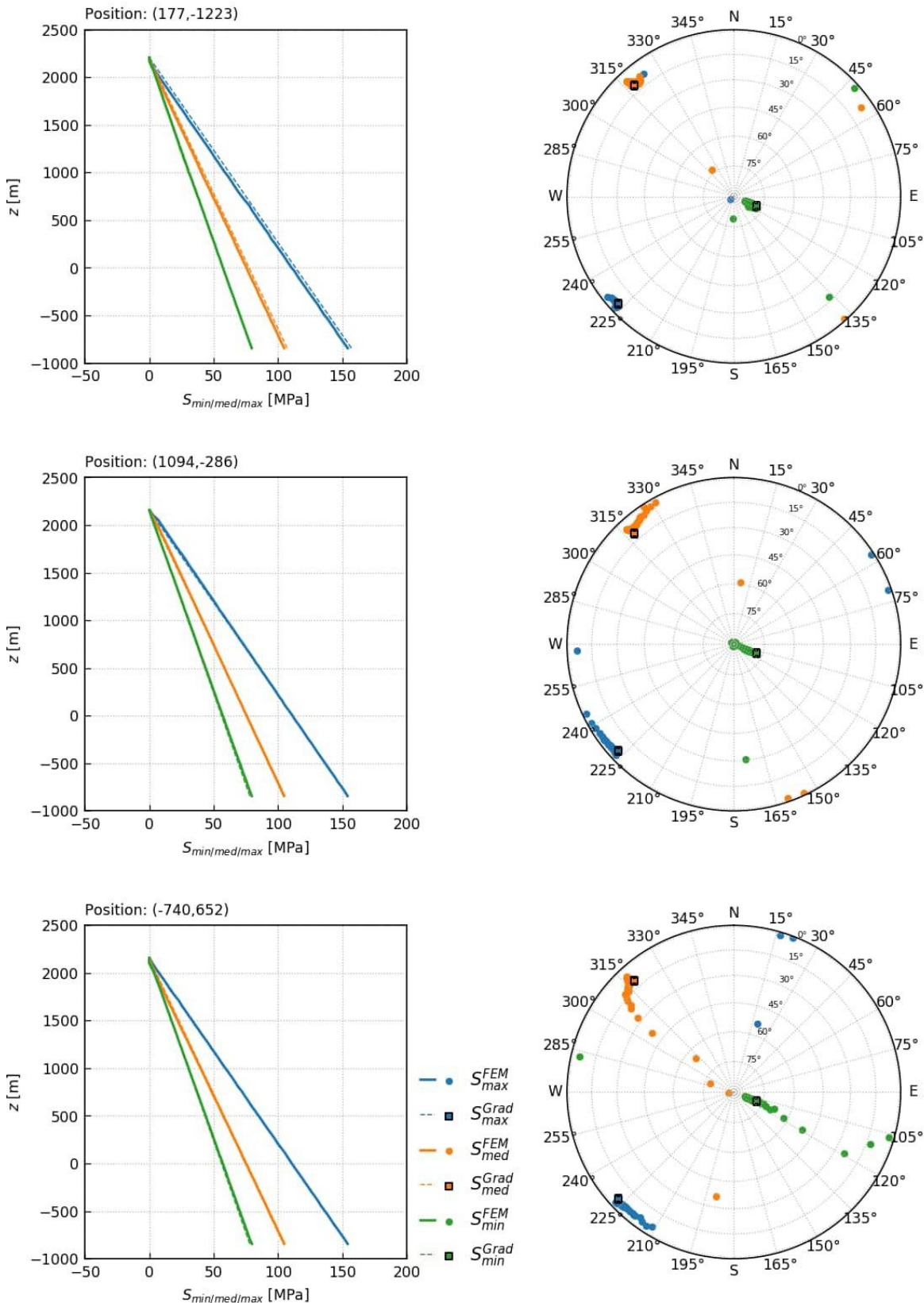


Figure 2-3 Simulated pre-mining stress state along a vertical sample path for three locations in the model space.

LITHOLOGY MODEL

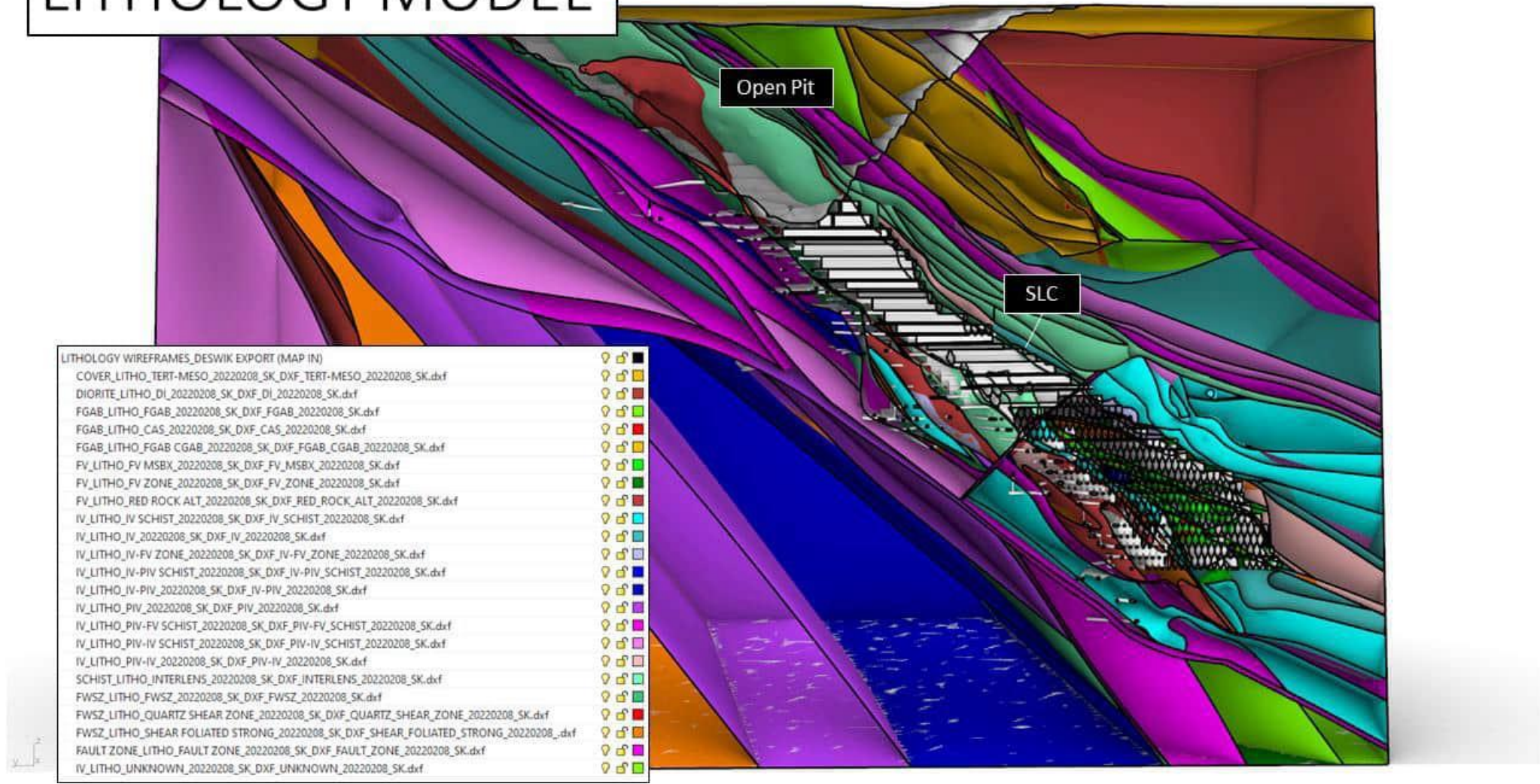


Figure 2-4: Perspective view showing the main rockmass domains in the model.

EVOLUTION MINING: ERNEST HENRY SLC TO 1150 mRL CAVE PROPAGATION & SUBSIDENCE ASSESSMENT

Table 2-3: Material properties for the Ernest Henry numerical simulations.

MAT #	Name	Code	Input Parameters					LRx: Calculated Rockmass Parameters								
			Density (kg/m ³)	UCS (MPa)	GSI	Anisotropy		Stage	Plastic strain	E (GPa)	ν	s	m	a	d	e
						n	s									
1	COVER SEQUENCE	COVER	2,400	10	30	1.0	1.0	Peak	$\epsilon_0 = 0.00$	2.92	0.25	6.34E-5	0.31	0.53	0.05	0.60
								Transition	$\epsilon_1 = 0.03$	2.92	0.25	6.16E-5	0.31	0.53	0.05	0.60
								Residual	$\epsilon_2 = 13.02$	2.92	0.25	1.00E-5	0.30	0.53	0.00	0.60
2	DIORITE	DIO	2,700	70	50	1.0	1.0	Peak	$\epsilon_0 = 0.00$	16.34	0.25	4.68E-4	0.92	0.51	0.15	0.60
								Transition	$\epsilon_1 = 0.50$	15.70	0.25	2.96E-4	0.80	0.51	0.13	0.60
								Residual	$\epsilon_2 = 10.56$	14.36	0.25	1.00E-5	0.50	0.51	0.00	0.60
3	FINE GRAIN ALBATITE	FGAB	2,700	93	48	1.0	1.0	Peak	$\epsilon_0 = 0.00$	18.87	0.25	3.83E-4	1.00	0.51	0.17	0.60
								Transition	$\epsilon_1 = -$	-	-	-	-	-	-	-
								Residual	$\epsilon_2 = 8.15$	16.89	0.25	1.00E-5	0.57	0.51	0.00	0.60
4	FELSIC VOLCANIC	FV	2,700	137	68	1.0	1.0	Peak	$\epsilon_0 = 0.00$	28.32	0.25	2.83E-3	2.27	0.50	0.38	0.60
								Transition	$\epsilon_1 = 1.04$	23.55	0.25	6.33E-4	1.45	0.50	0.24	0.60
								Residual	$\epsilon_2 = 6.86$	20.08	0.25	1.00E-5	0.71	0.50	0.00	0.60
5	INTER VOLCANIC	IV	2,700	100	50	1.0	1.0	Peak	$\epsilon_0 = 0.00$	22.28	0.25	1.27E-3	1.49	0.51	0.25	0.60
								Transition	$\epsilon_1 = 0.90$	19.92	0.25	4.62E-4	1.10	0.51	0.18	0.60
								Residual	$\epsilon_2 = 8.70$	17.53	0.25	1.00E-5	0.59	0.51	0.00	0.60
6	SCHIST	SCH	2,700	100	60	1.0	1.0	Peak	$\epsilon_0 = 0.00$	19.94	0.25	4.68E-4	1.10	0.51	0.18	0.60
								Transition	$\epsilon_1 = 0.01$	19.92	0.25	4.62E-4	1.10	0.51	0.18	0.60
								Residual	$\epsilon_3 = 7.81$	17.53	0.25	1.00E-5	0.59	0.51	0.00	0.60
7	PIV	PIV	2,700	104	50	1.0	1.0	Peak	$\epsilon_0 = 0.00$	22.71	0.25	1.27E-3	1.52	0.51	0.25	0.60
								Transition	$\epsilon_1 = 0.84$	20.39	0.25	4.83E-4	1.14	0.51	0.19	0.60
								Residual	$\epsilon_2 = 8.38$	17.86	0.25	1.00E-5	0.61	0.51	0.00	0.60
8	FWSZ	FWSZ	2,700	129	60	1.0	1.0	Peak	$\epsilon_0 = 0.00$	22.33	0.25	4.68E-4	1.28	0.51	0.21	0.60
								Transition	$\epsilon_1 = -$	-	-	-	-	-	-	
								Residual	$\epsilon_2 = 5.54$	19.62	0.25	1.00E-5	0.69	0.51	0.00	0.60

Table 2-3 (Cont'd): Material properties for the Ernest Henry numerical simulations.

MAT #	Name	Code	Input Parameters					LRx: Calculated Rockmass Parameters								
			Density (kg/m ³)	UCS (MPa)	GSI	Anisotropy		Stage	Plastic strain	<i>E</i> (GPa)	<i>v</i>	<i>s</i>	<i>m</i>	<i>a</i>	<i>d</i>	<i>e</i>
						<i>n</i>	<i>s</i>									
9	HWSZ	HWSZ	2,700	129	50	1.0	1.0	Peak	$\epsilon_0 = 0.00$	22.33	0.25	4.68E-4	1.28	0.51	0.21	0.60
								Transition	$\epsilon_1 = -$	-	-	-	-	-	-	
								Residual	$\epsilon_2 = 5.54$	19.62	0.25	1.00E-5	0.69	0.51	0.00	0.60
10	FAULT ZONE (INTERNAL)	FLT_ZONE	2,700	100	50	1.0	1.0	Peak	$\epsilon_0 = 0.00$	19.94	0.25	4.86E-4	1.10	0.51	0.18	0.60
								Transition	$\epsilon_1 = 0.01$	19.92	0.25	4.62E-4E	1.10	0.51	0.18	0.60
								Residual	$\epsilon_2 = 7.81$	17.53	0.25	1.00E-5	0.59	0.51	0.00	0.60
11	FAULT EXPLICIT STRONG	FLT_STRG	2,700	78	50	1.0	1.0	Peak	$\epsilon_0 = 0.00$	17.44	0.25	4.68E-4	0.97	0.51	0.16	0.60
								Transition	$\epsilon_1 = 0.33$	16.95	0.25	3.41E-4	0.88	0.51	0.15	0.60
								Residual	$\epsilon_2 = 9.76$	15.33	0.25	1.00E-5	0.52	0.51	0.00	0.60
12	FAULT EXPLICIT MODERATE	FLT	2,700	58	47	1.0	1.0	Peak	$\epsilon_0 = 0.00$	14.08	0.25	3.47E-4	0.78	0.51	0.13	0.60
								Transition	$\epsilon_1 = 0.48$	13.63	0.25	2.28E-4	0.69	0.51	0.11	0.60
								Residual	$\epsilon_2 = 11.45$	12.72	0.25	1.00E-5	0.46	0.51	0.00	0.60
13	DISCRETE FRACTURE NETWORK	DFN	2,700	58	47	1.0	1.0	Peak	$\epsilon_0 = 0.00$	14.08	0.25	3.47E-4	0.78	0.51	0.13	0.60
								Transition	$\epsilon_1 = 0.48$	13.63	0.25	2.28E-4	0.69	0.51	0.11	0.60
								Residual	$\epsilon_2 = 11.45$	12.72	0.25	1.00E-5	0.46	0.51	0.00	0.60
14	HOST ROCK	HOST	2,700	100	60	1.0	1.0	Peak	$\epsilon_0 = 0.00$	22.28	0.25	1.27E-3	1.49	0.51	0.25	0.60
								Transition	$\epsilon_1 = 0.90$	19.92	0.25	4.62E-4	1.10	0.51	0.18	0.60
								Residual	$\epsilon_3 = 8.70$	17.53	0.25	1.00E-5	0.59	0.51	0.00	0.60

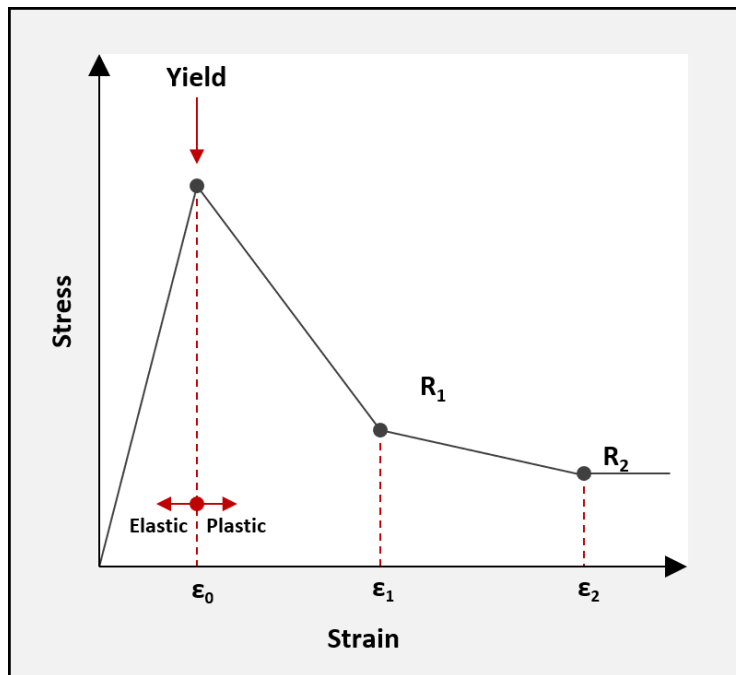


Figure 2-5: Indicative rockmass softening curve demonstrating the plastic strain transition points ϵ_1 and ϵ_2 .

2.7 Structural model resolution

The structural model that was implemented in these numerical simulations was the same as that which was implemented for the Cave Rotation Options Assessment project that BE conducted in early 2022 (Campbell, 2022). This structural model consists of eighty-one discrete faults, seven volume faults (i.e. shear zones) and four discrete fracture network (DFN) groups throughout the mine space, one in the open pit and three for the underground. Note that each DFN group contains simulated discontinuities in multiple set orientations. **Table 2-4** presents the complete list of structures and DFN groups that were explicitly built into the model. It is important to note that the structural model used in these Ernest Henry simulations has been substantially upgraded since the surface subsidence assessment that BE conducted in 2021 (see Beck, 2021). This upgrade is positive, as the resolution and detail of the structural representation of the deposit has been significantly improved, which in turn aids in simulation forecast accuracy. As a result, it should be expected that the current forecasts will not be directly comparable to those of earlier simulations which were based on another structural model of the mine with less detail.

The resolution of the available structural information allows mine-scale and precinct scale interpretations of the model results. This means that average strains across the rockmass between modelled structures can be simulated and interpreted, but local strains due to structures smaller than those modelled explicitly cannot develop in the model. To obtain forecasts of potential peak strains, which may be needed to assess the potential for locally high deformation levels around individual pieces of SLC infrastructure, a model incorporating structures with persistence smaller than the scale of the excavations themselves would be needed.

With the current model, we therefore cannot provide detailed stability forecasts of individual tunnels, SLC rings or large chambers etc, because stability forecasts depend largely on the excavation-scale structures. The model does allow general interpretations of excavation stability based on, for example, forecast deformation arising from weaker rockmass conditions, mine or intermediate scale structures and adverse geometric configurations or sequences, but explicit forecasts are not possible without greater detail on the rockmass characteristics.

Table 2-4 List of all fault structures included in the Ernest Henry model.

EXPLICIT FAULTS

F_EHFAULT_AD
 F_FAULT_06_LWR_HW
 F_FAULT_09_HW
 F_FAULT_AA_HW
 F_FAULT_AD_FW
 F_FAULT_AH
 F_FAULT_AQ
 F_FAULT_BJ
 F_FAULT_D_HW
 F_FAULT_FRILLNECK_20_HW
 F_FAULT_FRILLNECK_30_HW
 F_FAULT_KOMODO_30_FW
 F_FAULT_MAJ_10_HW
 F_FAULT_MAJ_ZONE_01_WEST_FW
 F_FAULT_MAJ_ZONE_01_WEST_HW
 F_FAULT_S
 F_FAULT_SHINGLEBACK_10_FW
 F_FAULT_SW_AREA_01_HW
 F_FAULT_T
 F_FAULT_U
 F_FV_SW_RED_ROCK_BLOCK_01_HW
 F_FW_SHEAR_FOL_ZONE_01B_FW
 F_FW_SHEAR_FOL_ZONE_01B_HW
 F_FW_SHEAR_FOL_ZONE_01C_HW
 F_FW_SHEAR_FOL_ZONE_01_FW
 F_FW_SHEAR_FOL_ZONE_01_HW
 F_INTERLENS_SPLAY_01_HW
 F_INTERLENS_SPLAY_04_HW
 F_INTERLENS_SPLAY_05_FW

EXPLICIT FAULTS

F_INTERLENS_SPLAY_06B_HW
 F_INTERLENS_SPLAY_06C_FW
 F_INTERLENS_SPLAY_06_HW
 F_INTERLENS_SPLAY_07B_HW
 F_MAJ_FWSZ_02_HW
 F_MAJ_FWSZ_EAST_FW
 F_MAJ_FWSZ_EAST_HW
 F_MAJ_FWSZ_HW
 F_MAJ_FWSZ_LWR_02_FW
 F_MAJ_FWSZ_LWR_02_HW
 F_MAJ_FWSZ_LWR_FW
 F_MAJ_FWSZ_LWR_HW
 F_MAJ_FWSZ_UPPER_FW
 F_MAJ_FWSZ_UPPER_HW
 F_MAJ_HW
 F_MAJ_HWSZ_02-UPPER_HW
 F_MAJ_HWSZ_02_FW
 F_MAJ_HWSZ_FW
 F_MAJ_HWSZ_FW_
 F_MAJ_HWSZ_FW_WEST
 F_MAJ_HWSZ_HW
 F_MAJ_HWSZ_HW_
 F_MAJ_HWSZ_HW_WEST
 F_MAJ_HWSZ_UPPER_FW_
 F_MAJ_HWSZ_UPPER_HW
 F_MAJ_INTERLENS_SHEAR_FW
 F_MAJ_INTERLENS_SHEAR_UPPER_FW
 F_MAJ_MARSHALL_10_FW
 F_MAJ_MARSHALL_10_HW

EXPLICIT FAULTS

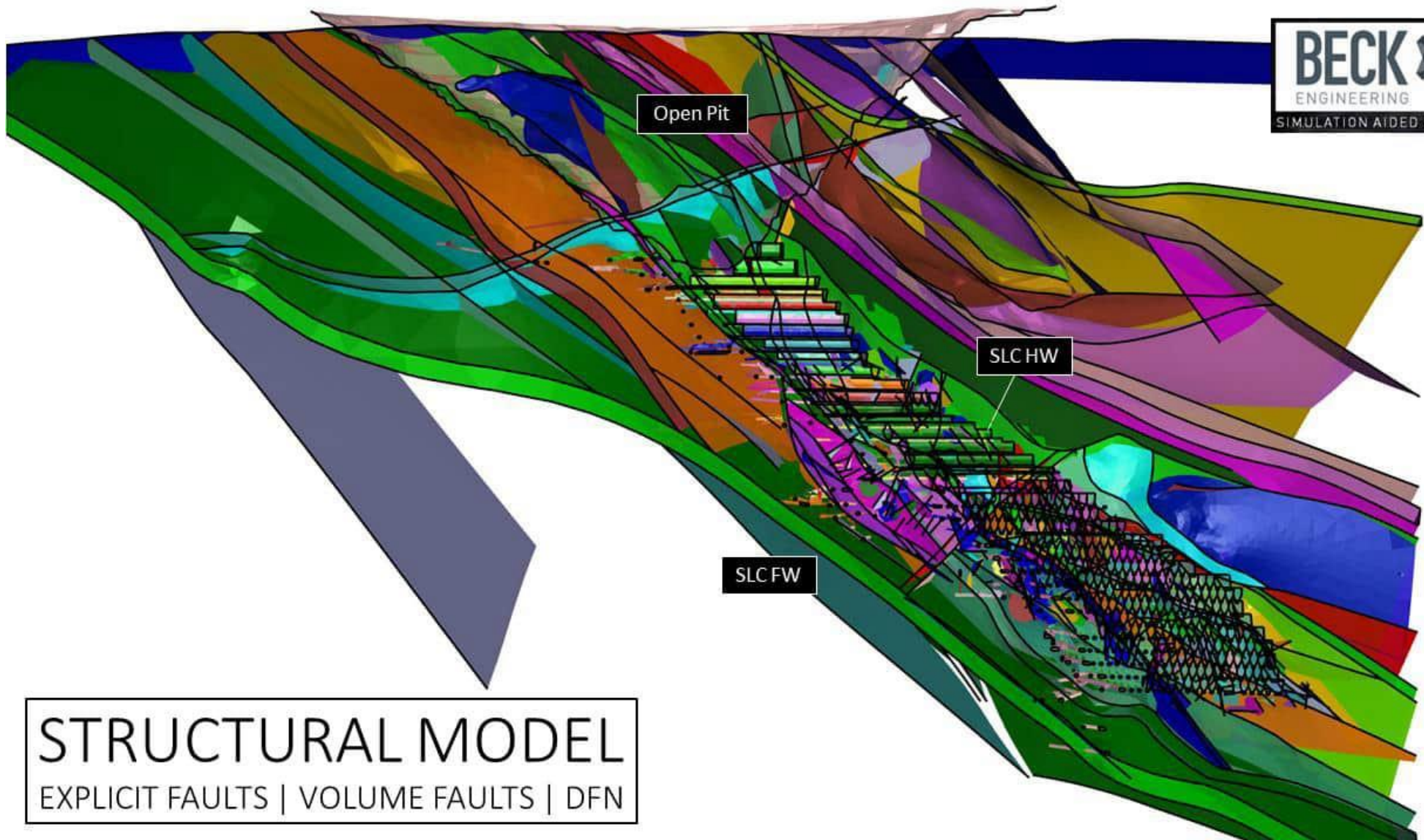
F_MAJ_PIT_INTERLENS_01_FW
 F_MAJ_PIT_INTERLENS_01_HW
 F_MAJ_PIV_SHEAR_01_HW
 F_MAJ_WEST_SHEAR_ZONE_01_FW
 F_MAJ_WEST_SHEAR_ZONE_01_HW
 F_MAJ_WEST_SHEAR_ZONE_02_FW
 F_MAJ_WEST_SHEAR_ZONE_02_HW
 F_MARSHALL_SZ_FW
 F_MARSHALL_SZ_HW
 F_QTZ_SHEAR_01_FW
 F_QTZ_SHEAR_02_FW
 F_QTZ_SHEAR_03_FW
 F_QTZ_SHEAR_05_FW
 F_SHEAR_FOL_ZONE_01_FW
 F_SHEAR_FOL_ZONE_01_HW
 F_SHEAR_FOL_ZONE_02_FW
 F_SHEAR_FOL_ZONE_02_HW
 F_SHEAR_FOL_ZONE_03_FW
 F_SHEAR_FOL_ZONE_03_HW
 F_SWSZ_FW
 F_SWSZ_HW
 F_TERTIARY_MESO_UNCONFORMITY
 F_INTERLENS_SPLAY_06D_HW

VOLUME FAULTS

F_FAULT-MAJ_ZONE_02_FW
 F_FAULT-MAJ_ZONE_02_HW
 F_FAULT_AB_FW
 F_FAULT_AB_HW
 F_FAULT_AM_FW
 F_FAULT_AM_HW
 F_FAULT_MAJ_05_FW
 F_FAULT_MAJ_05_HW
 F_FAULT_MAJ_06_FW
 F_FAULT_MAJ_06_HW
 F_FAULT_MAJ_08_FW
 F_FAULT_MAJ_08_HW
 F_FAULT_MAJ_ZONE_01_FW
 F_FAULT_MAJ_ZONE_01_HW

EXPLICIT DFN SETS

FLT_DFN
 FLT_DFN_SETB
 FLT_DFN_SETA
 FLT_DFN_PIT



STRUCTURAL MODEL
EXPLICIT FAULTS | VOLUME FAULTS | DFN

Figure 2-6 Structural model of the Ernest Henry mine.

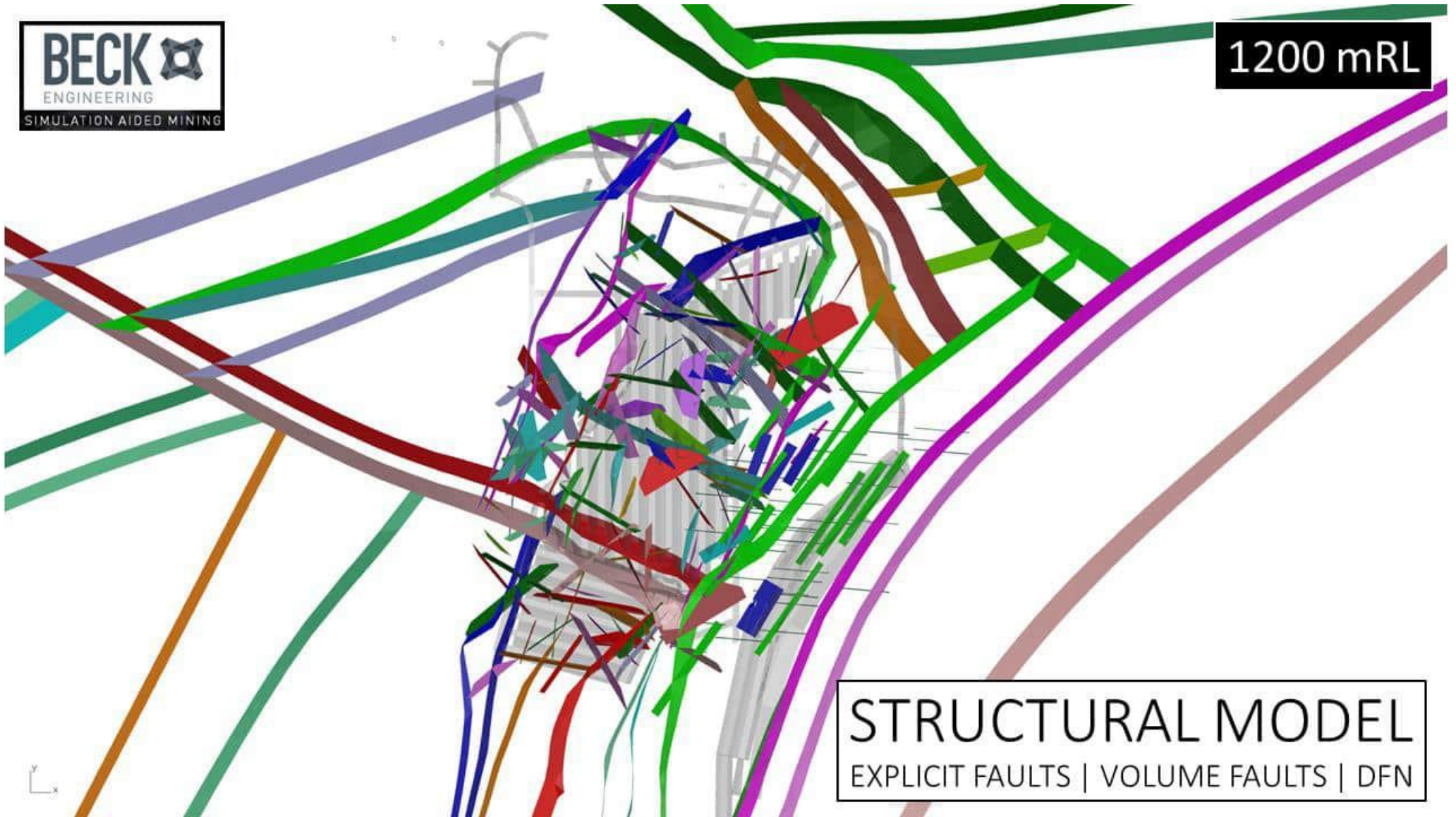
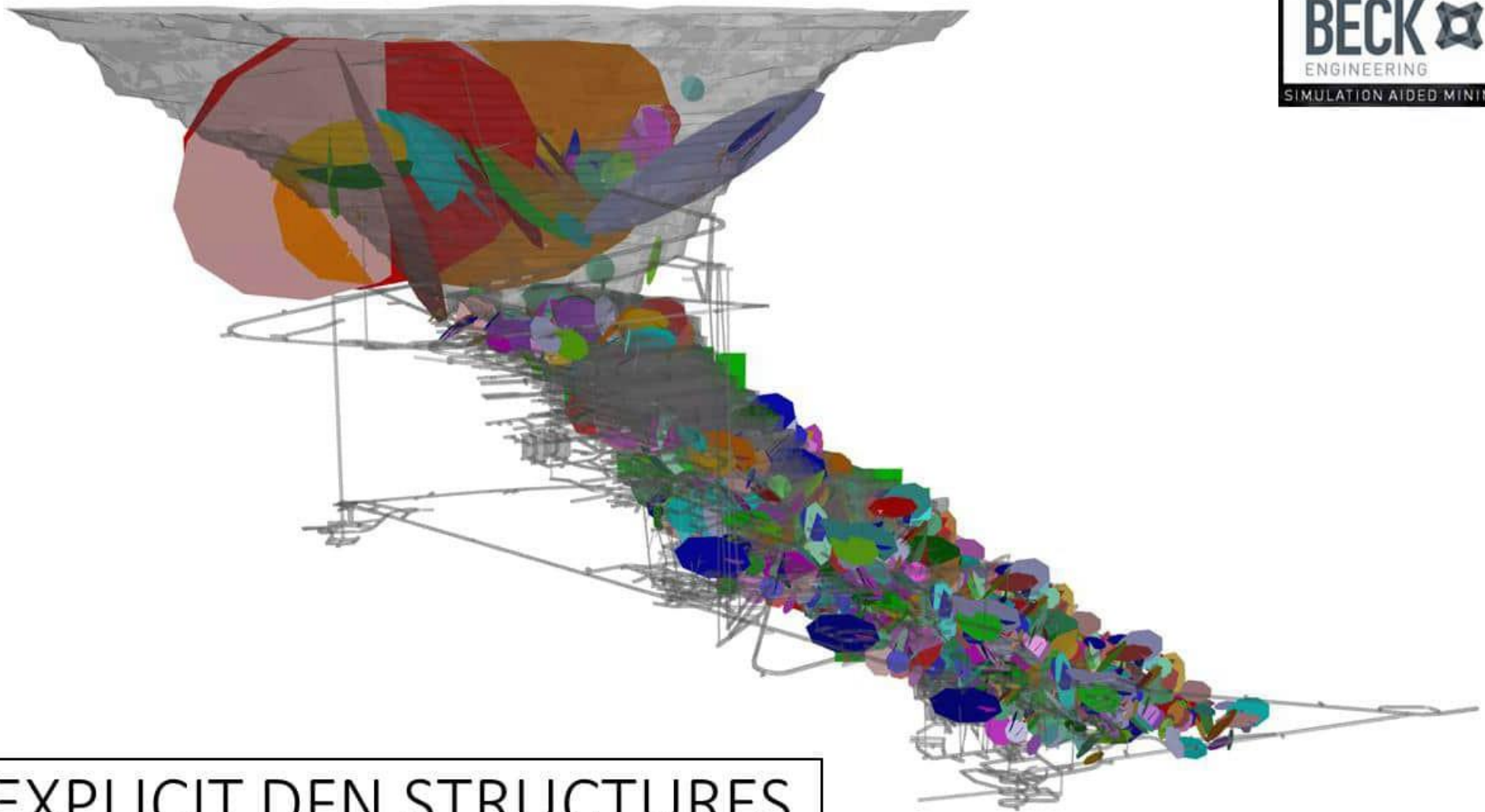


Figure 2-7 Structural model of the Ernest Henry mine (Top view, clipped at 1200 mRL).



EXPLICIT DFN STRUCTURES

Figure 2-8 DFN groups of explicitly modelled intermediate and small-scale structures.

2.8 Hydrogeological Conditions

Numerical simulations of the Ernest Henry mine conducted as a part of this project were hydro-mechanically-flow coupled models. The methodology for applying the groundwater in the model, including re-flooding of the mine over a simulated period of 100 years post mine-closure, is outline below:

- The initial hydrological properties of the local geology were provided to BE by EHM. These values are listed in **Table 2-5** and summarised in **Table 2-6**. The hydraulic conductivities applied in the model were taken from previous hydro-geology bore field assessments by AGE (2017).
- The pre-mining groundwater elevation was set to 134m AHD (2,134 mRL in mine grid) as an external boundary condition. The boundaries of the model were approximately 3.5 km away from the mine. This reflects the pre-mining groundwater level as defined by AGE (2017).
- At each stage in the model as the mine advances and the cave grows, the excavations and new and old cave are assumed to be drained by firing the pore water pressure at the void boundary to near-zero. This becomes an internal boundary condition and the permeability in the damaged rock around the cave is adjusted to account for the mining-induced fracturing.
- As the cave grows and plastic strain (rockmass damage) evolves, the hydraulic conductivities change as a function of the equivalent deviatoric plastic strain using the equation below. In simple terms, as rock becomes more damaged, it cracks and dilates and the hydraulic conductivity increases.

$$K_w(PST) = K_{w0} \exp\{a \cdot PST\} \leq K_{wmax} .$$

- A schematic illustrating the effects of rockmass damage to hydraulic conductivity is provided in **Figure 2-9**. A graphical representation of hydraulic conductivity relative to LogP (a logarithmic function of plastic strain in the rockmass) is provided in **Figure 2-10**.
- The long-term post-mining groundwater level is attained by allowing the cave and excavations to flood. This is achieved by incrementally removing the 'fully drained' internal boundary condition on the cave walls and excavations. The final groundwater level² is taken according to the assumed water elevation after a simulated period of 100 years, i.e., the flooding is completed and no associated future change in water level occurs. An example of this incremental phreatic surface recovery is illustrated in **Figure 2-11**.
- Simulation of large storm events was not included explicitly in the model. However, flooding and rainfall events are included in the groundwater elevation forecasts completed by AGE (2017) and the groundwater / pit water levels were used in the pit flooding inputs to 100 years post mining. This method is a means to account for the effects of rainfall and flooding in the groundwater inputs to the simulation.
- The drawdown of the underground mine is not included in the groundwater and pit water level forecasts by AGE (2017). This assessment required the underground mine to also be flooded as the groundwater levels gradually return to the 100m ASL elevation (as specified by AGE, 2017 in the water balance model).
- It is also important to note that BEs hydro-coupled simulation forecast for the long-term, post-mining (+100 years) phreatic surface level represents the long-term, mean far-field phreatic surface. Forecasts do not take into consideration the short-term fluctuations in the phreatic surface that may occur as a direct consequence of the mine's closure infrastructure, such as bunded stormwater catchment boundaries and directed run-off channels into the surface reservoirs, including the open pit and cave zone. This is expected to be addressed in detail with future mine closure and rehabilitation studies.

² As simulated in the Abaqus numerical model for excavation stability assessment purposes. Refer to forthcoming reports by AGE (2023) groundwater impact assessment and ATC Williams (2023) final void water balance for the final void water level incorporating surface features and mine closure planning.

Table 2-5 Water inflow and hydraulic conductivity for EHM.

Table 2-6 Hydraulic conductivity values applied to the major geological domains in the model.

Hydrological Unit	k_{w0} [m/s]	k_{max} [m/s]
MAT_WEATHERED	1.16E-08	1.15741E-06
MAT_HOSTS	5.79E-09	5.79E-07
MAT_FAULTS	5.79E-07	5.79E-05
MAT_F4	1.74E-06	1.74E-04
MAT_F5	6.37E-07	6.37E-05
MAT_MFLT	1.16E-08	1.16E-06
MAT_HWSZ_SZ	6.48E-08	6.48E-06

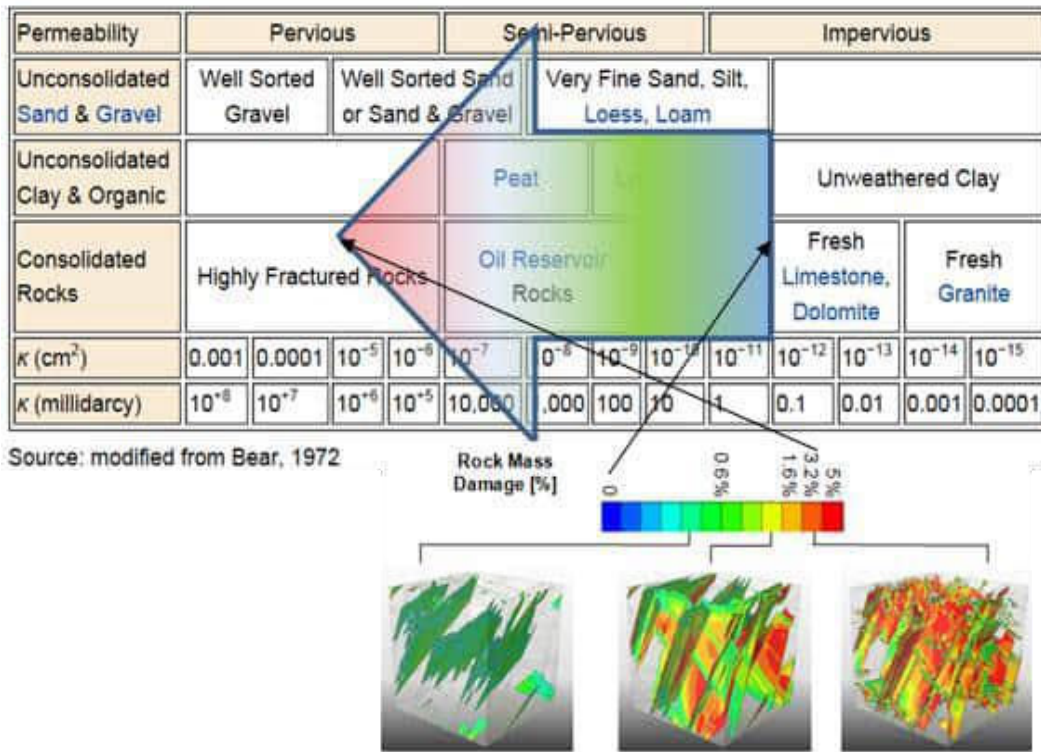


Figure 2-9 Variation of hydraulic conductivity as a function of rockmass damage.

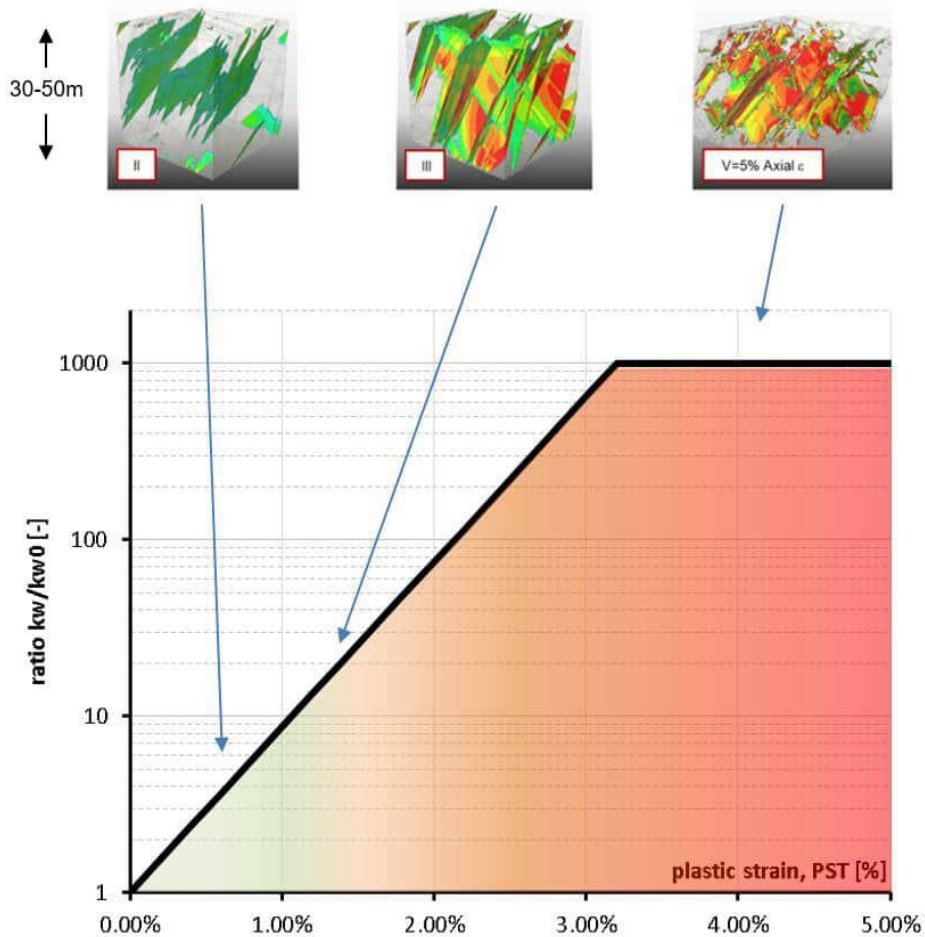


Figure 2-10 Example of variation of hydraulic conductivity (Y-axis) with LogP (X-axis) in the hydro-coupled model.

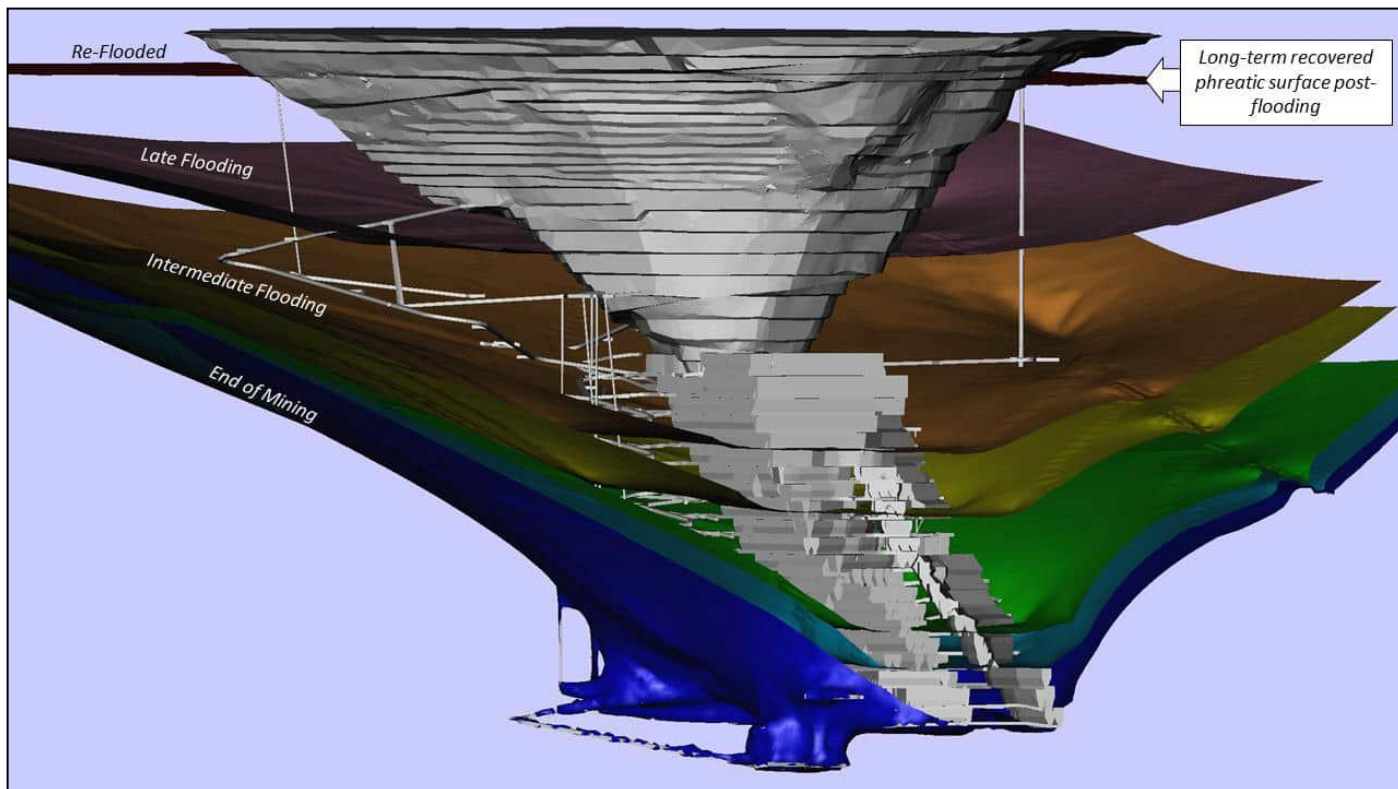


Figure 2-11 Evolution of the phreatic surface recovery to near pre-mining levels following mine closure and re-flooding.

2.9 Mining methods, geometry & sequence

The model simulation domain extended approximately 3 km from the open pit and underground workings in order to eliminate artificial boundary loading effects (**Figure 2-12**). The models included the complete life-of-mine excavation geometry and lithological/structural models in high detail, as illustrated in **Figure 2-13** and comprising:

- The open pit and nearby waste dumps,
- Underground development (i.e. exploration drives, declines, accesses, crosscuts and other capital infrastructure),
- SLC production rings and slots,
- The main hoist shaft and major ventilations shafts,
- Geotechnical domains and geological structures, as described above.

A graphical representation of the mining sequence for the simulated excavation geometry is illustrated in **Figure 2-14**. The main stages of the numerical simulation are summarised in **Table 2-7**:

Table 2-7 Summary of model sequences with corresponding calendar dates and milestones.

Frame #	SLC to 1150 mRL
F000	Model start
F001-F046	Historic open pit mining (to 2011)
F047 - F090	Historic underground mining (2011 Q3 to 2022 Q3)
F091	Current mining (2022 Q4)
F092 - F115	Future underground mining (2023 Q1 to 2028 Q2)
F115	End of underground mining
F116 - F121	Groundwater recharge and pit flooding (Up to 100 years post mining)

MODEL BOX

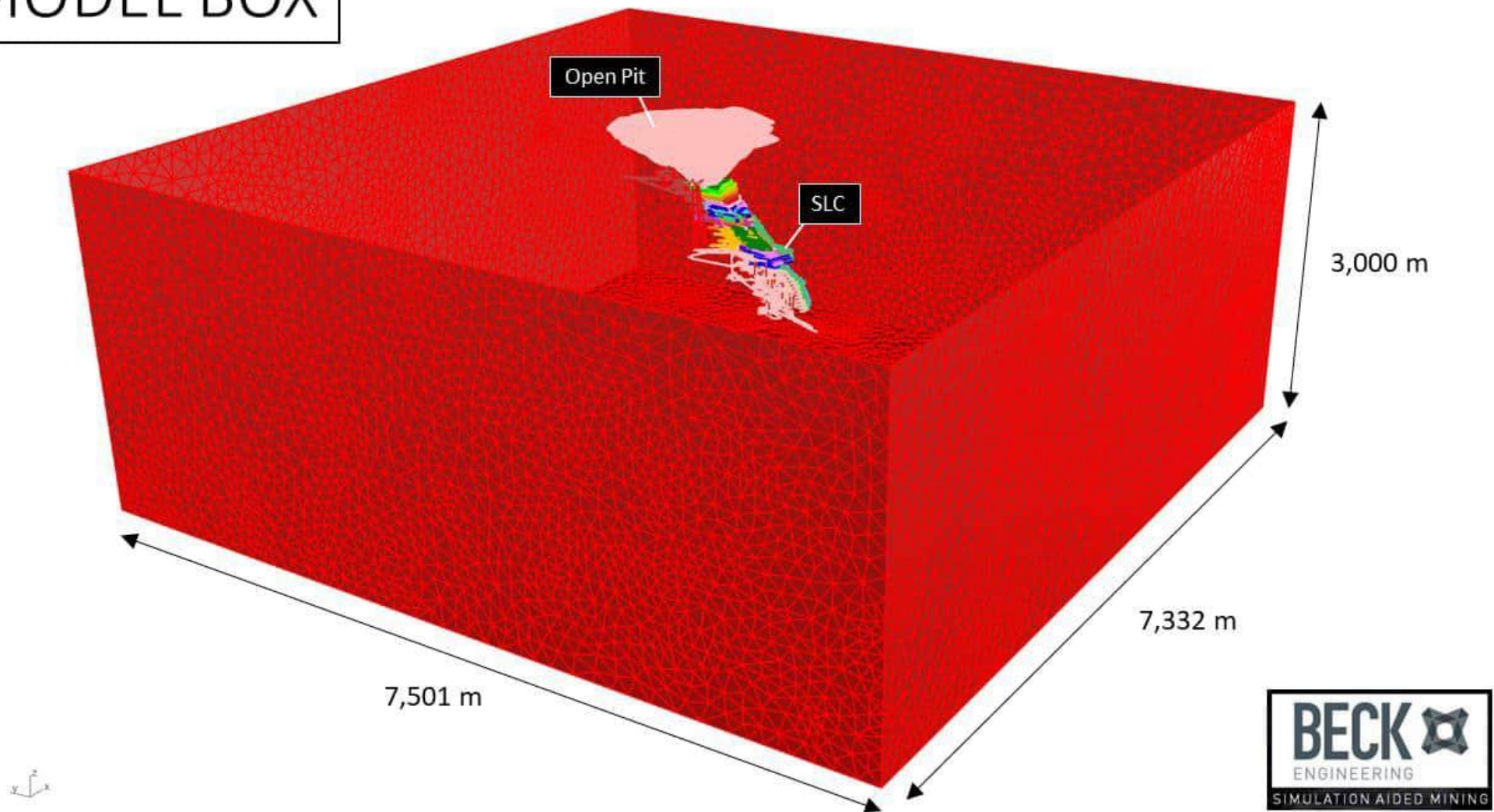


Figure 2-12 Global geometry of the finite-element simulation domain for the Ernest Henry models.

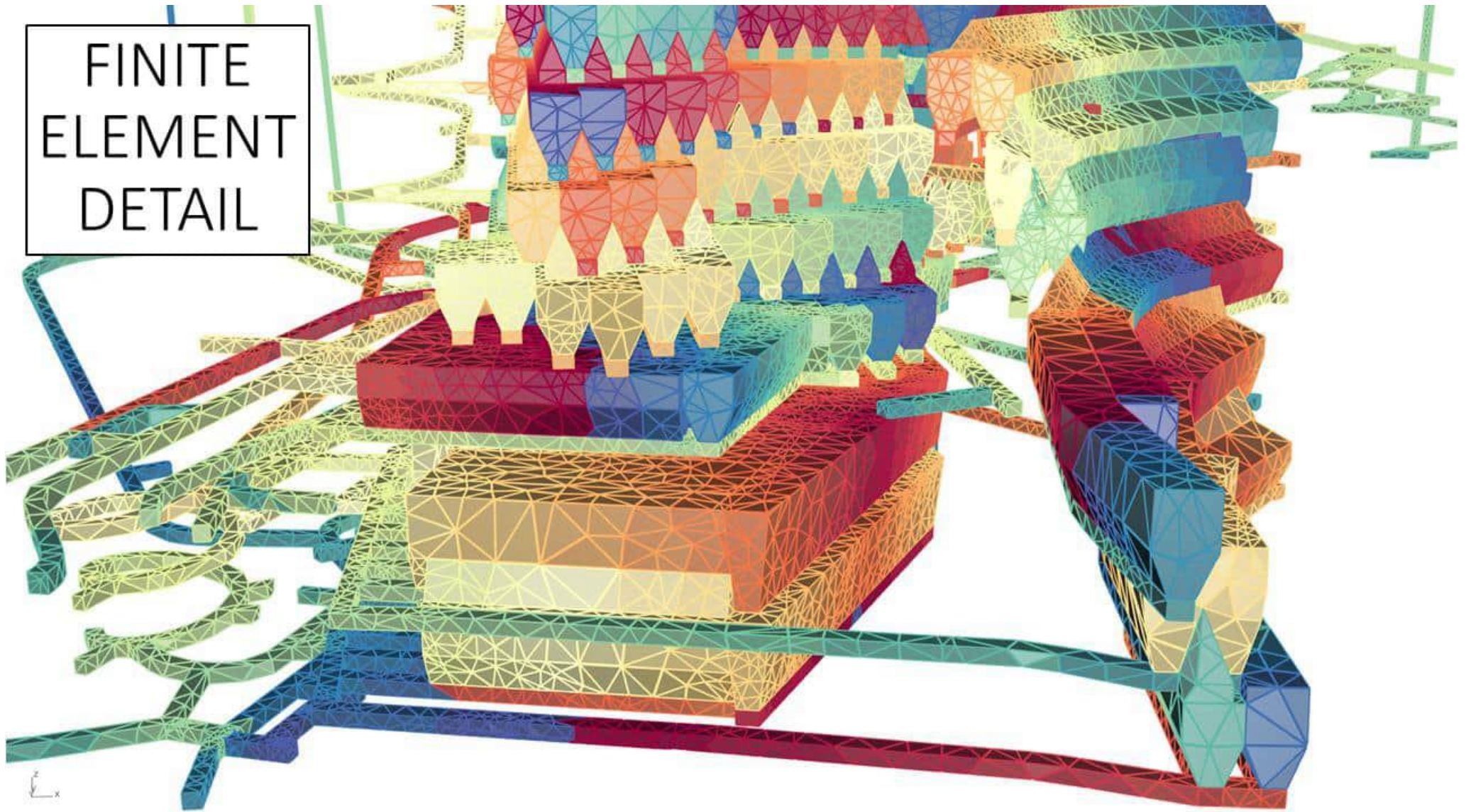


Figure 2-13 Geometric detail of the finite element representation of underground mining excavations of the future SLC.

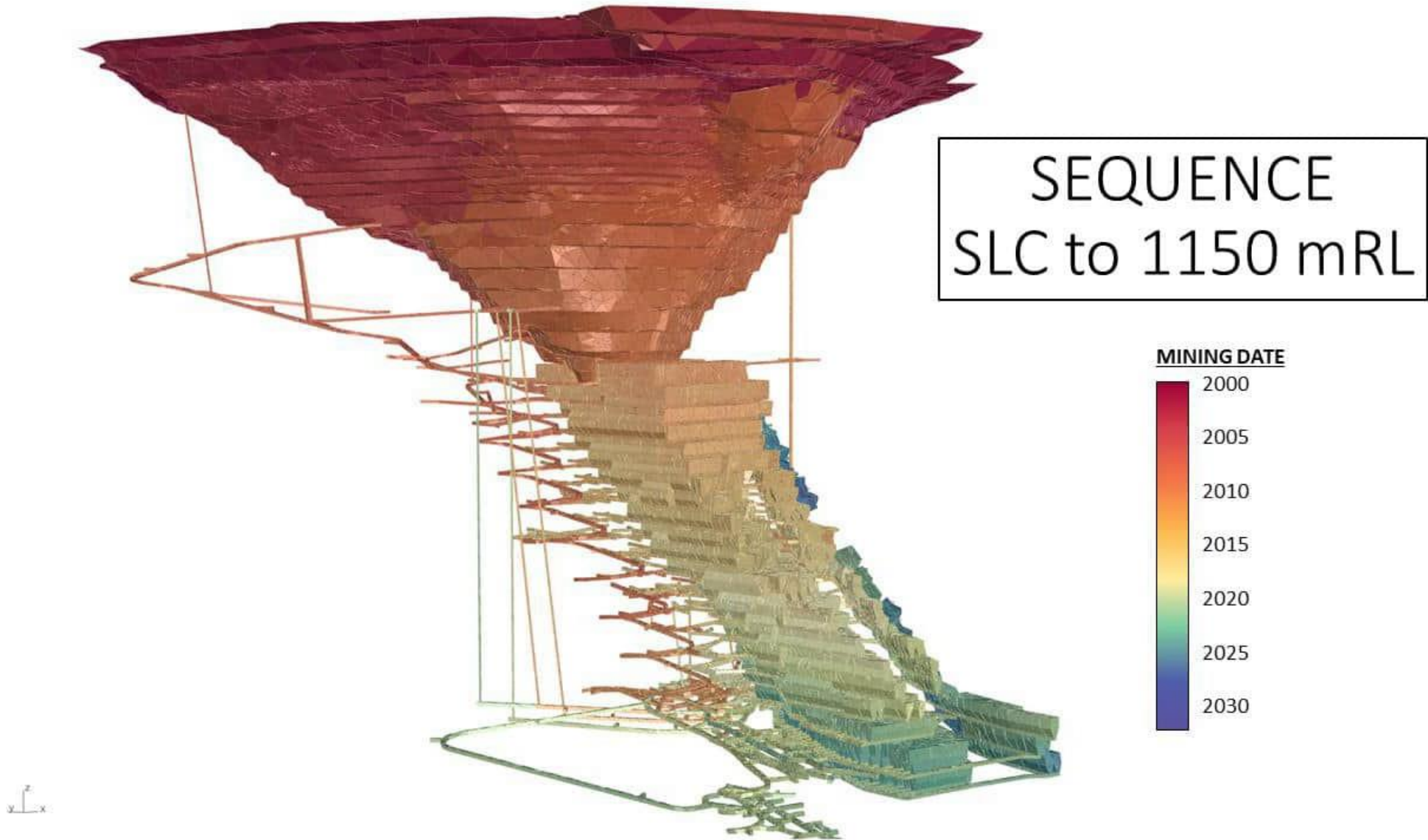


Figure 2-14 Simulated extraction sequence for the open pit and underground mining.

2.10 Draw schedule

Actual and planned production bugged tonnes were provided to BE by Snowden Consultants (on behalf of EHM) and exported from the file *COMBINED_PFS_C&C_1st Pass_Rev1_20221005_Export.duf* then input to the FS4 flow simulation as provided. Earlier records of production draw actuals were merged with the more recent data. The spatial distribution of production tonnages in the draw schedule are illustrated in **Figure 2-15** and **Figure 2-16**.

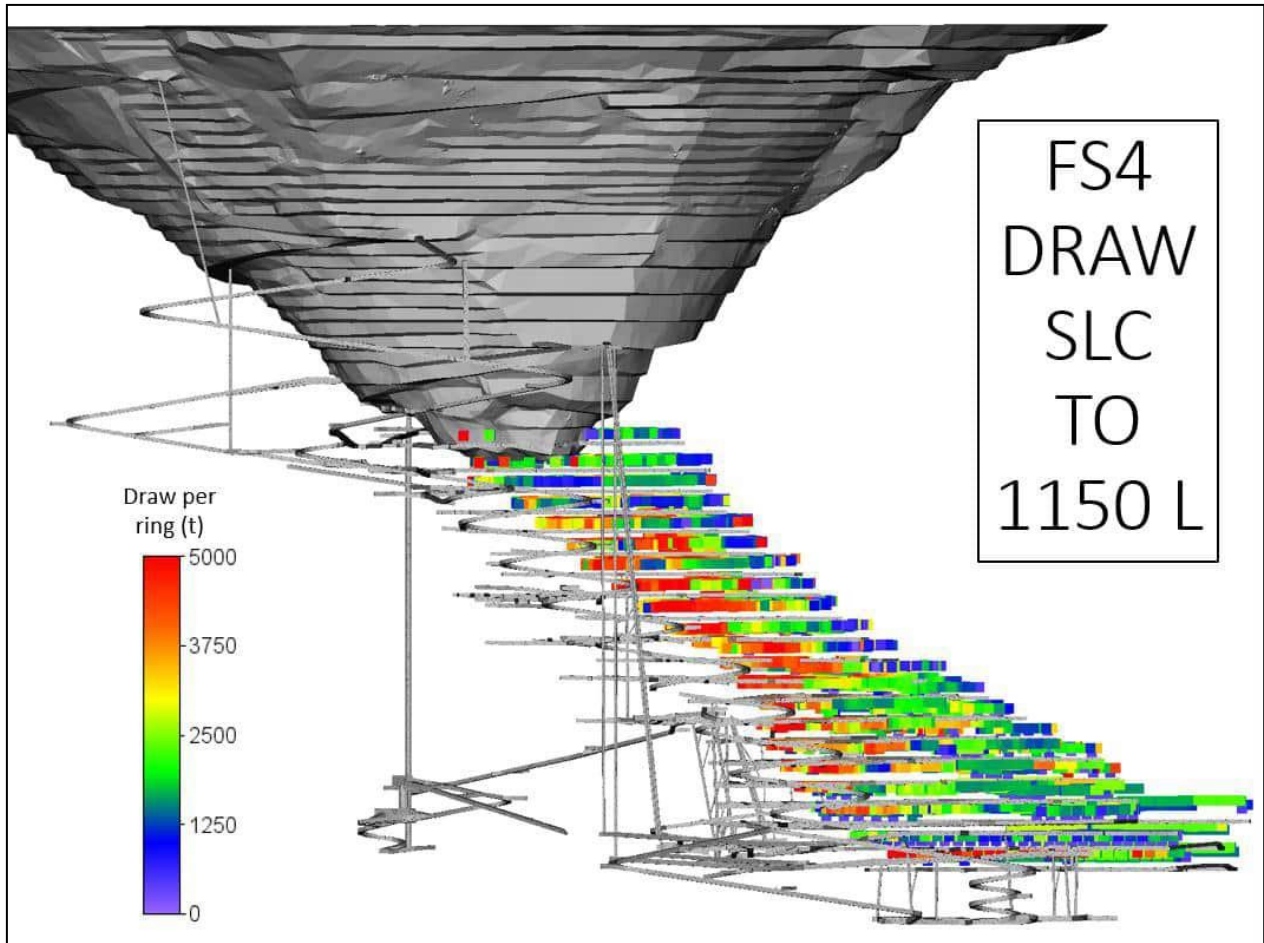


Figure 2-15 Planned production draw tonnes input to the FS4 flow simulation.



Figure 2-16 Example of simulated production draw for one sublevel of the SLC (top view, 1200 Level).

2.11 Calibration

Our previous numerical simulations of the Ernest Henry mine have undergone a comprehensive process of calibration of the material strength properties over many years (see Beck, 2021 and Campbell, 2022). These calibrations have been undertaken by comparing model forecasts of seismicity, displacement and rock mass damage to measured data such as underground seismic activity and surface displacements, such as INSAR and headframe movement, and adjusting the model inputs until a close match was achieved. Considering these existing calibration results, which carried over into the current phase of modelling, the focus of our current simulation calibrations was on optimising the caving criterion for the mechanical-flow coupled simulation (see Section 2.2).

The spatial extent of the surface subsidence crater forecast by the numerical model was calibrated to a geo-referenced aerial photograph of the Ernest Henry site taken in mid-2022. The model was calibrated by varying the caving criteria defined earlier in Section 2.2 and re-running the model until a match was achieved. Only one calibration run was required to achieve a good match. Furthermore, the surface displacement forecasts of the model were calibrated to a number of GPS station displacement datasets over the period 2019 to 2022. The GPS data were collected at several locations around the southern crest of the open pit, directly adjacent the high scarp that has formed at the limit of the subsidence crater. A close match was achieved between the modelled and real extent of the subsidence crater and the position of the cave scarp. In most locations around the southern pit crest, the difference between the modelled and measured cave scarp position, as determined from the latest georeferenced photographs, was within the range of 10 to 20 m.

A mine-scale view of the calibrated model forecast of the cave propagation to 2022 Q4 is illustrated in **Figure 2-17**. The latest aerial photograph of the cave zone, taken in mid-2022 and focusing on the southern end of the subsidence zone, is illustrated in **Figure 2-18**. This figure shows the position of the cave scarp that has formed at the boundary between the active zone of material flow and rilling (i.e. the subsidence crater) and the zone of open tension fractures where large blocks are progressively becoming unstable and toppling into the crater. The match between the model forecast and real subsidence crater extents is illustrated in **Figure 2-19**. The position of the various GPS stations is also illustrated and the condition of those stations is noted. One of the stations for which data was provided has recently been lost into the cave. The model correctly forecasts that event. In general, a close match to cave extents has been achieved throughout most of the crater, although the model does slightly overestimate the crater size in the east.

Comparison between the model forecasts and GPS-measured displacements in the east-west direction (dU_x), north-south direction (dU_y) and vertical direction (dU_z) during the period 2019 Q4 to 2022 Q4 are illustrated in **Figure 2-20** to **Figure 2-22**, respectively. These images show a continuous horizontal section of the model displacement forecasts taken at the original surface elevation together with the point locations of the GPS stations, coloured according to displacement magnitude. The quality of the modelled displacement match to the GPS improves with increasing distance from the cave scarp. That is, the model more closely matches the GPS data farther away from the scarp edge. GPS stations located outside the zone of major tension fractures around the scarp edge generally show a close match with the model, but a less accurate match is observed with GPS stations located within the major tension fracture zone. This is expected and can be attributed to the complex process of progressive block instability and toppling failure of large blocks of weathered and caprock material at the edge of the cave scarp. The controls on this process include the local geology, such as weathering intensity, depth of caprock/weathering and small-to-intermediate-scale near-surface structures, which are not known in detail or included in the model.

Modelled surface displacements during calendar year 2022 were also compared to measured INSAR data (**Figure 2-23**). The 2022 INSAR data indicated a zone of ~ 50 mm/yr horizontal displacement along the southeast and southwest rim of the cave zone, which was well matched to the model forecasts in terms of the movement magnitude and spatial extent of that zone. Note that the model displacement forecasts shown to the left in **Figure 2-23** present the displacements at the surface and in the intact sidewalls of the cave zone, not the displacements of the muckpile surface. The closeness of the modelled and measured displacement data indicated that the strength properties of the rock materials and faults in the model were appropriate.

Overall, a close calibrated match has been achieved for the purposes of forecasting the cave propagation, subsidence crater limits and global displacements for the major mine infrastructure surrounding the cave zone and open pit. However, the model should not be used to forecast the timing of small-scale toppling failures at the cave scarp.

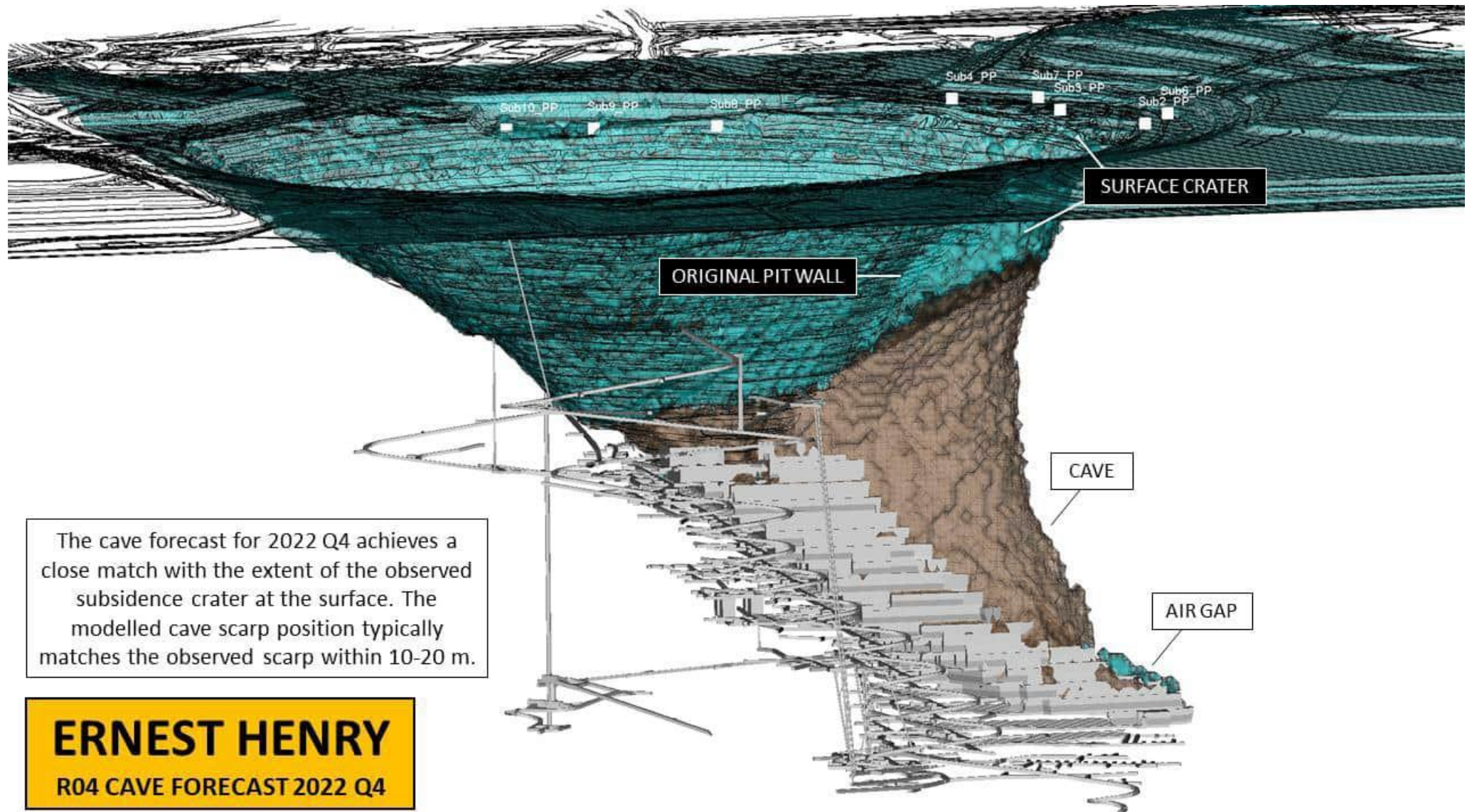


Figure 2-17 Mine-scale view of the calibrated model forecast for cave propagation as at 2022 Q4.

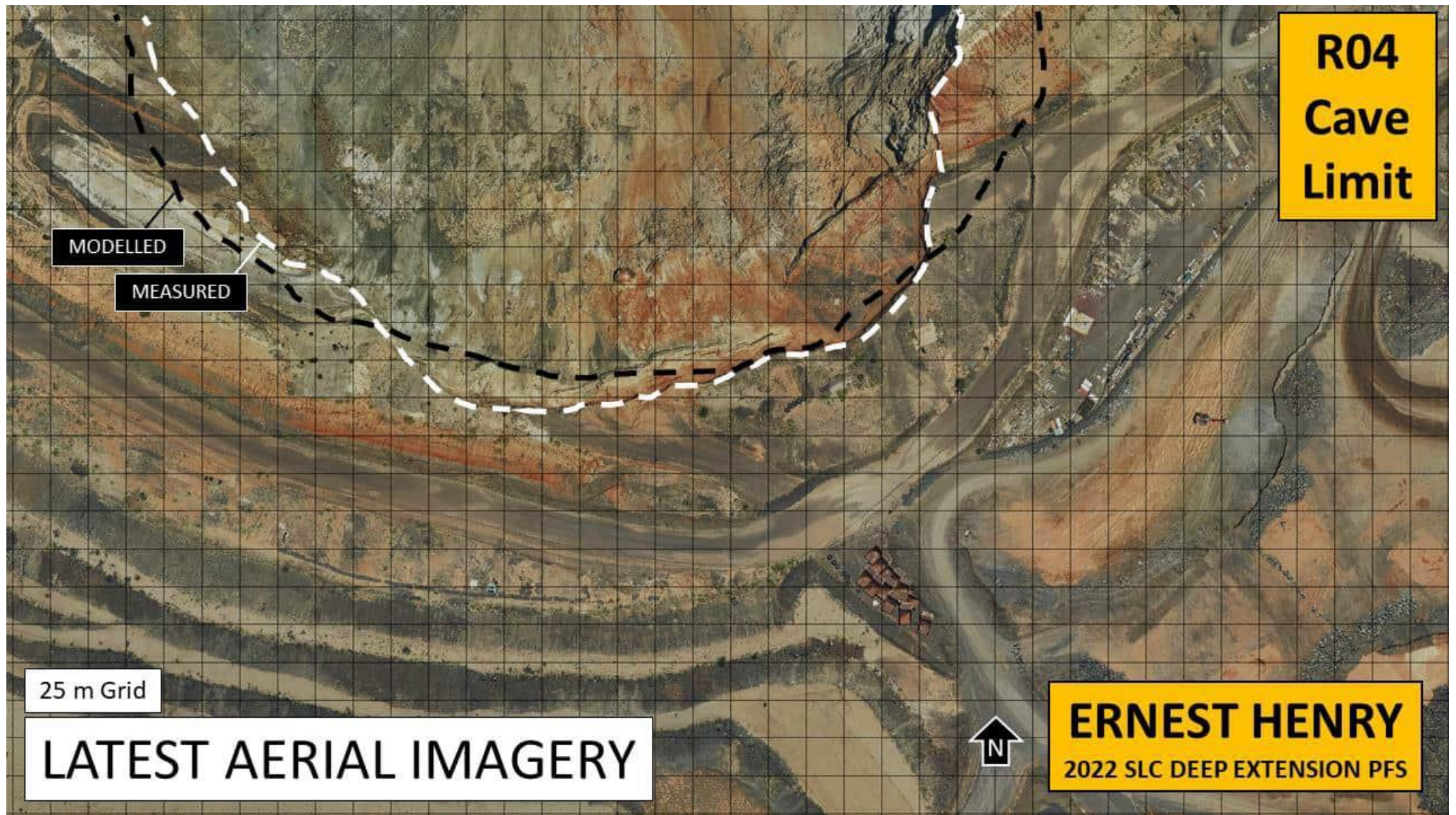


Figure 2-18 Latest aerial photograph showing the southern limits of the surface subsidence crater.

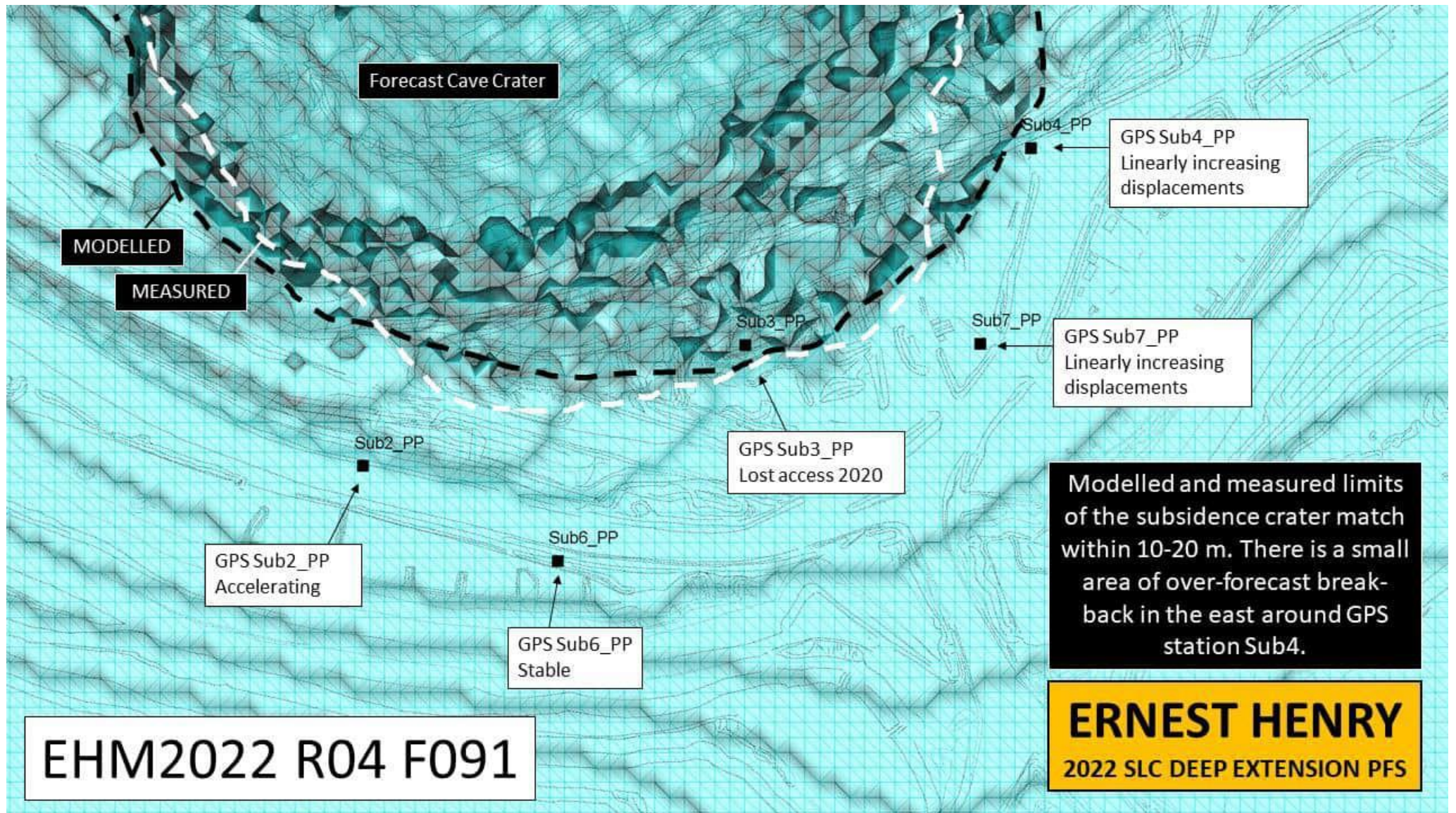


Figure 2-19 Match between modelled and observed spatial extent of the surface subsidence crater in 2022.

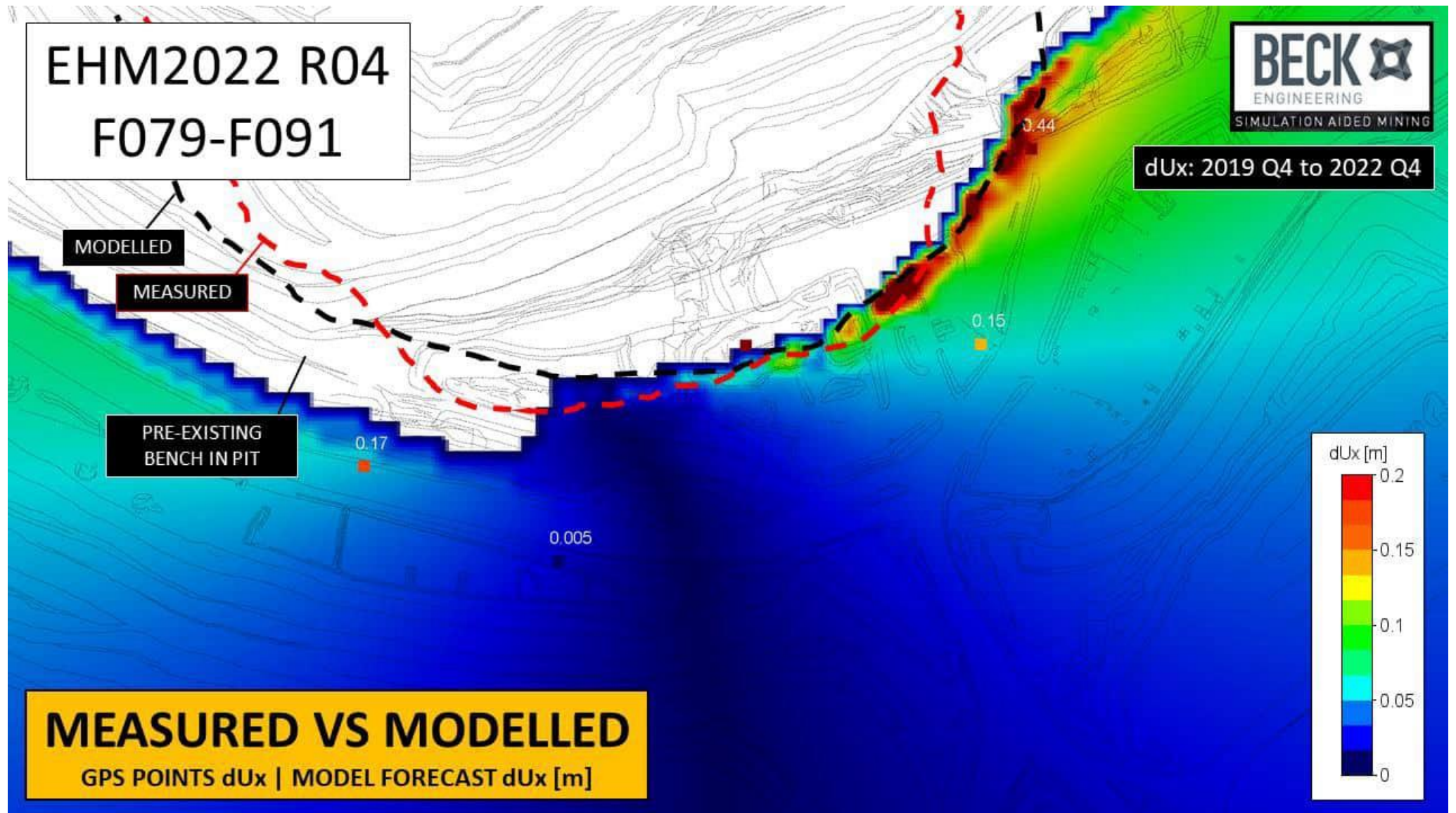


Figure 2-20 Modelled versus measured displacement match in the X (east) direction in (2019 Q4 to 2022 Q4).

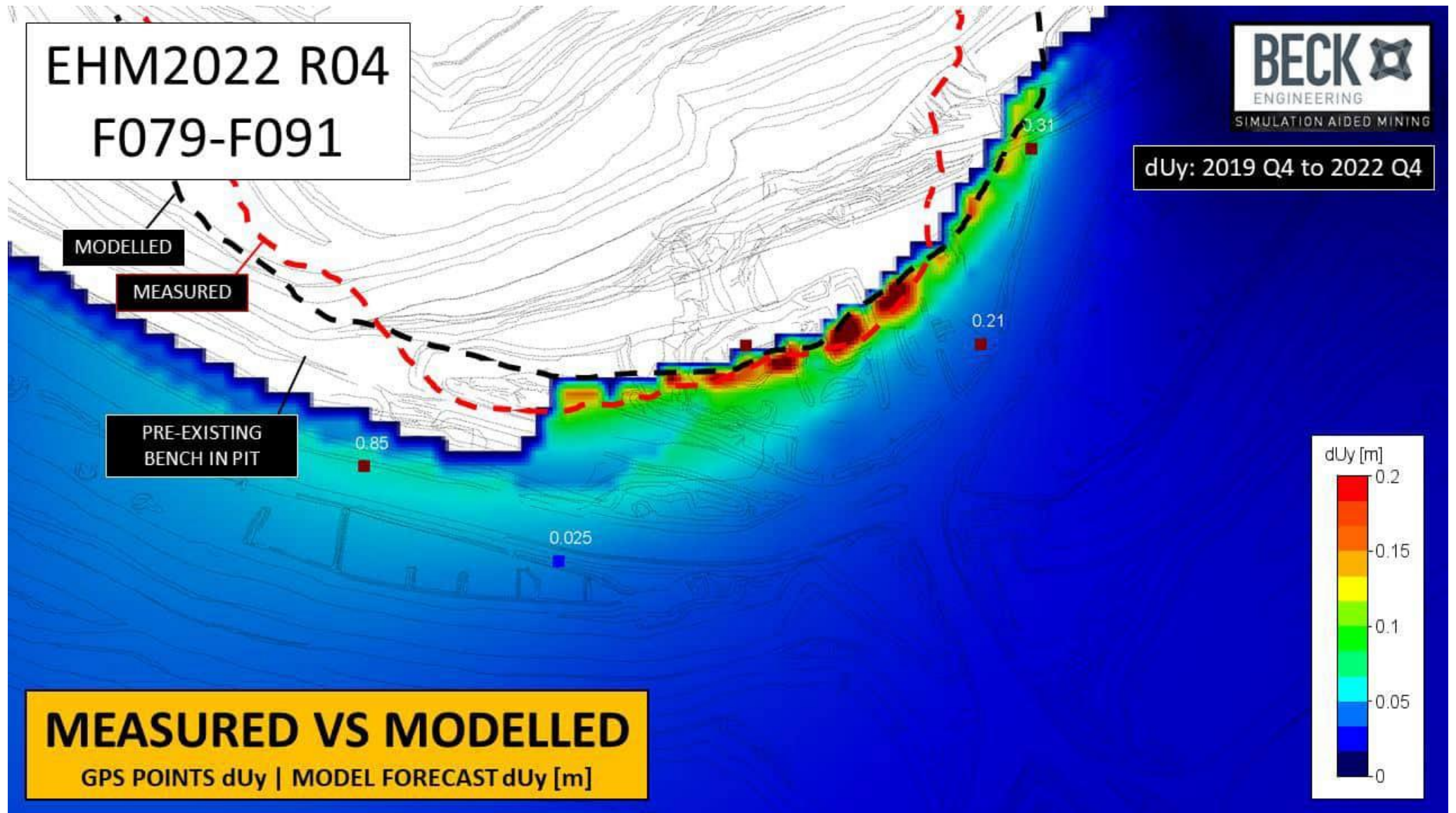


Figure 2-21 Modelled versus measured displacement match in the Y (north) direction (2019 Q4 to 2022 Q4).

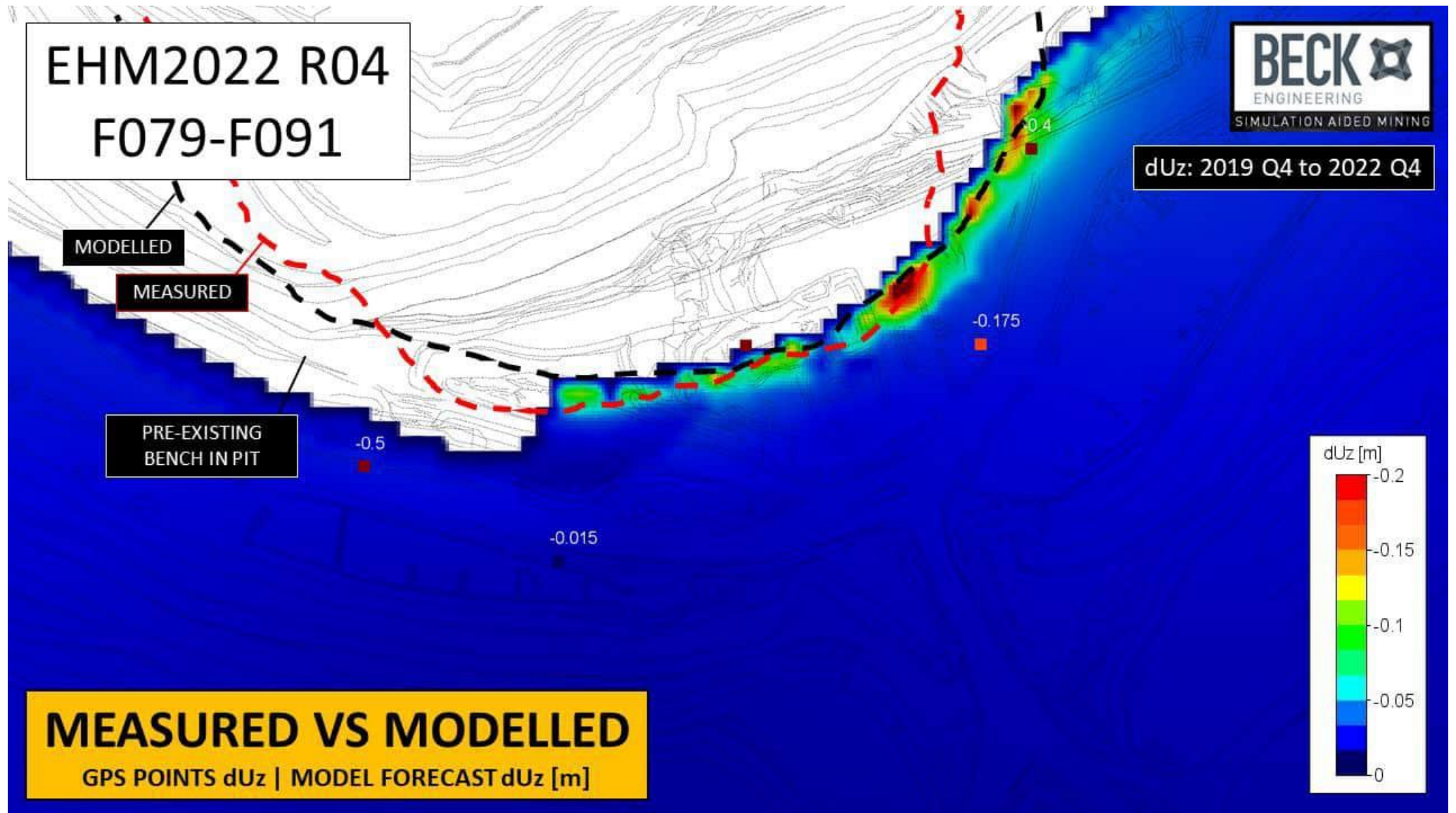


Figure 2-22 Modelled versus measured displacement match in the Z (vertical) direction (2019 Q4 to 2022 Q4).

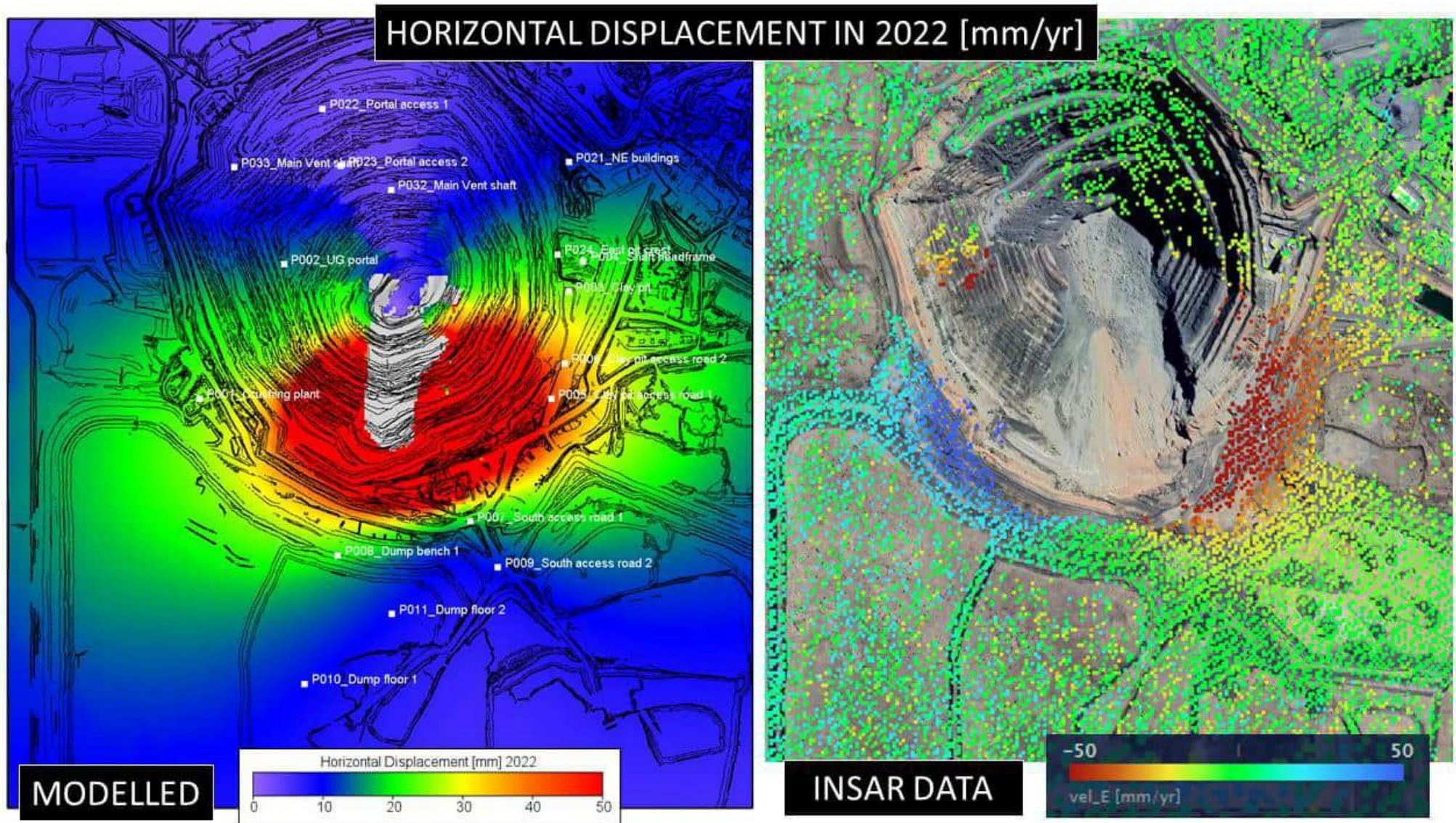


Figure 2-23 Comparison of modelled and measured (via INSAR) surface displacement during 2022.

3 FORECASTS, INTERPRETATION & DISCUSSION

This section summarises the model results, including:

- The open pit and underground mine interaction, including cave propagation,
- Slope stability of the open pit, with particular focus near to the subsidence crater,
- Surface displacement forecasts,
- Groundwater recovery after mine closure and flooding.
- Forecast volumes of the cave zone, in-pit muckpile and caved region of the southern waste dump.

The results are best reviewed and interpreted using 3D visualisation software such as Voxler. Presented here is a summary of the results and our interpretation of the forecast rockmass behaviour, possible impacts on mining activities and risk mitigation measures, where necessary.

3.1 Rockmass damage scale

Figure 3-1 shows BE's rockmass damage scale. Rockmass damage is plotted on a logarithmic scale called logP, where $\log P = \log_{10}(1000\epsilon_p + 1)$ and ϵ_p is the deviatoric equivalent plastic strain. This damage allows a wide range of plastic strain magnitudes to be plotted with a convenient linear colour scale. The damage scale in terms of stress and strain is shown in **Figure 3-2**. In caving mines:

1. Minor rockmass damage indicates a low likelihood of instability.
2. Moderate rockmass damage indicates an increased likelihood of instability, particularly in hangingwalls and crowns of large-scale excavations or around the cave.
3. Significant rockmass damage is characterised by relatively high frequency of instability, leading to reduced recovery and productivity, higher dilution, increased ground support rehabilitation and associated mining costs.
4. Very significant rockmass damage is characterised by severe stability problems for large cavities, affected underground development or surface infrastructure. This often necessitates alternative mining methods and/or infrastructure replacement.

It is essential to note that these damage categories are indicative only. Persistent structures present at length scales below the inherent resolution of the model are likely to exist and these would strongly influence the stability of both development and production mining excavations.

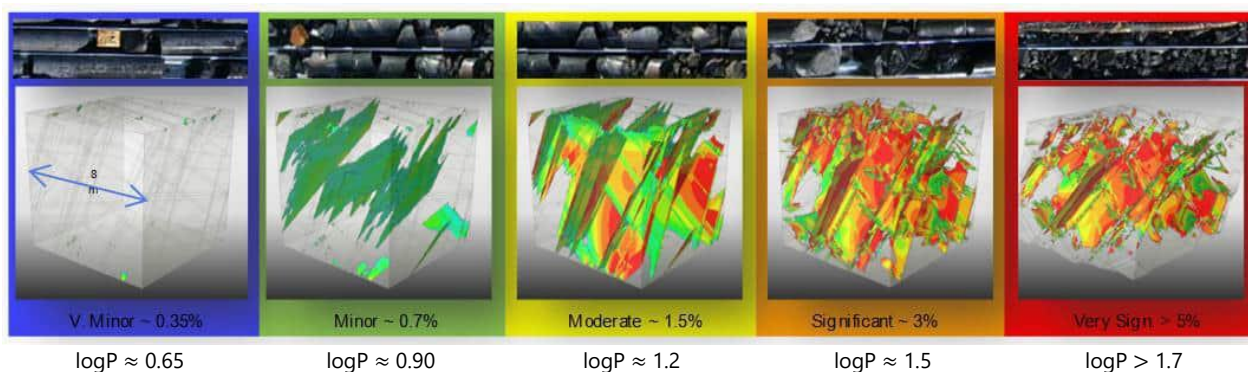


Figure 3-1: Rockmass damage scale.

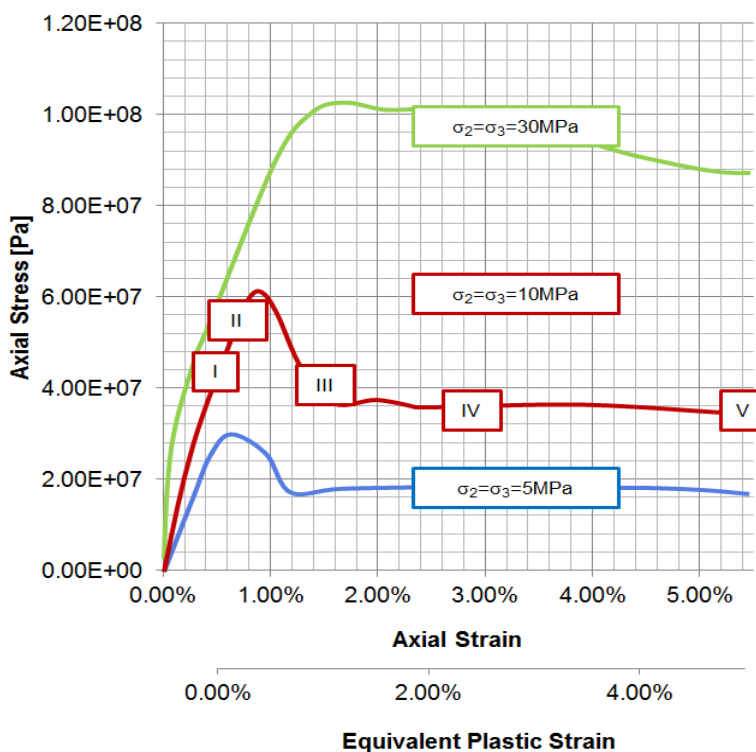
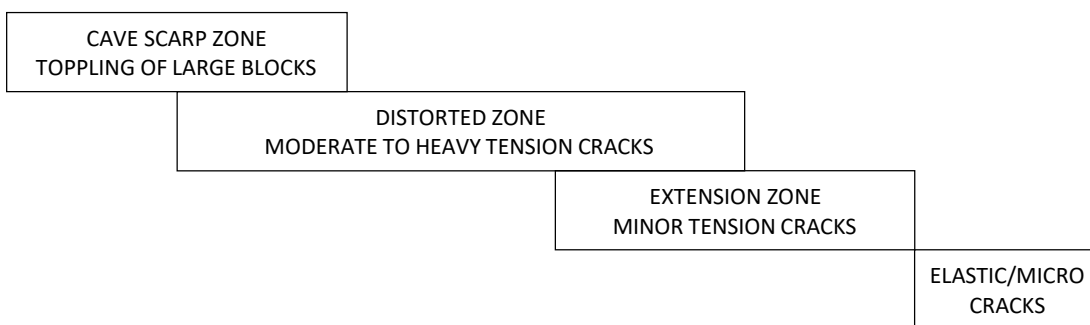


Figure 3-2 Stress vs. Strain chart showing corresponding rockmass damage levels.

A set of quantitative classification criteria for the appreciation of surface subsidence impact around caving mines is shown in Table 3-1.

Table 3-1 Surface subsidence impact classification criteria.

DESCRIPTION				
Very significant movement with moderate to heavy fracturing with scarp formation and toppling failure of large blocks into the subsidence crater	Very significant movement with moderate fracturing with localised heavy fracturing or scarp formation	Moderate movement with minor fracturing	Minor movement with sparse hairline cracks	Minor movement with no visible cracks



Degree of Influence	Very Severe		Severe	Moderate	Slight	Negligible
Subsidence or Horizontal Displacement	> 5-10 m	> 2 m	> 1 m	> 0.5 m	> 0.2 m	< 0.2 m
Horizontal Strain	~ 10 ⁻¹	~ 10 ⁻²	> 3 x 10 ⁻³	> 1.5 x 10 ⁻³	> 0.5 x 10 ⁻³	< 0.5 x 10 ⁻³
Angular Distortion	~ 10 ⁻¹	~ 10 ⁻²	> 7 x 10 ⁻³	> 3 x 10 ⁻³	> 1 x 10 ⁻³	< 1 x 10 ⁻³
Plastic Strain	> 5 %	1 - 5 %	0.7 - 1 %	0.3 - 0.7 %	0.1 - 0.3 %	< 0.1 %

3.2 Forecasts – SLC to 1150 mRL

This section presents the modelling forecasts of the final, calibrated numerical simulation of the mine design. The results include forecasts of rockmass damage, ground displacements, mining-induced strain, cave propagation and groundwater recharge for the mining period as well as a simulated period of 100 years following the completion of mining.

- A recent photograph of the Ernest Henry cave zone is presented in **Figure 3-3**.
- This subsidence assessment simulated a sublevel caving (SLC) method of underground mining extending down to the 1150 mRL elevation in both the main cave as well as the southeast lens or the Ernest Henry orebody. Underground mining at Ernest Henry is currently underway at the 1225 mRL, approximately, and the SLC to the 1150 mRL is currently planned to be completed in 2027 Q3. A comparatively small amount of remnant SLC mining is also scheduled in the simulation beyond 2027 in some of the upper levels of the southeast lens, the mining of which officially completes the mine plan for this design. A north-facing image of the as-built and planned mining excavations of the SLC to 1150 mRL design, as simulated in the model, is shown in **Figure 3-4**.
- The simulated mine plan for the SLC to 1150 mRL design includes a total of 73,421,118 tonnes of production draw, which would consist mostly of blasted ore and a small amount of waste material necessary to draw in order to facilitate continuous cave propagation.
- Following completion of the SLC to 1150 mRL and remnant SLC mining in some upper levels by the late 2020's, the mine is simulated as being closed. The de-watering pumps in the underground mine sumps and near-mine bore field would then be decommissioned. Groundwater recharge into the previously de-watered mining zone would then occur, result in gradual re-flooding of the underground and open pit voids, including the cave zone. This recharge was simulated in the hydro-mechanical coupled model and the gradual recovery of the phreatic surface is illustrated in **Figure 3-5**. Eventually, a stable long-term equilibrium is reached whereby the phreatic surface maintains a stable elevation near surface and the long-term post-mining groundwater elevation is established. The model indicates that the re-flooding of the mine will eventually result in the post-mining phreatic surface recharging to a stable equilibrium at the 2100 mRL elevation.
- The open pit was mined until 2011 and formed the original "mine void". The SLC caving method of mining was then initiated directly beneath the open pit. The caving method has caused the southern wall of the open pit to progressively collapse (to cave) over time. The caving process is a necessary part of the mining method in order to avoid the formation of an airgap. The caving process results in surface effects, such as ground movements, cracking and formation of a deep depression on surface directly above the cave, which is filled with broken "caved" rock. These surface effects are generally termed "subsidence".
- The progressive growth of the cave above the underground mining for selected time periods in the future mine plan, including the +100 years post mining equilibrium forecast, are shown in **Figure 3-6** to **Figure 3-12**. These figures show the outline of the cave zone. That is, the region of the rockmass which has been progressively undercut by SLC mining, causing collapse of the overlying rock and formation of a zone of unconsolidated, broken rock, which dynamically flows towards the production horizons of the mine as more ore is removed from the active drawpoint levels. The images also show a coloured volume rendering of the forecast rockmass damage severity around the cave and mine workings, as per the damage severity classification scheme described in Section 3.1.
- The forecasts indicate that the orebody continues to cave until the SLC to 1150 mRL is complete. During this period of mining the cave continues to break-back towards the south and beyond the limits of the original open pit. The cave eventually causes a portion of the southern waste dump to become undercut and this waste dump material enters the cave zone.
- After the mine is closed, and de-watering infrastructure decommissioned, the phreatic surface is forecast to gradually recover to the 2100 mRL, which is approximately 56 m below the natural ground surface elevation. A series of phreatic surfaces for the end of mining period, early, intermediate and late stages of re-flooding and +100 years post-mining equilibrium stage of groundwater recharge are illustrated in the cut away sections depicted in **Figure 3-13** to **Figure 3-15**. The forecasts indicate that practically the entire underground mine, including the decline, crusher, levels and main hoist shaft eventually become fully flooded, as well as most of the open pit and cave zone. Only the top ~ 10 m of the main hoist shaft and upper 56 m of the open pit benches

and cave zone would remain as open unflooded mine voids over the long-term post-mining period. The entry to the underground mine via the decline portal would also be inaccessible below the final groundwater level.

- Plan views showing the evolution of the cave zone extents on surface and the surrounding rockmass damage are presented in **Figure 3-16** to **Figure 3-20**. These results indicate the location of the cave zone with respect to the critical mine infrastructure as well as the spatial extent of the damaged and fractured zone of rock surrounding the cave and how these conditions are forecast to change over time. Comparison of **Figure 3-19** and **Figure 3-20** illustrates the effect that flooding of the pit has on the degree of rockmass damage to the open pit benches. The increase in damage that occurs due to pit flooding is largely superficial, due to the pore water pressure effects within the rockmass during flooding. Localised small-scale instabilities of some batters and berm crests of the open pit could be expected to occur during the flooding process.
- Long-sections of the cave zone shape and rockmass damage forecast for the end of mining and after 100 years of groundwater recharge post-mining are illustrated in **Figure 3-21** and **Figure 3-22**, respectively. These images confirm that the increase in pit slope damage due to the flooding process is only superficial, with only a *Minor* damage influence forecast to extend ~ 10 m into the slope as a direct result of the flooding process, with minimal change in areas of higher pre-existing rockmass damage. It is noteworthy that an increase in damage is also forecast throughout the AM fault zone in the deep footwall. However, the damage on that fault resulting from groundwater recharge is not forecast to progress above a *Minor* severity and the fault only interacts with some isolated underground development which would be long-since flooded and inaccessible. The fault does not intersect the open pit and shows no influence on slope stability.
- Underground mining-induced displacement forecasts (i.e. excluding open pit induced displacements) taken at the end of the underground mining and after 100 years of groundwater recharge post-mining are shown in **Figure 3-23** and **Figure 3-24**, respectively. The figures define the 500 mm, 250 mm and 150 mm contours of total displacement relative to the cave zone limits, mining excavations and surface. It should be noted that the displacements throughout most of the mine space are elastic in nature, given that plastic deformations would be limited to the zone of plastic strain around the immediate abutments of the cave.
- The displacement magnitudes and directions induced by the groundwater recharge during the post-mining period are illustrated in long-section in **Figure 3-25**. The forecast indicates that the effect of flooding on the rockmass is up to 100 mm of uplift throughout a broad region of the hangingwall of the orebody and a lesser volume of the footwall. This response is primarily an elastic response in the rock mass at a large length scale. In short, the drawdown of the groundwater during mining causes minor downward movement (subsidence) and then groundwater recharge after mining partially reverses this process, causing an uplift effect. This uplift effect would occur over a long time period (i.e. decades) as the flooding occurs. As a result, the effect on slope stability in the open pit would be *Negligible* in terms of both open pit slope stability and the size of the mining void.
- Plan views showing the underground mining-induced surface displacements at the end of the mining and after 100 years of groundwater recharge post-mining are shown in **Figure 3-26** and **Figure 3-27**. A subsidence impact severity classification scheme is also shown to indicate the nature of the impact at the surface considering the forecasts. Note that the displacement results inside the cave zone limits are the displacements of the intact but fractured rock in the sidewalls of the cave, not the displacements of the caving/flowing unconsolidated rock inside the cave itself. The forecasts indicate that groundwater recharge to the mining precinct and cave zone results in an elastic rebound effect, whereby the global surface displacements partially return to their pre-mining. The magnitude of this elastic rebound is less than 75 mm throughout most of the surface precinct.
- The current cave zone extents are depicted in **Figure 3-28**. Annual forecasts of the spatial limits of the cave zone expression at the surface, i.e. the subsidence crater, to the end of mining and at 100 years groundwater recharge post-mining are depicted in **Figure 3-29** to **Figure 3-35**. These figures show plan views of the cave zone forecast superimposed over the 2022 geo-referenced aerial imagery of the mine site as well as the surveyplan of the mine infrastructure. The cave zone is forecast to begin to consume the southern waste dump in 2024. The southward propagation of the cave continues until the underground mining is completed, with comparatively large steps in cave growth during 2024 and 2026. The cave eventually consumes a significant portion of the southern waste dump, which rills into the crater. The cave is forecast to encroach on the equipment laydown yard and clay pit access haul roads adjacent the southeast pit crest by late 2024 and consume those areas during 2025. The cave zone continues to propagate towards the south over time.

- The forecast annual rate of cave zone growth towards the south direction at the surface is summarised in **Table 3-2**. The cave zone propagates most rapidly towards the due south direction, but also to the southeast and southwest less rapidly.

Table 3-2 Forecast annual rate of cave growth towards the south direction at the surface.

Date	Original Open Pit Southern Crest	
	38207 mN	
	Cave Zone South Limit	Annual Cave Growth
2022 Q4	38270 mN	-
2023 Q4	38190 Mn	80 m
2024 Q4	38080 mN	110 m
2025 Q4	38010 mN	70 m
2026 Q4	37870 mN	140 m
2027 Q4	37840 mN	30 m
End of Mining	37840 mN	0 m
+100 YEARS	37840 mN	0 m

- The final shape and dimensions of the mine voids at the end of the mining and + 100 years of groundwater recharge, including the open pit and underground workings, cave zone and surface subsidence crater, are shown throughout **Figure 3-36** to **Figure 3-39**. We note the following:
 - o The final end of mining cave zone is approximately 1,005 m high, extending from the lowest production horizon of the SLC at 1150 mRL to the natural surface at 2155 mRL. The cave zone is funnel shaped, owing to the geometry of the undercutting SLC mine and pit interaction. The cave zone forms a crescent-shaped crater throughout the southern pit crest area.
 - o There are no significant air gaps forecast to remain within the cave zone upon completion of the mine plan. Therefore, with good cave management practices, the risk of a sudden subsidence event on surface during the post-mining and flooding period, related to collapse of an air-gap within the cave zone, is considered to be extremely low.
 - o The final expression of the cave zone on the surface is forecast to reach 1,375 m from north-to-south and 1,100 m east-to-west at its widest point. The cave zone is also forecast to extend 370 m south of the original southern crest of the open pit. The final cave zone partially consumes the southern waste dump, nearby haul roads and laydown yard.
- Various views of the cumulative displacements, post open pit mining, and mining-induced zone of fracturing around the cave zone and underground infrastructure are illustrated in **Figure 3-40** to **Figure 3-44**.
- Our forecasts of the severity of the subsidence impact to surface infrastructure at the end of mining and after 100 years of groundwater recharge, based on the methodology proposed by Boscardin & Cording (1989), are illustrated in **Figure 3-45** to **Figure 3-47**. We note the following:
 - o At the end of mining the subsidence impacts of a *Severe* or *Very Severe* nature close to the level of the natural ground surface are confined to the zone of toppling within the upper part of the subsidence crater and within 35-50 m around the immediate perimeter of the scarp that forms along the crater edges. Impacts of a *Moderate* severity occur within ~ 75 m of the edge of the crater, in some locations. *Very Slight* impacts extend up to 200 m from the crater edge. This is more often the case towards the eastern side of the mine. *Very Slight* impacts do not extend as far from the subsidence crater towards the south and western sectors. Further afield, the subsidence impacts are forecast to be *Negligible*.

- After 100 years of groundwater recharge post-mining there is a slight expansion of the *Slight* subsidence impact zone, primarily around the Clay Pit Access Road, but no apparent change in the *Moderate* or more heavily subsidence-affected regions. The changes induced by flooding of the mine are minimal and would not justify any increase in the exclusion zone over time.
- The contours of surface subsidence impact severity at the natural surface elevation at the end of mining and after 100 years of groundwater recharge and the suggested long-term exclusion zone boundary are presented in **Figure 3-48** and **Figure 3-49**. The suggested exclusion zone is defined as the strain-affected zone at the surface plus an additional stand-off of 50 m. We suggest the exclusion zone to be defined on this basis and considering any minimum legislated requirements, with permanent solid rock earth bunds of 1.5 m minimum height as well as regular signage installed so as to restrict vehicle and foot access.
- Mine closure rehabilitation activities requiring heavy vehicle access into the subsidence area may be possible up to, but not beyond, the *Moderate* subsidence impacted zone, as shown by the contour line in **Figure 3-48**, under suitable safety controls identified via risk assessment and considering actual stability at the time.
- The mining-related voids, including the open pit and underground excavations and cave zone, and their respective volumes at selected times throughout the mining, are illustrated in **Figure 3-50** to **Figure 3-53**. A summary of the forecasts is presented in **Table 3-3**. Void space within the cave is assumed to be ~ 17.5 %.

Table 3-3 Summary of mining-related voids relative volumes at selected times.

	Volume (m ³)			
	2022 Q4	2024 Q4	2026 Q4	End of Mining
Original Open Pit	245,176,980	"	"	"
All Underground Excavations (Tunnels, Shafts & SLC Rings)	19,900,467	23,706,995	26,465,874	26,901,948
Cave Volume*	49,446,811	85,361,097	163,525,457	170,614 464
In-Pit Cave Muckpile	8,468,614	17,918,739	28,987,250	31,576,916
Southern Waste Dump Entered Cave	None	223,842	5,610,702	7,019,705

* Cave volume includes volume of in-pit cave muckpile (i.e. flows into open pit).

- The southern waste rock dump would be partially undermined by the SLC mining to 1150 mRL and in excess of seven million tonnes of the existing dump material is forecast to become mobilised into the subsidence crater.
- The southern waste rock dump consists of unconsolidated material of various compositions and this material can be expected to slump and rill into the cave zone during mining. This process could occur gradually, as the material is undermined from below, or suddenly, as a series of slumping events or circular-style failures as the cave propagates through the dump. A combination of instability mechanisms is likely to impact the waste dump material over time, until a final slope geometry forms at the completion of the caving process.
- The final profile of the southern waste rock dump immediately beyond the rim of the cave zone is most likely to form a rill slope at the natural angle of repose of the dump material. The profile of the caved material within the crater is also forecast to form a shallow rill angle. In that case, it is likely that the final waste dump profile would remain stable. However, steeper and possibly unstable slopes could potentially form around the final subsidence crater edge, particularly if recompacted weathered clays are contained within the dump or if the cave sidewalls directly below the dump form more steeply than the model forecasts.
- Depending on the cave sidewall and subsidence-affected waste dump profile at the end of mining, some localised slumping or circular-style slope failures of the waste dump around the rim of the cave zone could potentially occur several years after mining has concluded. These areas would not be safe to access or remediate at the time of mine closure, due to being unstable at the edge of the subsidence crater.
- Aside from the subsidence-induced stability impacts to the southern waste dump around the cave zone, as defined in **Table 3-1** and delineated in **Figure 3-48** and **Figure 3-49**, the caving process is not forecast to have any adverse stability impact on the remaining portion of the southern waste dump.

In summary, our main findings and conclusions from the model forecasts are:

- The planned underground mining of the SLC to 1150 mRL results in progressive caving of the orebody and the surface expression of the cave zone continues to propagate and expand, primarily towards the south, southeast and southwest. Relatively large steps in cave growth occur during 2024 and 2026.
- The cave zone eventually consumes in excess of 7 million cubic metres of the southern waste dump. The waste dump material would rill into the subsidence crater and open pit. The Clay Pit Access haul road and nearby laydown yard is also consumed by the cave over time, beginning in 2024.
- There are no significant air gaps forecast to remain within the cave zone at the conclusion of the underground mine plan and no further growth of the cave is forecast as a result of groundwater recharge and mine flooding.
- After decommissioning the mine dewatering infrastructure and bore field, the groundwater recharge is forecast to gradually return to a long-term phreatic surface at the 2100 mRL, which is approximately 56 m below the natural ground surface elevation.
- Re-flooding of the rock mass in the mining precinct has a minor uplift displacement effect on the rock mass. It also causes a modest but superficial increase in rock mass damage to the open pit walls. Minor batter-scale instabilities of the pit walls could occur during the re-flooding process due to local pore water pressure increase at the batter face, but no large scale pit slope instability is forecast at any time.
- The AM fault in the deep footwall of the underground does also experience a modest damage increase during flooding, but no adverse effect would be apparent at the surface and this fault does not intersect the open pit slopes.



Figure 3-3 South wall of the Ernest Henry open pit and cave zone (photo taken January 2023).

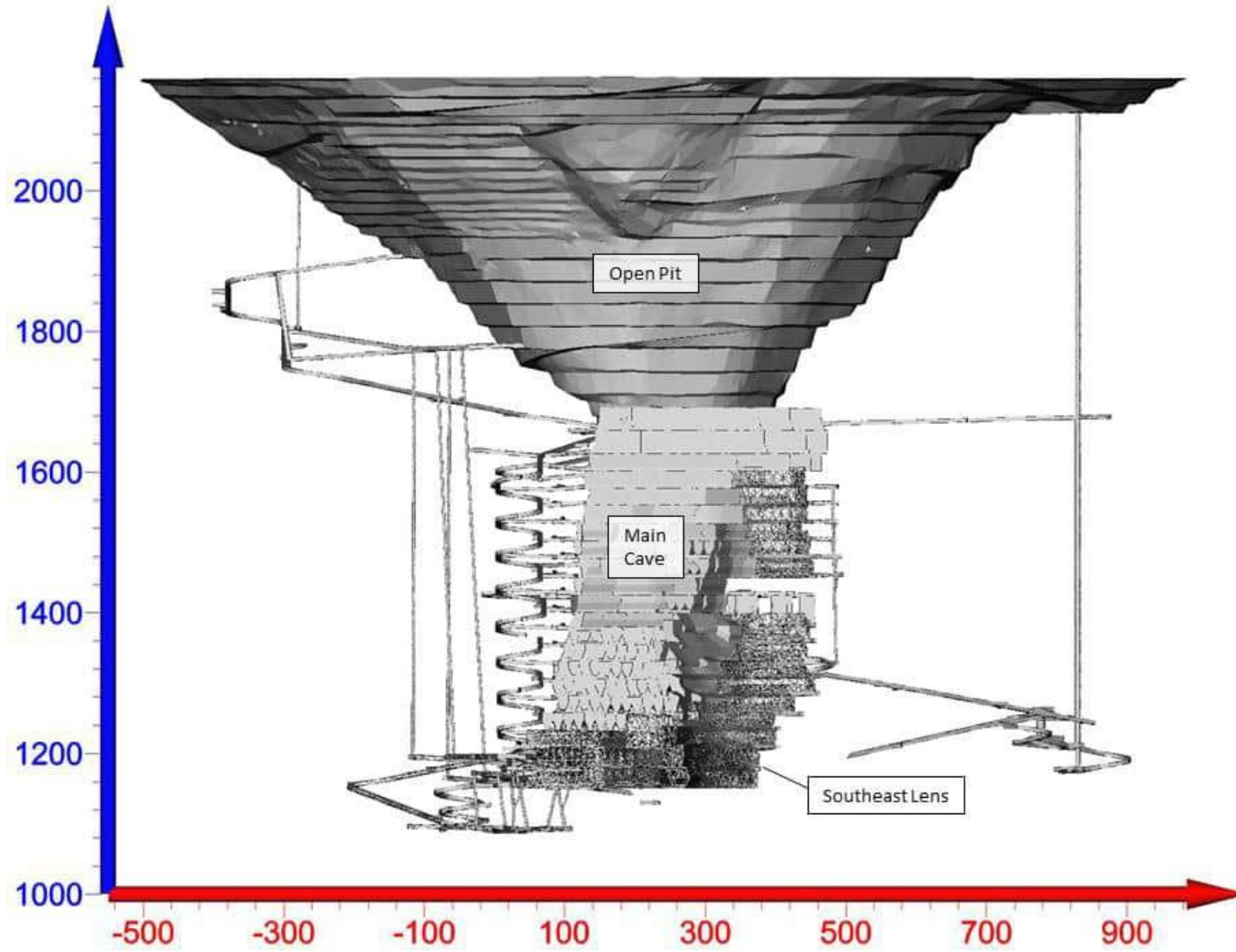


Figure 3-4 Current mining geometry (solid) and future mining to 1150 mRL (wireframe), view north.

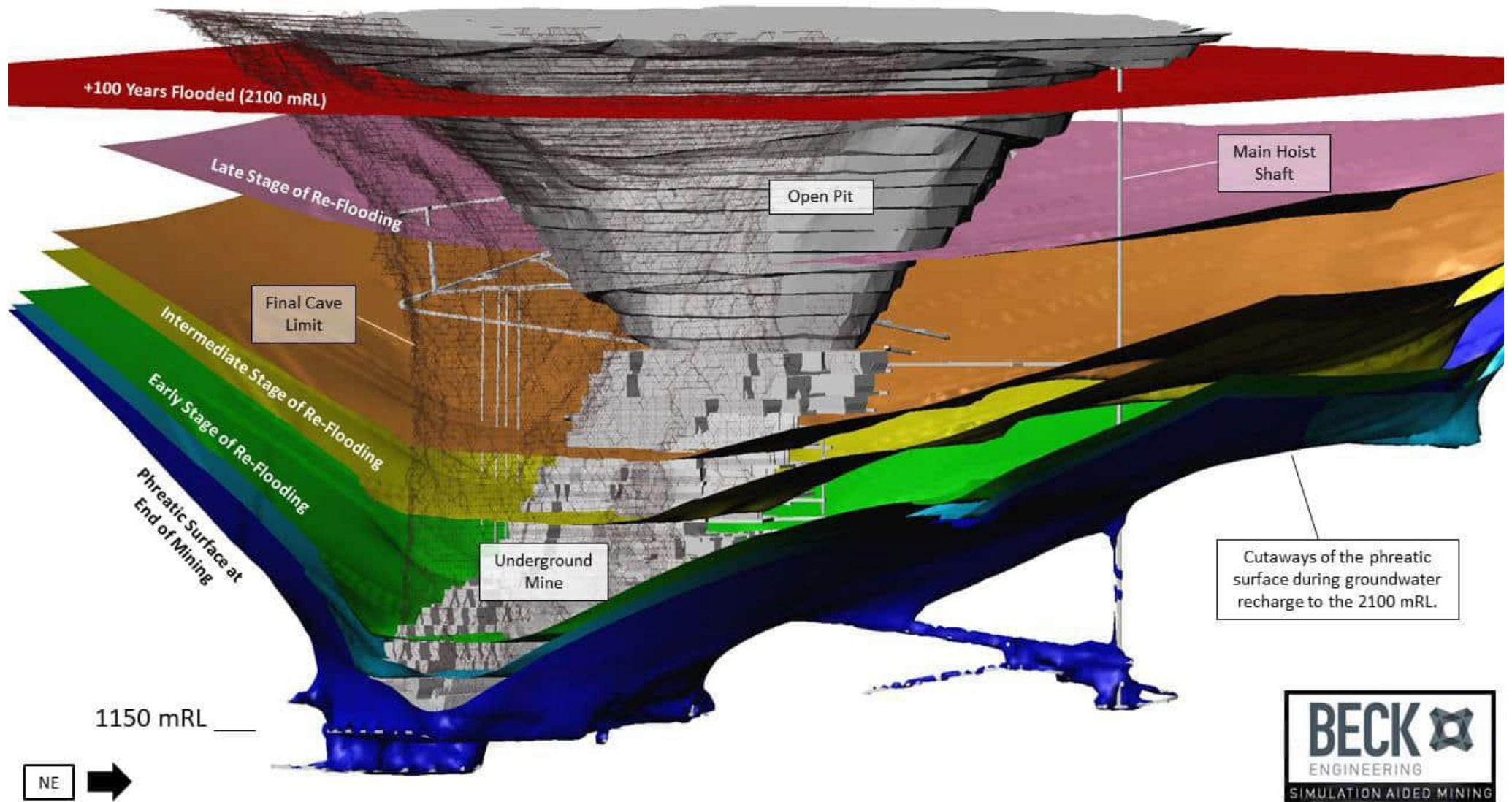


Figure 3-5 3D view of the phreatic surface evolution at stages of re-flooding from the end of mining to 100 years after mine closure, view northwest.

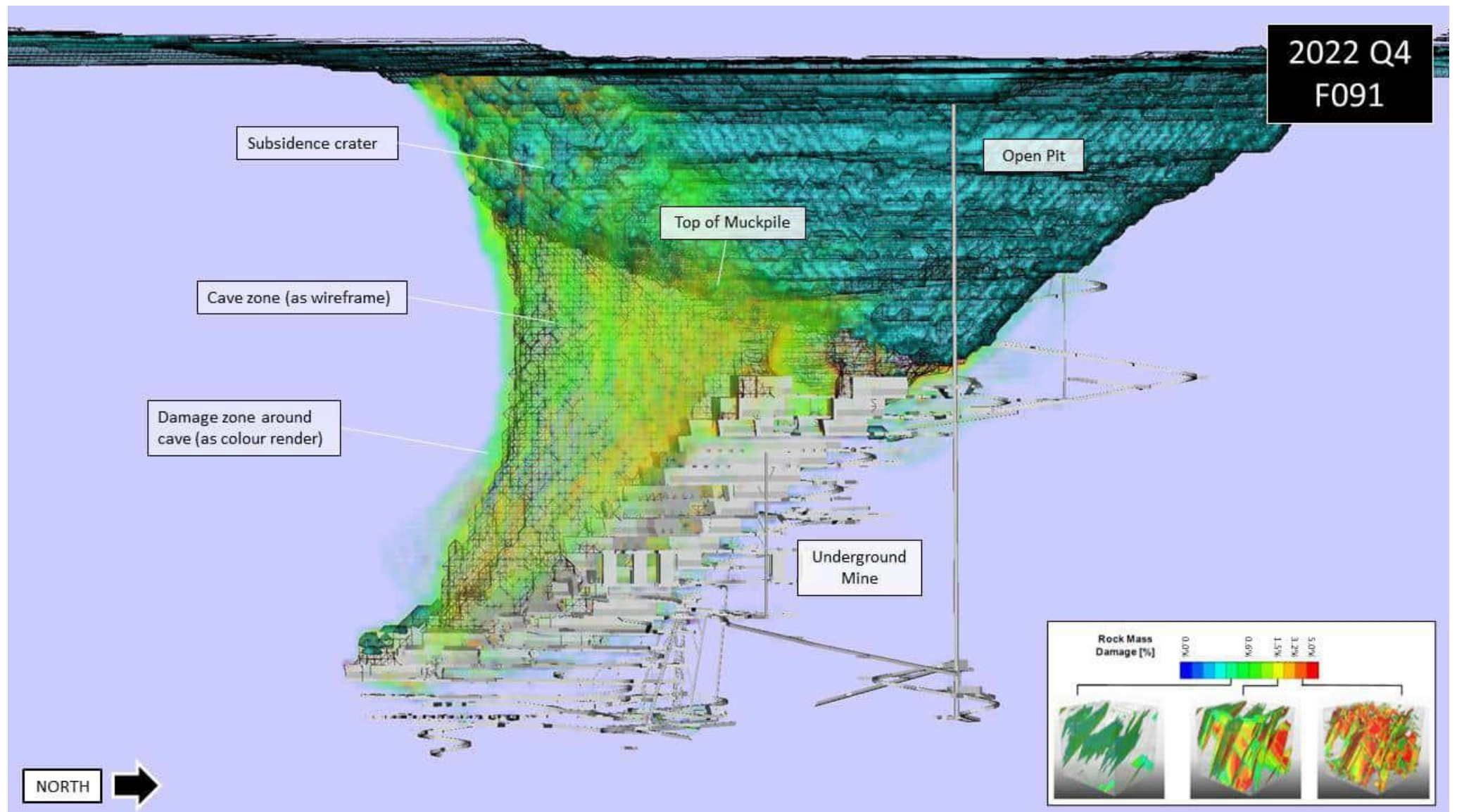


Figure 3-6 Cave and damage zone forecast for mining to 2022 Q4 (F091), view west.

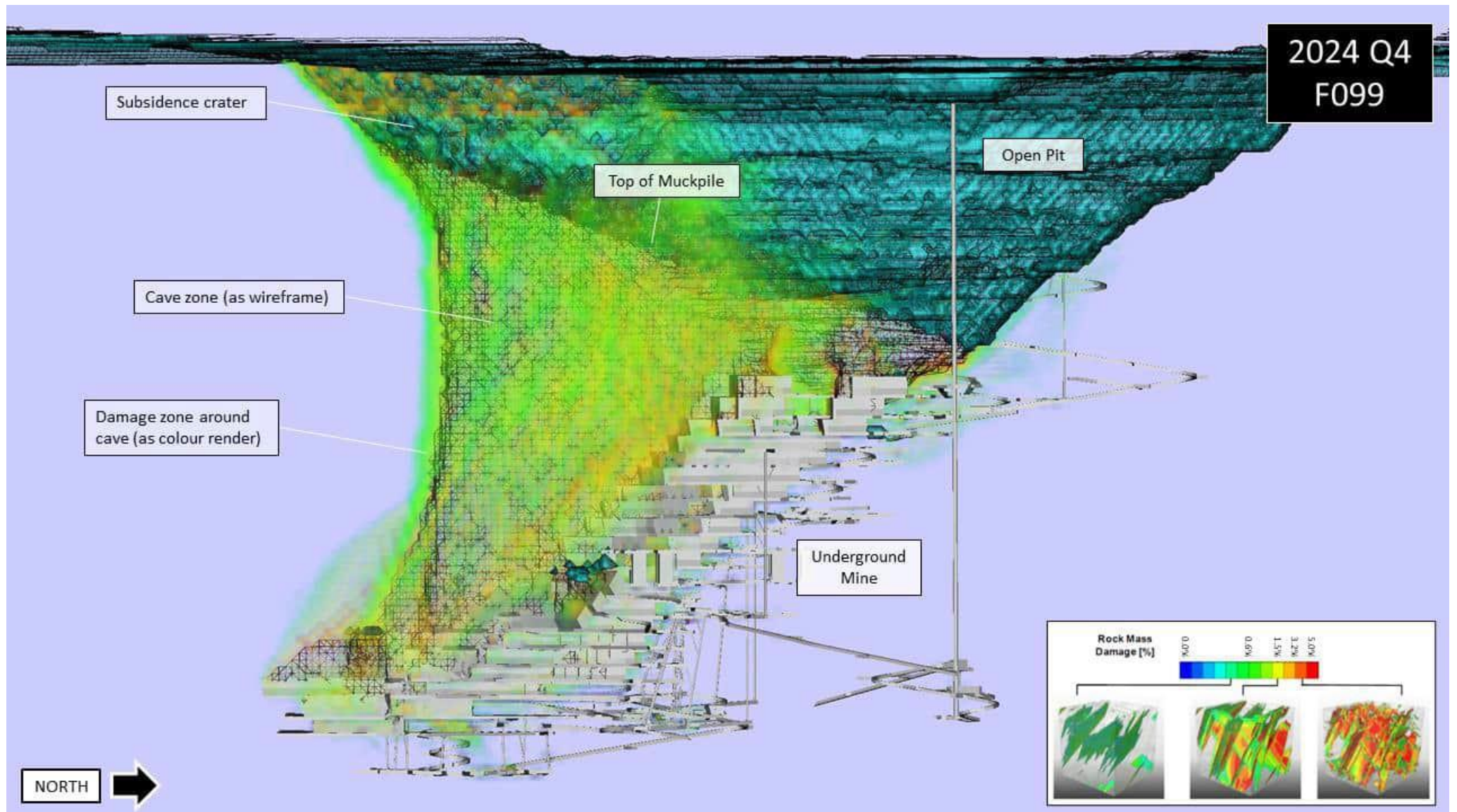


Figure 3-7 Cave and damage zone forecast for mining to 2024 Q4 (F099), view west.

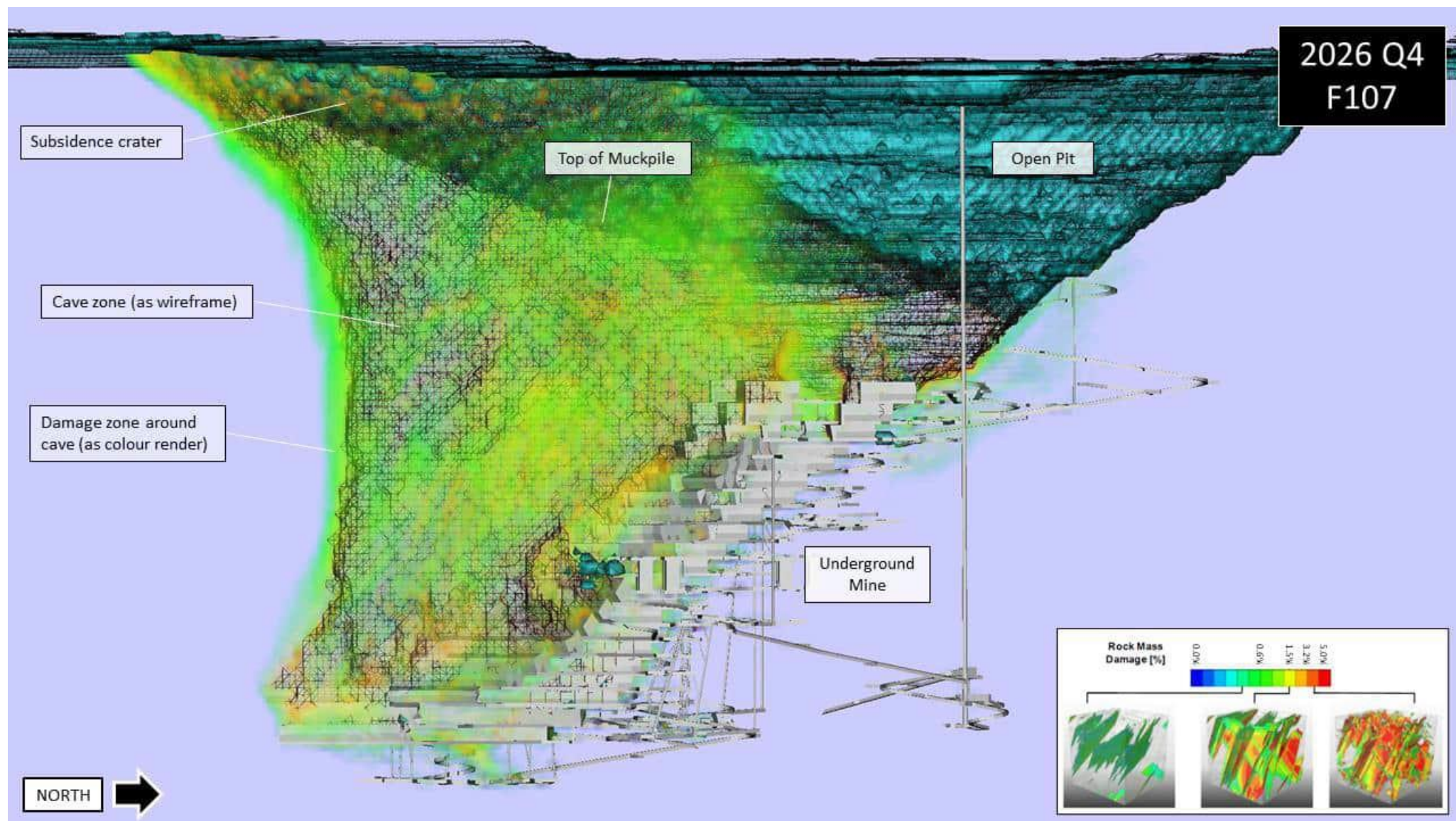


Figure 3-8 Cave and damage zone forecast for mining to 2026 Q4 (F107), view west.

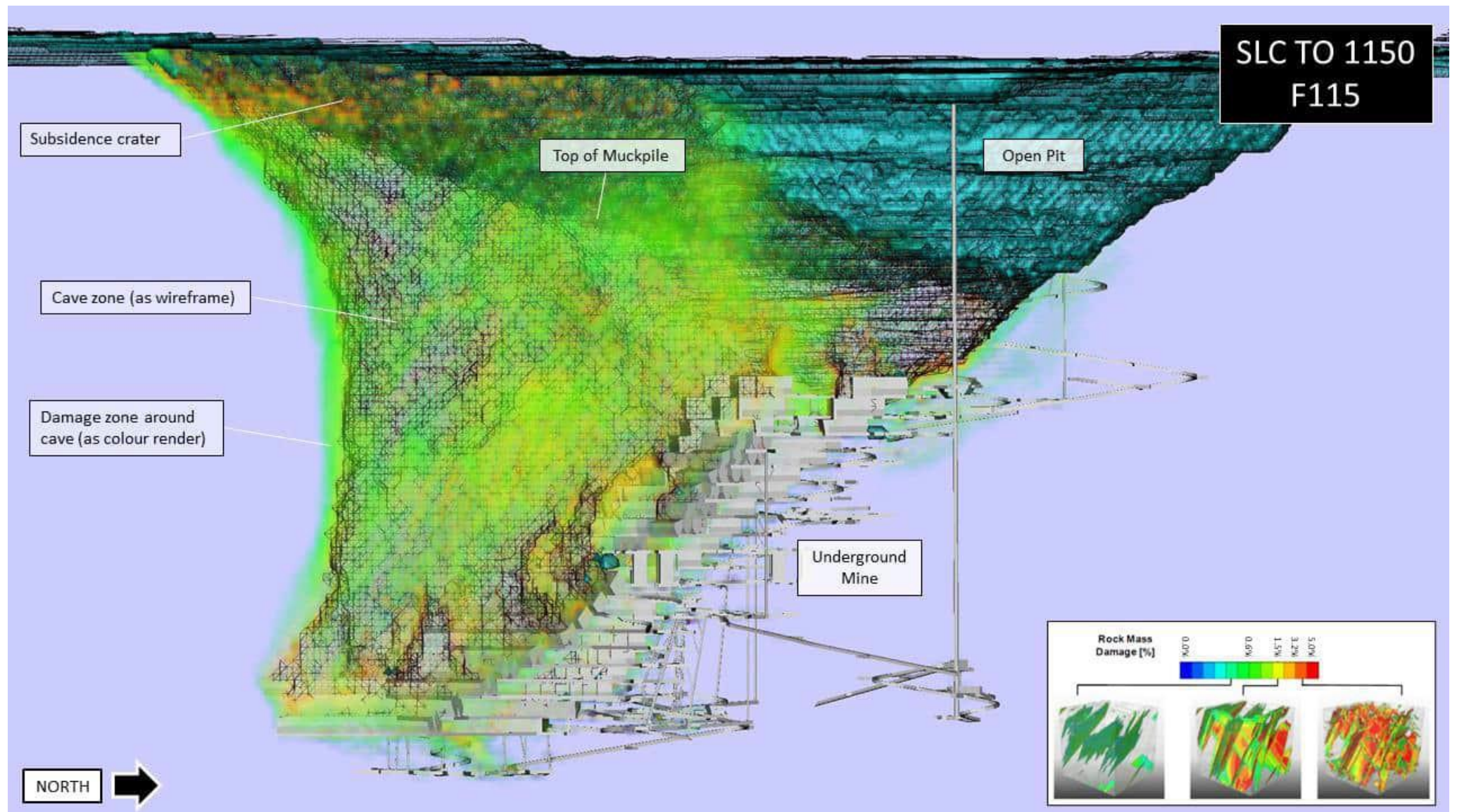


Figure 3-9 Cave and damage zone forecast at the conclusion of underground mining to 1150 mRL (F115), view west.

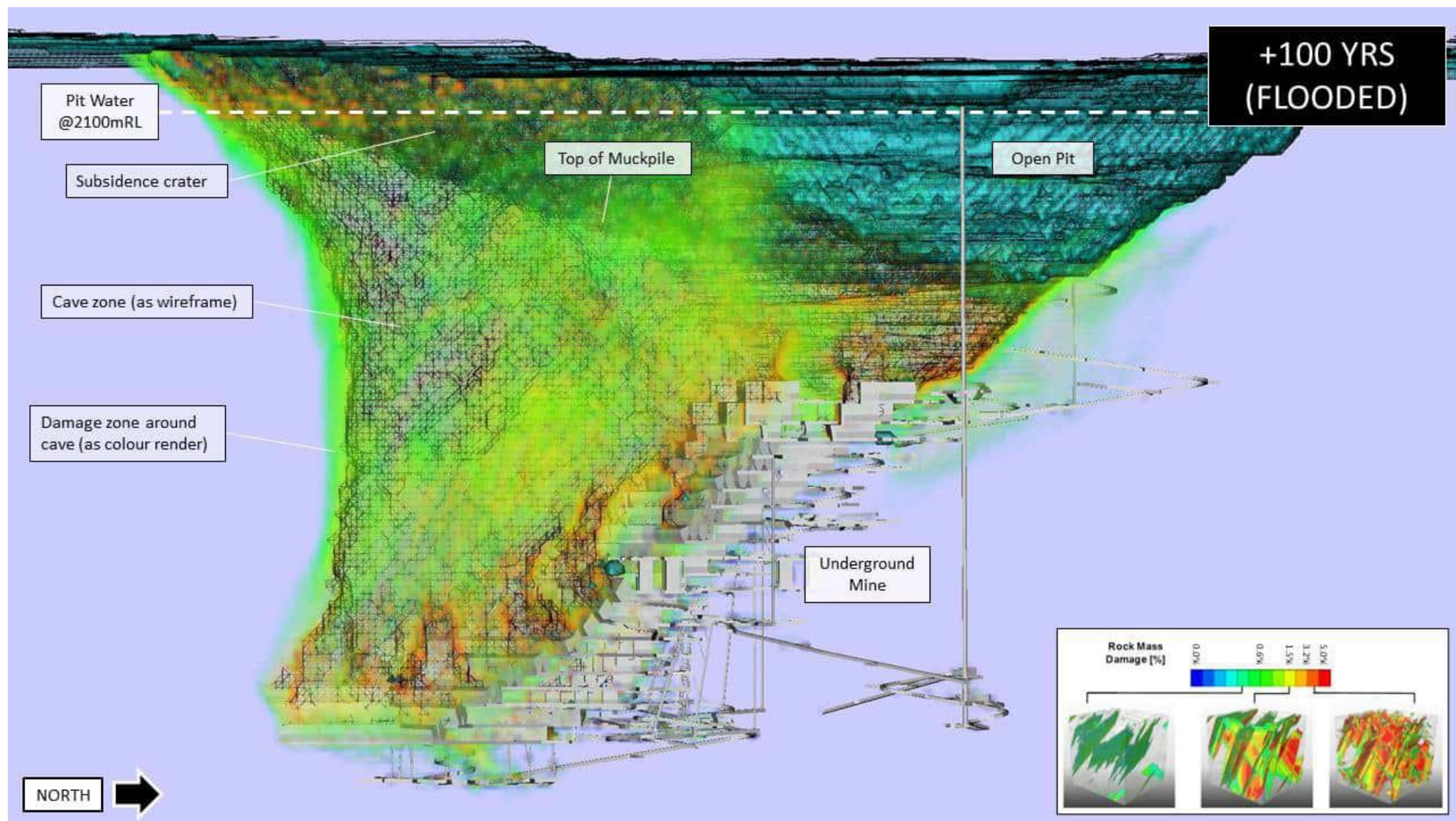


Figure 3-10 Cave and damage zone forecast 100 years after completion of mining with water @ 2100 mRL, view west.

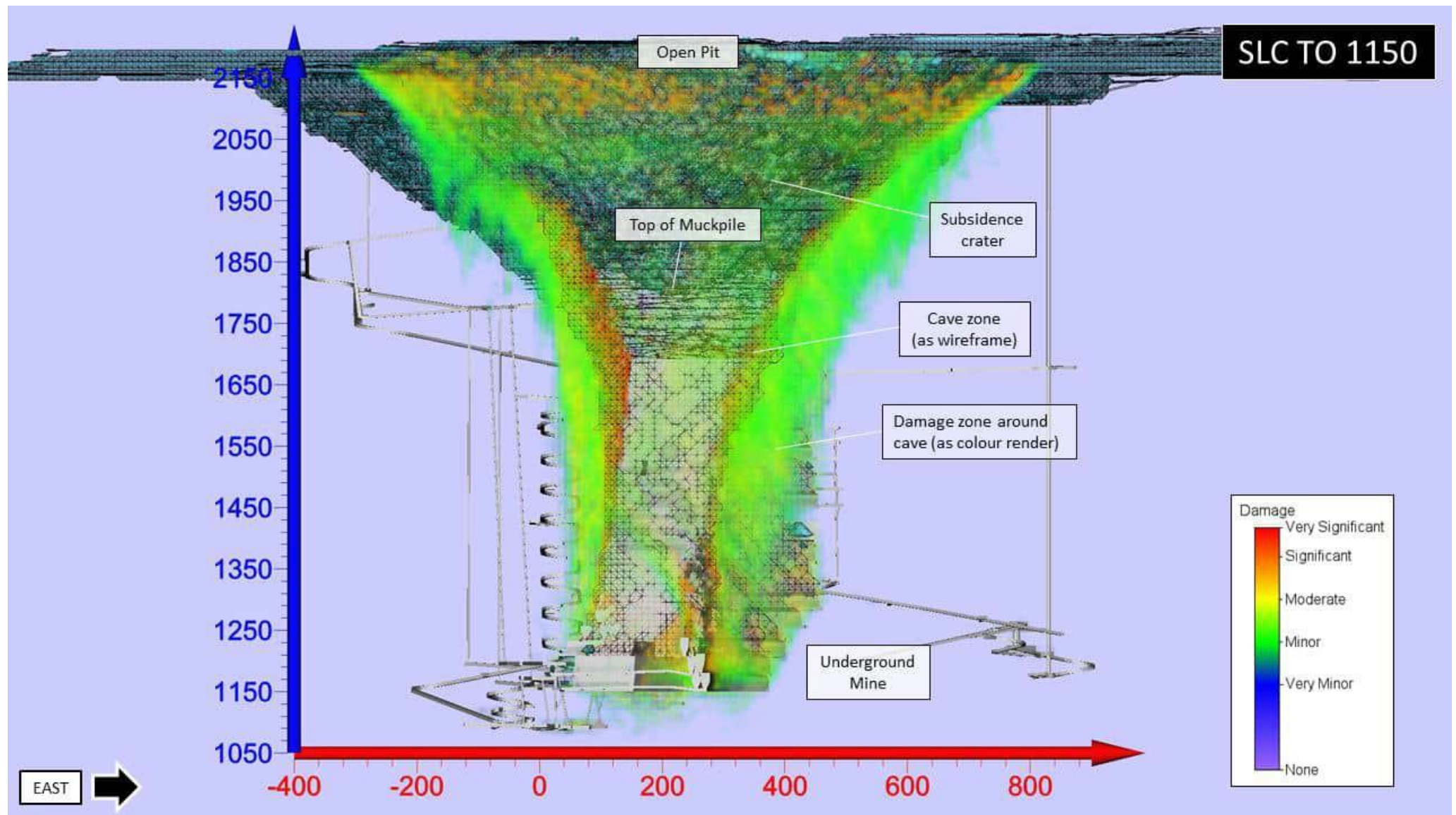


Figure 3-11 Cave and damage zone forecast at the conclusion of underground mining (i.e. SLC to 1150 mRL), view north.

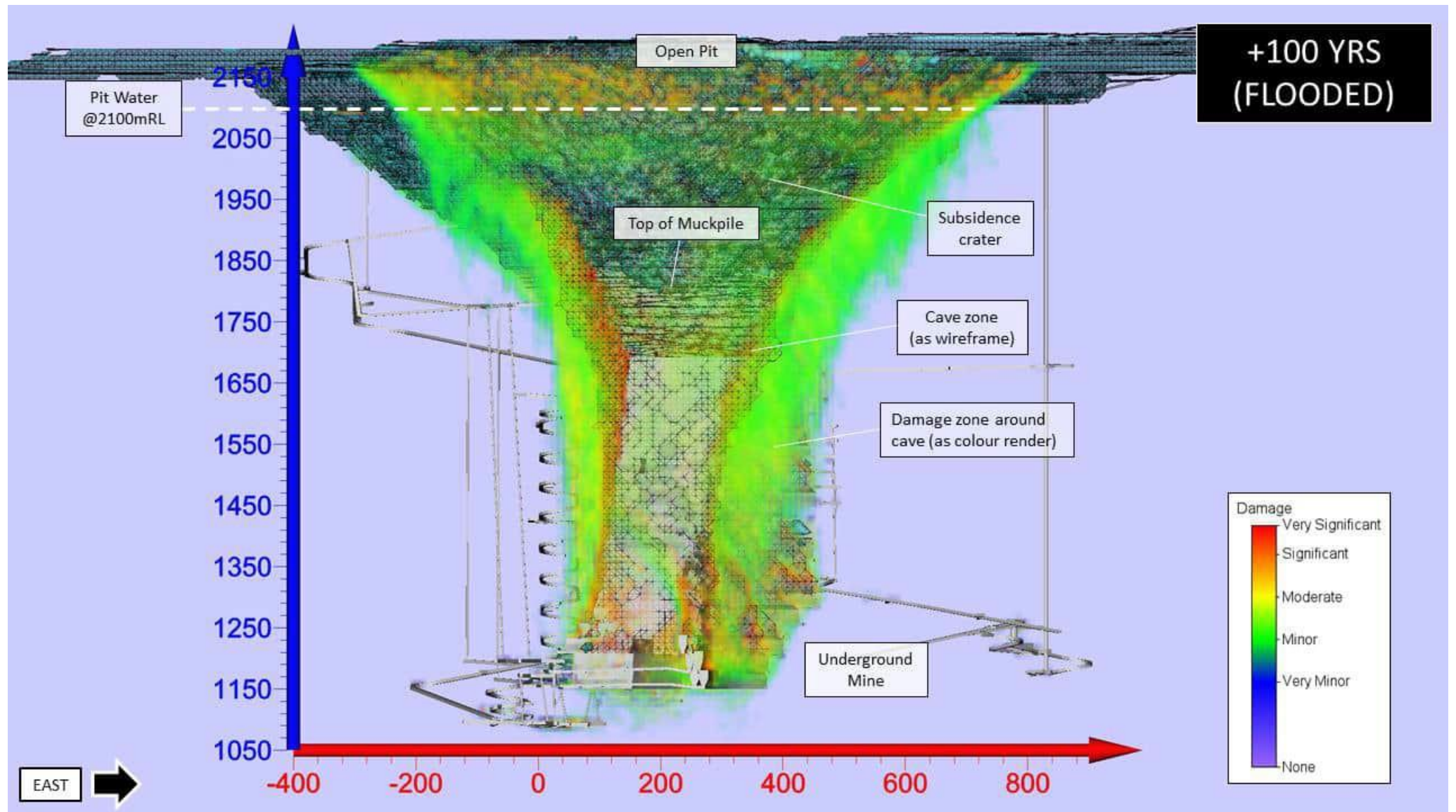


Figure 3-12 Cave and damage zone forecast 100 years after completion of mining with water @ 2100 mRL, view north.

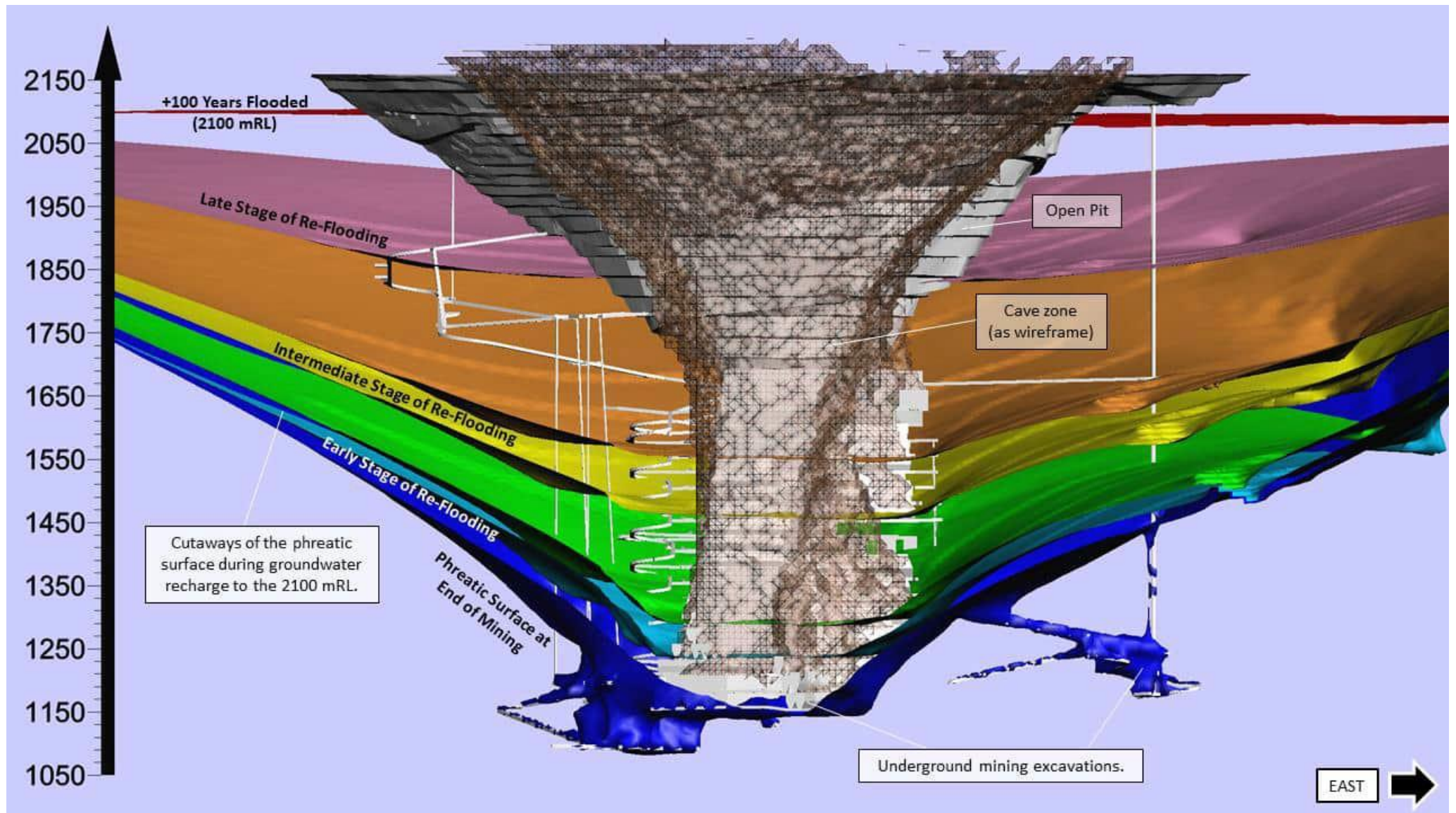


Figure 3-13 Cut away section showing the phreatic surface evolution during groundwater recharge and cave/pit flooding (inclined slice along SLC hangingwall), view north.

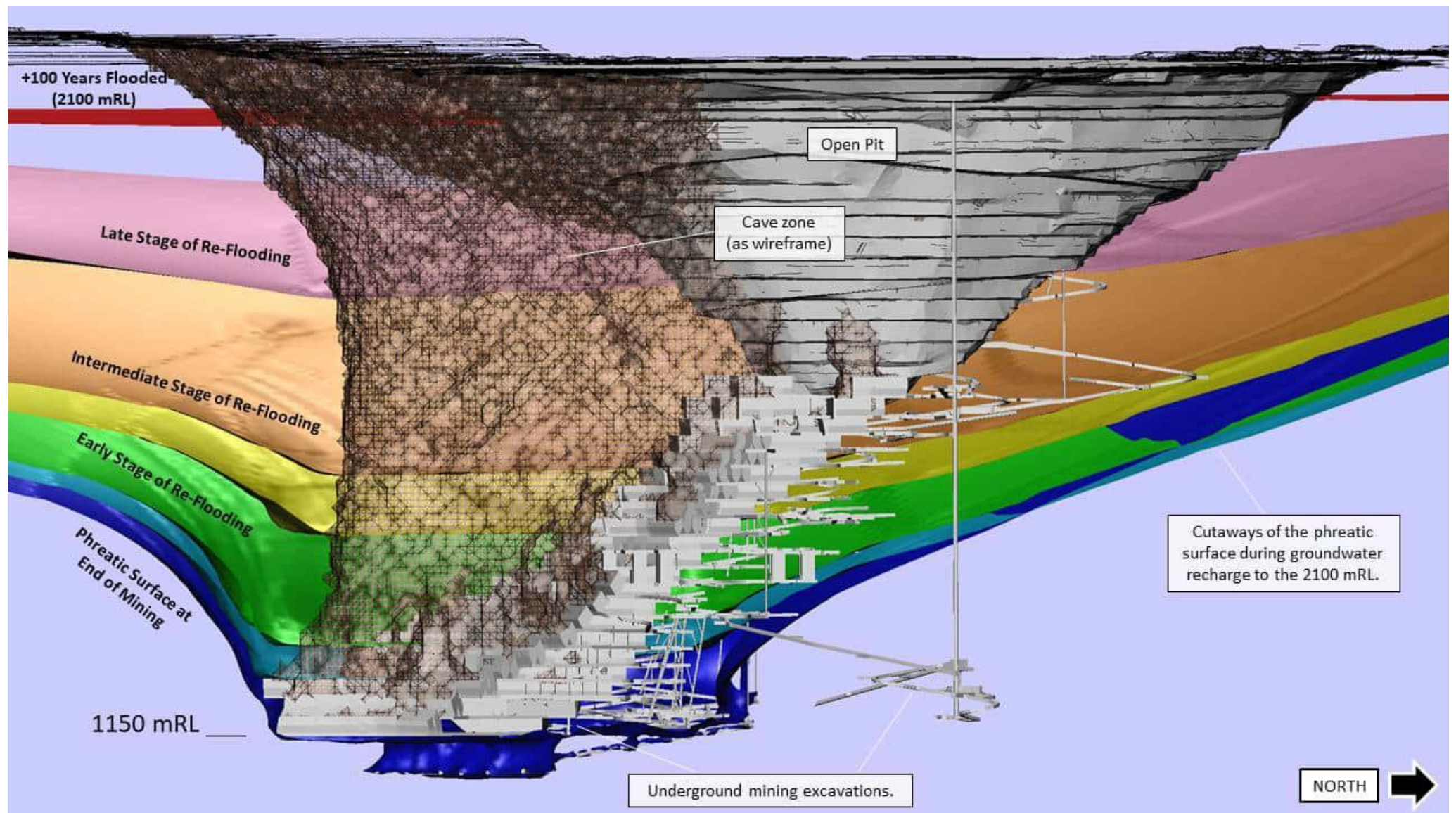


Figure 3-14 Cut away section showing the phreatic surface evolution during groundwater recharge and cave/pit flooding (sliced at easting central to SLC), view west.

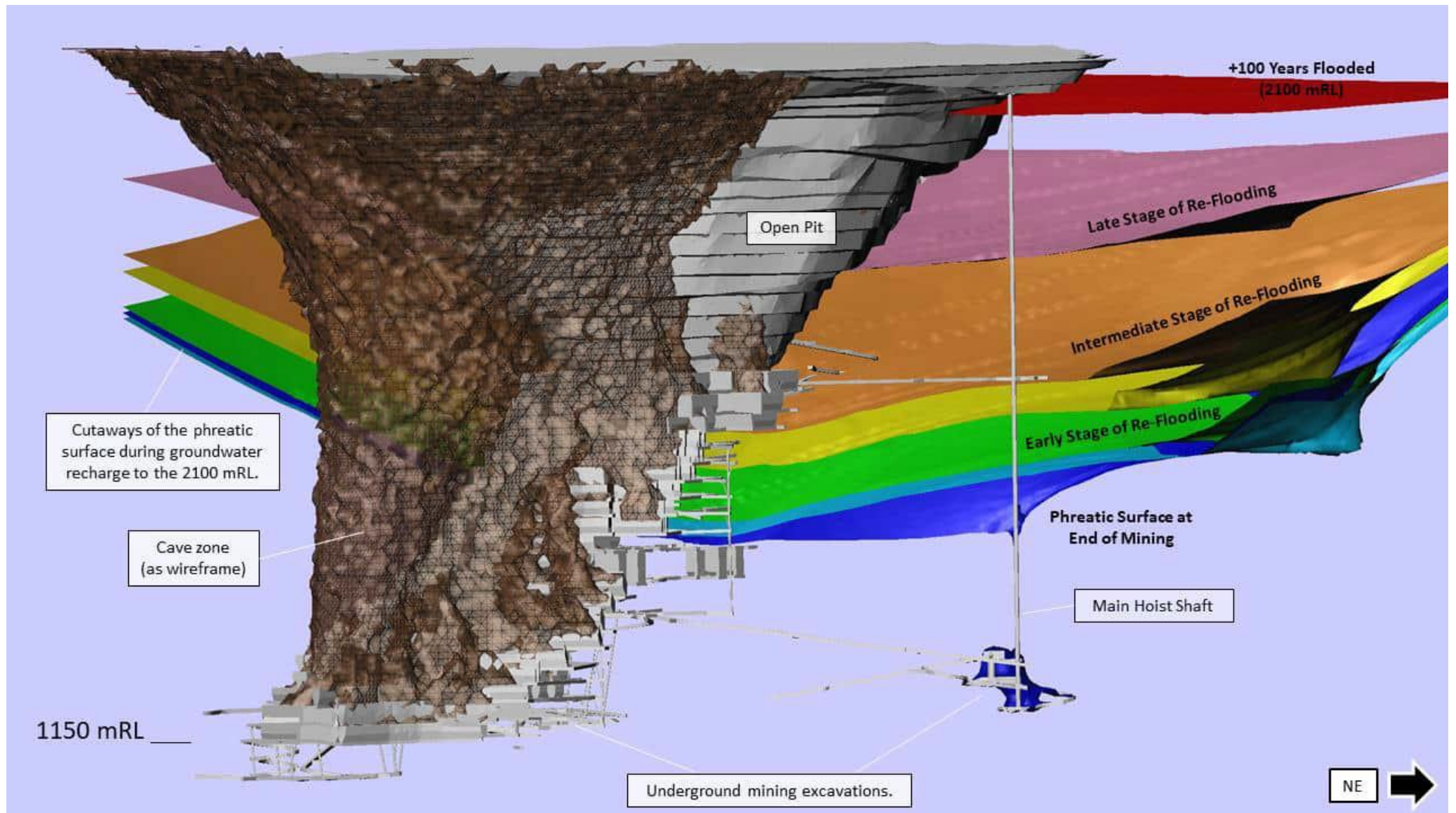


Figure 3-15 Cutaway section showing phreatic surface evolution during groundwater recharge and cave/pit flooding (sliced at main hoist shaft northing), view northwest.

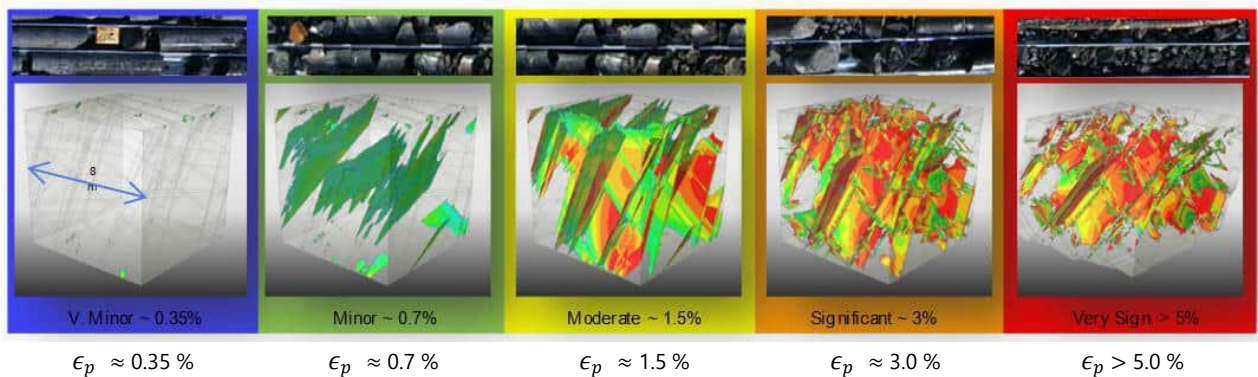
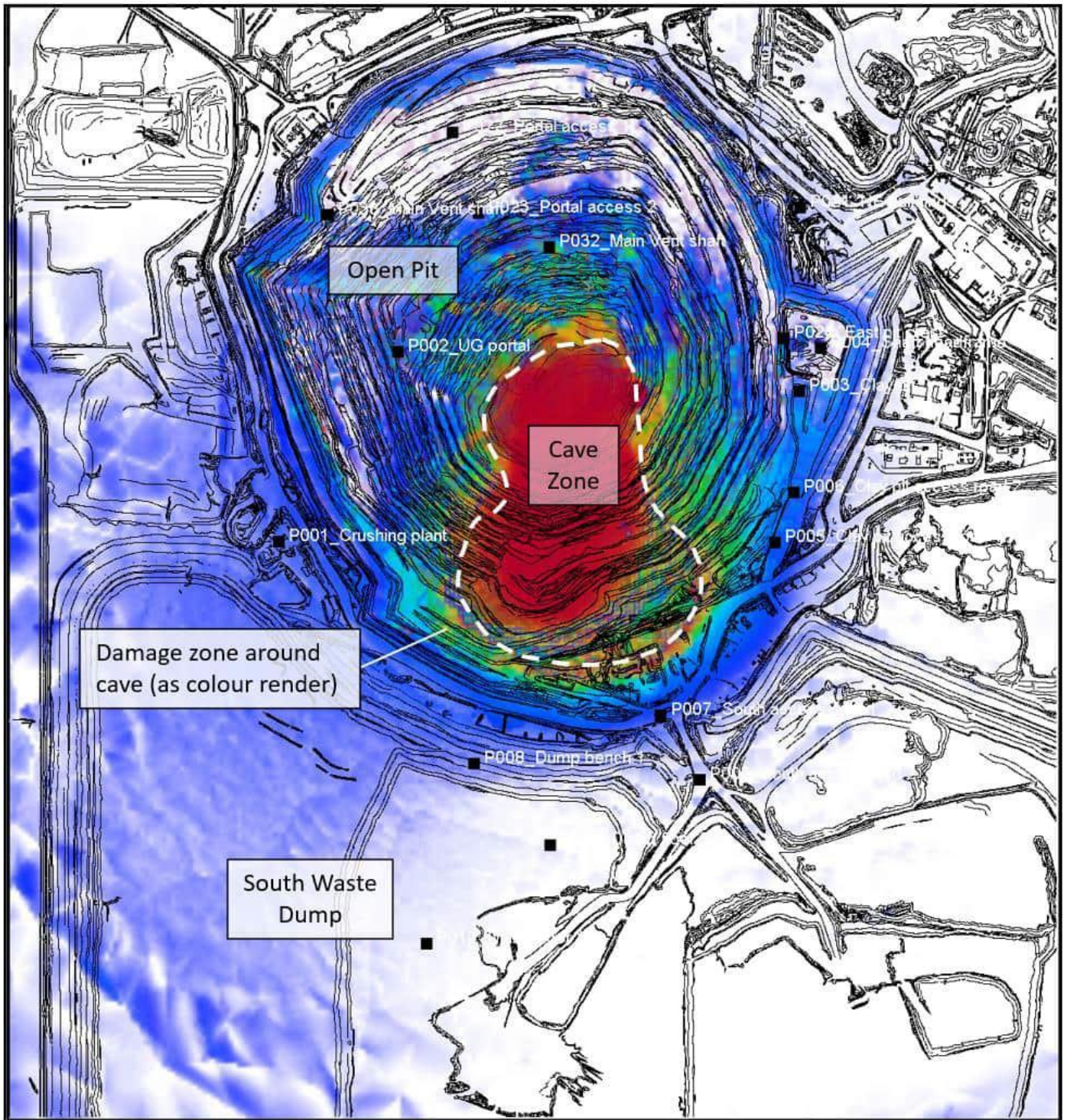


Figure 3-16 Plan view showing forecast rockmass damage and cave outline (2022 Q4).

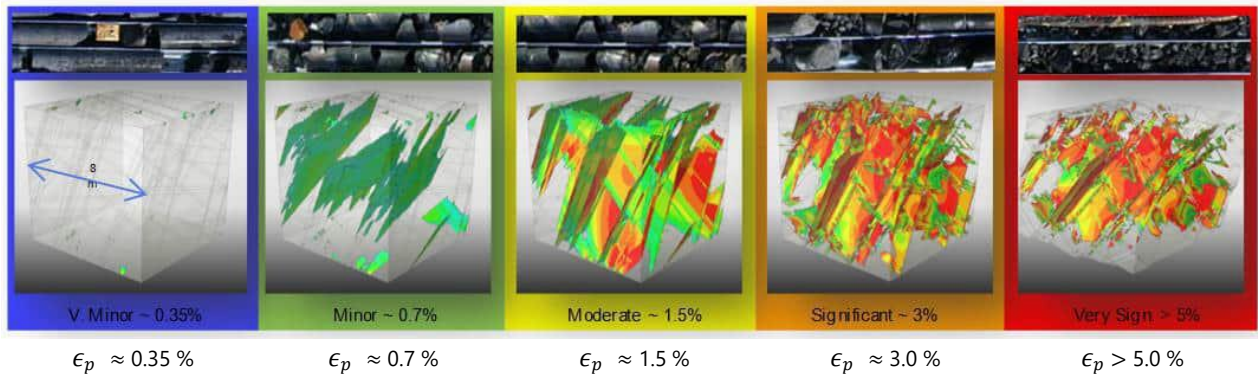
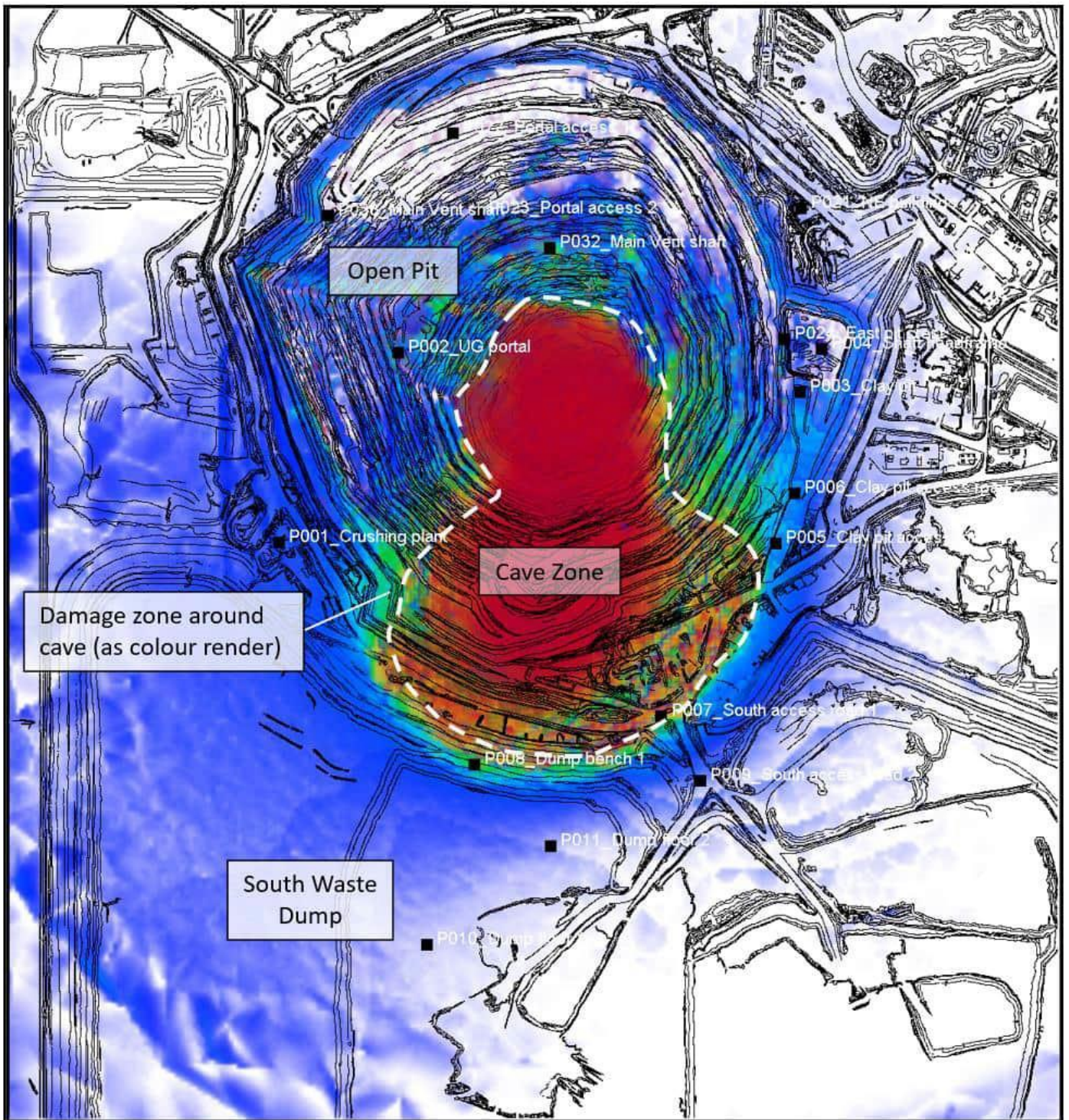


Figure 3-17 Plan view showing forecast rockmass damage and cave outline (2024 Q4).

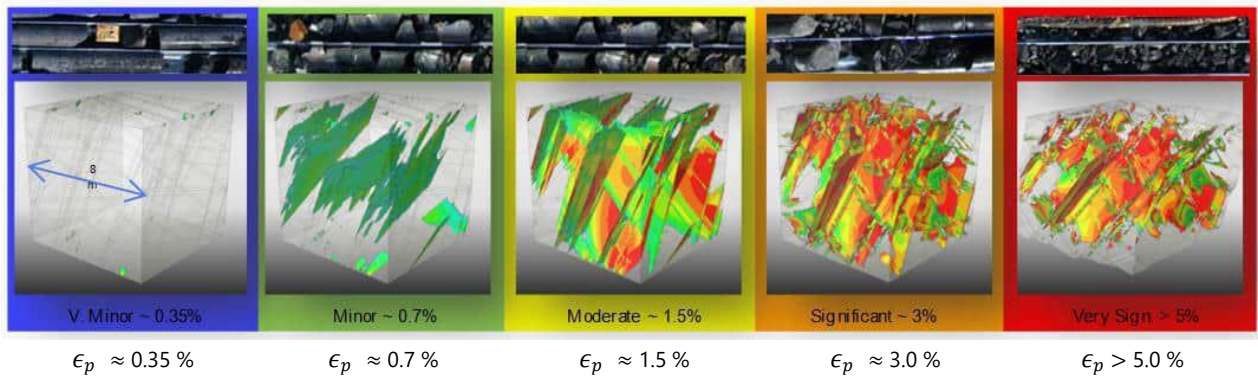
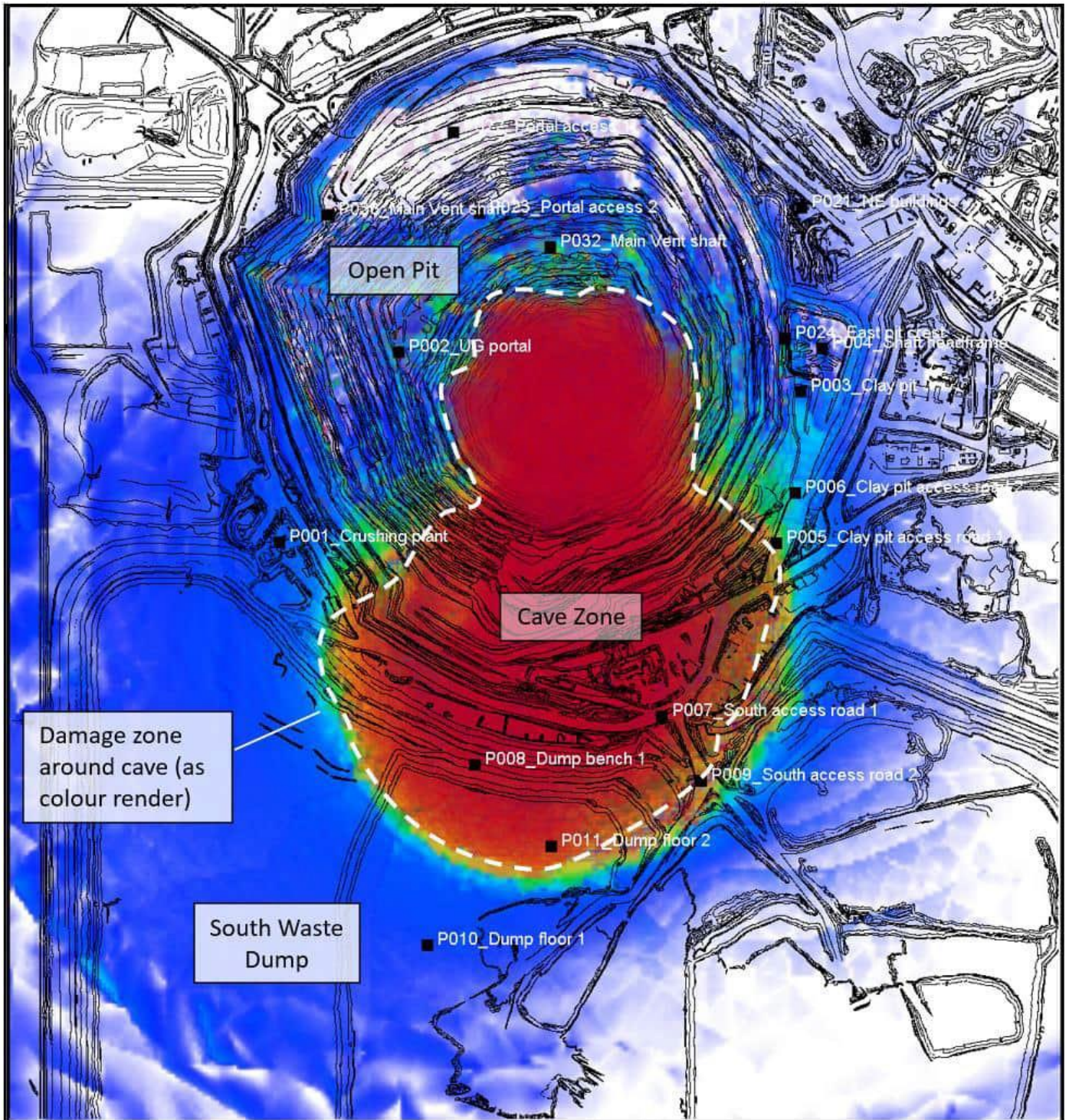


Figure 3-18 Plan view showing forecast rockmass damage and the cave outline (2026 Q4).

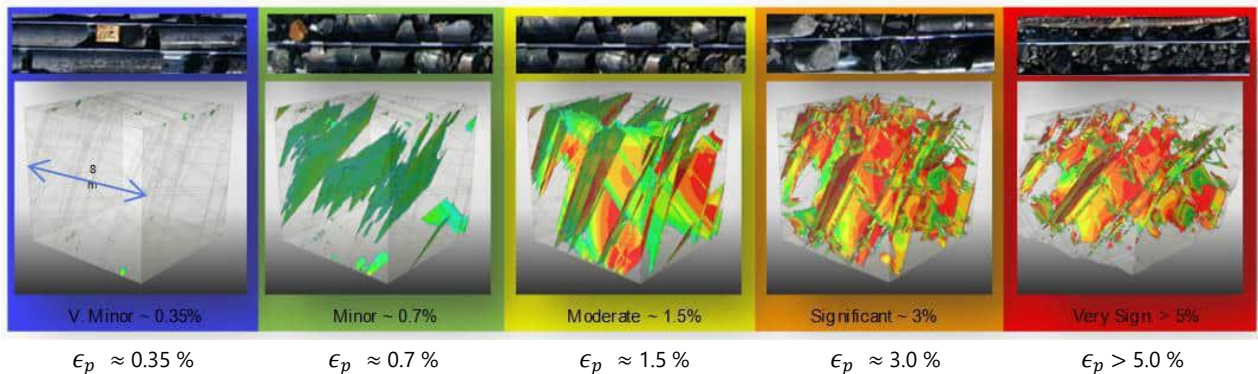
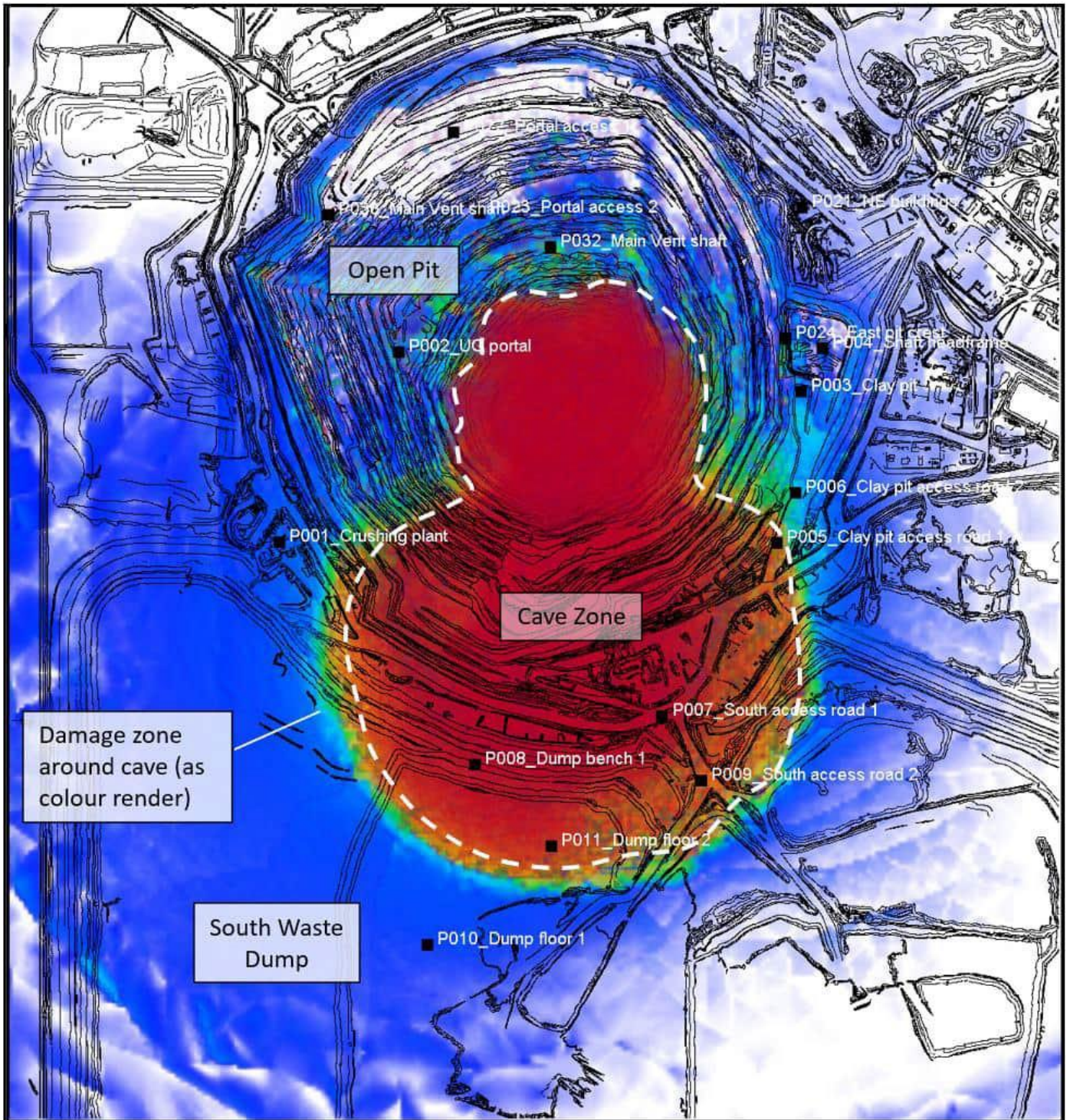


Figure 3-19 Plan view showing forecast rockmass damage and the cave outline at the end of mining and before pit flooding.

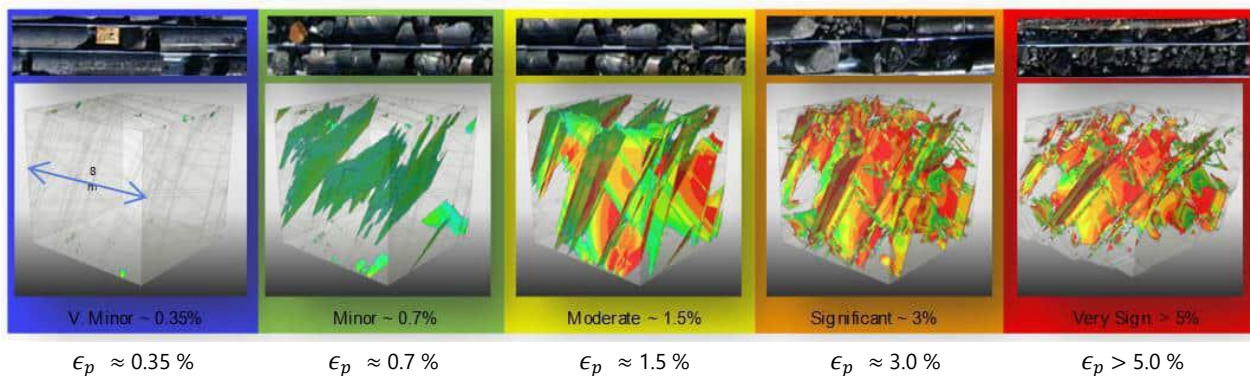
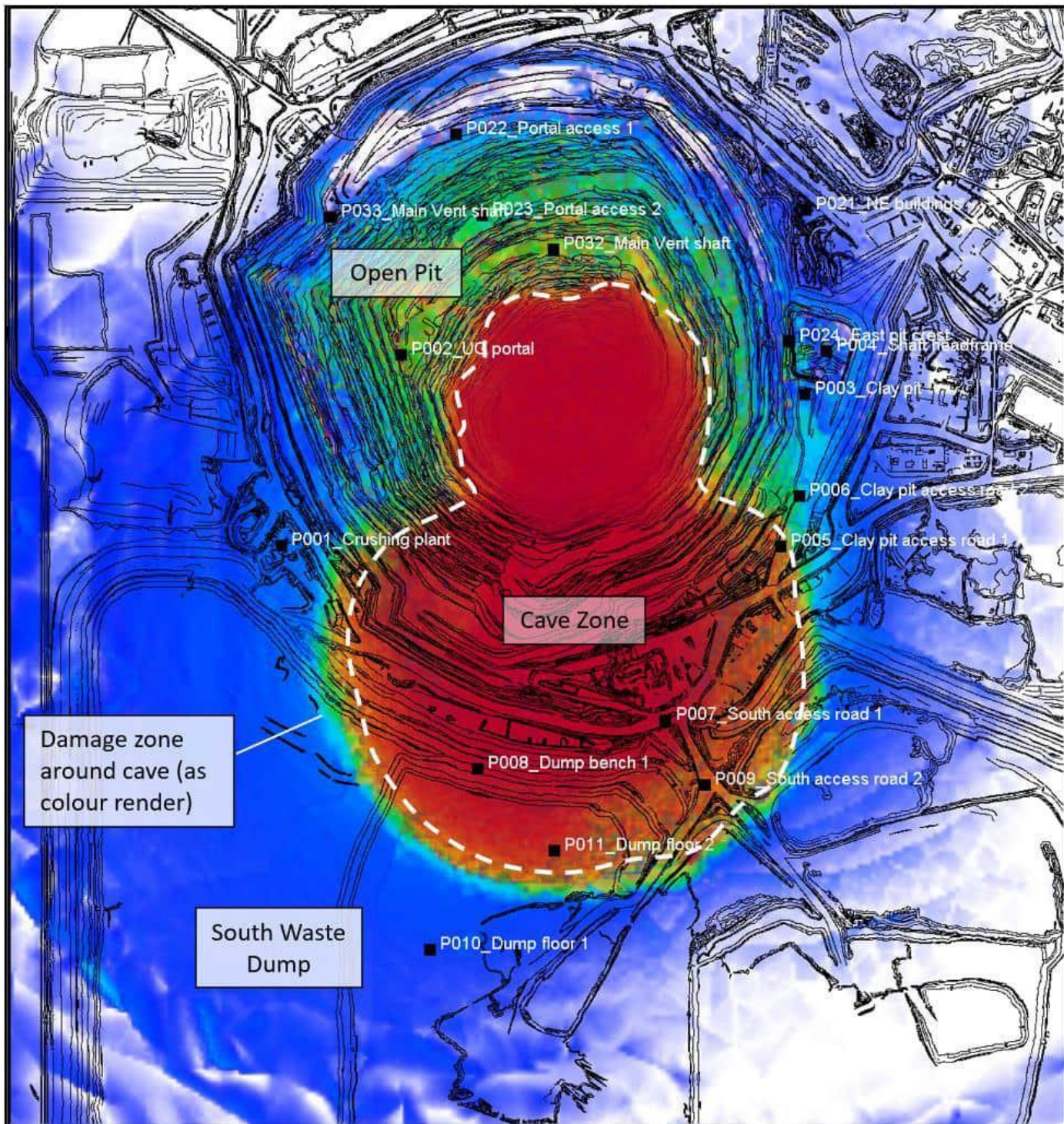


Figure 3-20 Plan view showing rockmass damage and the cave outline after 100 years of groundwater recharge post-mining.

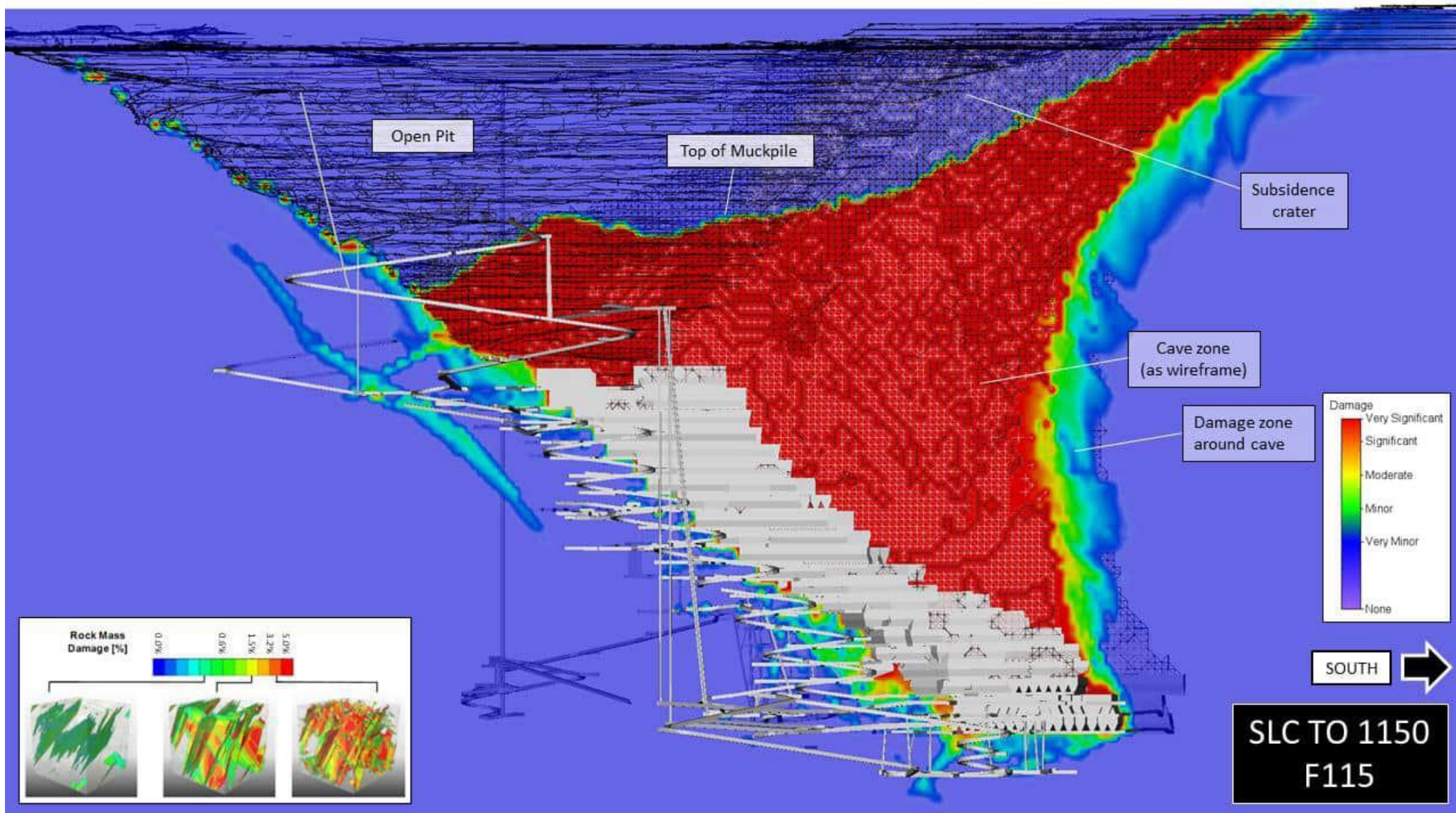


Figure 3-21 Long section of forecast rockmass damage and the cave zone at the end of mining to 1150 mRL (view east).

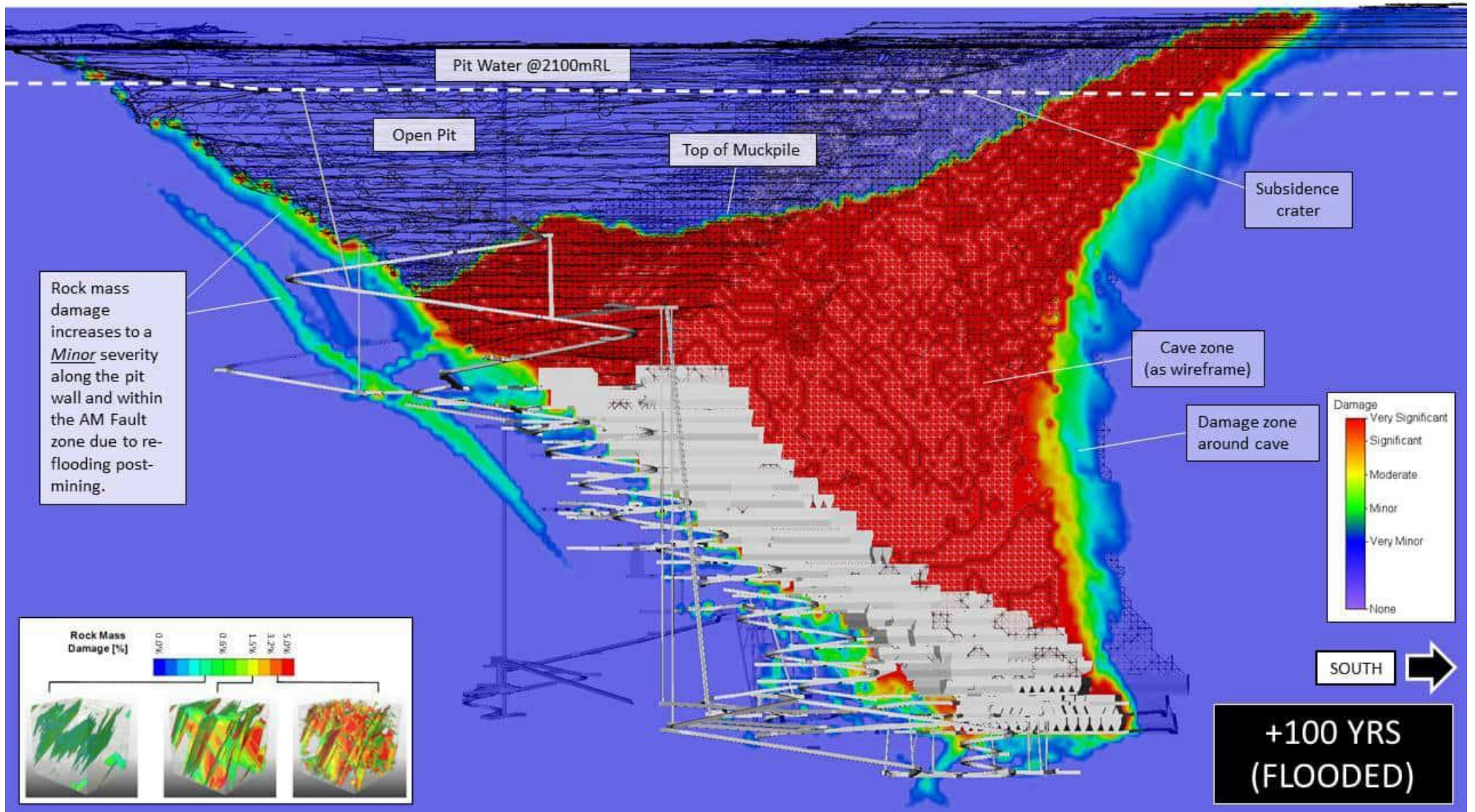


Figure 3-22 Long section of forecast rockmass damage and the cave zone after 100 years of groundwater recharge post-mining (view east).

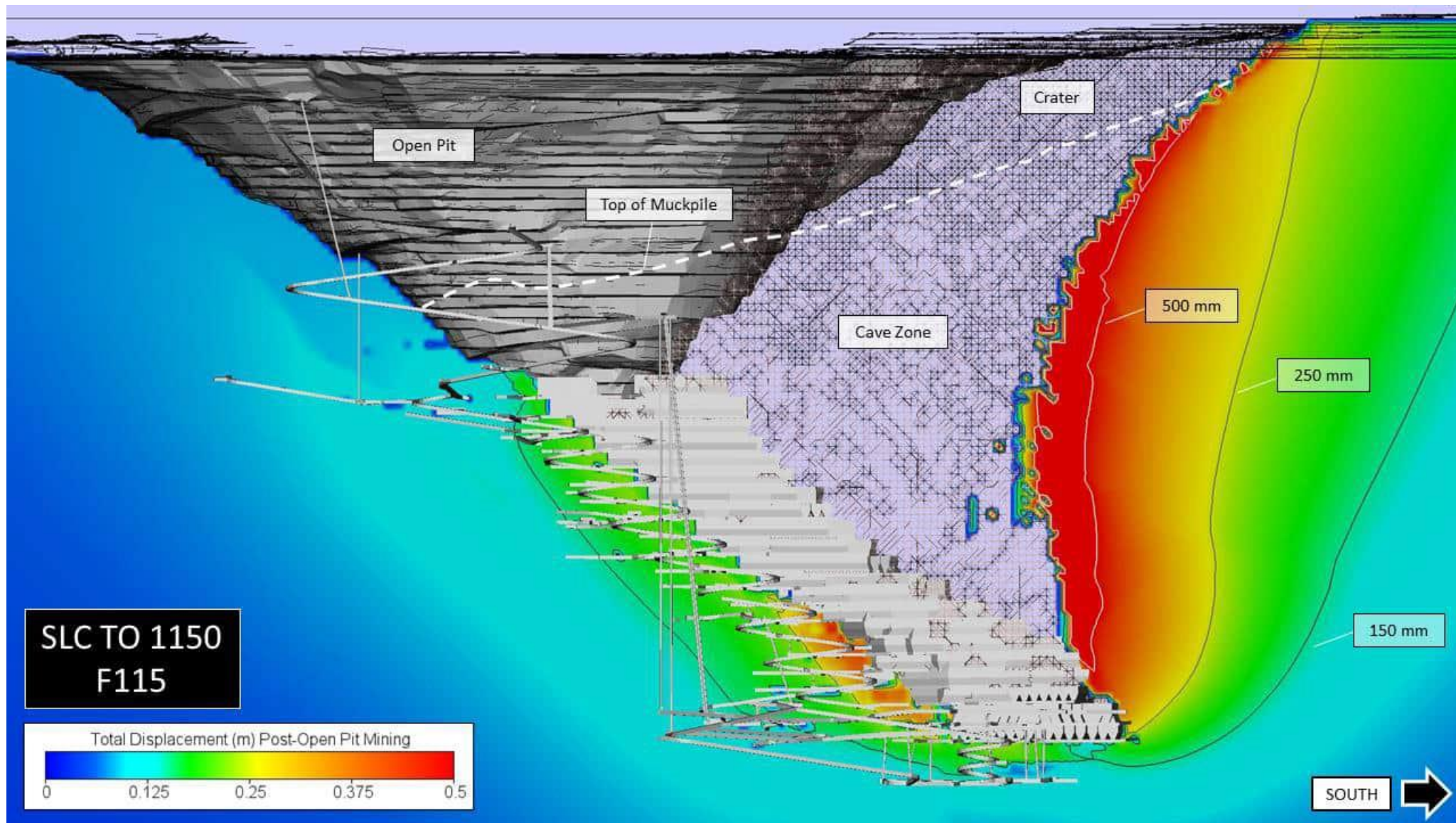


Figure 3-23 Long section of total displacement (post open pit mining) at the end of mining to 1150 mRL (view east).

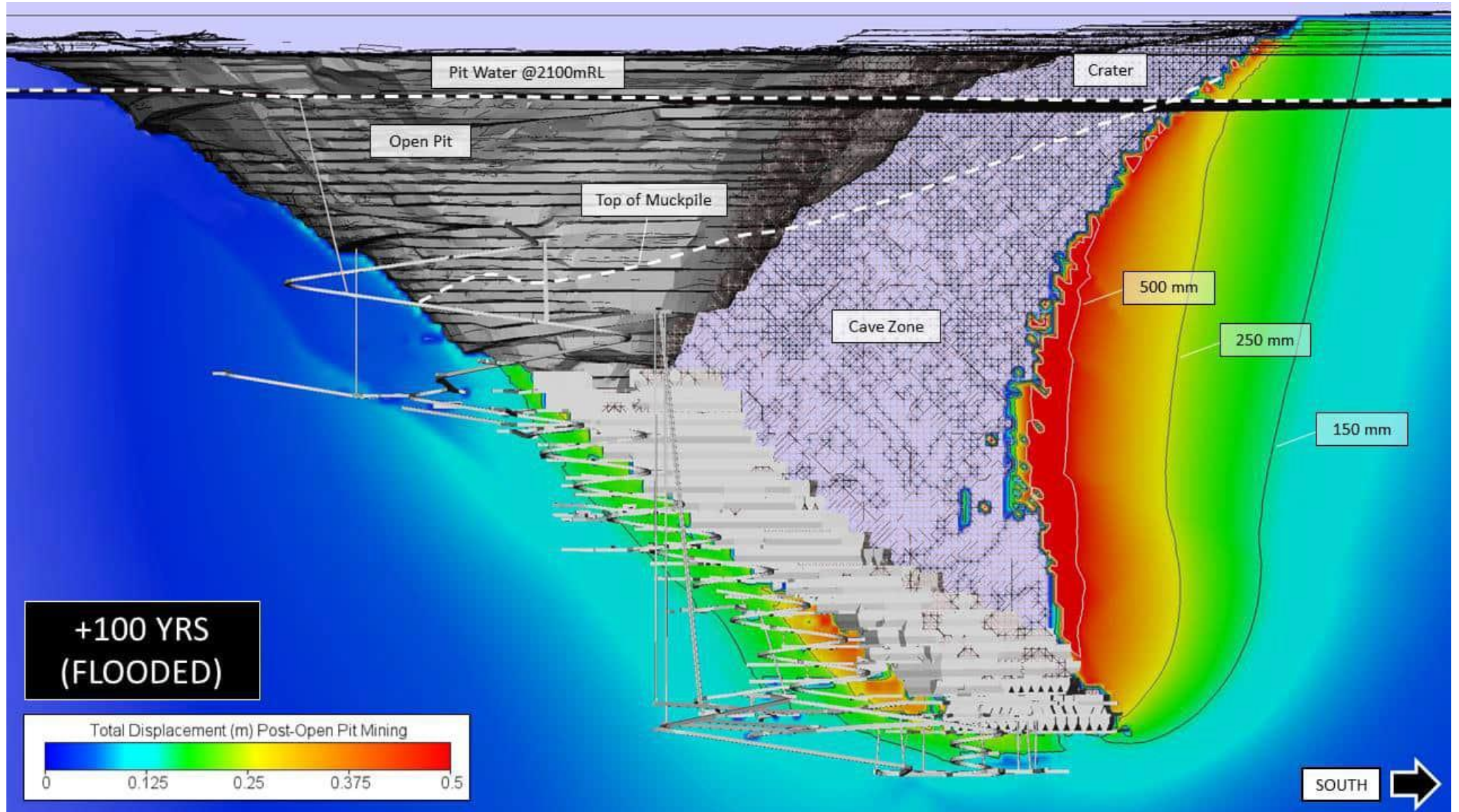


Figure 3-24 Long section of total displacement (post open pit mining) after 100 years of groundwater recharge (view east).

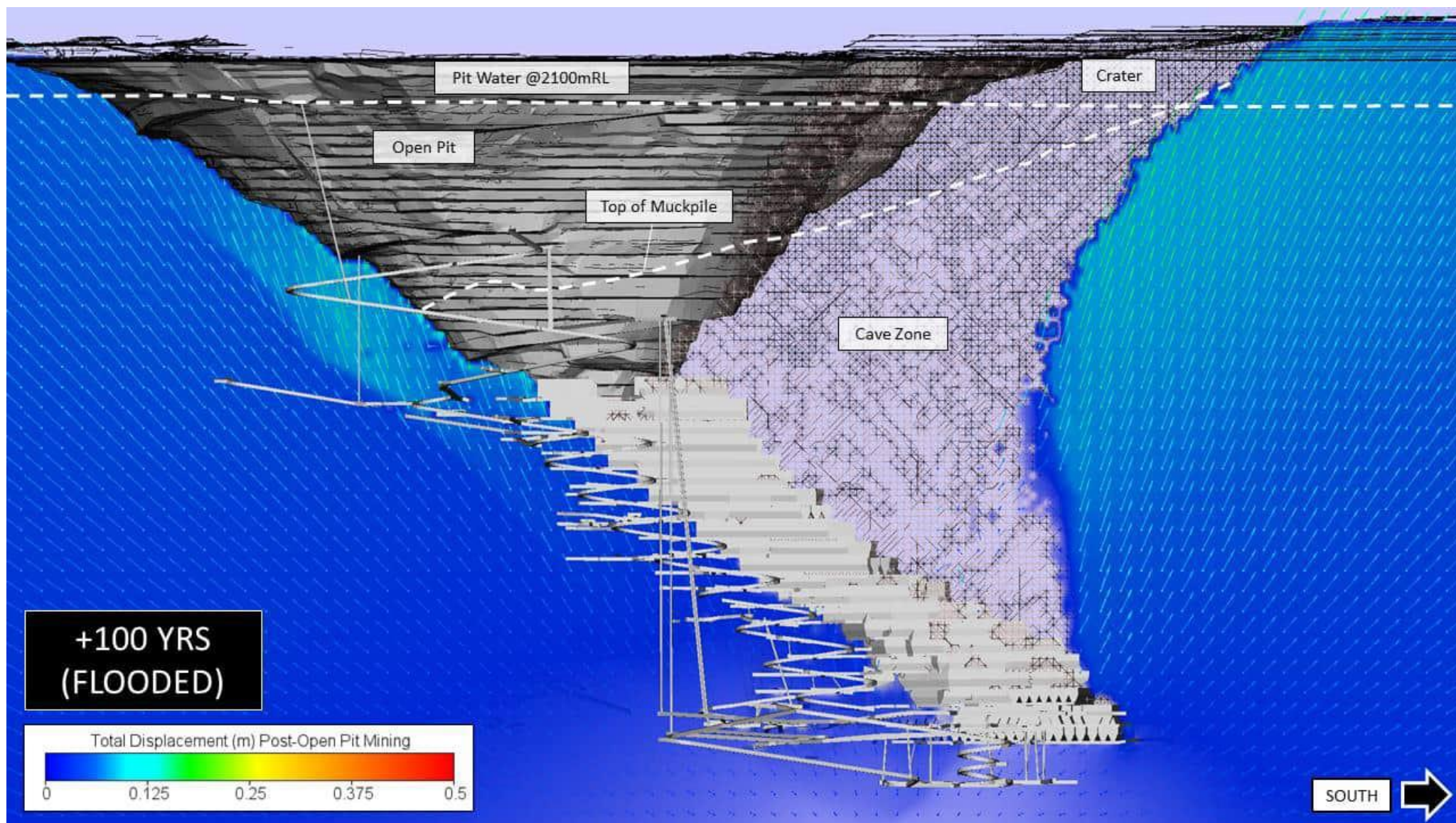


Figure 3-25 Long section showing displacement magnitude and direction induced by groundwater recharge to the long-term equilibrium (view east).

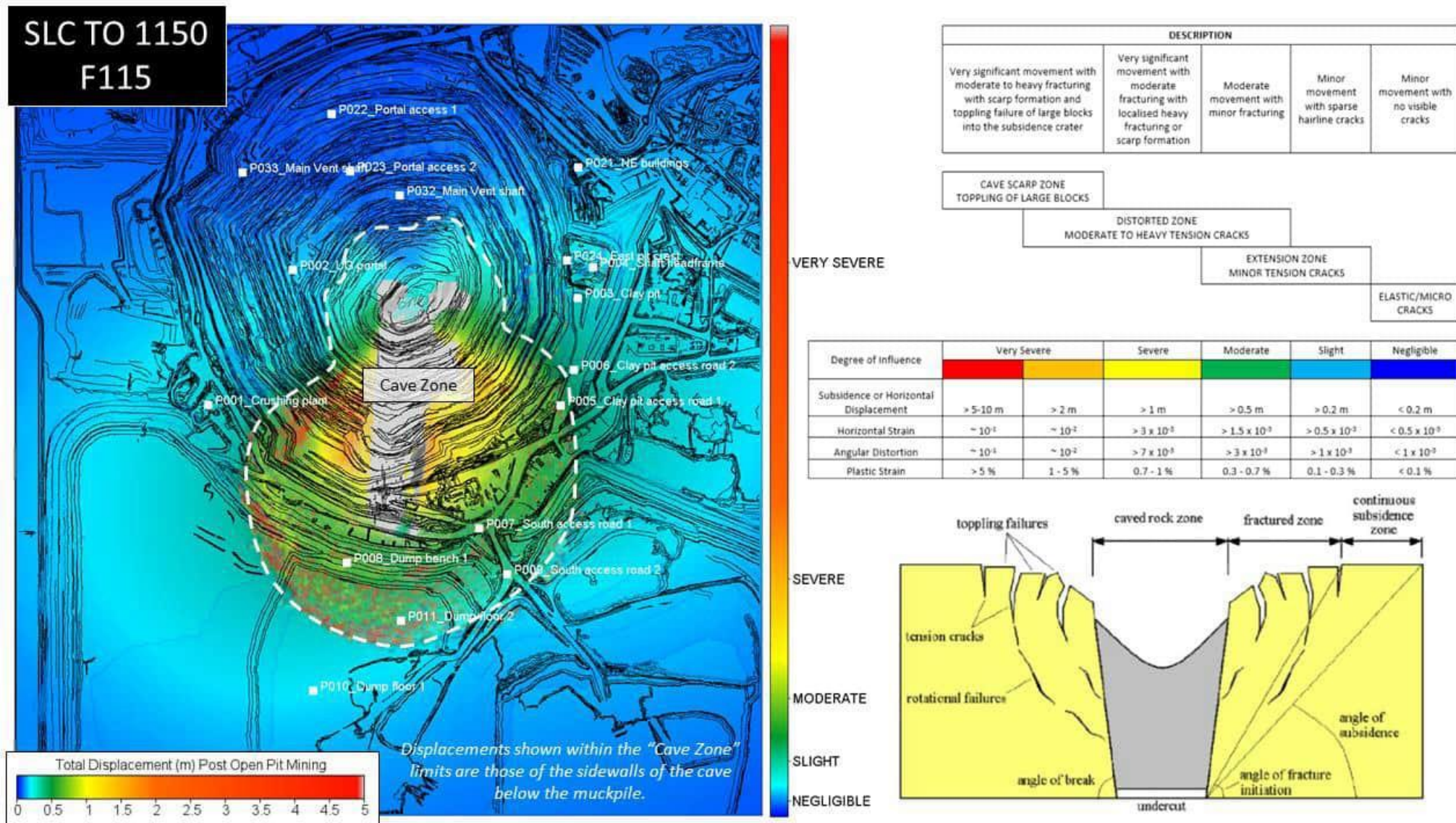


Figure 3-26 Forecast surface movement due to underground mining the SLC to 1150 mRL, before groundwater recharge.

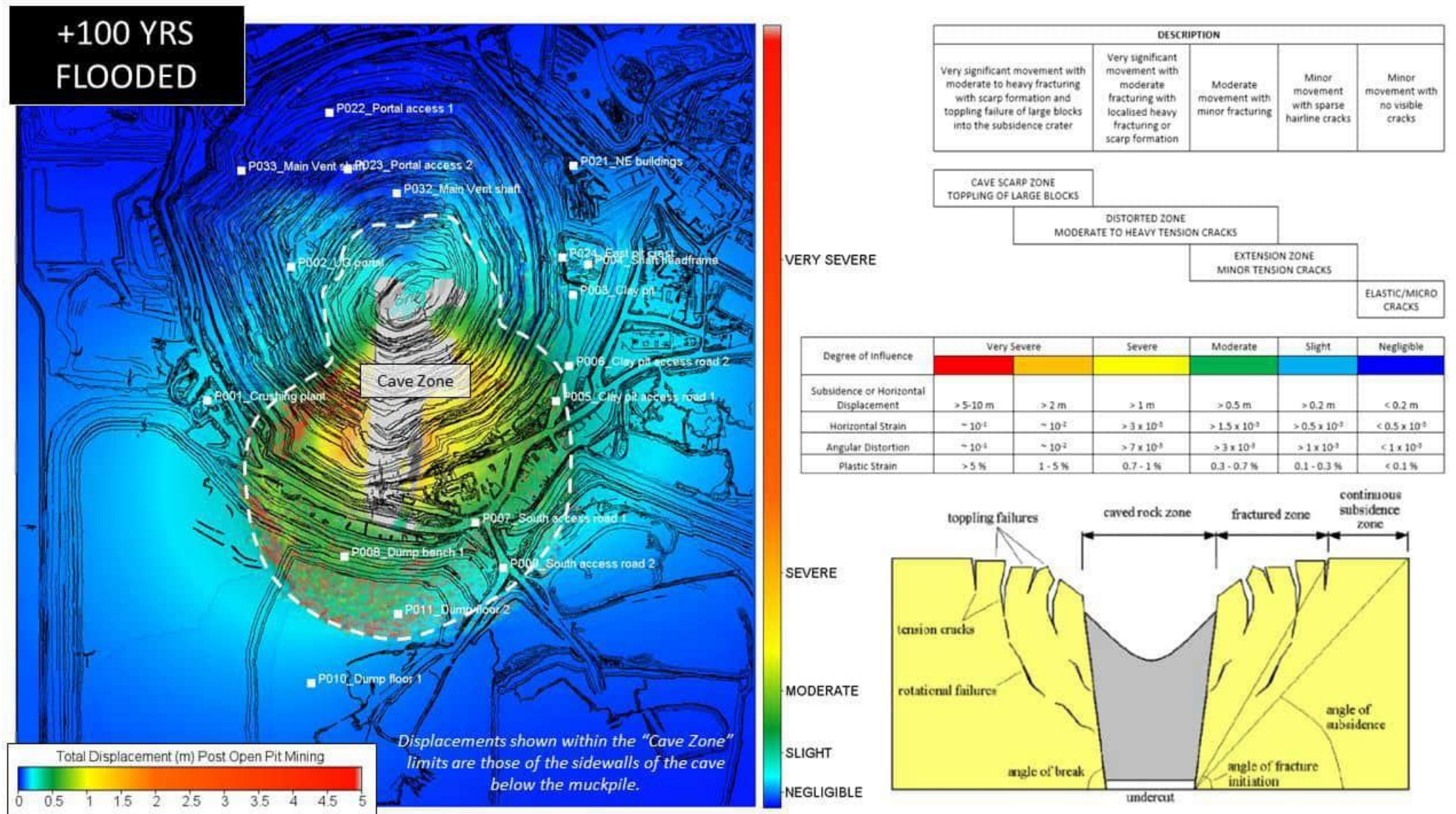


Figure 3-27 Forecast surface movement due to underground mining the SLC to 1150 mRL and after 100 years of groundwater recharge.

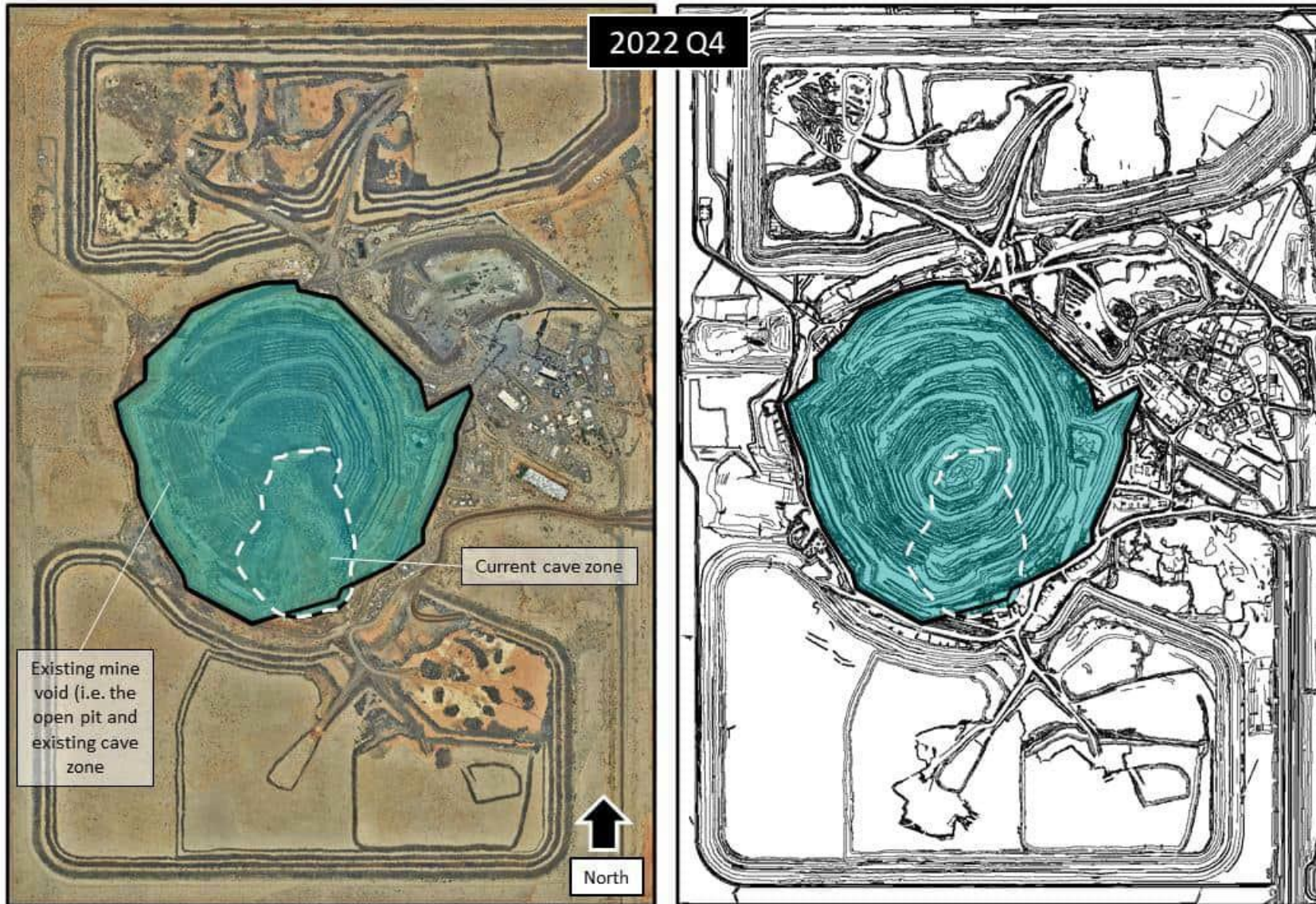


Figure 3-28 Spatial extent of the surface subsidence crater (cave zone) at the present time (2022 Q4).

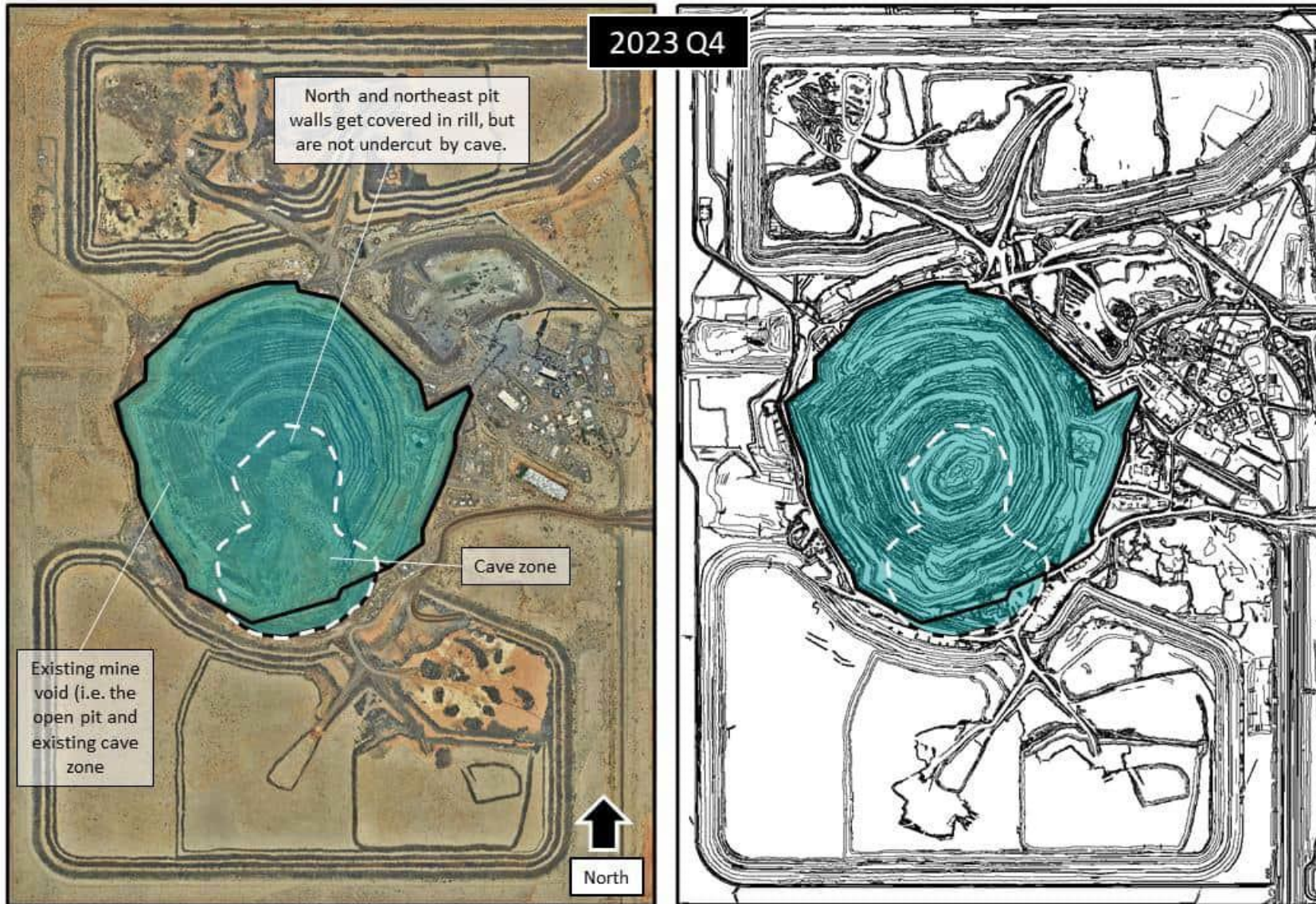


Figure 3-29 Forecast spatial extents of the subsidence crater (2023 Q4).

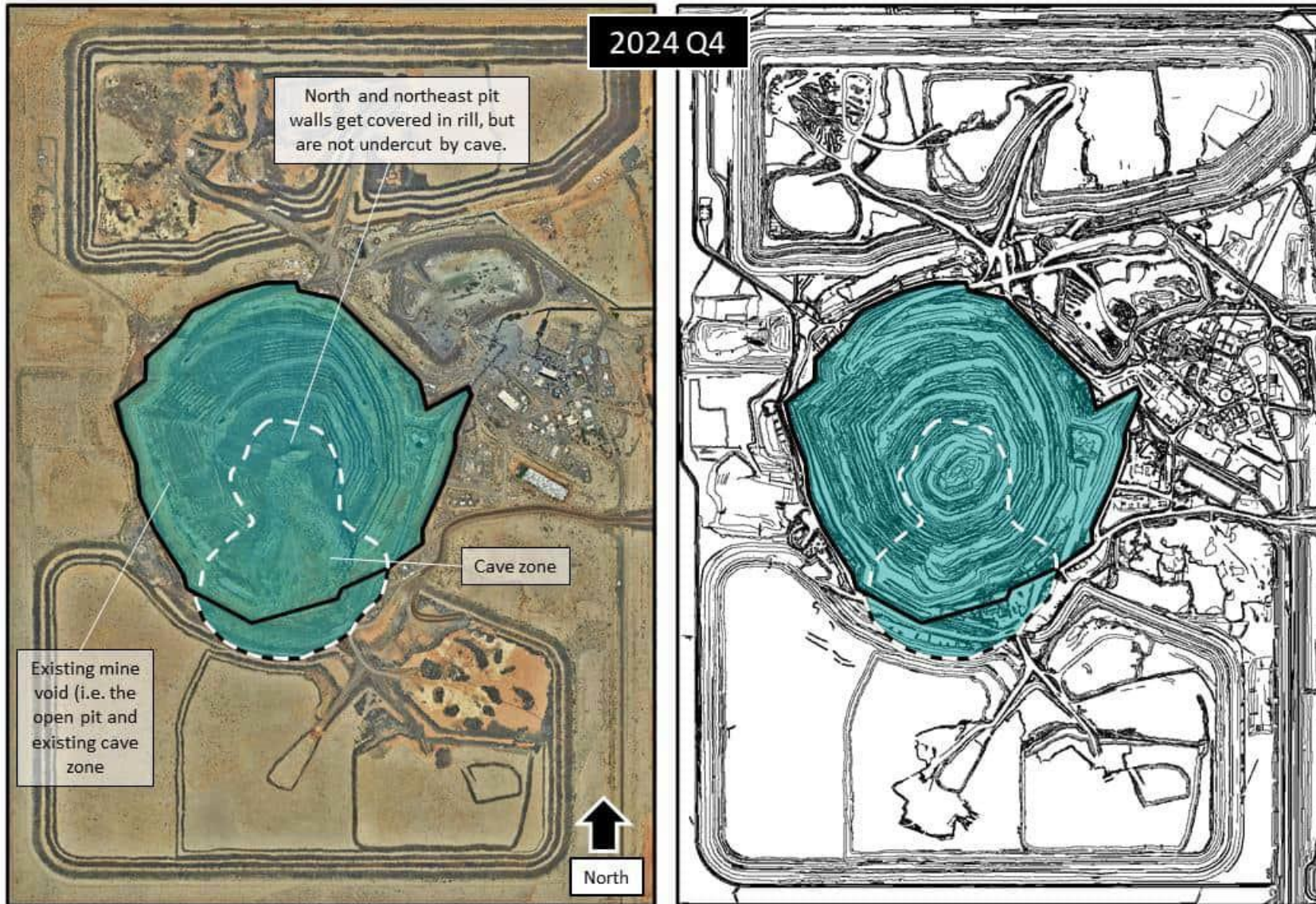


Figure 3-30 Forecast spatial extents of the subsidence crater (2024 Q4).

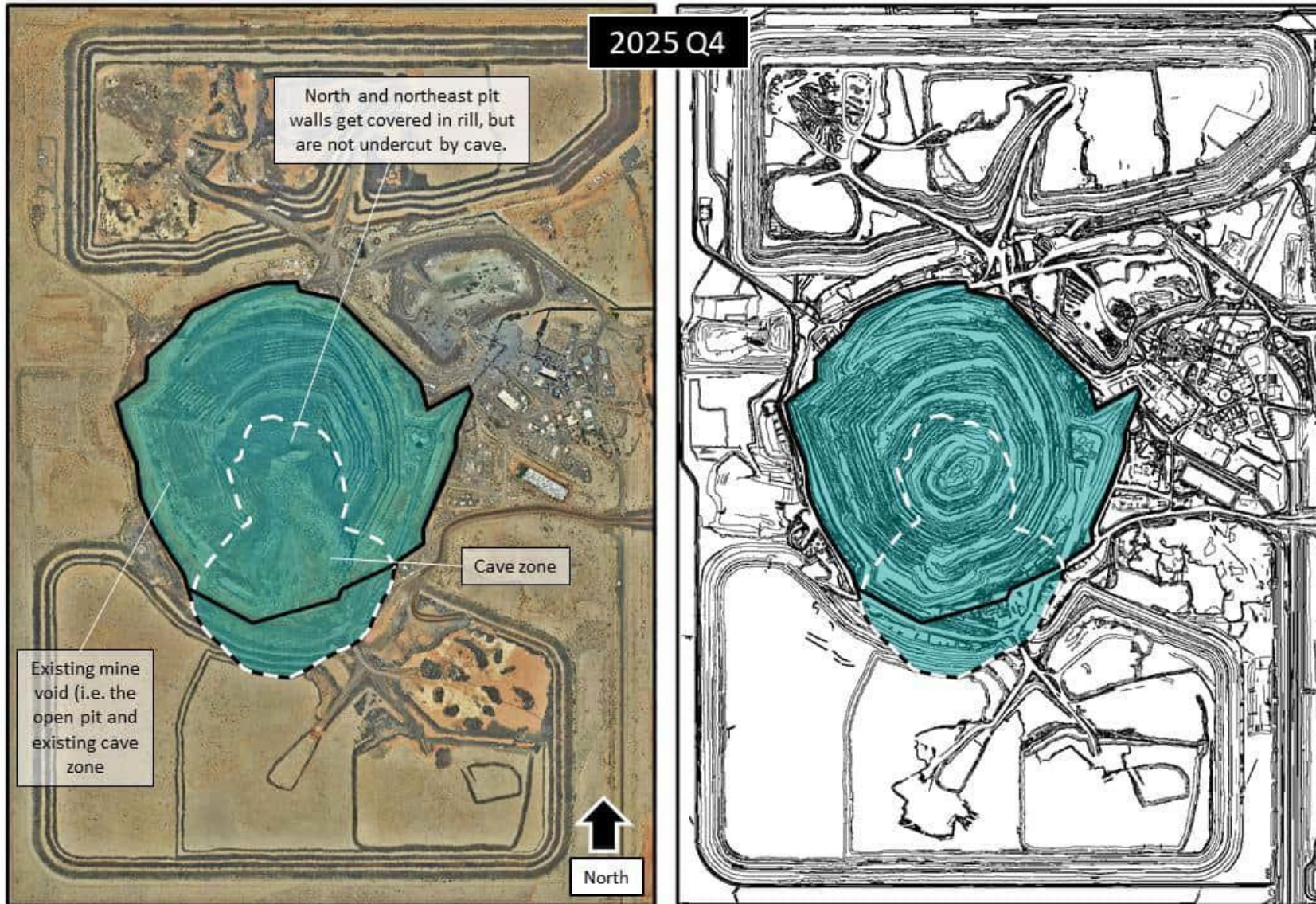


Figure 3-31 Forecast spatial extents of the subsidence crater (2025 Q4).

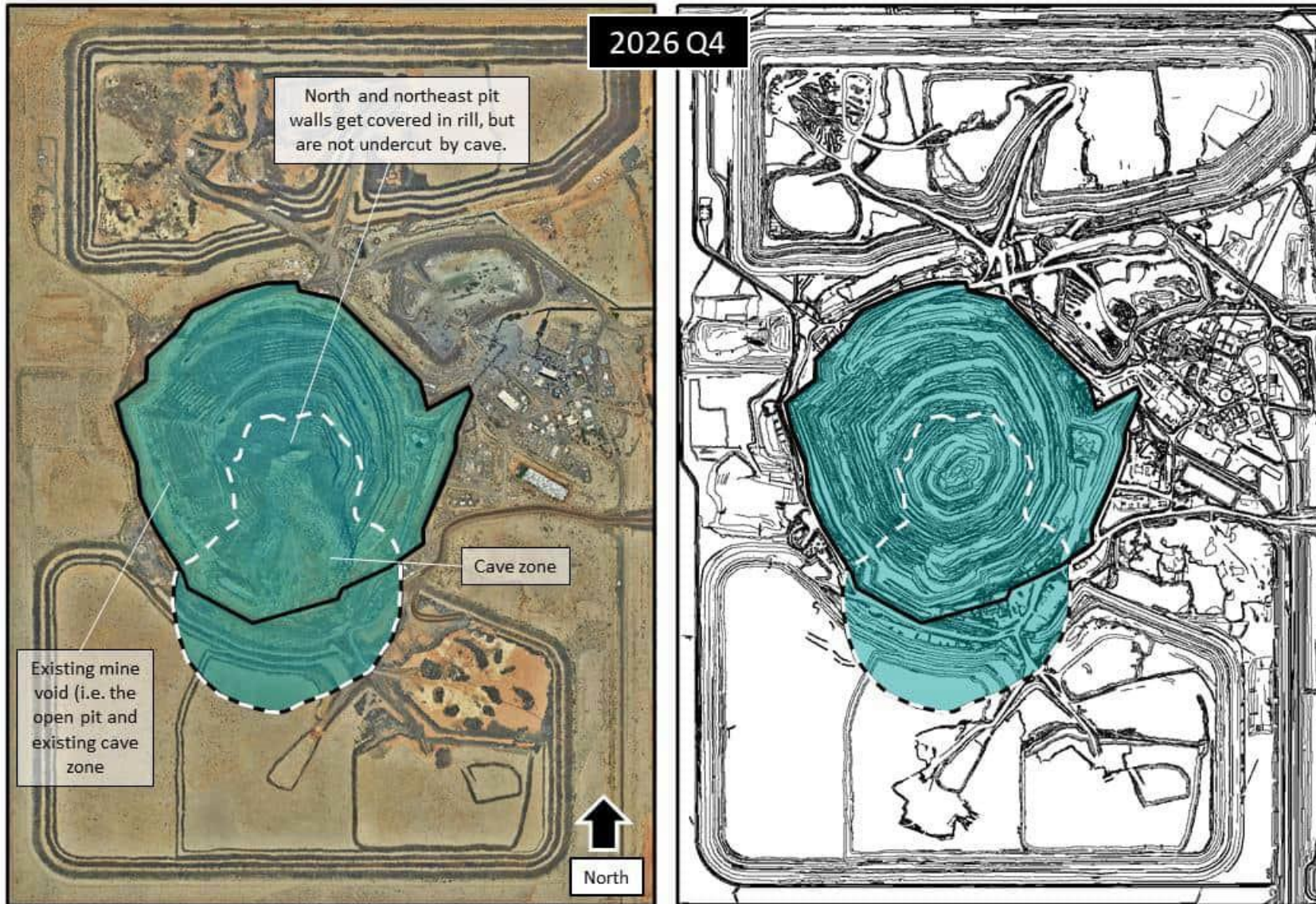


Figure 3-32 Forecast spatial extents of the subsidence crater (2026 Q4).

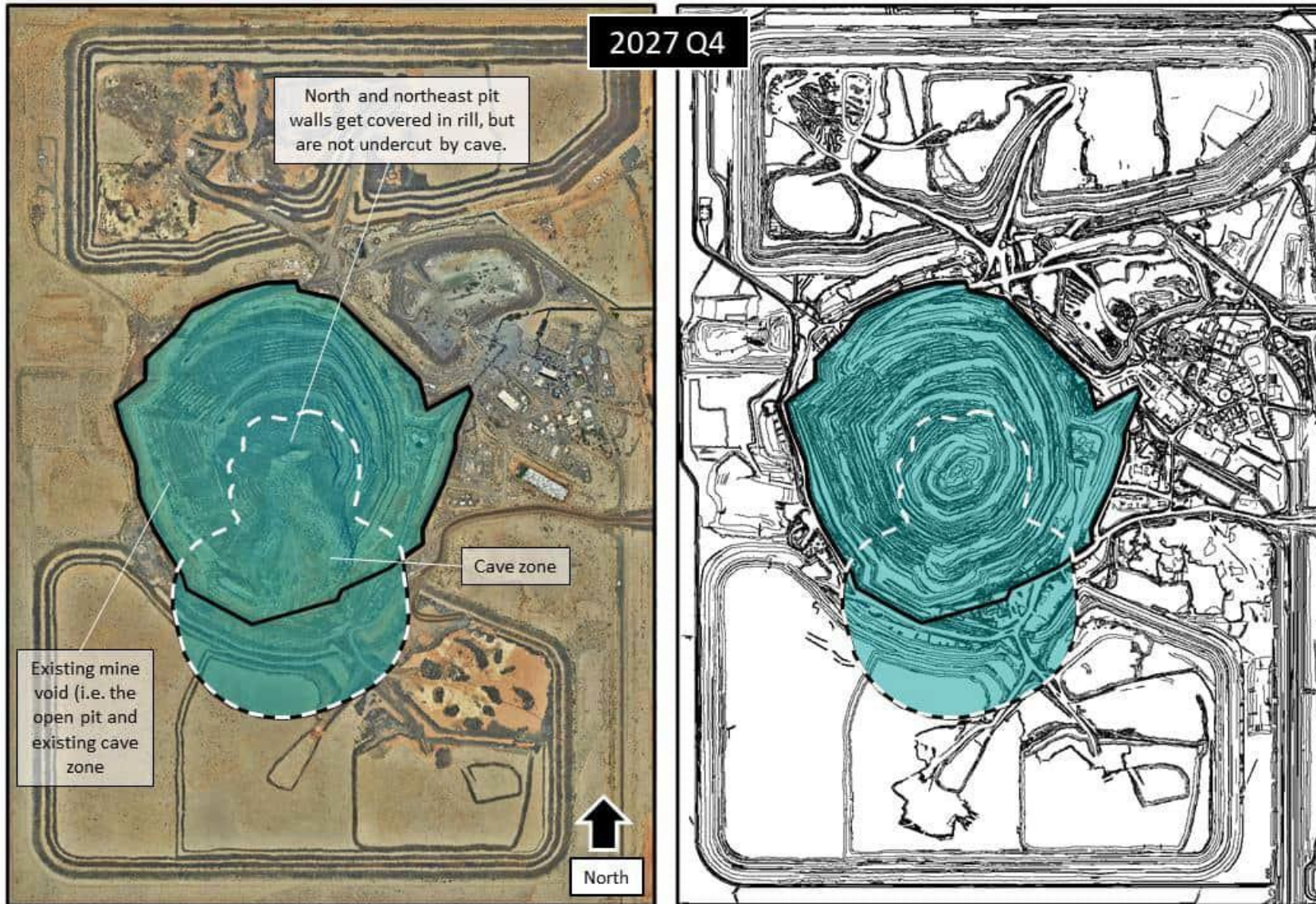


Figure 3-33 Forecast spatial extents of the subsidence crater (2027 Q4).

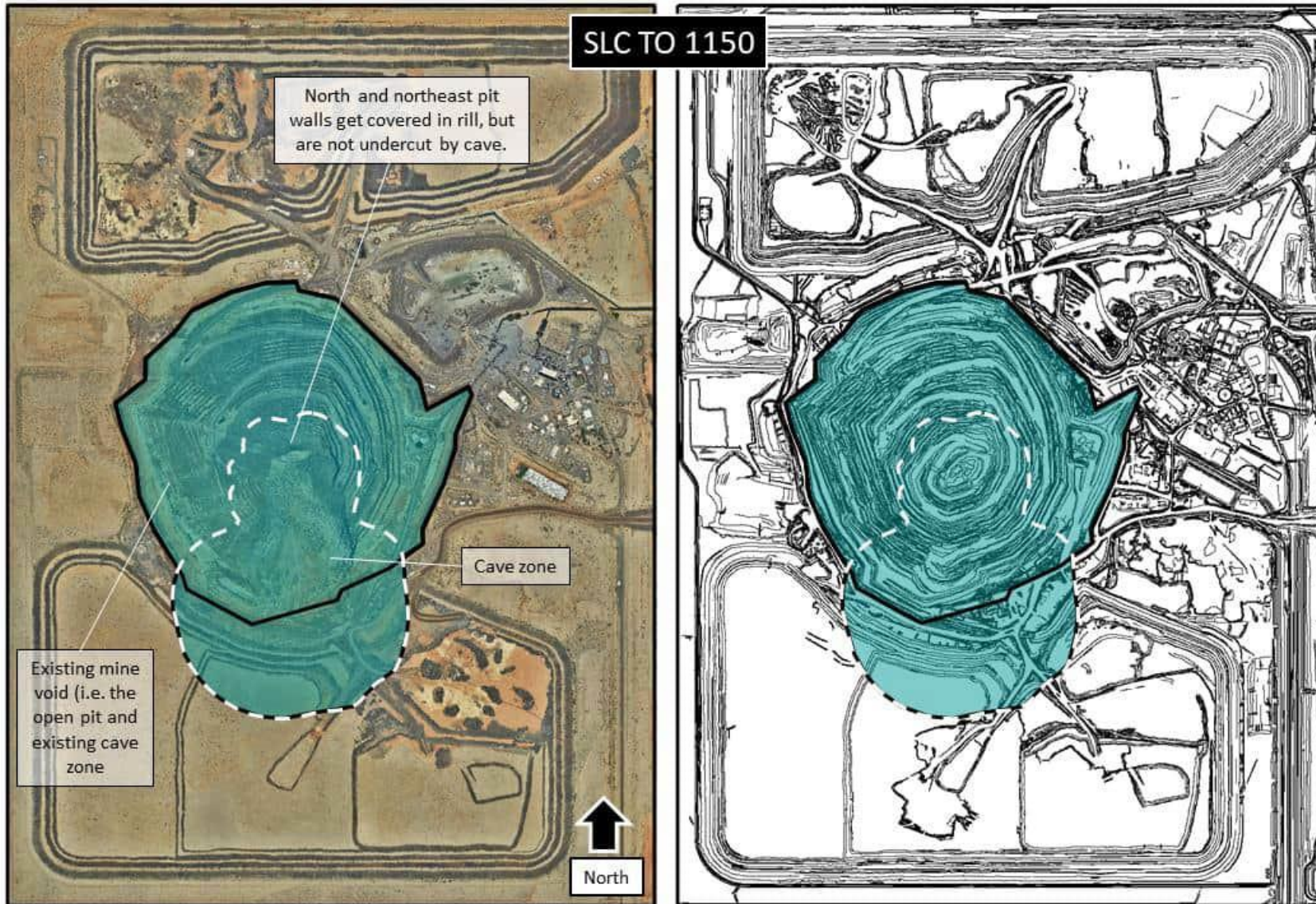


Figure 3-34 Forecast spatial extents of the subsidence crater (end of mining to 1150 mRL).

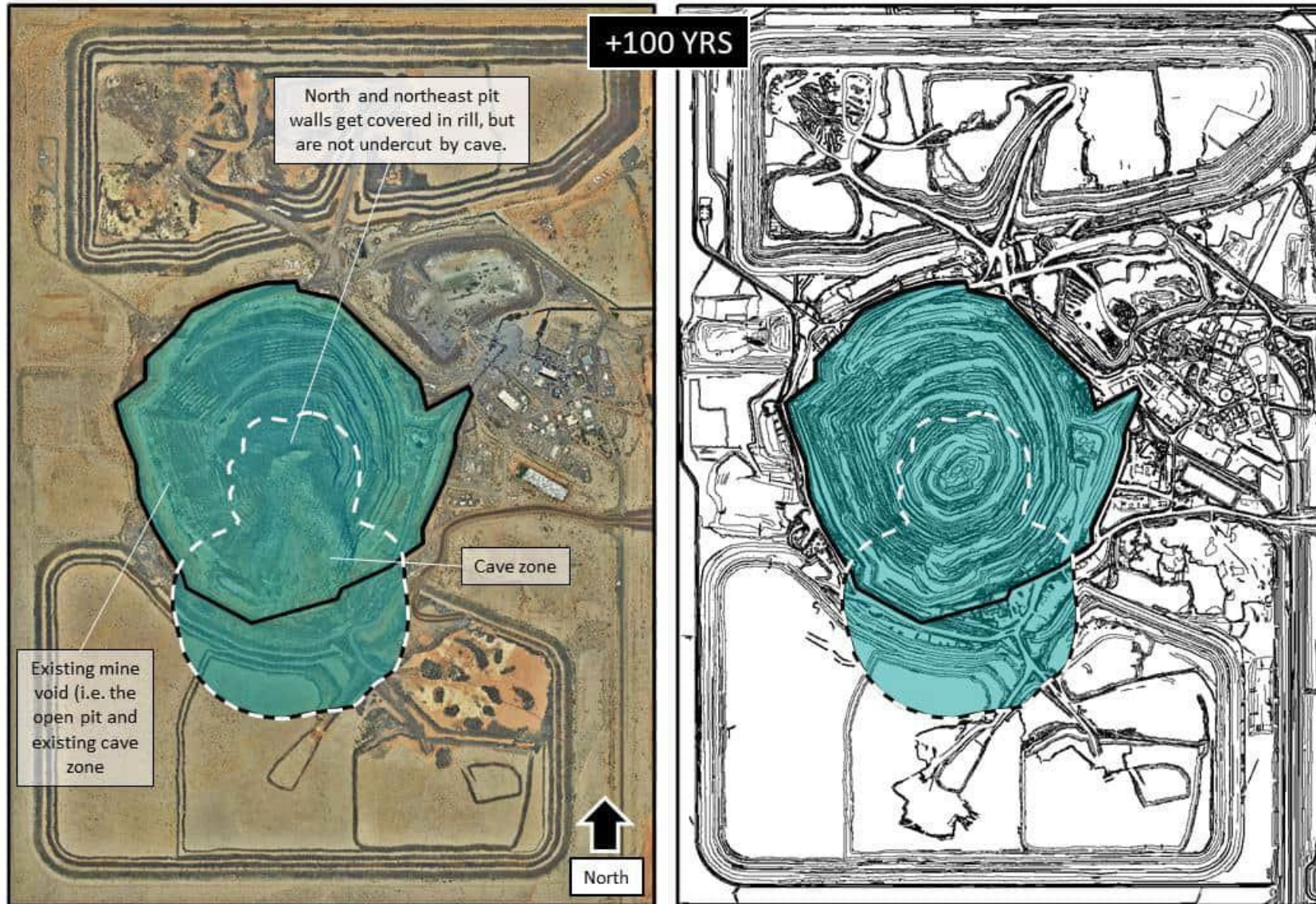


Figure 3-35 Forecast spatial extents of the subsidence crater (end of mining +100 years).

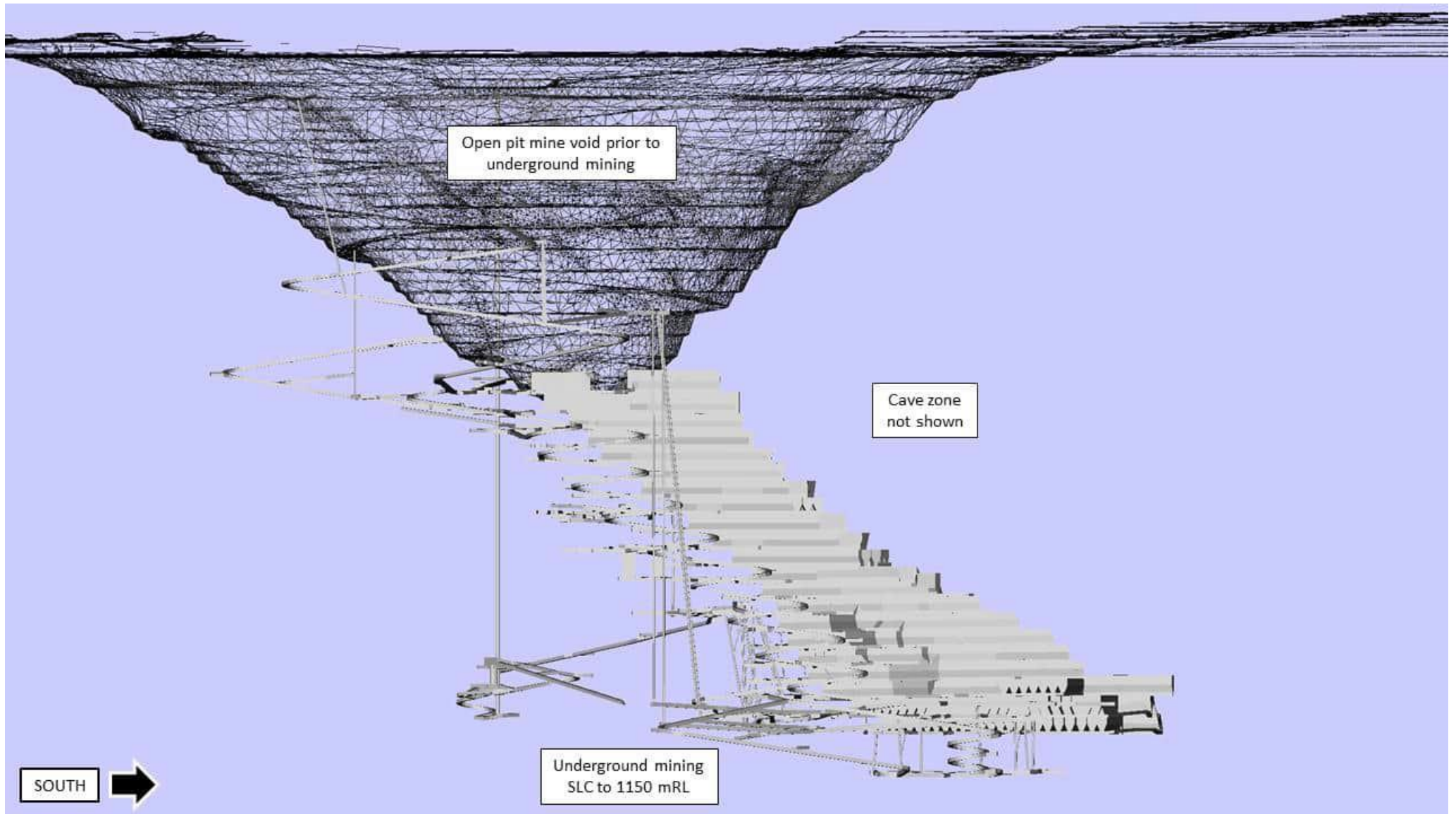


Figure 3-36 The final geometry of the excavated mine voids, including the open pit and underground mine, at the end of mining (view east, cave not shown).

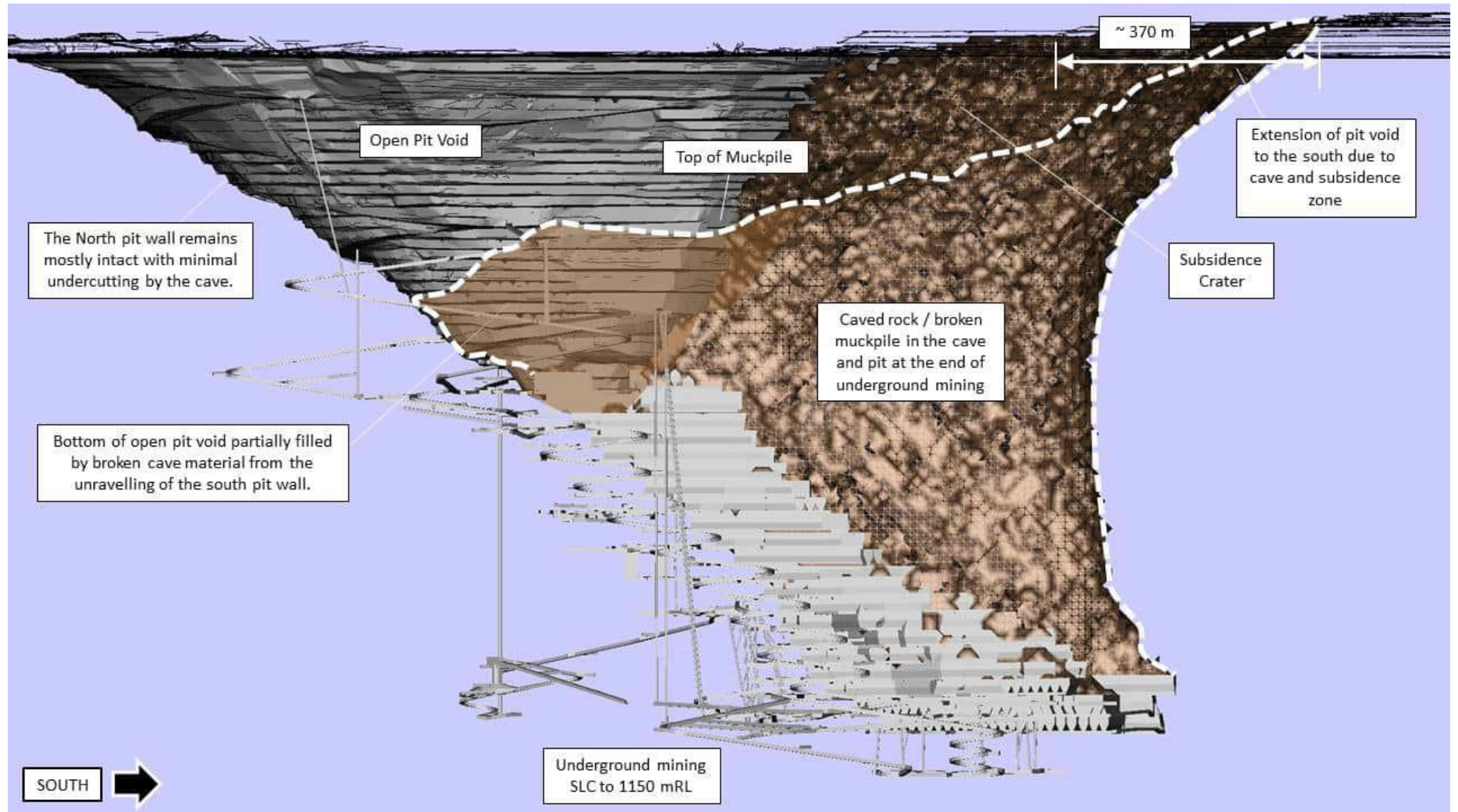


Figure 3-37 Final shape of the excavated mine voids and cave zone, showing the final surface profile of the rilling muckpile inside the subsidence crater (view east).

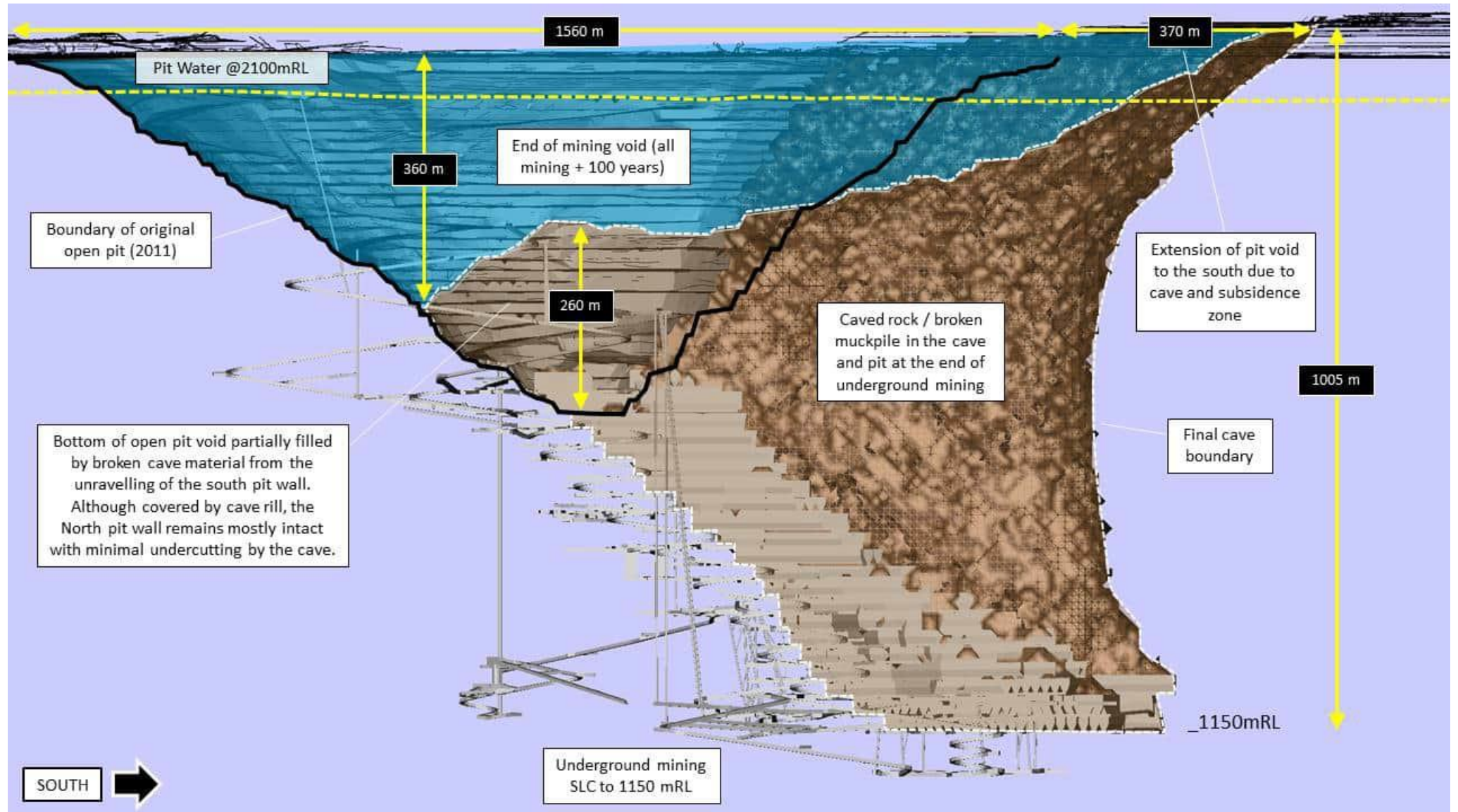


Figure 3-38 Final shape of the excavated mine voids and cave zone showing the major dimensions (view east).

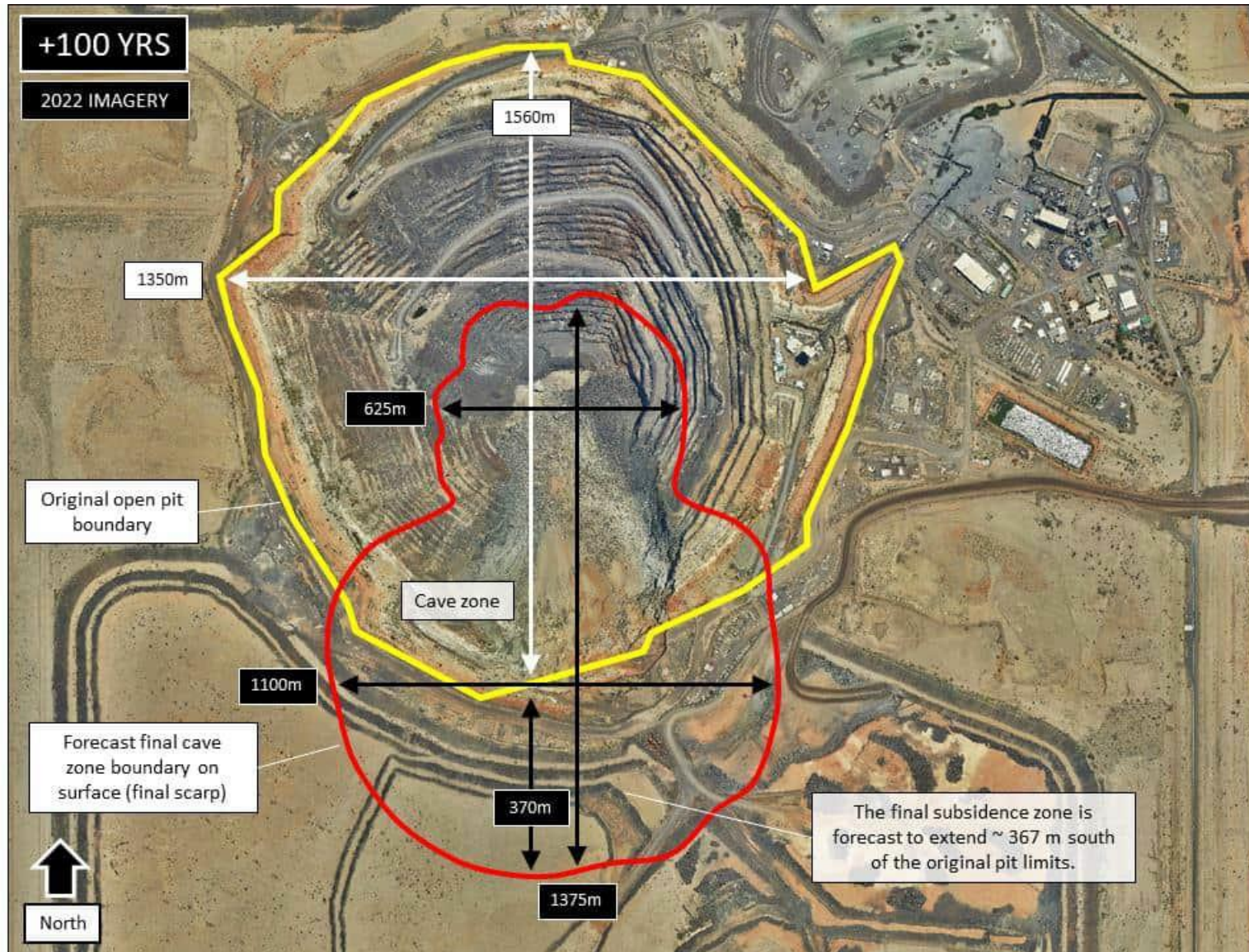


Figure 3-39 Final geometry of the original open pit and cave zone expression at the surface and the major dimensions (top view).

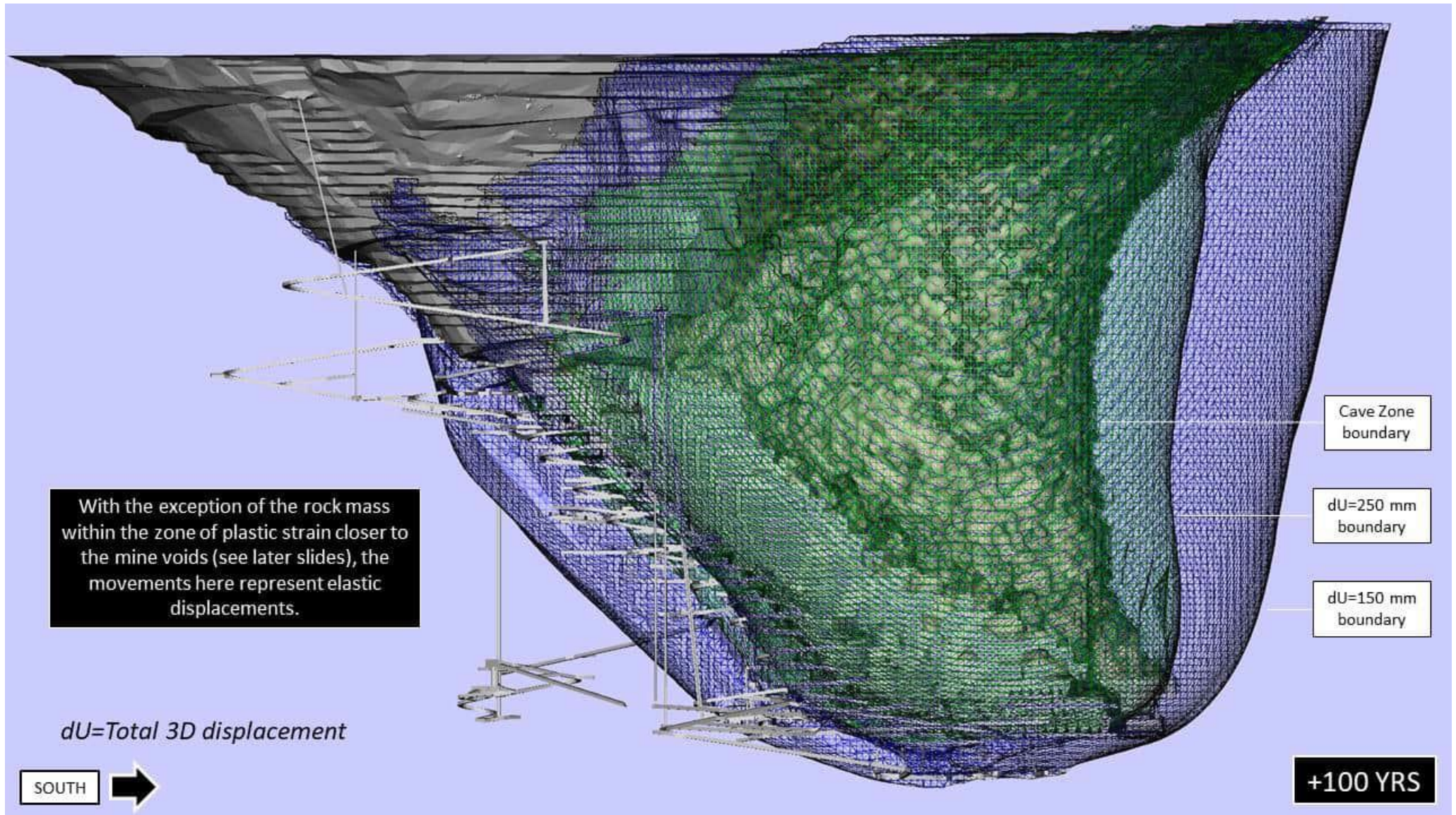


Figure 3-40 Isosurfaces of underground mining-induced displacement after 100 years of groundwater recharge (view east).

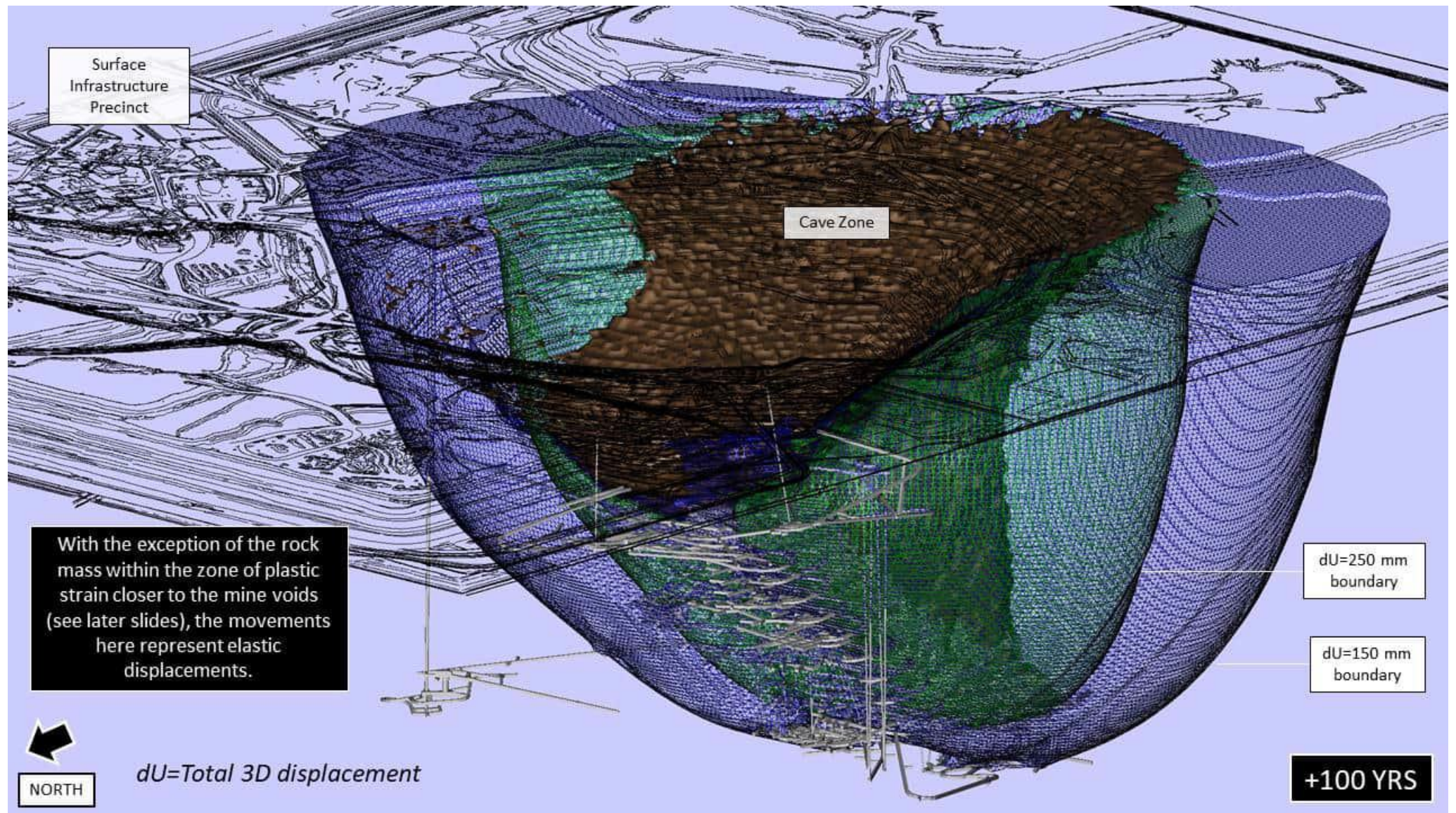


Figure 3-41 Isosurfaces of underground mining-induced displacement after 100 years of groundwater recharge (perspective view).

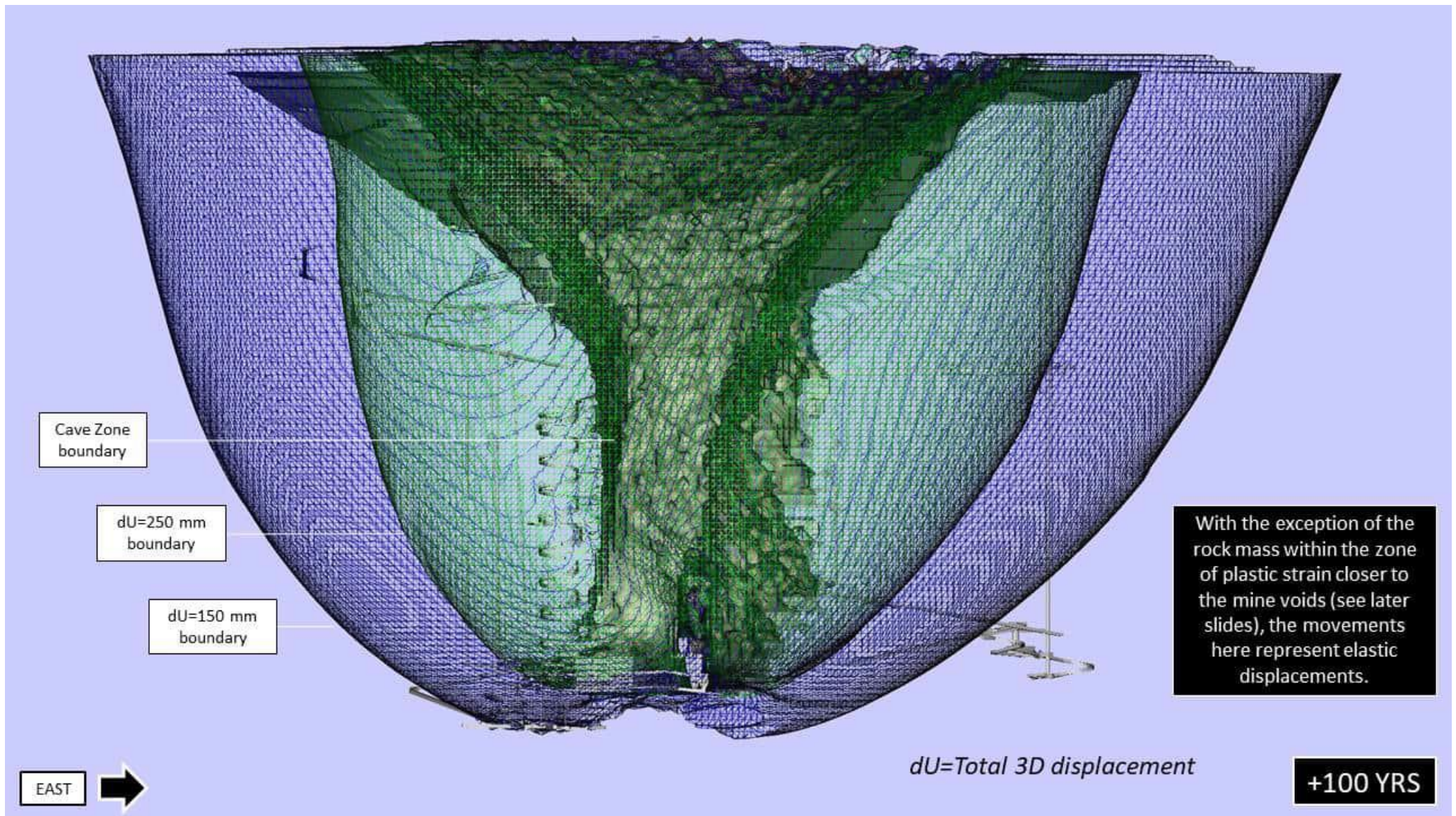


Figure 3-42 Isosurfaces of underground mining-induced displacement after 100 years of groundwater recharge (view north).

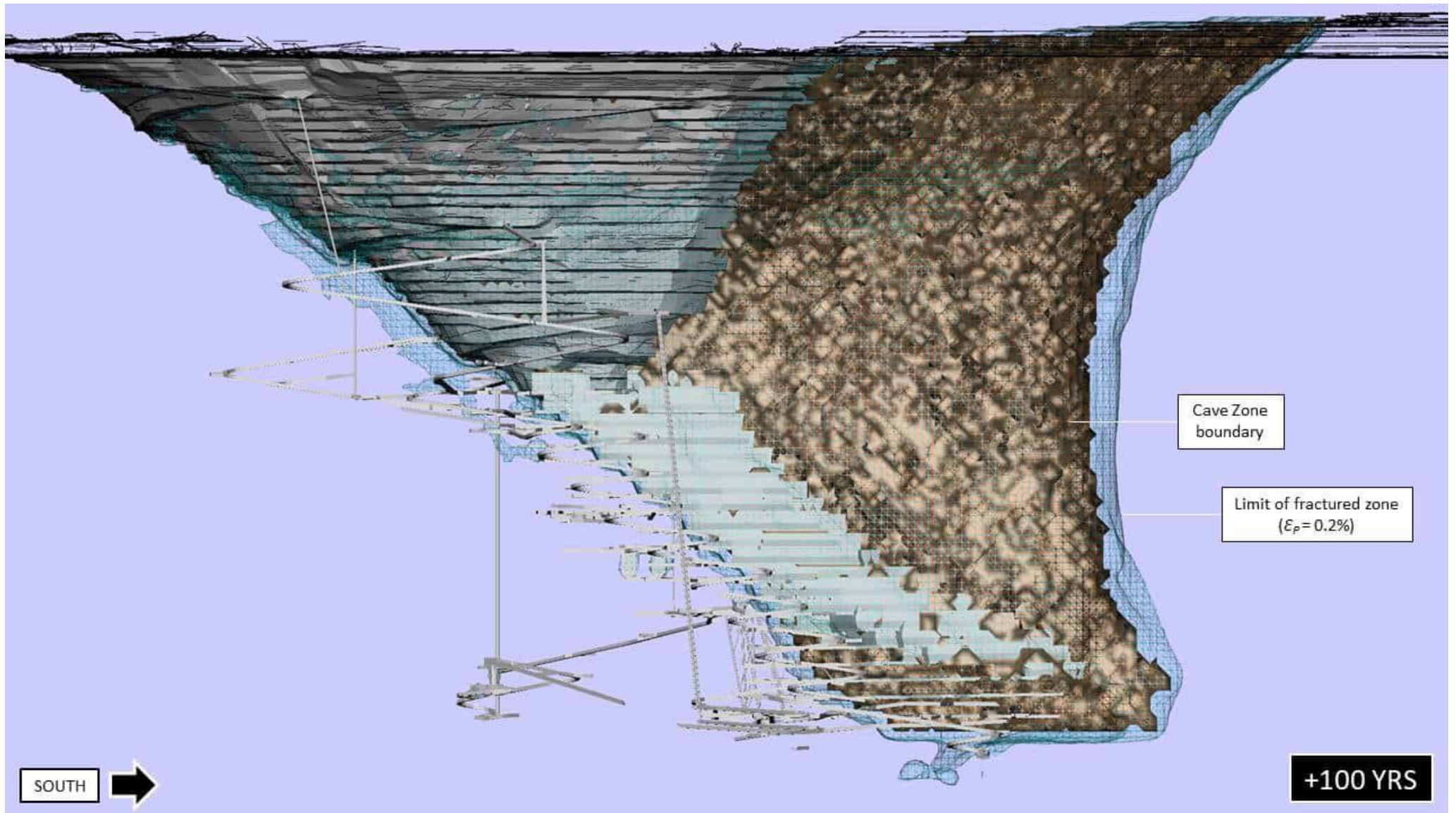


Figure 3-43 Isosurface of the caving-induced fracture zone (plastic strain of 0.2 %) relative to the cave boundary at the end of mining + 100 years flooding (view east).

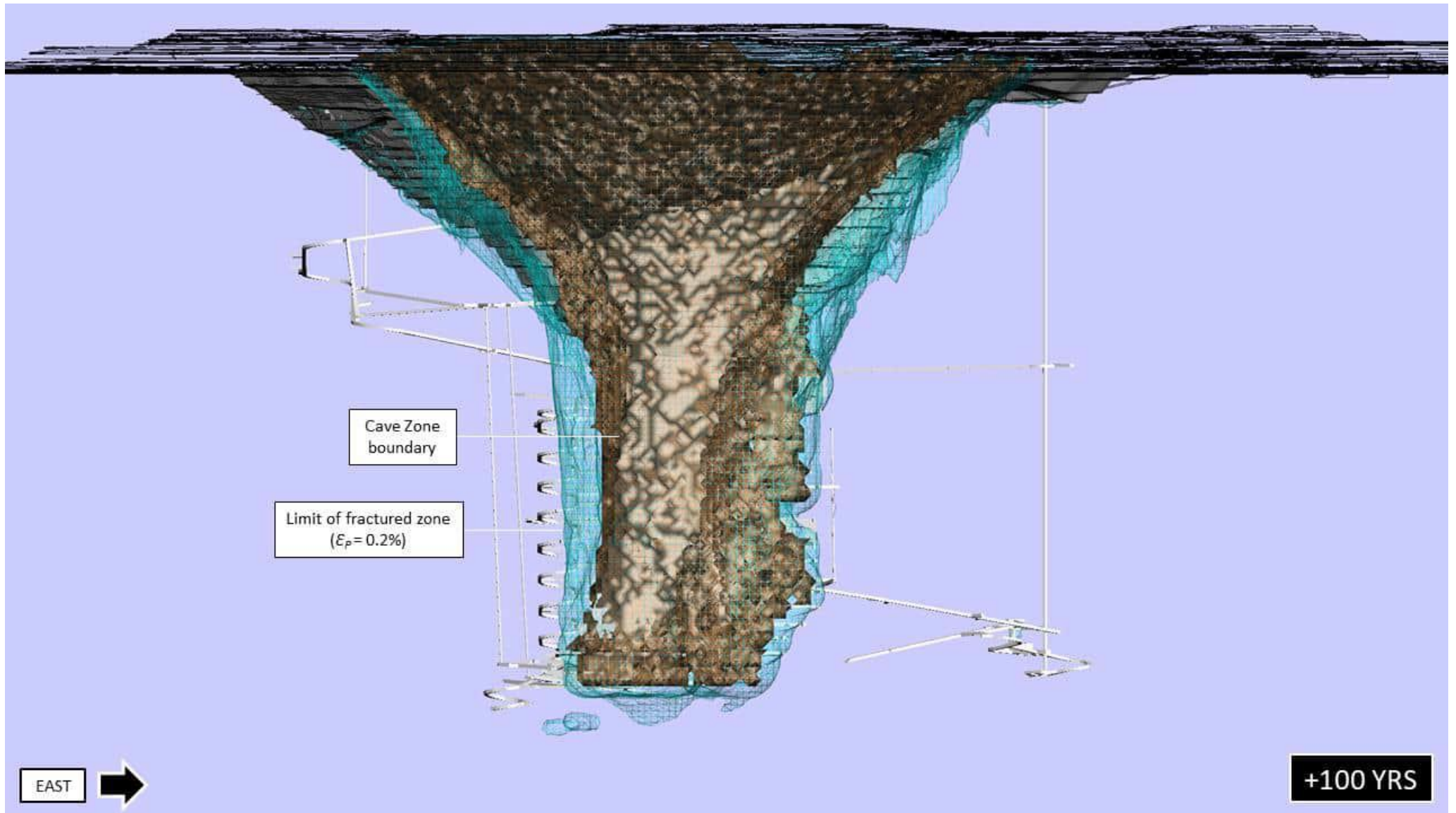


Figure 3-44 Isosurface of the caving-induced fracture zone (plastic strain of 0.2 %) relative to the cave boundary at the end of mining + 100 years flooding (view north).

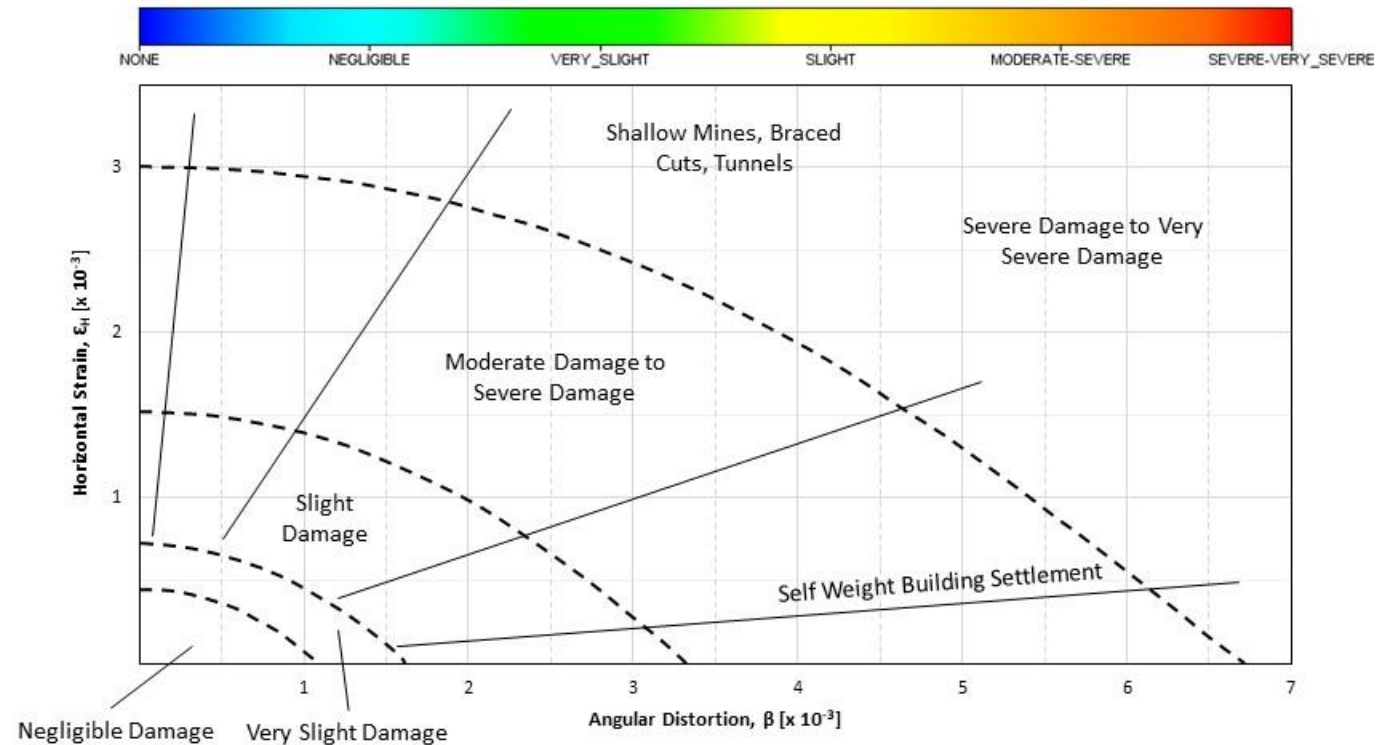
Horizontal Strain (ϵ_H) and Angular Distortion (β) (i.e. ratio of differential settlement of two points to their horizontal spacing) can have a significant impact on surface infrastructure, especially shaft headframes, chimney stacks, wide concrete foundations for vent fans, pipeline footings, roads etc.

A methodology for assessing the impact of subsidence on surface infrastructure is based on Boscardin & Cording (1989), also known as the Harrison Plot. This can be used to classify and assess the severity of the impact to critical assets located close to mining excavations like open pit slopes, underground caves or stoping blocks.

The plot is only applicable for surface infrastructure, not underground facilities. It is primarily formulated for rigid surface infrastructure, but can be used for other structures, like earth dams, as a high-level, first-pass subsidence impact assessment.

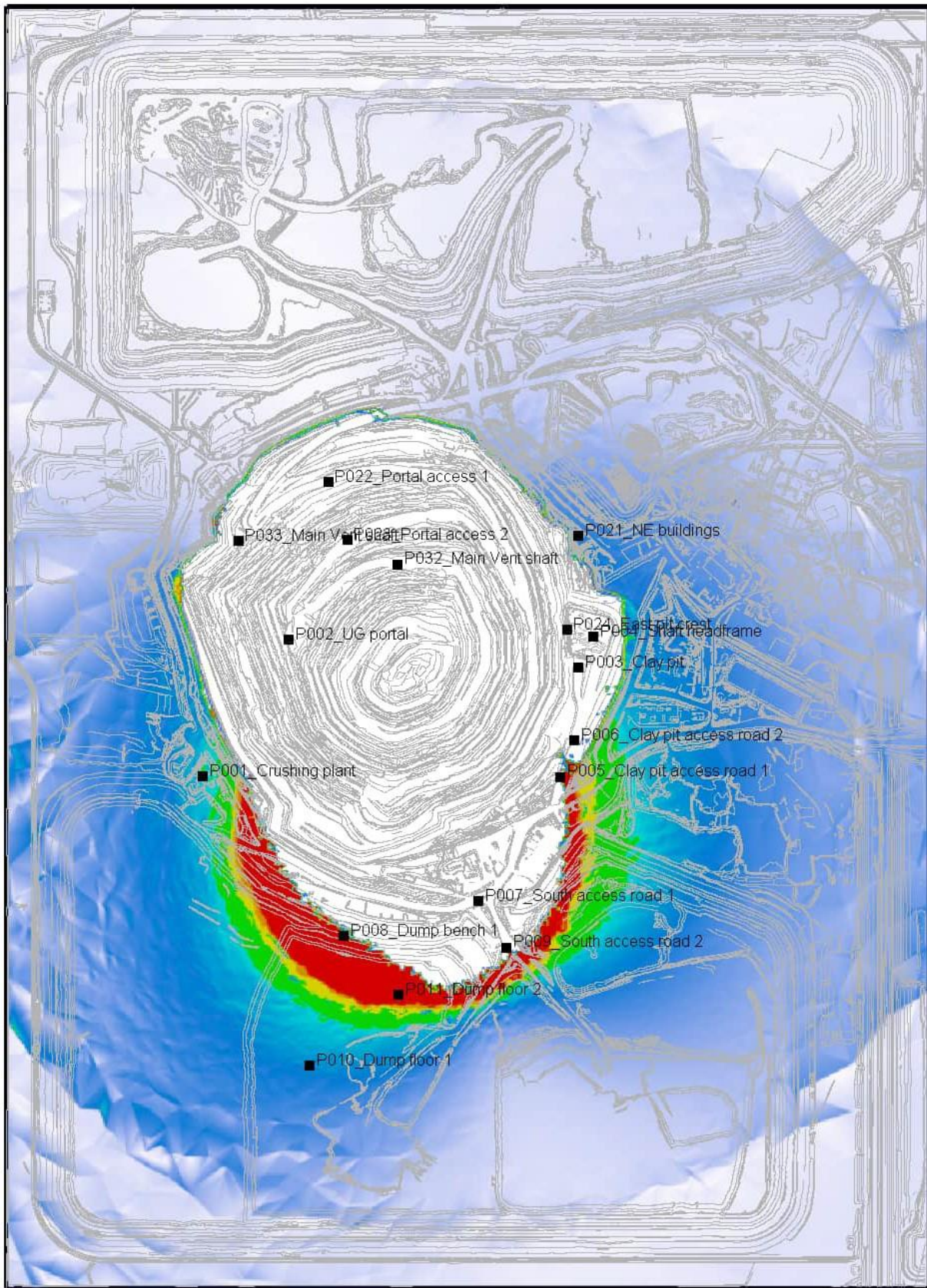
If a particular asset plots as Moderate impact or higher, BE suggest that an assessment of the horizontal strain & angular distortion tolerance limits should be conducted by a relevant structural expert.

SURFACE INFRASTRUCTURE IMPACT SEVERITY



Boscardin, M. & Cording, E., 1989. Building response to excavation induced settlement. *Journal of Geotechnical Engineering*, 115(1).

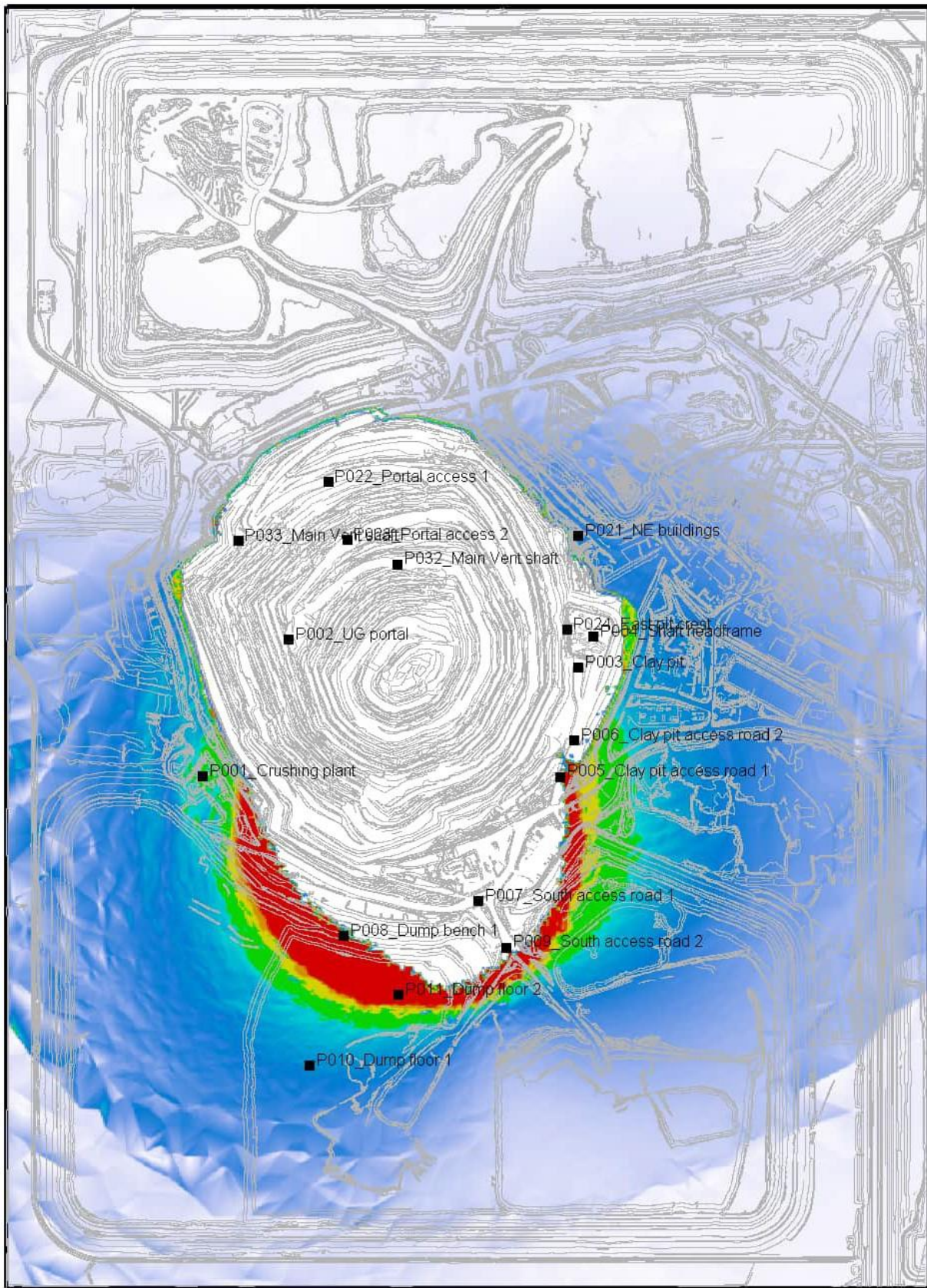
Figure 3-45 Surface infrastructure subsidence impact severity assessment scheme based on Boscardin & Cording (1989).



SUBSIDENCE IMPACT SEVERITY (BOSCARDIN & CORDING, 1989)



Figure 3-46 Surface subsidence impact severity forecast at the end of mining.



SUBSIDENCE IMPACT SEVERITY (BOSCARDIN & CORDING, 1989)



Figure 3-47 Surface subsidence impact severity forecast after 100 years of groundwater recharge post-mining.

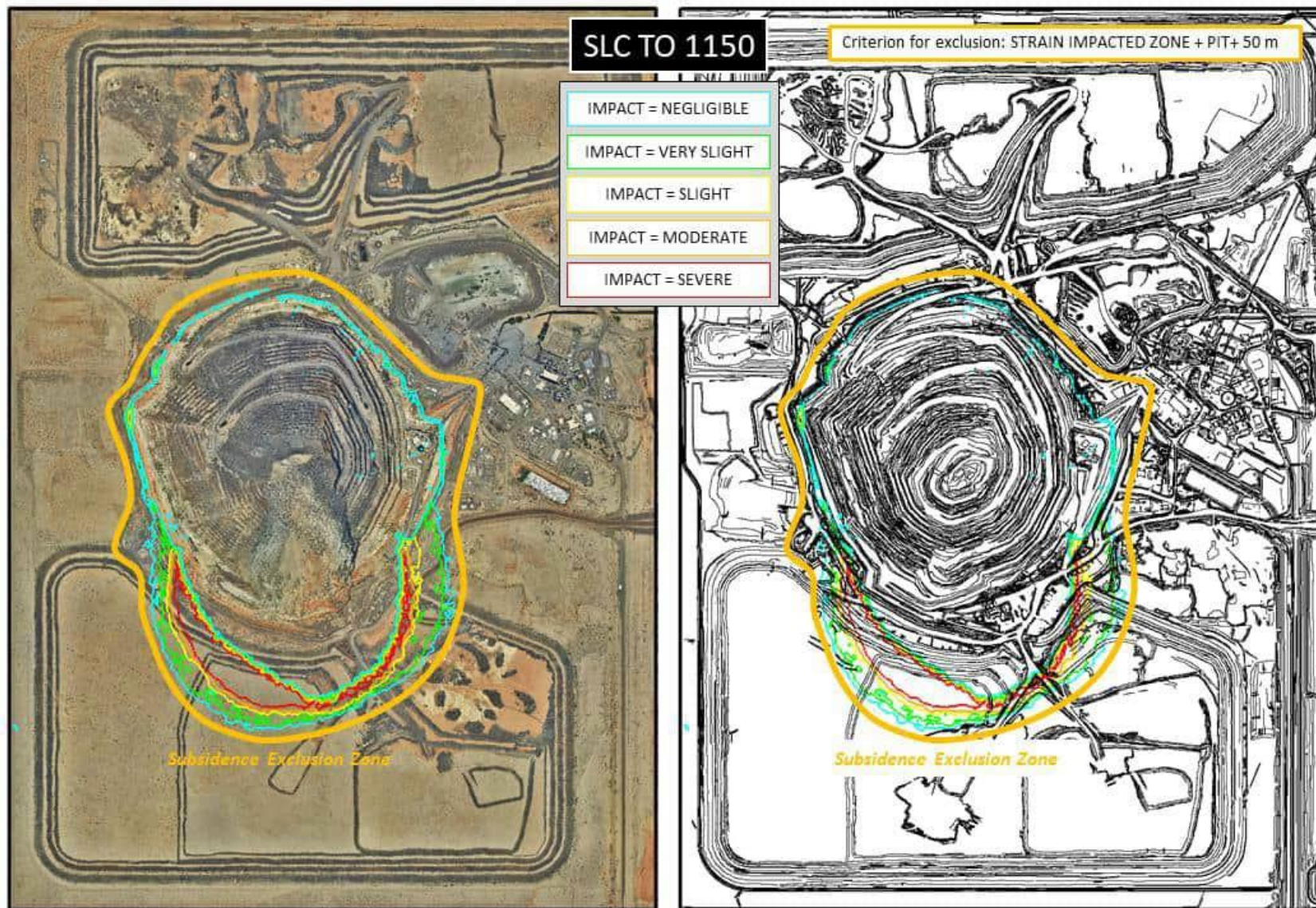


Figure 3-48 Contours of surface subsidence impact severity at the 2156 mRL at the end of mining and proposed long-term exclusion zone boundary.

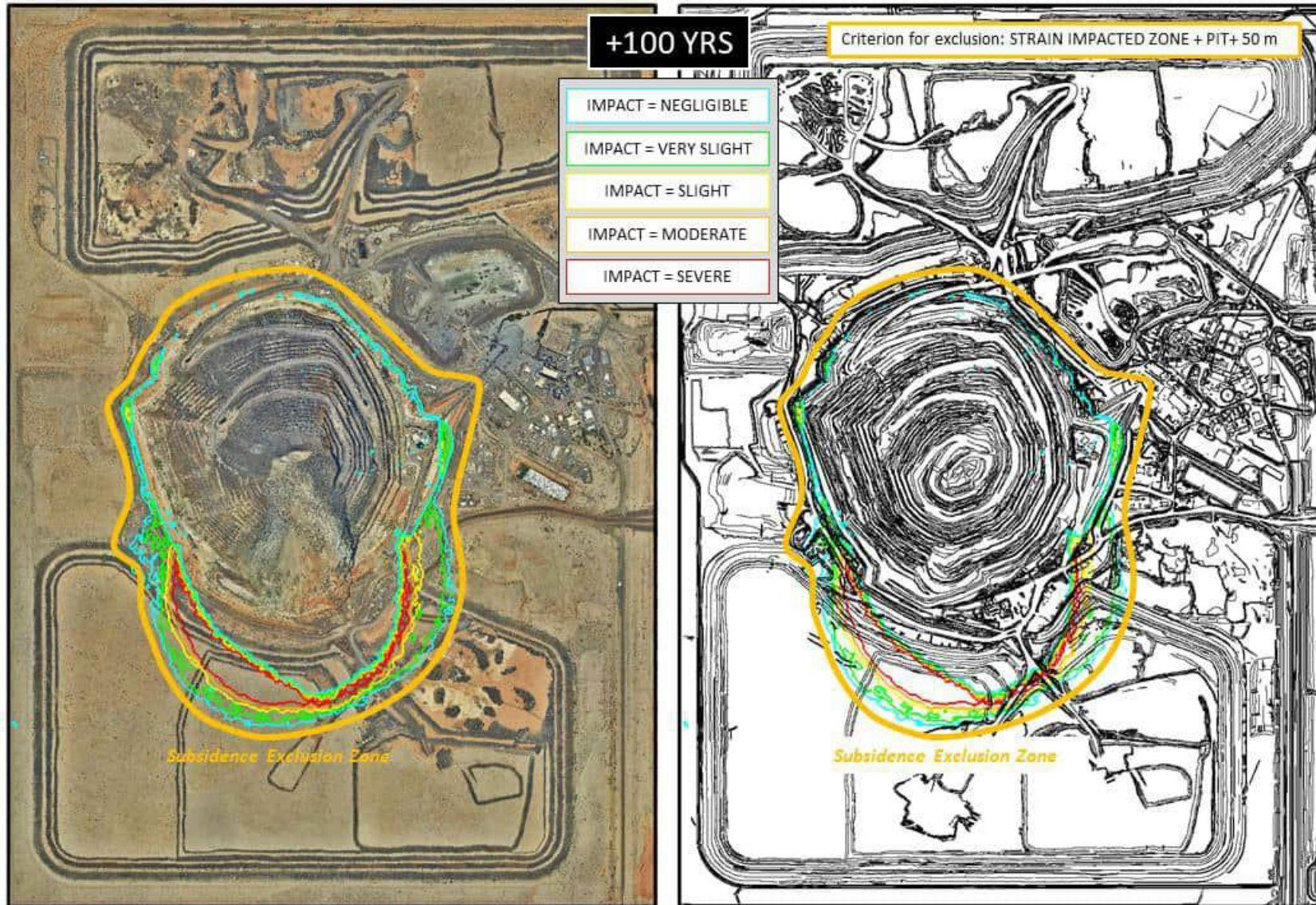


Figure 3-49 Contours of surface subsidence impact severity at the 2156 mRL after 100 years of groundwater recharge post-mining and proposed long-term exclusion zone boundary.

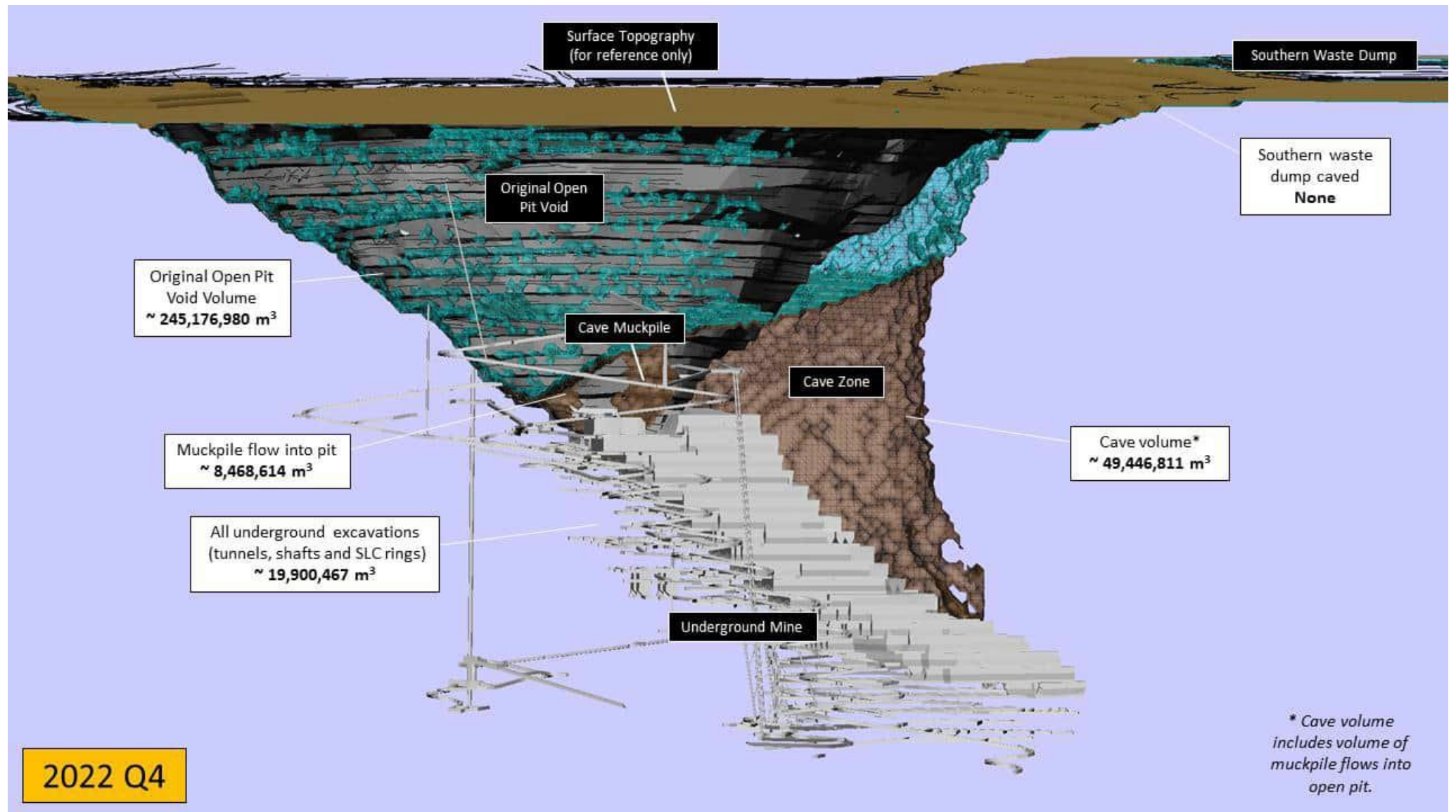


Figure 3-50 Mining-related voids and the cave zone and their respective volumes (2022 Q4).

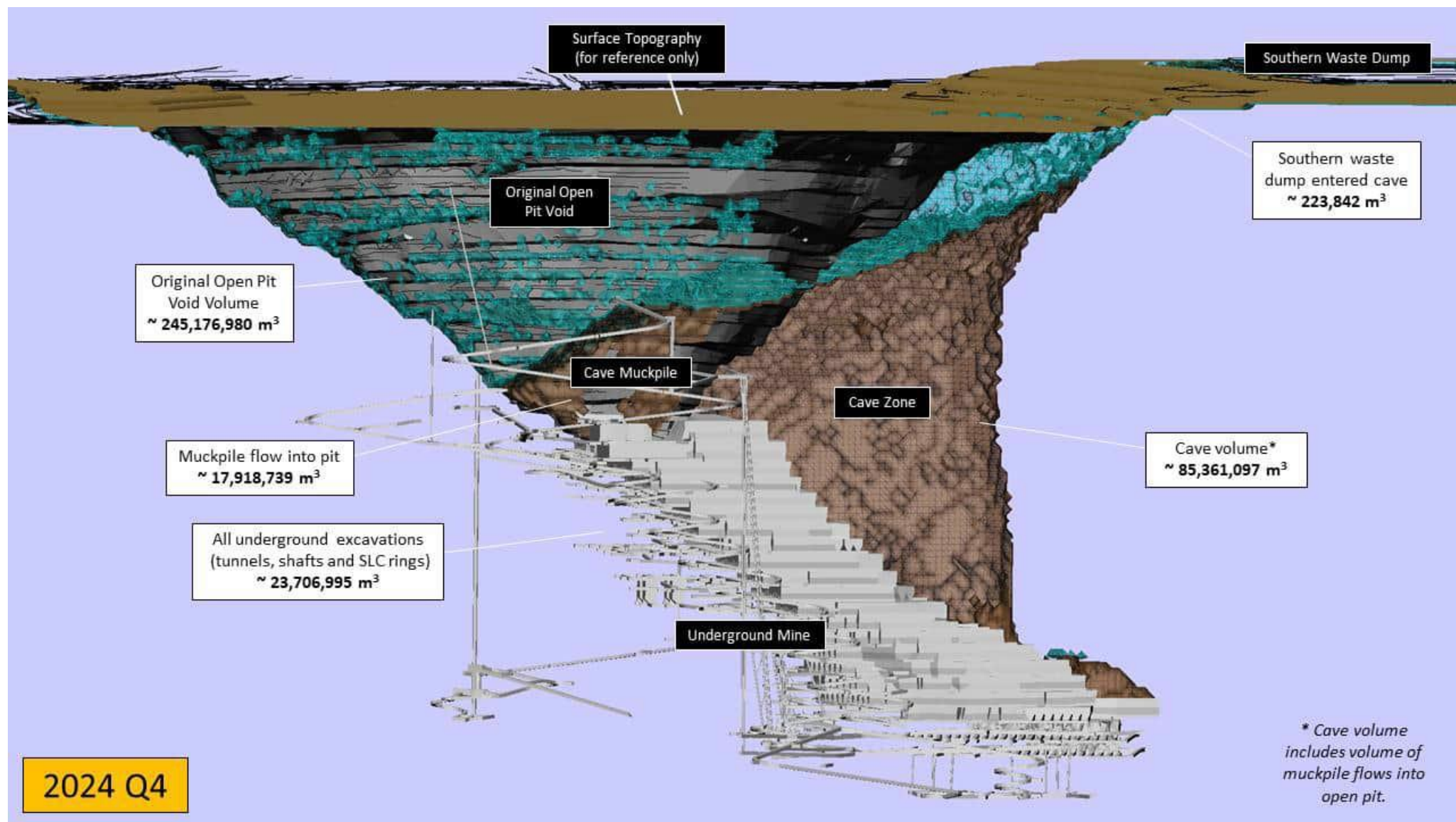


Figure 3-51 Mining-related voids and the cave zone and their respective volumes (2024 Q4).

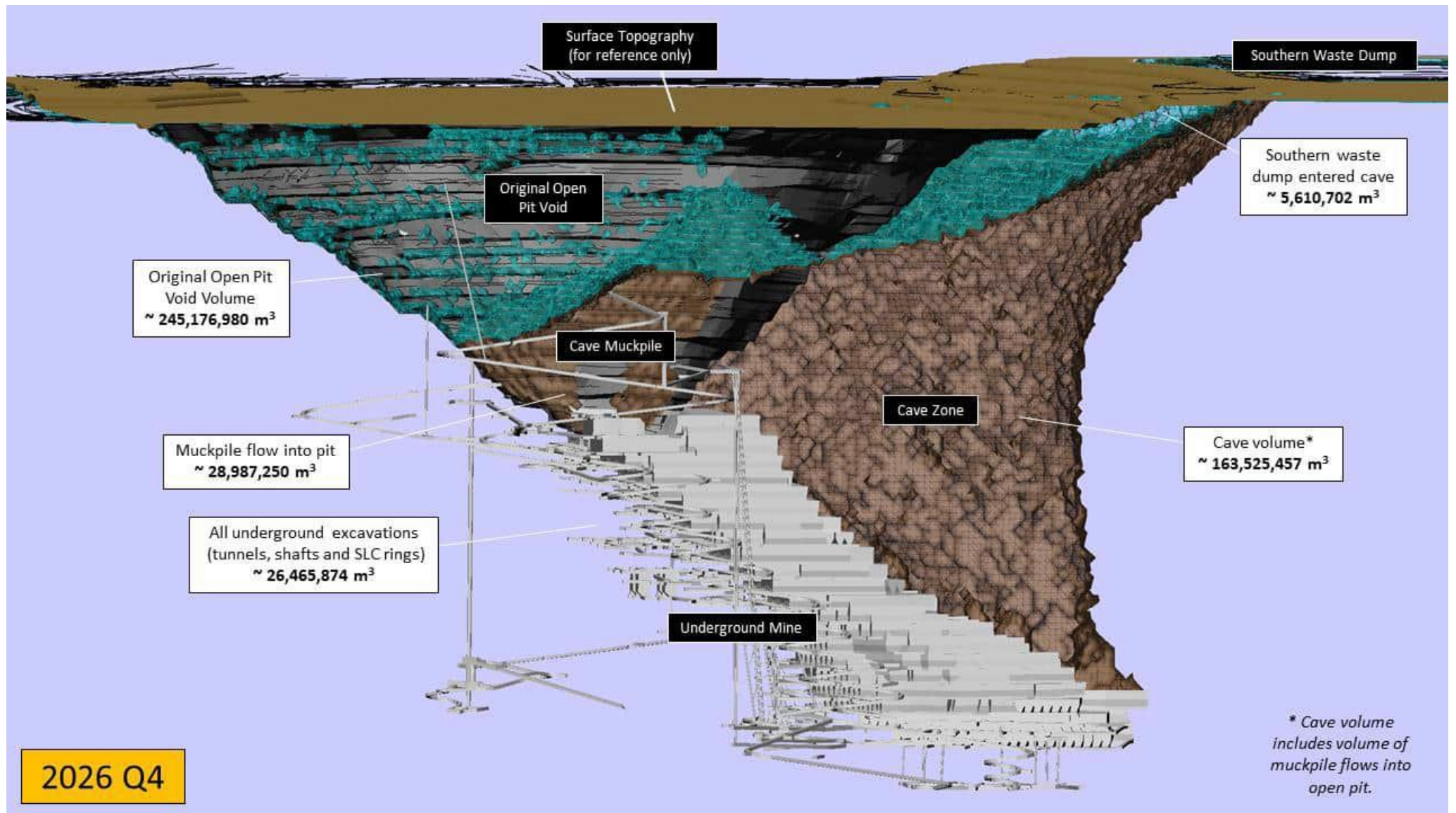


Figure 3-52 Mining-related voids and the cave zone and their respective volumes (2026 Q4).

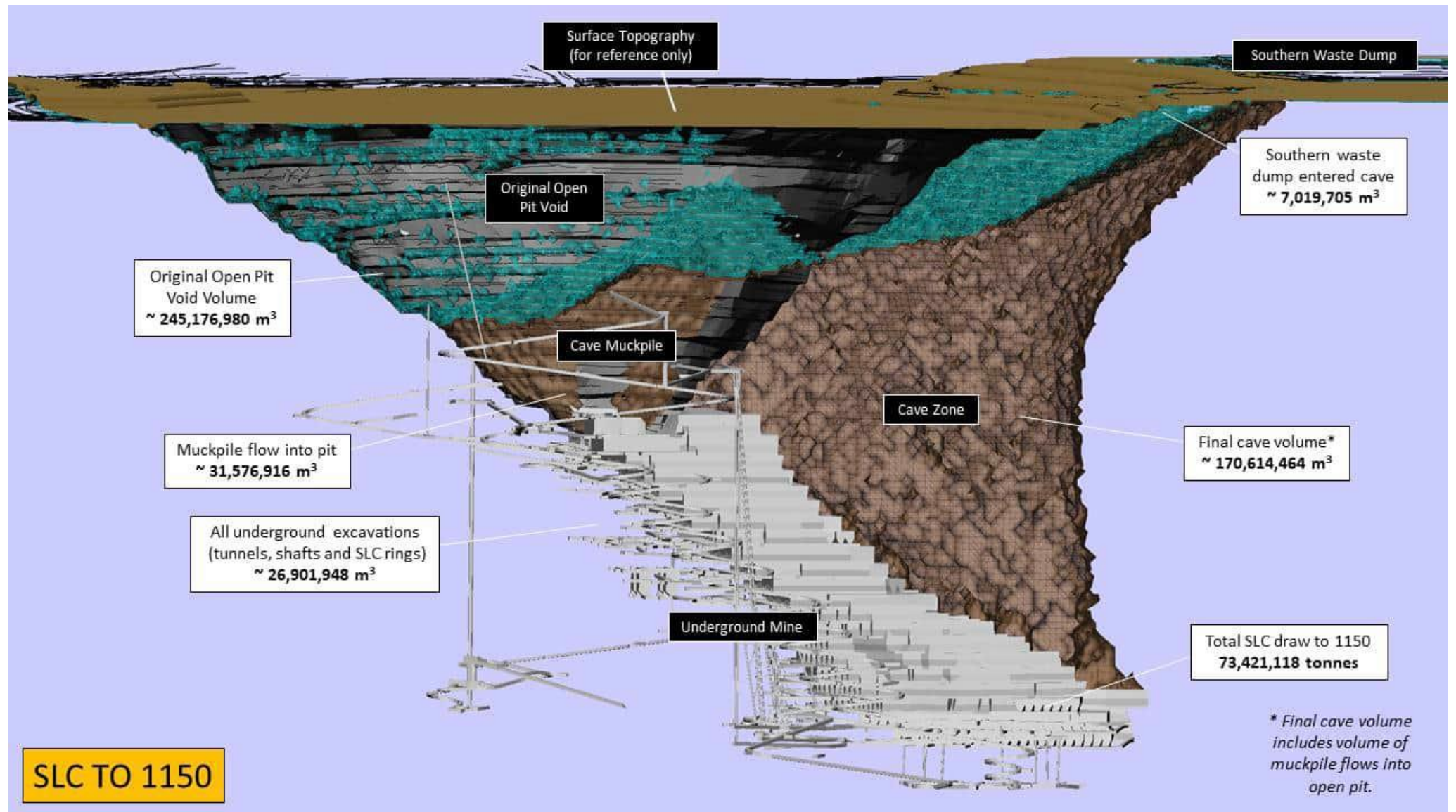


Figure 3-53 Mining-related voids and the cave zone and their respective volumes at the end of mining to 1150 mRL.

3.3 Other mechanisms of post closure movement

Post closure deformation due to the other mechanisms are generally negligible in comparison to the effects of mining and groundwater effects previously outlined. Secondary post mining effects are discussed here for completeness and to assist Ernest Henry mine in planning and risk management.

Meaningful creep or changes in deformation after closure of a mine (any mine, not specifically EHM) could be caused by:

- Chimneying due to collapse of underground excavations
- Ongoing changes in the cave (consolidation, degradation, rilling or propagation of voids) leading to a change in shape and stiffness. This includes creep effects of the cave muckpile (broken rock in the cave zone)
- Erosion
- Weathering

Chimneys due to collapsed excavations

One role of exclusion zones is to prevent exposure to chimneys to surface that could occur if mine workings collapse and the failure propagates to surface. This can only occur if there are large unfilled voids at a shallow depth.

Two examples where significant changes occurred after mining ceased were above the Ipswich Coal mines in Queensland and the Poseidon Nickel Mine in Western Australia. In these cases, chimneying above open voids lead to plug collapse at surface >20 and 100 years after mining ceased, respectively.

At this time, no such voids are planned at EHM and the SLC has no large unfilled airgap as this is avoided by careful cave management. This means the risk of chimney failure at EHM is not applicable / negligible.

We suggest that the scenario at EHM is closer to the scenarios at Goldex, Big Bell and Perseverance, as in these cases the mines were mature, full of caved material and there were no relevant pillars above voids that could collapse, leading to delayed changes in the geometry of excavations in the mine. At Ipswich and Poseidon, there were numerous voids and pillars at the end of mining.

In summary, the risk of chimneying at EHM is considered negligible as there are no large excavations (i.e. stopes) that are left unfilled that are close to surface.

Consolidation/settlement

Consolidation/settlement of emplaced granular materials is generally divided into primary and secondary parts.

- Primary consolidation arises from the application of loads to emplaced or disturbed materials. As the displacements and loads are solved as part of the FE computations and the model comes to equilibrium at each step, this is already accounted for in all plots of subsidence and strain in this report.
- Secondary consolidation, or creep is essentially compression of the voids, or pore space in a granular medium over time. It is usually calculated using the following equation:

$$\Delta \epsilon_s = \frac{C_a}{1 + e_p} \log \frac{t_2}{t_1}$$

C_a is the coefficient of secondary consolidation; e_p is the void ratio and ϵ_s is the increment of vertical strain between time t_2 and time t_1 .

There are no estimates in literature for C_a for damaged rocks because broken rock is so stiff, the potential for settlement is seen as negligible:

- In the cracked zone, (nearest edges of subsidence) the change in porosity due to damage is extremely small.
- In the scarp/toppling zone, the change in porosity is very small.
- Even within the cave, the maximum % voids is probably no more than 10-25%, the rocks are coarse and granular and the cave is relatively stiff.

As such, the only potential for any secondary settlement is in the cave zone itself, and this would likely be very small. The majority of this settlement occurs during the operating mine life and the effects post mining are considered negligible.

As a starting point for an observational program, we can make some conservative assumptions to make a first pass assessment of secondary settlement potential.

For now, if one uses the following (Figure 3-54) approximation of settlement curves, applied to the FE model results for e_p (part of the solution in the large strain model) it is possible to estimate secondary settlement. This simpler approximation of the secondary settlement equation is used because no meaningful C_a for rock is available in literature and no conservative value results in settlement in a meaningful timeframe.

As such, this extremely conservative overestimate (Figure 3-54) is not intended to be a final forecast, but rather a starting point that can be tested and updated over time, by measuring actual movements where no draw and no horizontal movements due to rilling are taking place. Within a few years, a suitable reference C_a should be able to be bracketed.

The data suggests that even for this extremely conservative estimate, secondary consolidation in the caved zone should not exceed around 0.5mm per meter of cave height and would likely be much less. This calculation is conservative because the cave plunges/is inclined and much of this, if any occurs, will occur rapidly in the context of mine closure.

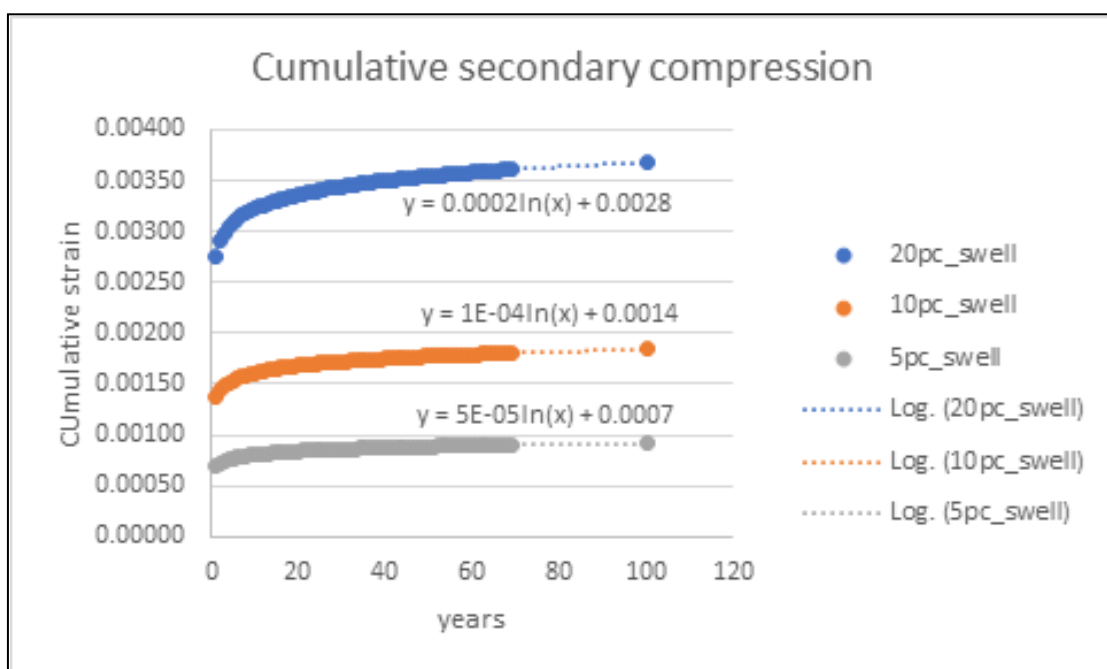


Figure 3-54 Assumed settlement curves for the cave muckpile.

As the cave will be safely within the exclusion fence or bund, mining settlement or creep effects in the broken cave material below the water level in the pit will have no meaningful (or measurable) effect on the mine stability or local environment.

Weathering

Sometimes 'weathering' is referenced as a risk, which we take to mean either accelerated chemical degradation of the failed and fractured rock in and around the cave due to exposure to air and water, the mechanical impacts of mixing of surface (weathered) material with fresh broken rock, or else, erosion due to weather.

There are no backfill areas in the mine that are subject to weathering or significant weakening due to chemical effects. The upper geological layer at EHM is a zone of consolidated soil, sand layers and shales. This cover sequence has already undergone significant weathering as part of its geological formation over millions of years. The open pit is now over 20 years old and exposures of the cover sequence in the upper regions of the pit have not experienced any significant degradation or erosion effects. Superficial erosion due to surface water run-off is observable in the pit. However, these effects are very localised and do not have an impact at a mine scale, do not impact wall stability or (significantly) impact the size of the final mine void.

While it is important to appreciate the impacts of weathering of near surface materials or already weathered materials that may become mixed into the cave on cave flow for operational safety reasons, we do not think that weathering of the fractured zone and caved material can have an appreciable impact on subsidence at EHM, as no significant degradation of drained or flooded materials has been observed so far. If degradation were to occur, the negligible impacts of such degradation on subsidence should be confined to inside the caved zone. The effects of weathering on mine stability and subsidence are considered negligible for the Ernest Henry mine.

Erosion

Assessment of erosion was not part of this scope. This includes erosion from overland water flow, or erosion of the material in the subsidence / caved zone. We note that no simulation has the precision or resolution to make reliable forecasts of erosion except to help in planning and designing abandonment bunds by confirming that they are outside the fractured or heavily subsided zone. Generally, most mines ensure that the final containment/exclusion fence or bund is at an elevation above the whole of the crater, so that excess erosion will be wholly inside the containment/exclusion fence or bund. We also note that very minor and superficial erosion due to surface water run-off is observable in the pit. However, these effects are negligible and do not have an impact at a mine scale or impact stability of the open pit.

4 CONCLUSIONS, RECOMMENDATIONS & LIMITATIONS

Main findings

1. This project updates the cave shape and surface subsidence forecasts for the Ernest Henry mine, which were previously made by Board, et al. (2009), as a part of the feasibility assessment for underground mining. BE's numerical simulation implements a mechanical-flow-hydro coupled simulation framework, in the Abaqus Explicit finite element and FS4 flow codes, in order to realistically simulate the complex physics of the underground sublevel caving mining process, as well as the inter-dependencies between mining and the local hydrogeology. This modelling approach has been used at Ernest Henry for several years and the forecasts of cave performance and subsidence have been robustly calibrated to numerous real observations during that time.
2. Close calibration between several iterations of BEs model forecasts and real observations at the mine have been achieved over several years utilising a combination of seismic data, surveys of the actual cave muckpile profile, aerial photography as well as GPS and INSAR displacement readings at the surface. Further information on those calibrations is available to review in prior reports by Beck (2021) and Campbell (2022). The model calibration was updated for this 2023 phase of surface subsidence modelling and assessment.
3. Historic sublevel caving operations at the Ernest Henry mine have resulted in a progressive collapse and unravelling of the southern wall of the original open pit mine. This process of caving is forecast to continue as the SLC operations advance to the 1150 mRL. This is a necessary part of the cave mining process in order to prevent the formation of an airgap. A zone of rock mass damage envelops the cave zone, as does a zone of rock mass movement, with the magnitude of the displacements being highest around the immediate cave zone boundary and decreasing with distance away from the cave.
4. Beyond the immediate limits of the cave zone and subsidence crater that the cave creates on the surface, the east, west and north original walls of the open pit are forecast to remain stable as the underground mining of the SLC operations advances as deep as the 1150 Level.
5. When SLC operations are completed on the 1150 Level, the cave zone will extend from the 1150 mRL to the 2156 mRL in the south of the mining zone. At that time, the cave is forecast to have propagated southwards as far as the 37840 mN position (mine grid), which is approximately 370 m to the south of the southern-most point of the original crest of the open pit mine.
6. The cave zone is forecast to propagate into the southern waste dump (volume ~ 112,000,000 m³) during 2024. Given the forecast final extents of the cave zone on surface, a total of 7,019,705 m³ or 6.3 % of the southern waste dump material is expected to become progressively undercut by the cave over time and enter the subsidence crater (i.e. flow zone). Some of the waste dump material could be expected to rill into the original open pit. All caved waste dump material would be contained within the final subsidence crater.
7. Approximately 31,576,916 m³ of caved rock is forecast to fill the lower benches of the open pit at the end of the 1150 SLC mining. This material would be primarily composed of broken rock which has caved from around the orebody, as well as some waste dump material that has rilled into the cave from above.
8. The top of the cave muckpile would have a variable shape after mining, with some basin sections and also steeper slopes being created due to the subsidence and rilling effects of the broken material during the caving process. The depth of the surface subsidence crater will vary, but our forecasts indicate a maximum depth in the order of 360 m below the natural ground level, once the SLC is completed to the 1150 mRL.
9. Decommissioning of the mine dewatering and bore field pumps after mining the SLC to the 1150 mRL would result in a gradual flooding of the underground and open pit mine. Our hydro-mechanically coupled simulation of the post-mining period of flooding indicates that the groundwater table would re-charge up to the 2100 mRL³, which is approximately 56 m below the natural ground surface elevation. All excavations of the underground and open pit mine would be flooded below this elevation.

³ This elevation of the final post-mining phreatic surface is simulated in the Abaqus numerical model for excavation stability assessment purposes. It represents the long-term far-field mean phreatic surface elevation and does not account for the detailed surface catchment features and mine closure planning.

10. The effect of re-flooding the rock mass and mine voids is an uplift effect to the rock mass in the order of 100 mm or less, with the larger uplift effect occurring closer to the mine voids and mainly in the south (hangingwall) of the orebody. This occurs due to a poro-elastic rebound effect. The drawdown of the groundwater table creates a minor and temporary subsidence effect as an elastic displacement response of the rock mass. This process is reversed as the groundwater recharges after mining is completed and dewatering activities are ended. The 100 mm uplift occurs very gradually as the phreatic surface recovers, likely taking several decades.
11. As the groundwater table rises, there is a minor increase in rock mass damage in the open pit slopes due to pore water pressure increase. This damage transitions from a *Negligible* severity prior to groundwater recharge to a *Minor* severity in most areas. The damage effect is superficial in nature and typically extends ~ 10 m into the pit slope. As a result, minor batter scale instabilities of the pit slope could be expected to occur during flooding, such as loosening and sloughing of small rock blocks off the submerged parts of the pit slope. However, no major slope instability is indicated by the damage severity forecasts.
12. The AM fault in the deep footwall of the underground mine also experiences a modest damage increase during flooding but this is a managed risk with *Negligible* forecast impact, as this fault does not intersect the pit slopes and no adverse impact would be apparent at the surface. Affected underground excavations would be flooded, contained and completely inaccessible at the time.
13. The flow simulations do not indicate that any significant airgaps remain in the cave zone at the end of mining. Furthermore, at this time there are no voids such as large open stopes existing or planned to be excavated close to surface which have the potential to experience a "chimneying" style of instability and collapse over time after mining. As a result, there is a *Negligible* risk of further significant subsidence events occurring after mining is completed.

In summary, our main findings and conclusions from the model forecasts are:

1. The planned underground mining of the SLC to 1150 mRL results in progressive caving of the orebody and the surface expression of the cave zone continues to propagate and expand, primarily towards the south, southeast and southwest. Relatively large steps in cave growth occur during 2024 and 2026.
2. The cave zone eventually consumes in excess of 7 million cubic metres of the southern waste dump. For context, this represents 6.3 % of the 112 million cubic metres of the dump that exists at present. The waste dump material would rill into the subsidence crater and open pit. The Clay Pit Access haul road and nearby laydown yard are also consumed by the cave over time.
3. There are no significant air gaps forecast to remain within the cave zone at the conclusion of the underground mine plan and no further growth of the cave is forecast as a result of groundwater recharge and mine flooding.
4. After decommissioning the mine dewatering infrastructure and bore field, the groundwater recharge is forecast to gradually return to a long-term phreatic surface at the 2100 mRL, which is approximately 56 m below the natural ground surface elevation.
5. Re-flooding of the rock mass in the mining precinct has a minor uplift displacement effect on the rock mass. It also causes a modest but superficial increase in rock mass damage to the open pit walls. Minor batter-scale instabilities of the pit walls could occur during the re-flooding process due to local pore water pressure increase at the batter face, but no large scale pit slope instability is forecast at any time.

Recommendations

Given the findings of this assessment, BE recommend:

1. The closure plan for the mine should include the subsidence zone and areas of related geotechnical impacts. Permanent exclusion barriers, such as solid rock bunds, should be established around the subsidence zone to barricade and prevent vehicle, animal and foot access to the subsidence-affected region. The position of the barriers should be based on measured subsidence and a risk assessment after completion of all mining, however the subsidence extents are forecast. Permanent earth bunds to restrict access to the subsidence zone are recommended to be placed outside the *Negligible* subsidence impact contour (see Figure 3-48 & Figure 3-49) and around the waste dumps and open pit, plus a further stand-off of 30 m, or to legislated requirements.

2. Ongoing monitoring of cave propagation, groundwater conditions and subsidence effects using a range of geotechnical instrumentation. The mine already has a comprehensive monitoring programme underway. This should be continued and new instruments installed, as necessary, to monitor the evolution of conditions as the cave as it increases in size and replace any monitoring ability which may be lost over time, where safely accessible.
3. Ongoing subsidence model calibration and validation of forecasts or updates, as required from time to time.
4. Ongoing groundwater monitoring and regular verification of groundwater modelling through comparison to water balance and water system responses.

Limitations

In addition to the normal resolution limits associated with the current finite element model, the main limitations of this project are:

- A 3D groundwater model and current groundwater surface were not provided as part of this project. The groundwater in the model was simulated using the pre-mining groundwater level and hydraulic conductivities provided. The phreatic surface forecast do not account for the detailed surface catchment features and closure planning at the mine and are made for excavation stability assessment purposes only.
- The current understanding of rockmass strength properties, particularly at depth and/or in future mining areas where rock testing is limited.
- The current understanding of the in-situ stress regime at depth.
- Resolution of the structural model, especially close to surface where small and intermediate scale-structures can play a significant role in the evolution of the instability around the edges of the cave zone, but also in other areas, such as the cave abutments at depth.

Enquiries

Please direct further enquiries to the undersigned.



Christopher Drover

PhD MEngSc BE (Hons) BSc

Principal Engineer, Mining & Rock Mechanics

REFERENCES

- AGE, 2017. *Ernest Henry Mine 20th year bore field performance review*, technical report to Ernest Henry mine: prepared by Australian Groundwater and Environmental Consultants.
- Beck, D., 2021. *Open pit stability and surface subsidence assessment for mine closure planning at the Ernest Henry mine*, Technical report to Glencore: Beck Engineering, Sydney, Australia.
- Board, M., Poeck, E., Lorig, L. & Pierce, M., 2009. *Geotechnical analysis in support of the feasibility assessment for underground mining at Ernest Henry mine*, Technical report to Xstrata Copper: Itasca Consulting Group, Denver, USA.
- Campbell, A., 2022. *Assessment of cave rotation options for the Ernest Henry Sublevel Cave*, Technical report to Evolution Mining: Beck Engineering, Brisbane, Australia.
- Lee, M., Mollison, L., Campbell, A. & Litterbach, N., 2010. *Rock Stresses in the Australian Continental Tectonic Plate - Variability and Controls*. 11th IAEG Congress - Geologically Active New Zealand, September 2010.

APPENDIX A - LRX CONSTITUTIVE FRAMEWORK

Constitutive model and physical composition

The LR2 constitutive framework

The Levkovitch-Reusch 2 (LR2) constitutive framework is a package of tools that describe the stress-strain behaviour of rock masses and structures. The main features of LR2 are:

- The continuum regions of the rockmass are modelled as strain-softening dilatant materials. This means that as strain increases the material softens, weakens and dilates. All parameters can vary at different rates with respect to strain changes, and this allows approximation of complex stress-strain behaviour of real rock masses. A generalisation of the Hoek-Brown yield criterion (Hoek et al. 2002) was used for the continuous regions of the rockmass, as described below.
- The behaviour of explicit discontinuities is approximated using cohesive elements. These elements are used because they can capture the mechanical response of thin structures at large deformations, which normal tetrahedral finite elements cannot achieve effectively. Cohesive elements allow simulation of the discrete behaviour associated with structures and can be used to construct a rockmass model compromising continuum regions separated by discontinuities. The structures are free to dislocate, dilate and degrade.
- Small scale structures can be represented in detailed models explicitly as cohesive elements, or ubiquitously by smearing the effects of the joints within the continuum parts of the rockmass.
- Tetrahedral higher-order elements are used for the discretization of the model geometry. These are considered essential for FE models where large gradients of displacements and damage are expected.
- The LR2 framework includes provision for hydromechanical coupling when necessary which means that the material constitutive equations (governing mechanical behaviour) are solved at the same time as the equations governing fluid flow in porous media (Darcy's equation), or solved in sequential or staggered incremental schemes, depending on the problem. This means that the modelling framework can capture the effects of pore water pressure on the strength of the rock (as may caused by groundwater percolation through the rockmass itself).
- Seismic potential can be assessed by considering the modelled rate of energy release (RER), which is the maximum instantaneous rate of energy release within a unit volume during a model frame. RER can be correlated with seismic potential and has been successfully applied to forecast seismic potential in several projects. This requires calibration using seismic data for quantitative evaluations of seismic potential.

Model outputs include displacement, stress, strain and pore water pressure fields, where the presence of pore-water pressure is implemented. Plastic strain, reported as the plastic strain tensor or as scalar equivalent plastic strain measure, represents the amount of plastic rockmass deformation after yield. The plastic strain can be interpreted as rockmass damage and usually correlates well with most engineers' visual interpretation and intuitive understanding of rockmass damage. BE's damage scale is based on plastic strain (see further below how modelled rockmass damage can be interpreted).

Constitutive model for the continuum parts

The relation between stress, strain, strength and degradation is described by the constitutive model. Generally, constitutive models consist of 3 main parts:

- (i) a stress dependent yield criterion,
- (ii) a plastic strain potential, which describes how the material will deform as a consequence of changes in stress due to damage and
- (iii) a description of how stress and strain are related.

In the LR2 framework, a generic yield criterion is used that can approximate almost any common rock mechanics yield criterion. In BE models, Hoek-Brown is applied as the base case for most problems.

The starting point for the generic criterion that can approximate Hoek Brown, Mohr coulomb or other criteria is the Menetrey/Willam strength criterion (1), described by the following function

$$\left[\frac{q}{\sigma_{ci}} \right]^2 + m \left[\frac{r}{\sigma_{ci}} \right] - \frac{p}{\sigma_{ci}} - s = 0 \quad \text{A.1 1}$$

The material constants s and m are the measures of the cohesive and frictional strength, and σ_{ci} represents the uniaxial compressive strength of intact rock. Further,

$$p = -\frac{1}{3} \mathbf{I} \cdot \boldsymbol{\sigma} \text{ is the hydrostatic pressure,}$$

$$q = \sqrt{\frac{3}{2} \mathbf{S} \cdot \mathbf{S}} \text{ is the Mises equivalent stress and}$$

$$r = \left[\frac{9}{2} \mathbf{S} \cdot (\mathbf{S} \mathbf{S}) \right]^{1/3} \text{ is the third stress invariant}$$

with \mathbf{S} being the deviatoric part of the Cauchy stress $\boldsymbol{\sigma}$. The dependence on the third invariant is introduced via the convex elliptic function in the deviatoric stress plane

$$R(\theta, e) = \frac{4(1-e^2) \cos^2 \theta + (2e-1)^2}{2(1-e^2) \cos \theta + (2e-1) \sqrt{4(1-e^2) \cos^2 \theta + 5e^2 - 4e}} \quad \text{A.1 2}$$

Here, the variable θ , defined via $\cos 3\theta = (r/q)^3$, is the deviatoric polar angle (also known as Lode angle) and the material constant e is the deviatoric eccentricity that describes the "out-of-roundedness" of the deviatoric trace of the function $R(\theta, e)$ in terms of the ratio between the Mises stress along the extension meridian ($\theta = 0$) and the compression meridian ($\theta = \pi/3$). For $\theta = 0$ and $\theta = \pi/3$ the function becomes $1/e$ and 1 respectively. The convexity of $R(\theta, e)$ requires that $0.5 \leq e \leq 1$.

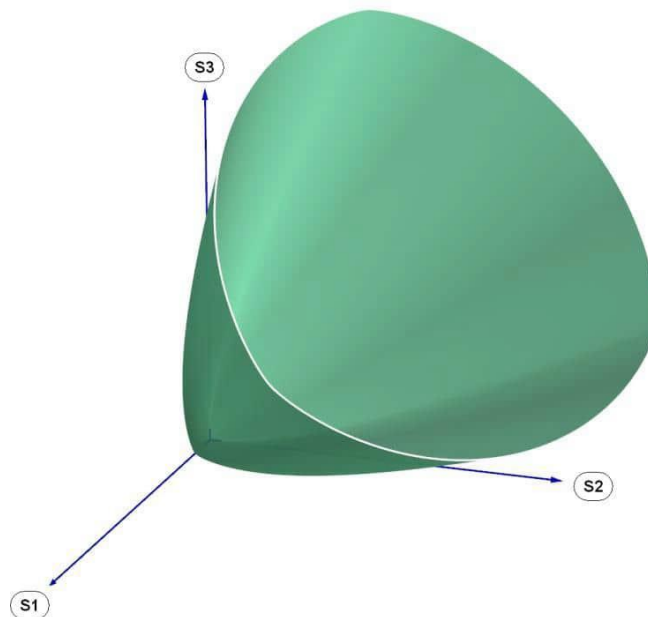


Figure A.1 1: Three dimensional representation of the Menetrey/Willam failure surface in the principal stress space

In the case of $e = 0.5$ the Menetrey/Willam failure function represents a circumscribed approximation of the Hoek-Brown (2) strength criterion

$$\left(\frac{\sigma_1 - \sigma_3}{\sigma_c} \right)^2 + m \sigma_3 = \sigma_c$$

σ_3

σ_{ci}

$$\begin{aligned} & - s \\ & = 0, \end{aligned}$$

A.13

where σ_1 and σ_3 are the major and minor principal stresses at failure. In order to recognize the similarity between the both criteria we rewrite the principal stresses representation using the relation between the stress invariants and the principal stresses

$$\sigma_1 = -p + \frac{2}{3}q \cos \theta \text{ and } \sigma_3 = -p + \frac{2}{3}q \cos (\theta + \frac{2}{3}\pi).$$

Inserting the upper expressions for the principal stresses into [3] one obtains the Hoek/Brown strength criterion in terms of the stress invariants

$$\left[\frac{2}{\sqrt{3}} \frac{q}{\sigma_{ci}} \sin (\theta + \frac{\pi}{3}) \right]^2 + m \left[\frac{2}{3} \frac{q}{\sigma_{ci}} \cos \theta - \frac{p}{\sigma_{ci}} \right] - s = 0. \quad \text{A.1 4}$$

Setting $e = 0.5$ results in an exact match between the both criteria at the extension and compression meridians. For $\theta = 0$ and $\theta = \pi/3$ both expressions are reduced respectively to

$$\left[\frac{q}{\sigma_{ci}} \right]^2 + m \left[\frac{2}{3} \frac{q}{\sigma_{ci}} - \frac{p}{\sigma_{ci}} \right] - s = 0 \quad \text{A.1 5}$$

$$\left[\frac{q}{\sigma_{ci}} \right]^2 + m \left[\frac{1}{3} \frac{q}{\sigma_{ci}} - \frac{p}{\sigma_{ci}} \right] - s = 0. \quad \text{A.1 6}$$

Thus, for $e = 0.5$ the Menetrey/Willam criterion can be considered as a circumscribed approximation of the Hoek/Brown function (Fig.A.1 2).

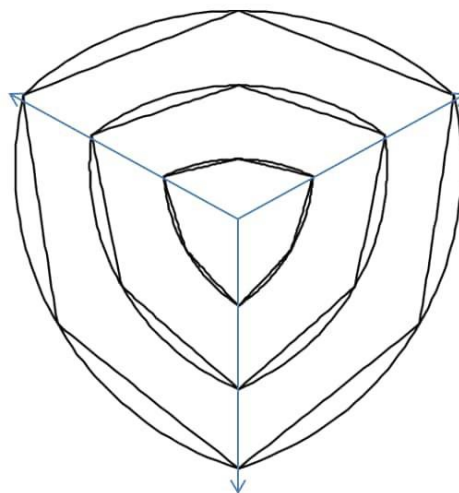


Figure A.1 2: Comparison between the Deviatoric traces of the Menetrey/Willam failure model (smooth curves) and the 1980 Hoek-Brown criteria at three levels of confinement in the principal stress space

In contrast to the Hoek/Brown model that doesn't account for the intermediate principal stress, the dependence on σ_2 in the case of the Menetrey/Willam criterion [1] is governed by the eccentricity parameter e . Increasing eccentricity values cause a higher dependence on σ_2 with the deviatoric trace of the Menetrey/Willam model approaching a circle (Fig A.1-3).

Thus, the Menetrey/Willam model possesses a material parameter that can be adjusted to match the true triaxial failure data if this is required.

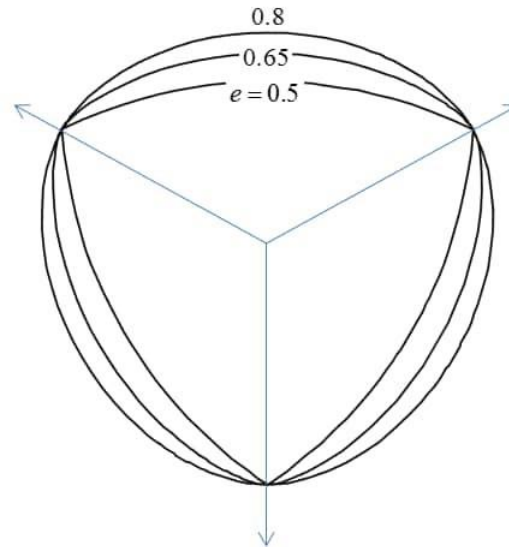


Figure A.1 3: Deviatoric traces of the Menetrey/Willam failure function for three different eccentricity values.

In 1992 the original Hoek/Brown criterion was extended (3) by an additional parameter a to the following form

$$\left(\frac{\sigma_1 - \sigma_3}{\sigma_{ci}}\right)^a + m \frac{\sigma_3}{\sigma_{ci}} - s = 0, \quad \text{A.1 7}$$

that allows to change the curvature of the failure envelope, particularly in the very low normal stress range to account for very low or zero tensile strength in heavily jointed or very poor rock masses. A corresponding extension of the Menetrey/Willam model takes the form

$$\left[\frac{q}{\sigma_{ci}}\right]^a + m \left[\frac{1}{3} \frac{q}{\sigma_{ci}} R(\theta, e) - \frac{p}{\sigma_{ci}}\right] - s = 0, \quad \text{A.1 8}$$

which is the failure criterion in the framework of the LR2 model.

Accordingly, the above failure function [7] can be considered as a circumscribed approximation of the 1992 Hoek/Brown (3) criterion.

The plastic strain potential is given by the relation:

$$\mathbf{D}_p = \lambda \frac{\partial G}{\partial \boldsymbol{\sigma}}, \quad \text{A.1 9}$$

where λ is the magnitude of the plastic strain increment and G is the flow potential

$$G = \sigma_{ci} \left[\frac{q}{\sigma_{ci}}\right]^a + \frac{1}{3} m R(\theta, e) - d_g p. \quad \text{A.1 10}$$

Here, d_g is the dilation parameter in the bulk. If the flow potential differs from the yield function the flow rule is non-associative which is the case for most geotechnical materials.

The model is implemented in such a way that all the strength parameters as well as the dilation and the Elastic modulus can be prescribed as piecewise linear functions of the equivalent plastic strain which is the accumulated deviatoric plastic strain

$$p_{eq}^{dev} = \int_0^{\|\mathbf{A}^{dev}\|} \lambda \left(\frac{\sigma}{\sigma_{ci}}\right) d\sigma \quad \text{A.1 11}$$

to account for the stress-strain behaviour of the rock type, i.e. s , m_b , d_g and the Youngs modulus are piecewise linear functions of p_{eq}^{dev} . $\|\mathbf{A}\|$ is the norm of a tensor \mathbf{A} and $(\mathbf{A})^{dev}$ the deviatoric part of a tensor \mathbf{A} .

Representation of explicit structure

The behaviour of explicit discontinuities is approximated using cohesive elements (formulation COH3D6 in ABAQUS). These elements are used because they can capture the mechanical response of thin structures at large strains, which normal tetrahedral finite elements cannot achieve effectively. Cohesive elements allow simulation of the discrete behaviour associated with structures and can be used to construct a rockmass model compromising continuum regions separated by discontinuities. The structures are free to dislocate, dilate and degrade. The constitutive behaviour of the cohesive elements can be defined using the LR2 continuum-based constitutive model, or a constitutive model specified directly in terms of traction versus separation with Coulomb yield criterion with cohesion.

The first approach is typically used to model layers of finite thickness, while the second approach is useful in applications for discontinuities of zero thickness such as fractures. Both models have the LR2 feature of elastic-plastic material behaviour in such a way that all the strength parameters as well as the dilation and the Elastic modulus can be prescribed as piecewise linear functions of accumulated plastic strain or the accumulated fault slip.

Discontinuities modelled with continuum LR2 material behaviour have the same set of material properties as LR2 bulk materials (s. chapter A.1.2 Constitutive model for the continuum parts).

The main feature of the traction-separation fault behaviour is the onset of the fault slip is described by the following cohesive-frictional criterion

$$\tau - p_n \tan \beta - c = 0 \quad \text{A.1 12}$$

with c and β being the fault cohesion and friction angle, respectively. Further, τ is the magnitude of the shear stress resolved onto the fault plane and p_n the normal stress acting across the fault. The kinematic of the fault slip deformation is described by the plastic strain rate

$$D_p = \dot{\gamma} [\text{sym}(\mathbf{s} \otimes \mathbf{n}) + \tan \psi \mathbf{n} \otimes \mathbf{n}] \quad \text{A.1 13}$$

with $\dot{\gamma}$ being the fault slip rate and ψ the fault dilation angle. Further, \mathbf{n} is the unit normal vector of the fault plane (i.e. the orientation of the finite element) and \mathbf{s} the unit vector into the direction of the resolved shear stress. The constitutive fault parameters c , β and ψ are prescribed as piecewise linear functions of the accumulated fault slip γ . The required parameter to define the mechanical behaviour of a traction-separation cohesive section are:

Table A.1 1: Material properties for traction-separation cohesive sections

D	Constitutive thickness	
ρ [kg/m ³]	Density	
E [GPa]	Elastic modulus	These parameters are a function of the accumulated fault slip.
ν	Poisson's ratio	
d	Dilation	
s	Fault cohesion	
a	Fault friction angle	

Extension for the case of transversal isotropy

The isotropic LR2 framework is extended for the case of transversal isotropy using the theory of liner stress transformation. The main assumption in this theory is that the anisotropic yield function of the actual stress σ is equivalent to an isotropic yield function of the linear transformed stress σ^*

$$f_{aniso}(\sigma) = f_{iso}(\sigma^*) \quad \text{A.1 14}$$

With this approach the usage of an arbitrary isotropic yield function is possible.

The linear stress transformation:

$$\sigma^* = L\sigma \quad \text{A.1 15}$$

is performed via a fully symmetric 4th order tensor L that has to satisfy the material symmetry conditions (similar to the elastic stiffness tensor). It is also called the stress weighting tensor. Depending on the material anisotropy type it has different number of independent material constants.

Rock with a population of parallel weakness planes or cracks can be considered as transverse isotropic. With x_3 axis being the symmetry axis and written in the material symmetry frame (Fig A.1-4),

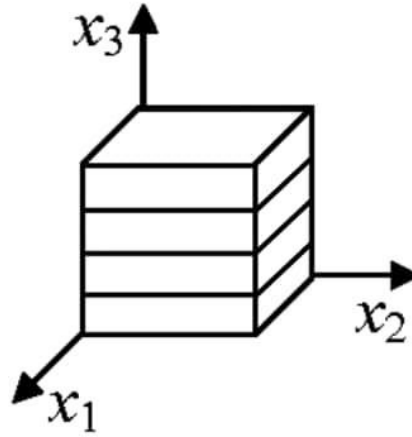


Figure A.1 4: Material symmetry frame of a transverse isotropic material.

L has the following form:

$$L_0 = \begin{pmatrix} n & 0 & 0 & 0 & 0 & 0 \\ 0 & n & 0 & 0 & 0 & 0 \\ 0 & 0 & 1 & 0 & 0 & 0 \\ 0 & 0 & 0 & n & 0 & 0 \\ 0 & 0 & 0 & 0 & s & 0 \\ 0 & 0 & 0 & 0 & 0 & s \end{pmatrix} \quad \text{A.1 16}$$

with only two independent material constants n and s .

To extend the LR2 framework for the case of transverse isotropy, the actual stress in the equation [8] is replaced by the stress transformed via [16]

$$\sigma^* = L\sigma = \begin{pmatrix} \sigma_{11}n \\ \sigma_{22}n \\ \sigma_{33} \\ \sigma_{12}n \\ \sigma_{23}s \\ \sigma_{13}s \end{pmatrix} \quad \text{A.1 17}$$

The meaning of the anisotropy constants s and n becomes clear if the yield function is analysed for the case of pure shear loading parallel to the cracks and of uniaxial compressive loading parallel to the cracks, respectively.

In the case of pure shear loading parallel to the cracks the yield condition reads:

$$f_{iso}(L\sigma) = f_{iso}(\sigma_{13}s) = 0$$

and $\sigma_{13}s = CS_{iso}$ follows. Accordingly, parameter s represents the reduction factor of the cohesive strength with respect to the isotropic case if shear loading is applied parallel to the cracks.

For the case of uniaxial compressive loading parallel to the cracks (loading direction x_1 or x_2) the yield criterion reads

$$f_{iso}(L\sigma) = f_{iso}(\sigma_{11}n) = 0$$

and $\sigma_{11}n = UCS_{iso}$ follows. Accordingly, parameter n represents the reduction factor of the uniaxial compressive strength with respect to the isotropic case if the uniaxial compressive load is applied parallel to the cracks. If compressive load is applied in x_3 direction $\sigma_{33} = UCS_{iso}$ follows which means that the uniaxial compressive strength perpendicular to the cracks is not influenced by them.

For an arbitrary direction of the uniaxial compressive load with respect to the material symmetry frame the stress weighting tensor L has to be transformed into the loading coordinate system. As a result, the simple diagonal shape is

lost and the components of the transformed stress tensor $\sigma^* = L\sigma$ attains shear components that depends also on constant s . Accordingly, the uniaxial compressive strength for such a transverse isotropic material depends on both anisotropy constants.

The pictures below show the dependence of UCS from the rotation angle of the load axis relative to x_3 axis for load direction varying from 0° (perpendicular to the cracks) to 90° (parallel to the cracks) for different combinations of s and n values.

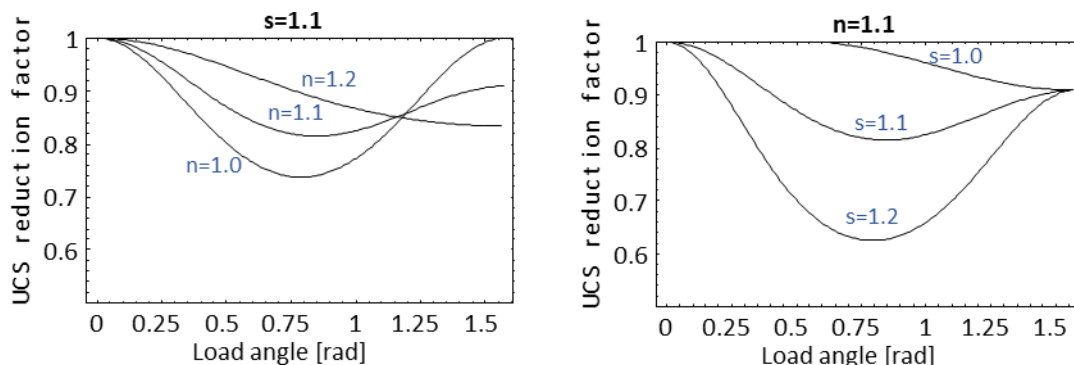


Figure A.1 5: Influence of the loading direction on UCS for different combinations of n and s values.

Model parameter to determine rock strength

The application of the constitutive model for a particular rock type or the mechanical behaviour of a discontinuity requires the determination of a set of model parameters. One common approach is to determine the model parameter with help of the GSI (geological strength index) system (see (3) and (4) for the application) and the value m_i (frictional strength of the intact rock mass). This allows an initial determination of elastic properties E and ν , the frictional strength of the broken rock m_b and the cohesive strength s as well as the dilation.

Table A.1 2: Material properties for continuum LR2 material.

UCS [MPa]	Uniaxial Compressive Strength	
GSI	Geological Strength Index	
m_i	Frictional strength of intact rock	
D	Damage parameter (Hoek-Brown)	
ρ [kg/m ³]	Plastic strain	
m_b	HB parameter for frictional strength of broken rock	These parameters are a piecewise linear function of the accumulated plastic strain.
E [GPa]	Elastic modulus	
ν	Poisson's ration	
d	Dilation	
s	cohesive strength parameter	
a	strength parameter	

A set of these parameters describes the onset of yielding for a rock type. To describe the post-yield behaviour of stress-strain relation of the rock the implementation of the constitutive model allows an arbitrary number of characteristic points to describe the stress-strain curve of the material. An example for the documentation of material properties is provided in the next figure:

EVOLUTION MINING: ERNEST HENRY SLC TO 1150 mRL CAVE PROPAGATION & SUBSIDENCE ASSESSMENT

Material property set: M12																							
Material	Code	UCS (MPa)	Density (kg/m ³)	k (m/s)	Peak							Transitional					Residual						
					mb	s	a	e	d	Eb (GPa)	v	PS_start	mb	s	d	Eb (GPa)	v	PS_start	mb	s	d	Eb (GPa)	v
Quartz andesite	QAND	90	2,700	1E-09	1.27	1.23E-03	0.503	0.6	0.079	8.71	0.25	0.5%	1.27	1.23E-03	0.079	8.71	0.25	1.5%	0.59	1.50E-04	0.018	1.67	0.25
Younger andesite	YAND	24	2,700	1E-08	0.55	1.25E-04	0.521	0.6	0.034	1.37	0.25	0.5%	0.55	1.25E-04	0.034	1.37	0.25	1.5%	0.37	4.16E-05	0.011	0.29	0.25
Undifferentiated ignimbrite	UDIG	60	2,700	1E-04	3.09	2.22E-03	0.505	0.6	0.193	5.81	0.25	0.5%	3.09	2.22E-03	0.193	5.81	0.25	1.5%	1.52	2.46E-04	0.048	1.86	0.25
Welded ignimbrite	WEIG	90	2,700	1E-08	4.19	3.87E-03	0.505	0.6	0.262	9.49	0.25	0.5%	4.19	3.87E-03	0.262	9.49	0.25	1.5%	1.91	3.35E-04	0.060	2.67	0.25
Unwelded sandy ignimbrite	UWIG	24	2,700	1E-04	4.07	1.17E-02	0.502	0.6	0.255	8.71	0.25	0.5%	4.07	1.17E-02	0.255	8.71	0.25	1.5%	1.45	4.68E-04	0.045	1.64	0.25
Lake sediments	LSED	2.4	1,900	1E-04	0.21	2.40E-04	0.530	0.6	0.013	0.37	0.25	0.5%	0.21	2.40E-04	0.013	0.37	0.25	1.5%	0.17	1.38E-04	0.005	0.28	0.25
Surface sediments	SSED	2.4	1,900	1E-04	0.21	2.40E-04	0.530	0.6	0.013	0.37	0.25	0.5%	0.21	2.40E-04	0.013	0.37	0.25	1.5%	0.17	1.38E-04	0.005	0.28	0.25
Alluvium	ALLU	12	1,700	1E-04	2.01	3.87E-03	0.505	0.6	0.126	3.46	0.25	0.5%	2.01	3.87E-03	0.126	3.46	0.25	1.5%	0.82	2.40E-04	0.026	0.82	0.25
Tuff	TUFF	12	1,700	1E-04	2.18	3.87E-03	0.505	0.6	0.136	3.46	0.25	0.5%	2.18	3.87E-03	0.136	3.46	0.25	1.5%	0.89	2.40E-04	0.028	0.82	0.25
Blue Shear	BLUE	2.4	2,100	1E-08	2.45	7.30E-04	0.515	0.6	0.153	0.65	0.25	0.5%	2.45	7.30E-04	0.153	0.65	0.25	1.5%	1.44	1.38E-04	0.045	0.28	0.25
Mineralised structures	QTVN	60	2,700	1E-04	0.65	1.97E-04	0.516	0.6	0.040	2.20	0.25	0.5%	0.65	1.97E-04	0.040	2.20	0.25	1.5%	0.31	3.04E-05	0.010	0.15	0.25
Other cohesive elements	COH1	2.4	2,700	Note 1	1.20	1.38E-04	1.000	0.6	0.075	0.50	0.25	0.5%	1.20	1.38E-04	0.075	0.50	0.25	1.5%	0.87	1.38E-04	0.027	0.50	0.25
Quartz andesite 2	QAND2	78	2,700	1E-09	1.11	8.55E-04	0.505	0.6	0.069	6.92	0.25	0.5%	1.11	8.55E-04	0.069	6.92	0.25	1.5%	0.51	1.50E-04	0.016	1.67	0.25
Quartz andesite 3	QAND3	66	2,700	1E-09	0.65	1.97E-04	0.515	0.6	0.040	2.20	0.25	0.5%	0.55	1.25E-04	0.034	1.37	0.25	1.5%	0.39	5.00E-05	0.012	0.40	0.25
Milking Cow		Elastic	Note 2	Note 3						0.05	0.25												
Backfill		Elastic	2,160	1E-04						0.05	0.25												
Underground voids		Elastic								1E-04	0.25												

- Notes**
- 1: Different k for cohesive elements not applied in this simulation.
 - 2: Density within the Milking Cow assumed to be the same as original rock.
 - 3: k within the Milking Cow assumed to be 1E-3 of k in original rock.

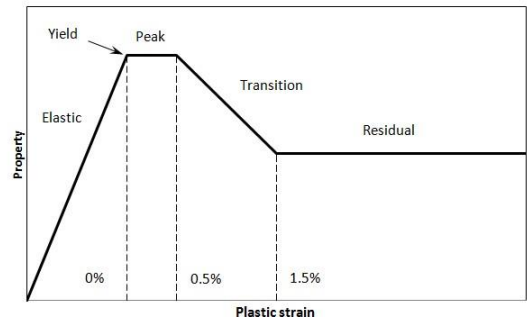


Figure A.1 6: Example for documentation of material properties of the LR2 framework.

Modelling softening behaviour

The image below shows frequently used idealizations for the softening behaviour of the rock materials. (P) denotes the peak strength material, (T) indicates the onset of softening and (R) examples for the residual strength level.

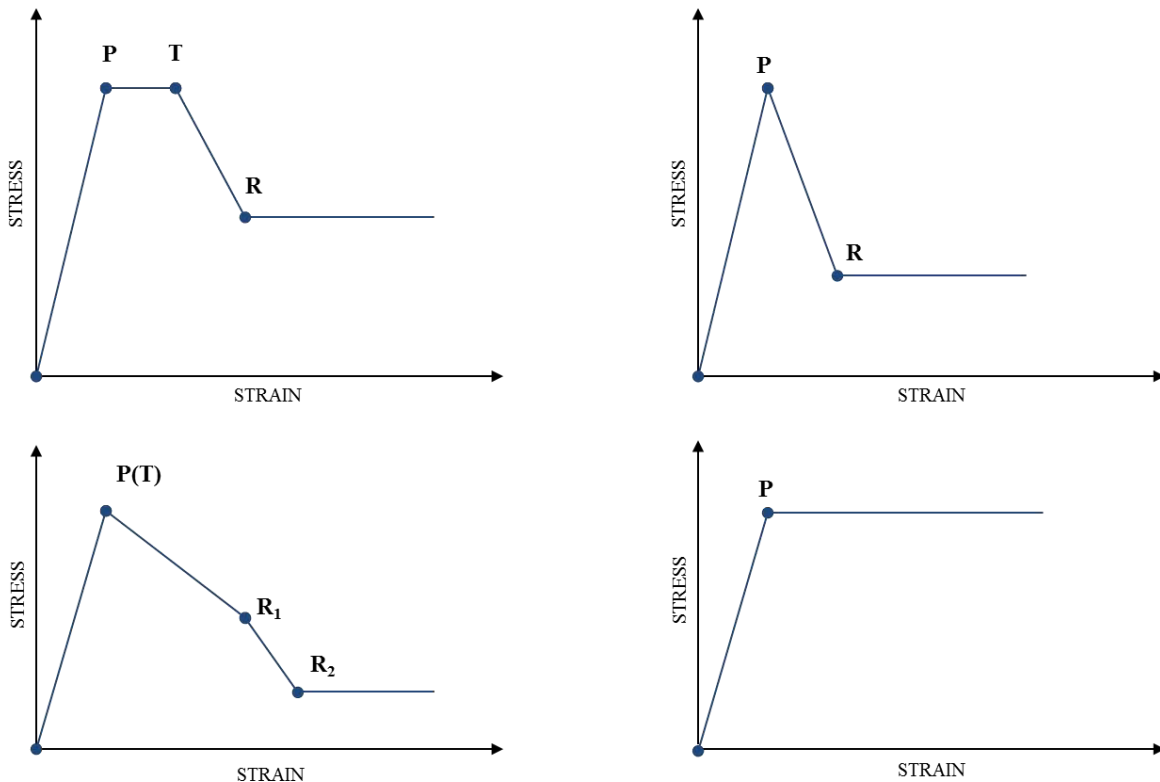


Figure A.1 7: Idealizations for the softening behaviour of the rock materials. (P) denotes the peak strength material, (T) indicates the onset of softening and (R) examples for the residual strength level.

In the LR2 framework the softening behaviour is introduced in such a way that all the strength parameters as well as the dilation and the Elastic modulus can be prescribed as piecewise linear functions of accumulated plastic strain to account for the stress-strain behaviour of the rock type, i.e. d_g , s and m_b and the Young’s modulus can evolve independently according to the available laboratory data or available description of the deformation and damage behaviour rock mass.

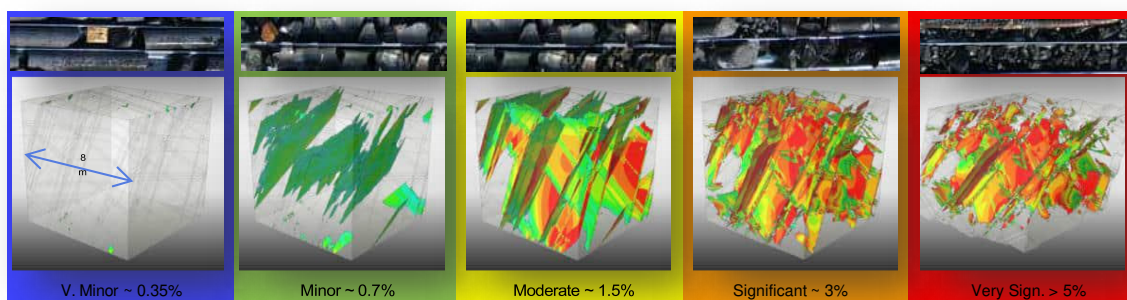
The common damage scale

As a purely phenomenological model the constitutive equations do not incorporate a damage variable that allows the direct quantification of the damage state of the rock.

For non-linear elastic-plastic models as used in the LR2 framework the rock mass damage is related to the amount of accumulated equivalent plastic strain, which is the amount of permanent (irreversible) rockmass deformation after yield. The table below shows a possible correlation of plastic strain values with the damage state of the rock. The specific correlation of plastic strain levels with damage states is often referred to as the “common damage scale (CSD)”, which can vary depending of the softening behaviour of the investigated rock.

Table A.1 8: Correlation of plastic strain values with the damage state of the rock.

Plastic strain	Damage state	Observed behaviour
>5%	Very significant	Gross distortion and comminution.
~3%	Significant	Extensive fracturing of intact rock.
~1.5%	Moderate	Constant load leads to increasing deformation.
~0.7%	Minor	No significant decrease in strength or stiffness.
<0.35%	None to very minor	Undisturbed in situ conditions.



Assessing seismic potential with RER

The mining of excavations in rock re-distributes stress and causes damage to the rock mass and discontinuities. The resulting reduction in strength and degradation in stiffness of the damaged rock and structures leads to further deformation and release of stored elastic strain energy.

One portion of this released energy is consumed by the damage process - frictional sliding and the creation of new surfaces. This energy cannot be retrieved, so is counted as ‘dissipated’. If the value of the released elastic energy is higher than the energy dissipated by the irreversible damage, the surplus is emitted into the surrounding rock. These release events are seismic events.

The magnitude (and/or the rate) of the released energy during these events can be measured in a mine using a seismic monitoring system or calculated using a model. The instantaneous, peak (i.e. maximum) rate of energy release from a volume of rock (i.e. the energy that is not dissipated) is the Rate of Energy Release (RER).

The calculated rate of energy release (RER) is used to represent seismic potential in the model. Levkovitch et al. (2013) describe RER in some detail. RER is calculated as follows:

Each model frame comprises many numerical time steps as part of the explicit FE solution procedure. For each time step, the instantaneous rate of energy release is calculated for each finite element. This is the change in elastic strain energy less the dissipated plastic energy, and represents the energy radiated from the element out into the surrounding environment. The dissipated plastic energy represents irreversible work done on the rockmass through processes such as friction on joint surfaces and creation of new fractures and is calculated from the plastic strain condition of the element.

The RER is the maximum value of the instantaneous rate of energy release calculated all the time steps during a model frame.

RER is recorded for every tetrahedral element and every cohesive element in the FE simulation at every frame. This allows RER to be calculated for the homogenised rockmass (represented with tetrahedral elements), and for the explicit structures (represented with cohesive elements). Both are important: The largest events are expected on structures, but many lower magnitude events are expected in the homogenised rockmass.

Mechanical response in the presence of pore-water pressure

In the LR2 framework the governing rock or soil is regarded as a deformable porous medium, consisting of a solid skeleton and a pore space. A fluid (e.g., water) may partially or fully saturate this pore space and is allowed to flow through connected pores, i.e. to permeate through the rockmass. Within the conceptual modelling approach both the skeleton and the voids are considered to be homogeneously smeared within the Representative Volume Element (RVE), where the proportion of pore volume space to the bulk volume is denoted as porosity.

At any material point in the model, the fluid is subjected to a fluid pressure. The spatial distribution of the fluid pressure does vary and results from the respective hydro-geological setting. This pressure is obtained as a result of a separate hydrological analysis.

The fluid interacts with the solid rock skeleton. In case of a single-phase water flow the respective fluid pressure acting on the solid skeleton is referred to as pore-water-pressure p_w , or, in case of a multi-phase flow, as wetting phase pressure.

The stresses of the entire RVE, denoted as total stresses, can be decomposed in two parts. One part is represented by the effective stresses of the solid skeleton, and the other part by the fluid pressure acting onto the solid skeleton. This is referred to as effective stress concept of Terzaghi (1936):

$$\boldsymbol{\sigma}_{tot} = \boldsymbol{\sigma}_{eff} + \alpha_B p_w \mathbf{1} .. \quad (\text{A.1 18})$$

The sign convention is such that p_w being positive in compression, and of $\boldsymbol{\sigma}$ negative in compression, i.e., $p = -1/3 \text{tr}(\boldsymbol{\sigma})$. Further, α_B denotes the Biot coefficient which is a material parameter depending on the rock type that is generally bound between $0 < \alpha_B \leq 1$. Typical values for the Biot coefficient are summarized in the literature for a range of materials. Total stresses are always used to fulfil the linear momentum (equilibrium). The constitutive response of the porous material, however, is always updated using the effective stresses. Hence, the presence of pore-water pressure reduces the skeleton stresses such that the effective confinement pressure is reduced and the material may be subject to earlier yielding. As a special case, a pore-water pressure exceeding the total confining pressure, i.e., $p_w > -1/3 \text{tr}(\boldsymbol{\sigma}_{tot})$, results in a plastic apex-mode deformation, also referred to as tensile cracking. This situation may arise in cases where a large p_w is present in a de-stressed material region, such as near a free surface.

Additional References

- (1) Terzaghi, K. (1936) "The shear resistance of saturated soils." Proceedings for the 1st. Intl. Conf. on Soil Mechanics and Foundation Engineering (Cambridge, MA), 1, 54-56.
- (2) Menetrey P. & Willam K.: "Triaxial failure criterion for concrete and its generalization", ACI Structural Journal. 92(3): 311-317, 1995.
- (3) Hoek, E. & Brown E.T.: "Empirical strength criterion for rock masses", Journal of the Geotechnical Engineering Division. 106(9): 1013-1035, 1980.
- (4) Hoek, E., Wood, D. and Shah, S.: "A modified Hoek-Brown criterion for jointed rock masses", Proc. rock characterization, symp. Int. Soc. Rock Mech.: Eurock '92, (J.Hudson ed.). 209-213, 1992
- (5) M. Cai et al. / International Journal of Rock Mechanics & Mining Sciences 44 (2007) 247–265
- (6) Reusch, F., Levkovitch, V. & Beck, D. : "Multi-scale, non-linear numerical analysis of mining induced deformation in complex environments" in "Rock Mechanics in Civil and Environmental Engineering" , Jian Zhao (Editor), Vincent Labiouse (Editor), Jean-Paul Dudd (Editor), Jean-Francois Mathier (Editor), CRC Press, 2010, 697-700.

- (7) Levkovitch, V., Reusch, F. & Beck, D. : "Application of a non-linear confinement sensitive constitutive model to mine scale simulations subject to varying levels of confining stress" in "Rock Mechanics in Civil and Environmental Engineering" , Jian Zhao (Editor), Vincent Labiouse (Editor), Jean-Paul Dudt (Editor), Jean-Francois Mathier (Editor), CRC Press, 161-164, 2010.

APPENDIX – MATERIAL STRENGTH ENVELOPE CHARTS

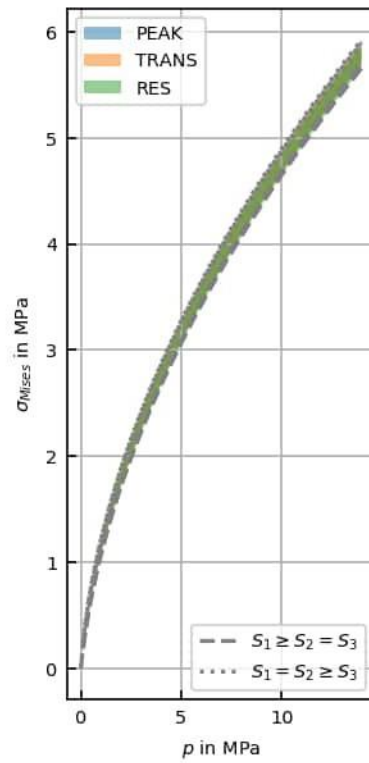
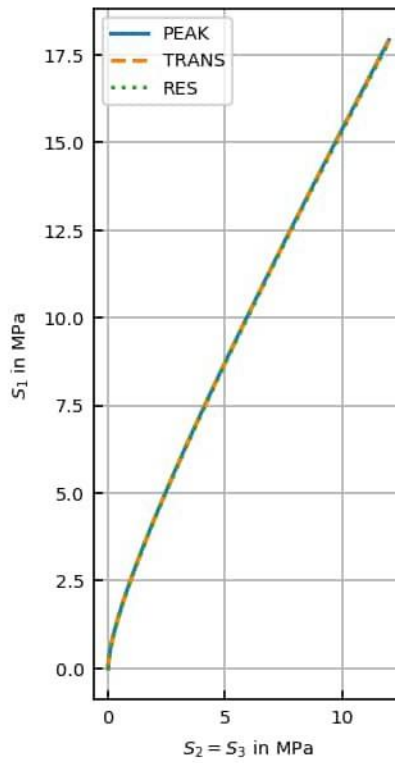
General Properties

Type	Computator V14.3 PLR
ρ [kg/m ³]	2400.00
UCS _i [MPa]	10.00
GSI	30.00
μ_{anis}	1.00
S_{anis}	1.00

LR2 Parameters

	PEAK	TRANS	RES
ϵ_{plast} [%]	0.00	0.03	13.02
E [GPa]	2.92	2.92	2.91
ν	0.25	0.25	0.25
s	6.34e-05	6.16e-05	1.00e-05
m_b	0.31	0.31	0.30
a	0.53	0.53	0.53
e	0.60	0.60	0.60
d	0.05	0.05	0.00

COVER



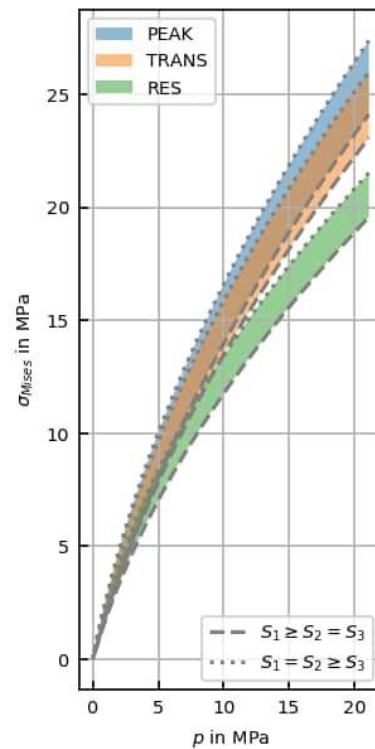
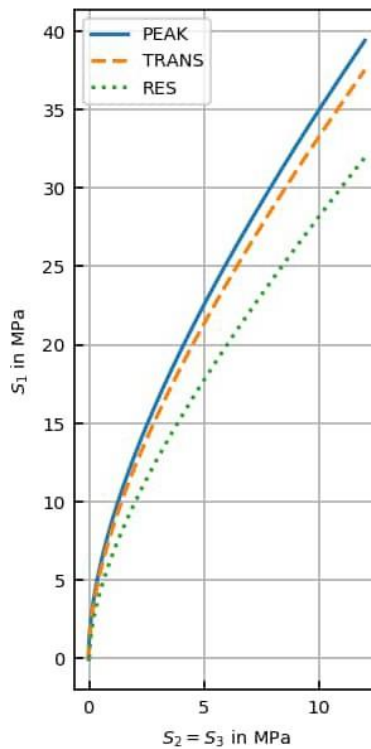
General Properties

Type	Computator V14.3 PLR
ρ [kg/m ³]	2700.00
UCS _i [MPa]	70.00
GSI	50.00
μ_{anis}	1.00
S_{anis}	1.00

LR2 Parameters

	PEAK	TRANS	RES
ϵ_{plast} [%]	0.00	0.50	10.56
E [GPa]	16.34	15.70	14.36
ν	0.25	0.25	0.25
s	4.68e-04	2.96e-04	1.00e-05
m_b	0.92	0.80	0.50
a	0.51	0.51	0.51
e	0.60	0.60	0.60
d	0.15	0.13	0.00

DIORITE



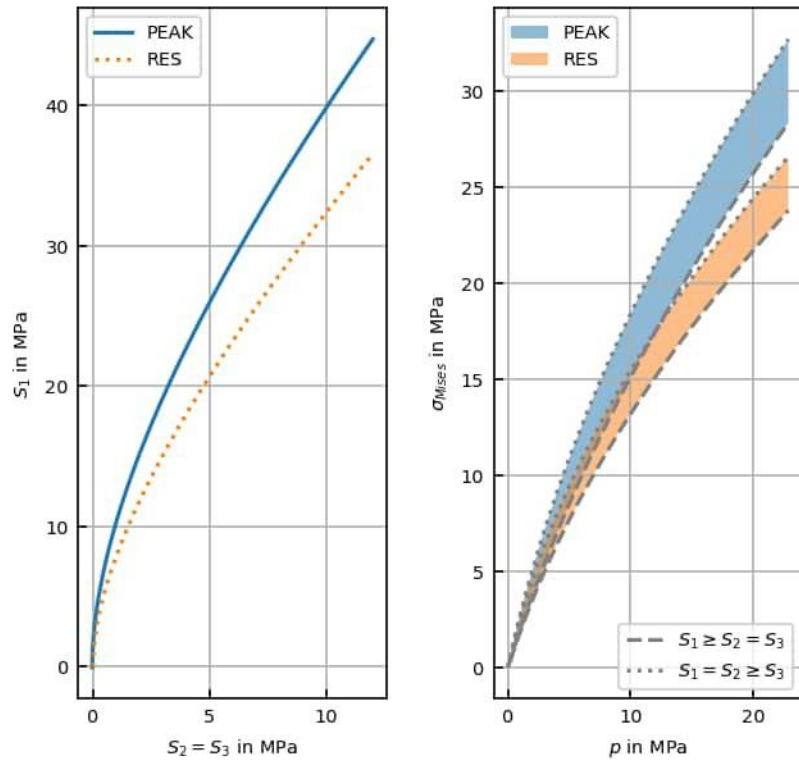
General Properties

Type	Computator V14.3 PLR
ρ [kg/m ³]	2700.00
UCS _i [MPa]	93.00
GSI	48.00
n_{anis}	1.00
s_{anis}	1.00

LR2 Parameters

	PEAK	RES
ϵ_{plast} [%]	0.00	8.15
E [GPa]	18.87	16.89
ν	0.25	0.25
s	3.83e-04	1.00e-05
m_b	1.00	0.57
a	0.51	0.51
e	0.60	0.60
d	0.17	0.00

FGAB



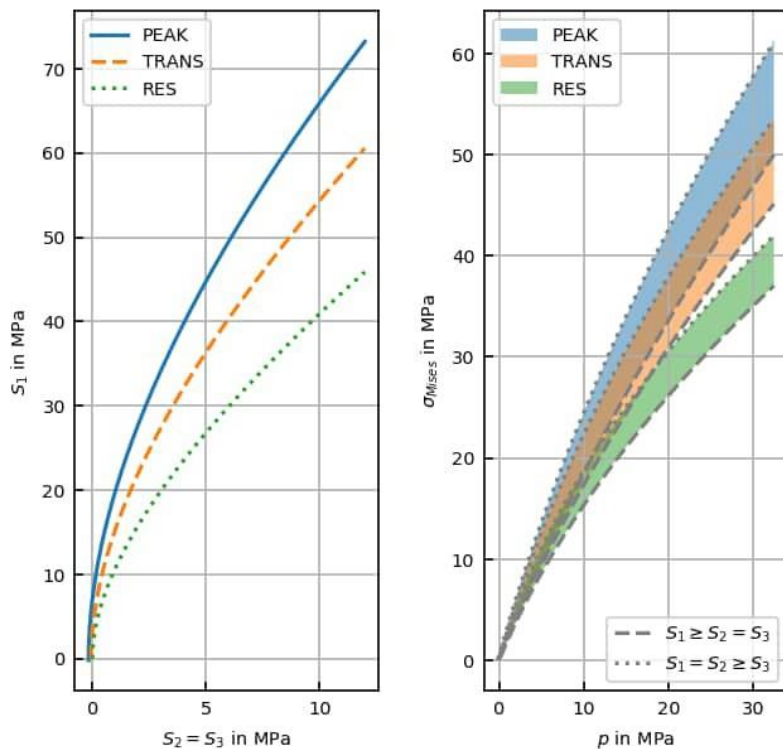
General Properties

Type	Computator V14.3 PLR
ρ [kg/m ³]	2700.00
UCS _i [MPa]	137.00
GSI	68.00
n_{anis}	1.00
s_{anis}	1.00

LR2 Parameters

	PEAK	TRANS	RES
ϵ_{plast} [%]	0.00	1.04	6.86
E [GPa]	28.32	23.55	20.08
ν	0.25	0.25	0.25
s	2.83e-03	6.33e-04	1.00e-05
m_b	2.27	1.45	0.71
a	0.50	0.50	0.50
e	0.60	0.60	0.60
d	0.38	0.24	0.00

FV



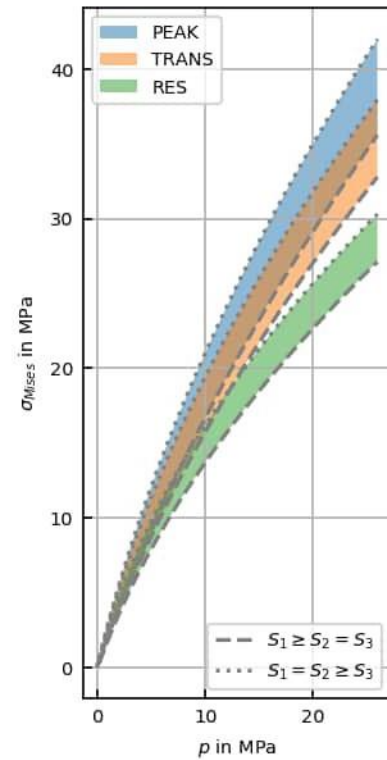
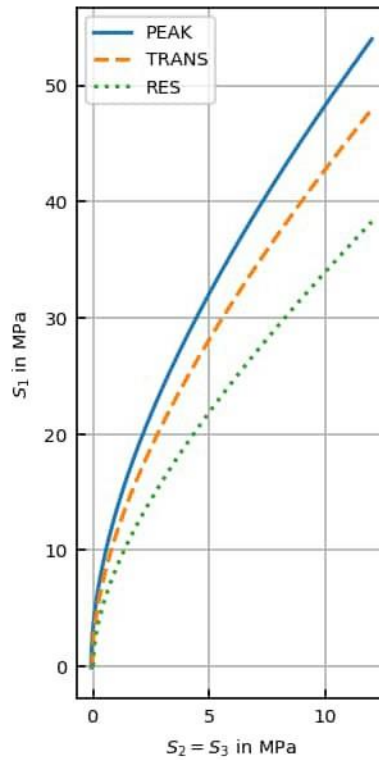
General Properties

Type	Computator V14.3 PLR
ρ [kg/m ³]	2700.00
UCS _i [MPa]	100.00
GSI	60.00
n_{anis}	1.00
s_{anis}	1.00

LR2 Parameters

	PEAK	TRANS	RES
ϵ_{plast} [%]	0.00	0.90	8.70
E [GPa]	22.28	19.92	17.53
ν	0.25	0.25	0.25
s	1.27e-03	4.62e-04	1.00e-05
m_b	1.49	1.10	0.59
a	0.51	0.51	0.51
e	0.60	0.60	0.60
d	0.25	0.18	0.00

IV



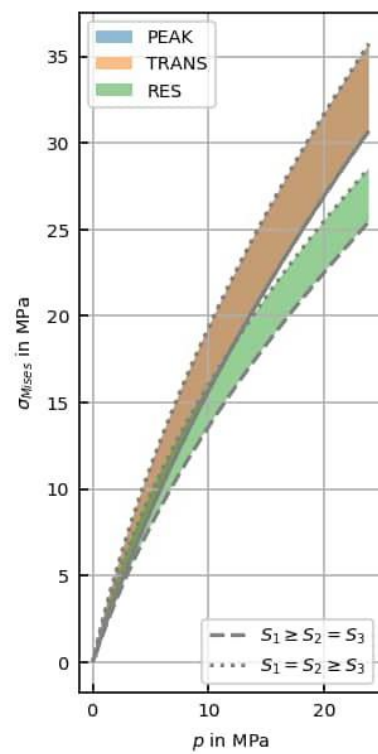
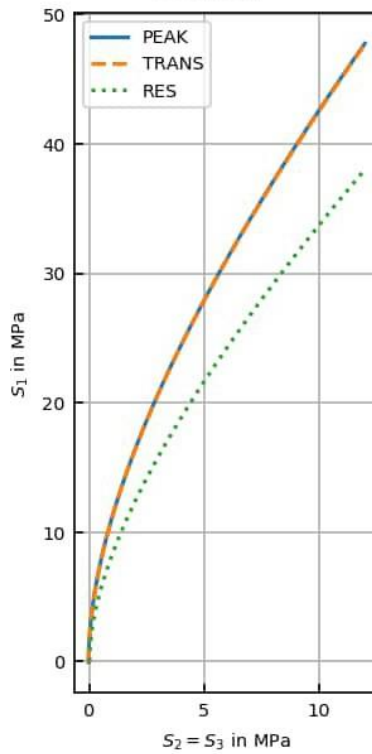
General Properties

Type	Computator V14.3 PLR
ρ [kg/m ³]	2700.00
UCS _i [MPa]	100.00
GSI	50.00
n_{anis}	1.00
s_{anis}	1.00

LR2 Parameters

	PEAK	TRANS	RES
ϵ_{plast} [%]	0.00	0.01	7.81
E [GPa]	19.94	19.92	17.53
ν	0.25	0.25	0.25
s	4.68e-04	4.62e-04	1.00e-05
m_b	1.10	1.10	0.59
a	0.51	0.51	0.51
e	0.60	0.60	0.60
d	0.18	0.18	0.00

SCHIST



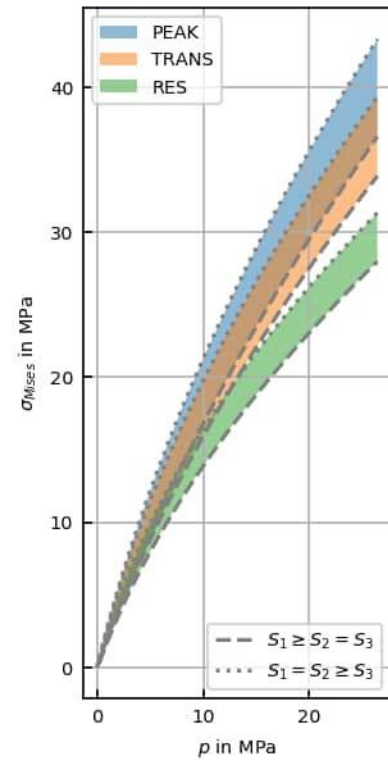
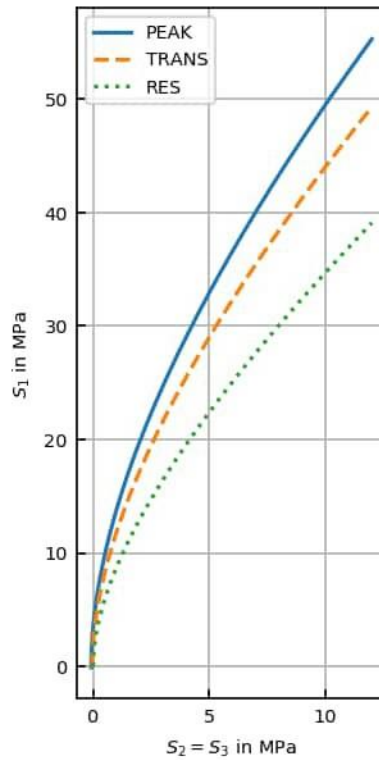
General Properties

Type	Computator V14.3 PLR
ρ [kg/m ³]	2700.00
UCS _i [MPa]	104.00
GSI	60.00
n_{anis}	1.00
s_{anis}	1.00

LR2 Parameters

	PEAK	TRANS	RES
ϵ_{plast} [%]	0.00	0.84	8.38
E [GPa]	22.71	20.39	17.86
ν	0.25	0.25	0.25
s	1.27e-03	4.83e-04	1.00e-05
m_b	1.52	1.14	0.61
a	0.51	0.51	0.51
e	0.60	0.60	0.60
d	0.25	0.19	0.00

PIV



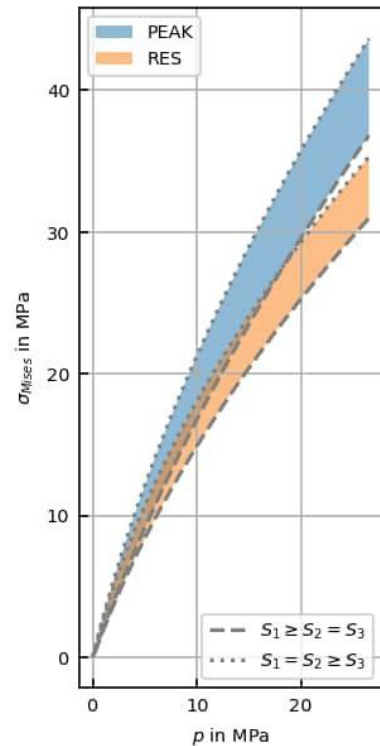
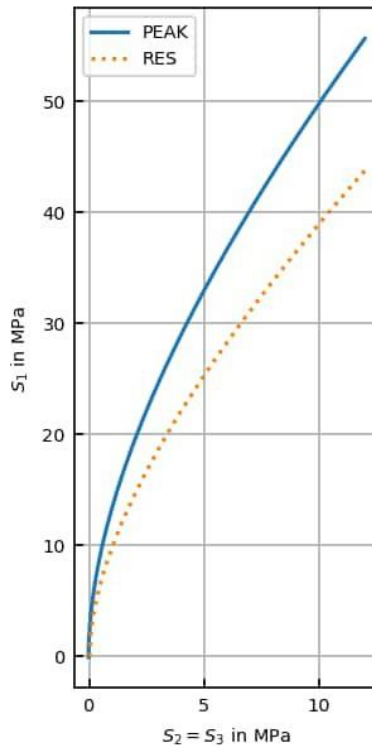
General Properties

Type	Computator V14.3 PLR
ρ [kg/m ³]	2700.00
UCS _i [MPa]	129.00
GSI	50.00
n_{anis}	1.00
s_{anis}	1.00

LR2 Parameters

	PEAK	RES
ϵ_{plast} [%]	0.00	5.54
E [GPa]	22.33	19.62
ν	0.25	0.25
s	4.68e-04	1.00e-05
m_b	1.28	0.69
a	0.51	0.51
e	0.60	0.60
d	0.21	0.00

FWSZ



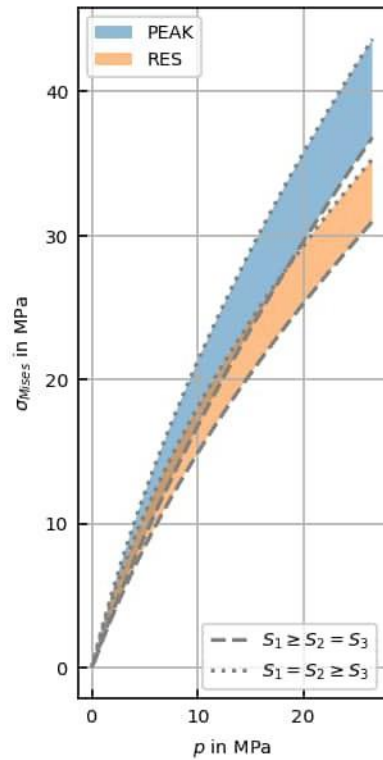
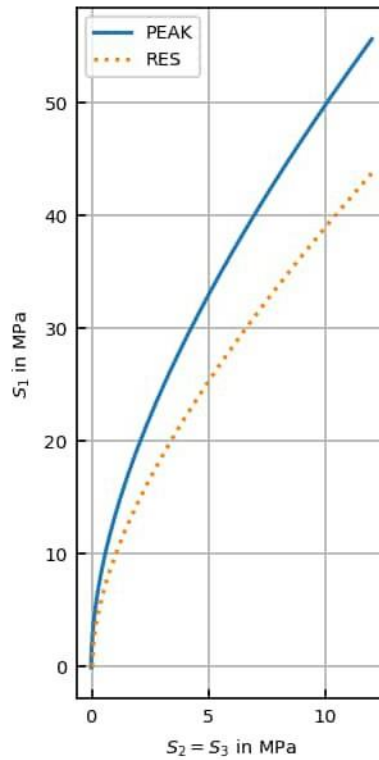
General Properties

Type	Computator V14.3 PLR
ρ [kg/m ³]	2700.00
UCS _i [MPa]	129.00
GSI	50.00
n_{anis}	1.00
s_{anis}	1.00

LR2 Parameters

	PEAK	RES
ϵ_{plast} [%]	0.00	5.54
E [GPa]	22.33	19.62
ν	0.25	0.25
s	4.68e-04	1.00e-05
m_b	1.28	0.69
a	0.51	0.51
e	0.60	0.60
d	0.21	0.00

HWSZ



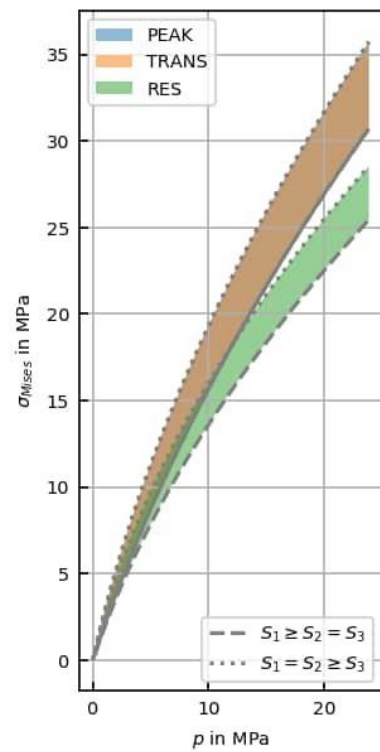
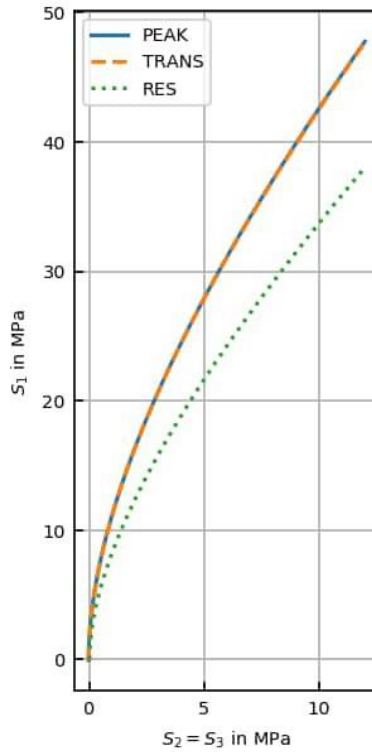
General Properties

Type	Computator V14.3 PLR
ρ [kg/m ³]	2700.00
UCS _i [MPa]	100.00
GSI	50.00
n_{anis}	1.00
s_{anis}	1.00

LR2 Parameters

	PEAK	TRANS	RES
ϵ_{plast} [%]	0.00	0.01	7.81
E [GPa]	19.94	19.92	17.53
ν	0.25	0.25	0.25
s	4.68e-04	4.62e-04	1.00e-05
m_b	1.10	1.10	0.59
a	0.51	0.51	0.51
e	0.60	0.60	0.60
d	0.18	0.18	0.00

FLT_ZONE



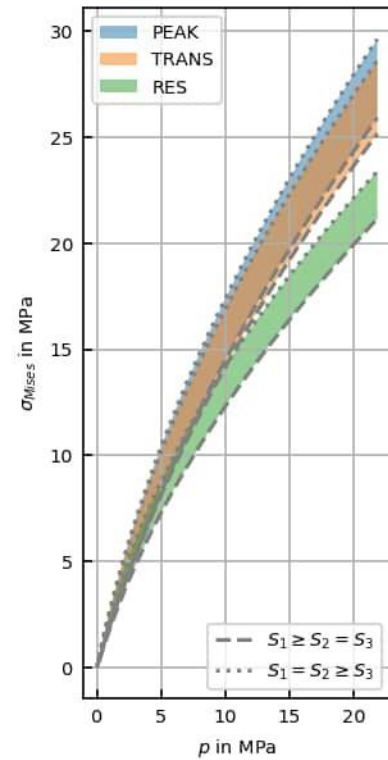
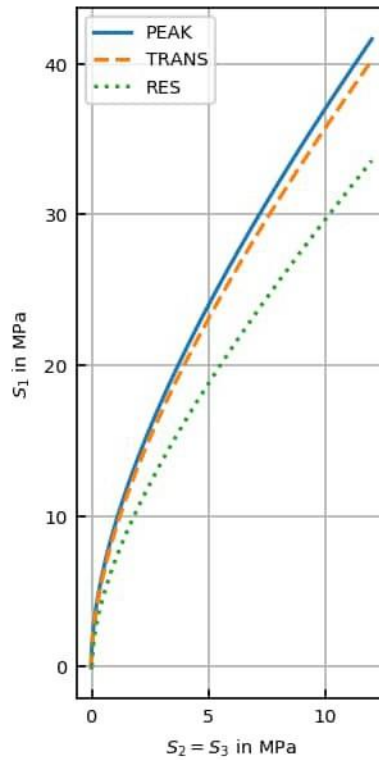
General Properties

Type	Computator V14.3 PLR
ρ [kg/m ³]	2700.00
UCS _i [MPa]	78.00
GSI	50.00
n_{anis}	1.00
s_{anis}	1.00

LR2 Parameters

	PEAK	TRANS	RES
ϵ_{plast} [%]	0.00	0.33	9.76
E [GPa]	17.44	16.95	15.33
ν	0.25	0.25	0.25
s	4.68e-04	3.41e-04	1.00e-05
m_b	0.97	0.88	0.52
a	0.51	0.51	0.51
e	0.60	0.60	0.60
d	0.16	0.15	0.00

FLT_STRG



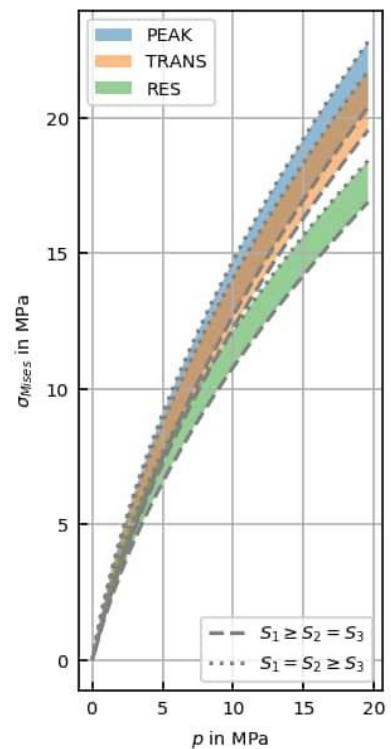
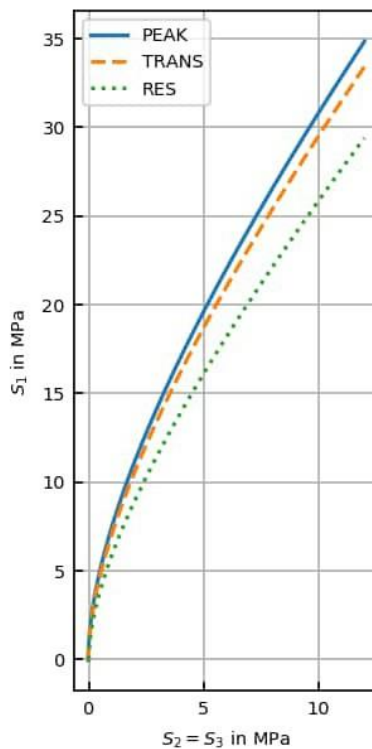
General Properties

Type	Computator V14.3 PLR
ρ [kg/m ³]	2700.00
UCS _i [MPa]	58.00
GSI	47.00
n_{anis}	1.00
s_{anis}	1.00

LR2 Parameters

	PEAK	TRANS	RES
ϵ_{plast} [%]	0.00	0.48	11.45
E [GPa]	14.08	13.63	12.72
ν	0.25	0.25	0.25
s	3.47e-04	2.28e-04	1.00e-05
m_b	0.78	0.69	0.46
a	0.51	0.51	0.51
e	0.60	0.60	0.60
d	0.13	0.11	0.00

FLT



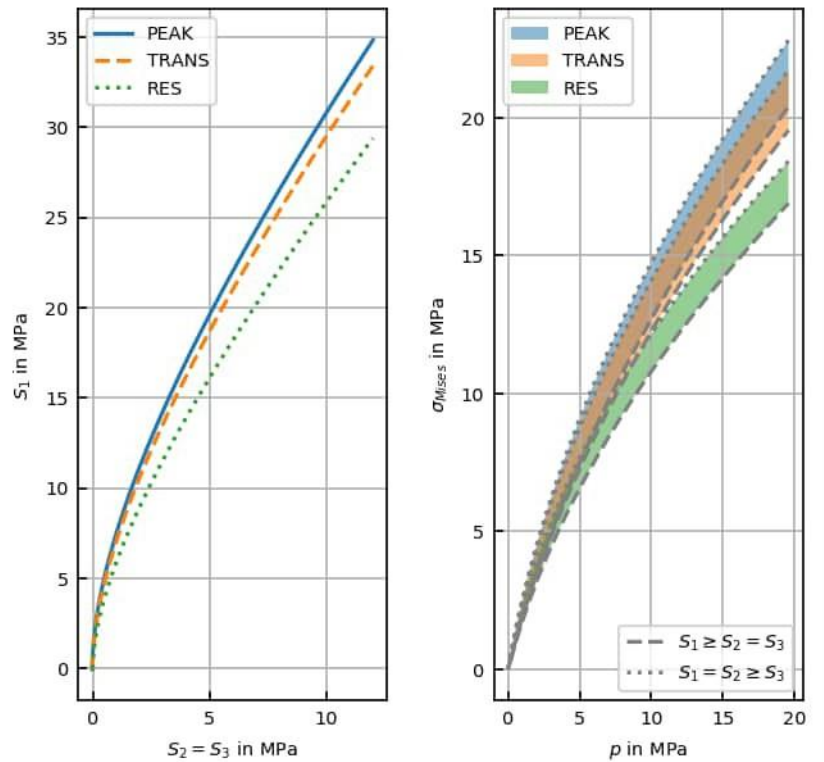
General Properties

Type	Computator V14.3 PLR
ρ [kg/m ³]	2700.00
UCS _i [MPa]	58.00
GSI	47.00
n_{aniso}	1.00
s_{aniso}	1.00

LR2 Parameters

	PEAK	TRANS	RES
ϵ_{plast} [%]	0.00	0.48	11.45
E [GPa]	14.08	13.63	12.72
ν	0.25	0.25	0.25
s	3.47e-04	2.28e-04	1.00e-05
m_b	0.78	0.69	0.46
a	0.51	0.51	0.51
e	0.60	0.60	0.60
d	0.13	0.11	0.00

DFN



General Properties

Type	Computator V14.3 PLR
ρ [kg/m ³]	2700.00
UCS _i [MPa]	100.00
GSI	60.00
n_{aniso}	1.00
s_{aniso}	1.00

LR2 Parameters

	PEAK	TRANS	RES
ϵ_{plast} [%]	0.00	0.90	8.70
E [GPa]	22.28	19.92	17.53
ν	0.25	0.25	0.25
s	1.27e-03	4.62e-04	1.00e-05
m_b	1.49	1.10	0.59
a	0.51	0.51	0.51
e	0.60	0.60	0.60
d	0.25	0.18	0.00

HOST

